



HAL
open science

Fatigue design for advanced energy systems using comprehensive, cyclic plasticity models

Zhenyu Yang

► **To cite this version:**

Zhenyu Yang. Fatigue design for advanced energy systems using comprehensive, cyclic plasticity models. Materials. Université Paris-Saclay, 2024. English. NNT : 2024UPAST094 . tel-04721609

HAL Id: tel-04721609

<https://theses.hal.science/tel-04721609v1>

Submitted on 4 Oct 2024

HAL is a multi-disciplinary open access archive for the deposit and dissemination of scientific research documents, whether they are published or not. The documents may come from teaching and research institutions in France or abroad, or from public or private research centers.

L'archive ouverte pluridisciplinaire **HAL**, est destinée au dépôt et à la diffusion de documents scientifiques de niveau recherche, publiés ou non, émanant des établissements d'enseignement et de recherche français ou étrangers, des laboratoires publics ou privés.

Durée de vie en fatigue et mécanismes de plasticité cyclique

*Fatigue design for advanced energy systems using
comprehensive, cyclic plasticity models*

Thèse de doctorat de l'université Paris-Saclay

École doctorale n°579 sciences mécaniques et énergétiques, matériaux et
géosciences (SMEMaG)

Spécialité de doctorat: Sciences des Matériaux

Graduate School : Sciences de l'ingénierie et des systèmes

Référent : Ecole Normale Supérieure Paris-Saclay

Thèse préparée dans l'unité de recherche **Service de Recherche en Matériaux et
procédés Avancés (Université Paris-Saclay, CEA)**, sous la direction de **Christian
ROBERTSON**

Thèse soutenue à Paris-Saclay, le 20 septembre 2024, par

Zhenyu YANG

Composition du jury

Membres du jury avec voix délibérative

| | |
|---|------------|
| Dr. Oliver Hubert Professeur, Ecole Normale Supérieure Paris-Saclay | Président |
| Dr. Marc Fivel Directeur de Recherche, Grenoble INP/CNRS | Rapporteur |
| Dr. Patrick Villechaise Directeur de Recherche, Ecole Nationale Supérieure de Mécanique et d'Aérotechnique | Rapporteur |
| Dr. Giacomo Aiello Ingénieur de recherche, EUROfusion | Examineur |
| Dr. Jeong-Ha You Professeur, Max Planck Institute of Plasma Physics | Examineur |

Titre: Durée de vie en fatigue et mécanismes de plasticité cyclique

Mots clés: dislocations, fissure, métaux, fatigue

Résumé: Cette thèse développe des modèles physiques permettant de prédire la durée de vie en fatigue des matériaux à structure cubique à faces centrées (CFC), en particulier l'acier inoxydable 316L. Ces modèles s'appuient sur des simulations de dynamique discrète des dislocations (DDD) réalisées précédemment. Le principal objectif de ce travail est d'adapter les modèles d'amorçage et de propagation à des conditions de chargement complexes (par exemple, l'effet de rochet associé à la présence de contrainte moyenne).

Notre modèle de propagation des fissures de fatigue de stade II reprends une équation de propagation semblable à la loi de Paris. Cette équation relie le taux de propagation des fissures à différentes variables d'évolution du matériau dans les conditions de chargement sélectionnées. En suite, sur la base d'un agrégat de grains extrait d'un échantillon de matériau réel, une étude stochastique est réalisée pour évaluer la dispersion de la durée de vie en fatigue sous différents chargements. Les résultats obtenus à partir de ce modèle concordent bien avec les données expérimentales sous différentes formes (durée de vie en fa-

tigue, taux de propagation, etc.) en termes de valeur absolue et de dispersion de la durée de vie en fatigue.

Le modèle d'amorçage des micro-fissures repose sur un mécanisme qui s'appuie sur le taux de croissance des extrusions (PSM) observées dans les grains de surface et prédites par les calculs DDD. Pour évaluer le taux de croissance des extrusions en fonction des conditions de chargement, de la forme des grains et de l'environnement (air, vide, etc.), un modèle général de fatigue est proposé pour prédire l'effet de rochet afin d'évaluer son impact sur l'amorçage des micro-fissures. Les deux modèles sont calibrés et validés à l'aide de données expérimentales sous diverses formes aussi.

Les résultats de ces deux modèles sont combinés pour fournir un modèle de prédiction de la durée de vie en fatigue couvrant une large gamme de chargements, divisés en deux catégories : l'une contrôlée par la propagation des fissures et l'autre par l'amorçage des fissures. Les résultats sont validés par comparaison avec les données expérimentales pour l'ensemble de la gamme de chargement sélectionné.

Title: Fatigue lifetime prediction based on dislocation-mediated plasticity mechanisms

Keywords: dislocations, cracking, metal, fatigue

Abstract: This thesis develops advanced physical models for predicting fatigue life in face-centered cubic (FCC) materials, particularly 316L stainless steel. Building upon previous discrete dislocation dynamics (DDD) simulations, the research focuses on the mechanisms of fatigue crack initiation and propagation under complex loading conditions (for instance, the ratcheting effect due to the presence of mean stress). This work introduces a Stage II fatigue crack propagation model and a micro-crack initiation model, based on the microscopic plasticity mechanisms observed in DDD simulations.

The Stage II fatigue crack propagation model summarized the findings of DDD simulations in the form of a Paris' law-like equation. This equation correlates the crack propagation rate to various internal material variables and loading conditions. Next, based on a grain aggregate extracted from an actual material specimen, a stochastic investigation is performed to evaluate the dispersion of fatigue lifetime under different loadings. The results obtained from this model are compared with applicable

experimental data in different forms (fatigue lifetime, propagation rate, etc.) in terms of both the absolute value and dispersion of the fatigue lifetime.

Our micro-crack initiation model is based on the extrusion growth rate of the persistent slip markings (PSM) observed on the surface of grains. Prior DDD simulations helped develop an equation to evaluate the extrusion growth rate based on the loading conditions, grain shape and other environmental factors. In this work, we developed a specific model accounting for the ratcheting effect in order to evaluate its impact on the PSM growth rate. Both the models are calibrated and validated using experimental data in various forms.

The findings of these two models are combined to provide a fatigue lifetime prediction model that covers a broad range of loading conditions. The model results highlight two distinct lifetime regimes: one controlled by the crack propagation and the other by the crack initiation. The results agree well with experimental data for the entire range of supported loadings.

Acknowledgements

This PhD thesis would not have been possible without the guidance, support, and encouragement of many people. I would like to take this opportunity to express my gratitude to those who have contributed to this work and made my journey a rewarding experience.

First and foremost, I would like to express my deepest gratitude to my supervisor, Dr. Christian ROBERTSON, for his invaluable guidance, constant support, and encouragement throughout this entire process. His insight, feedback, and patience have been instrumental in shaping this research. I am incredibly fortunate to have had a supervisor who cared so deeply about my work and consistently steered me in the right direction.

I am deeply grateful to SRMA/LC2M for providing an intellectually stimulating academic environment. The access to excellent resources, including the spacious office, robust servers, and the collaborative atmosphere, has played a significant role in fostering my intellectual development.

I would like to acknowledge the financial support I received from France Ambasad in China and Schneider Electric. Without this support, it would not have been possible to carry out this research. I would also like to extend my appreciation to Campus France for providing the necessary resources and support throughout my stay in France.

I would like to express my sincere gratitude to the French Embassy in China and Schneider Electric for their generous financial support, without which this research would not have been possible. I also extend my appreciation to Campus France for providing essential resources and support throughout my stay in France.

I am deeply grateful to Dr. Laurent DUPUY for his invaluable assistance with the NumoDis software during my research, and for his personal support during difficult times. I would also like to extend my heartfelt thanks to my friends, Sihan, Qiang, Dorian, Guanzhong, and Hao, for their unwavering support and encouragement both within and beyond the academic sphere. A special thank you to Dorian, whose help made it possible for me to pursue this opportunity in France.

Most importantly, I would like to express my profound gratitude to my family. To my parents, Haibo and Xiuying, and to my aunt and uncle, Haiyan and Chunshan, your unwavering love, support, and belief in me have been the foundation of my strength throughout this journey. Your sacrifices and constant encouragement have inspired me to persevere and reach this important milestone. I am also deeply thankful to my cousin, Yiyang, for always being there when I needed someone to talk to, offering both moral support and friendship. Finally, to Kasugano Sora, thank you for your love, compan-

ionship, and for being the source of strength that helps me move forward in life.

Introduction

Fatigue represents an important structural failure case in various industrial sectors, especially in those where safety is of paramount importance, such as the nuclear industry, aviation, and automotive fields. For instance, thermal fatigue has been identified as one important cause for a series of nuclear reactor shutdowns in France [1]. Thermal fatigue arises from cyclic temperature variations, leading to repeated stress within materials due to differences in thermal expansion. In the aviation industry, repeated cabin pressurization, take-off and landing cycles, as well as turbulence, all contribute to material fatigue [2]. Fatigue is also a factor that must be considered to enhance both the safety and economy of civil engineering structures [3]. Furthermore, materials manufactured using modern techniques, such as additive manufacturing or high-entropy alloys, are also subjected to fatigue damage [4, 5].

At the microscopic scale, cyclic stresses can cause an evolution in the material microstructure, notably through the accumulation and interaction of dislocations, which gradually change the material's mechanical properties. This process can lead to the emergence of cracks, whose eventual propagation may result in the structure's failure. Such damage analysis underscores the importance of defining a *fatigue life* for materials, corresponding to the period during which they can withstand cyclic loads without undergoing critical failure.

Fatigue can be categorized based on the amplitude of the applied load, leading to the distinction between high cycle fatigue (HCF) and low cycle fatigue (LCF) regimes. The demarcation between these two regimes is typically established based on the number of cycles needed to induce failure. Usual metallic material subjected to an HCF regime has a life expectancy of more than 10^5 cycles, whereas in the LCF context, failure generally occurs after before several 10^3 cycles. The predominant mechanisms differ between these two categories of fatigue: in the case of HCF, crack initiation plays a crucial role in determining the material's lifespan [6], whereas for LCF, crack propagation may become the dominant contribution. This conceptual distinction underpins the orientation of the fatigue models examined in this thesis, focusing on the mechanisms of crack initiation and propagation depending on the considered fatigue regime.

While the macroscopic behavior of materials subjected to cyclic loading is extensively documented, the microscopic mechanisms that contribute to fatigue damage remain incompletely understood. Investigating fatigue at the microstructural level is pivotal for grasping the initiation and progression of cracks, as well as for the formulation of predictive models for fatigue life. On one side, microscopic models offer insights into the mechanisms of fatigue,

which holds significant potential for the innovation of new materials and the enhancement of existing ones. On the other side, the advancement of predictive models for fatigue life, incorporating microscopic characteristics, not only enables more precise predictions of fatigue life but also facilitates the monitoring of fatigue damage in existing structures.

In metallic materials, the fatigue damage usually initiates at the material's surface. The observation of fatigue-induced surface evolutions was identified a century ago [7], paralleled by advancements in observational technologies and experimental methodologies. Presently, with the advent of atomic force microscopy (AFM) and scanning electron microscopy (SEM), the characteristics of surface relief due to fatigue damage are meticulously observed. It is now firmly established that, on the surfaces of metals, the formation of persistent slip bands (PSBs) and persistent slip markings (PSMs) directly influence the initial crack initiation [8, 9]. Additionally, the interplay between fatigue cracks and PSBs significantly influences crack propagation, at least during the early crack propagation stages. Nonetheless, experimental observations alone cannot comprehensively delineate the physical mechanisms by which dislocations within PSBs instigate crack initiation and propagation. Fortuitously, the evolution of dislocation dynamics, augmented by simulation tools (e.g., TRIDIS, which is highly cited in this thesis), and the exponential growth in computational power, have made it feasible to simulate the behavior of dislocations in substantial numbers. Although not directly manipulated in this thesis, the principles underlying these techniques are pivotal for understanding the models developed herein and will be expounded upon in a dedicated chapter.

Based on this detailed, comprehensive work, this thesis contributes to the construction of physical models of fatigue by considering sub-grain plasticity mechanisms observed in simulations and experiments, incorporating stochastic factors in an attempt to address the sub-grain to macroscopic scale transition. These models will also be validated and verified with experimental data conducted worldwide. The structure of this dissertation will be as follows:

1. The first chapter will provide a context study along with the methodology applied in the study. It will also include a detailed bibliography of the existing work surrounding the topic.
2. Chapter 2 introduces the concept of 3D dynamics of dislocation (DDD), the simulation software (TRIDIS and NumoDis), and the origin of the data used in this thesis.
3. Chapter 3 will discuss the study of the first model developed during the thesis, which is the Stage II fatigue crack propagation model. This includes the theoretical basis, the formulation of equations, and their

application to polycrystalline stainless steel, as well as the scale transition techniques.

4. Chapter 4 will delve into the initiation stage in HCF. This chapter includes all submodels that calculate the intermediate physical quantities used in the final model of fatigue life. It will also discuss the simulation of dislocation dipoles and the results of these simulations, which are used to enhance precision around dipole distribution.
5. Chapter 5 will conclude the thesis and outline perspectives for future work.
6. Finally, there will be a detailed appendix on the numerical techniques applied in the thesis, along with the programming conventions and the data utilized. This section aims to provide comprehensive insights into the computational approaches underpinning the research, ensuring transparency and reproducibility of the methods and findings presented.

Furthermore, all programs developed during the course of this thesis will be open source and accessible via the author's GitHub repository, with the exception of certain copyrighted data. This approach underscores a commitment to the open science movement, facilitating peer review, collaboration, and further research by making the tools and methodologies employed throughout the thesis widely available to the academic community and beyond.

Contents

| | | |
|----------|--|-----------|
| 1 | Context | 13 |
| 1.1 | Industrial context | 13 |
| 1.2 | Basic concepts of fatigue | 16 |
| 1.2.1 | HCF and LCF | 17 |
| 1.2.2 | Ramberg-Osgood model | 19 |
| 1.2.3 | Fatigue crack: different stages | 19 |
| 1.3 | Basic concepts of dislocation dynamics | 21 |
| 1.4 | Bibliography: Methods of studying and predicting fatigue life | 25 |
| 1.4.1 | Dislocation dynamics and fatigue | 25 |
| 1.5 | Summary of previous works | 26 |
| 1.5.1 | DDD simulations of fatigue behavior of 316L stainless steel | 26 |
| 1.5.2 | Study of the Stage I crack initiation (stage 0) | 33 |
| 1.5.3 | Study of the Stage I fatigue crack propagation (stage 1) | 37 |
| 1.5.4 | Conclusion | 43 |
| 1.6 | Objective of the thesis | 44 |
| 2 | Stage II crack propagation model | 47 |
| 2.1 | Introduction | 50 |
| 2.2 | Literature review of stage II fatigue crack propagation models | 51 |
| 2.3 | Development of the theoretical equations | 53 |
| 2.3.1 | Setup of the prior DDD simulations | 54 |
| 2.3.2 | Basic DD simulation results | 56 |
| 2.3.3 | Stage II crack propagation model | 61 |
| 2.3.4 | Conclusion of the theory and equation establishment | 67 |
| 2.4 | Numerical methods and applications | 68 |
| 2.4.1 | Simplifications and deductions | 68 |
| 2.4.2 | Integration method | 70 |
| 2.5 | Parameter sensitivity analysis | 71 |
| 2.5.1 | Effect of changable parameters | 72 |
| 2.5.2 | Influence of integration step size | 74 |
| 2.5.3 | Conclusion | 75 |
| 2.6 | Evaluation of the macro-scale fatigue lifetime using stochastic analysis | 77 |
| 2.6.1 | EBSD result file reading | 79 |
| 2.6.2 | Integration algorithm | 83 |
| 2.6.3 | Results and analysis | 85 |
| 2.7 | Conclusions | 90 |

| | | |
|----------|--|------------|
| 3 | General fatigue model and investigation of the ratcheting effect | 93 |
| 3.1 | Introduction | 93 |
| 3.2 | Brief review of ratcheting models | 95 |
| 3.3 | Theory and construction of the equations | 96 |
| 3.3.1 | Model construction and calculation | 98 |
| 3.3.2 | Numerical methods | 99 |
| 3.3.3 | Application of the mean stress | 100 |
| 3.4 | Results and discussion | 103 |
| 3.4.1 | Model output and interpretation | 103 |
| 3.4.2 | Study of the parameters and sensitivity analysis | 110 |
| 3.4.3 | Step load tests | 117 |
| 3.4.4 | Calibration of the ratcheting model | 119 |
| 3.4.5 | Cyclic stress-strain results | 124 |
| 3.4.6 | Representative ratcheting rate (<i>Abacus</i>) | 124 |
| 3.5 | Conclusions | 125 |
| 4 | Crack initiation model in HCF loading conditions | 129 |
| 4.1 | Micro-crack initiation: general ideas and concepts | 129 |
| 4.2 | Literature review of existing crack initiation models | 130 |
| 4.3 | Proposed crack initiation scenario and corresponding governing equations | 136 |
| 4.4 | Estimation of the number of slip bands (in single grains) | 139 |
| 4.4.1 | Analytical solution of the system | 141 |
| 4.4.2 | Experimental calibration of the number of slip bands | 143 |
| 4.5 | Estimation of the extrusion width evolutions | 148 |
| 4.6 | Results and discussion | 148 |
| 4.7 | Conclusion | 150 |
| 5 | Conclusion | 153 |
| 5.1 | Summary of the thesis | 153 |
| 5.2 | Future work | 155 |
| 6 | Appendix | 157 |
| 6.1 | Material details | 157 |
| 6.2 | Machine learning calibration process | 160 |
| 6.3 | Dipole strength distribution investigation | 163 |
| 6.3.1 | Simulation setup | 165 |
| 6.3.2 | Simulation results | 165 |
| 6.3.3 | Conclusion | 166 |

1 - Context

This initial chapter outlines the scope and context of this thesis. It provides the reader with essential background knowledge needed for understanding the thesis, covering the industrial context, fundamental concepts of fatigue and dislocation dynamics, established models for predicting fatigue life, and particularly, prior research in 3D dislocation dynamics simulations. The objectives of the thesis are clearly stated at the end of this chapter.

The chapter is organized as follows:

1. **Industrial context** discusses the importance of fatigue in industrial uses, especially in the nuclear and aerospace sectors. It also clarifies the relationship between the DEMO project, the MAT project, and this thesis.
2. **Basic concepts of fatigue** provides clear definitions of terms and concepts often used in this study. It explains the different stages of fatigue and the differences between High Cycle Fatigue (HCF) and Low Cycle Fatigue (LCF).
3. **Basic concepts of dislocation dynamics** introduces the basic principles of dislocation dynamics. Notable simulation software such as *TRIDIS* and *NumoDis* will be detailed.
4. **Bibliography: Methods of studying and predicting fatigue life** reviews existing models for estimating fatigue life and cyclic plasticity. It discusses the limitations of these models and highlights the importance of this research work.
5. **Summary of previous works** summarizes key simulation studies and the findings of Robertson and Depres from 2004 to 2020. The results from these studies will be often cited in later chapters.
6. **Objective of the thesis** clearly states the goals of the thesis, based on the discussions in the earlier sections.

1.1 . Industrial context

Fatigue is a critical issue in materials science, particularly in the design and operation of nuclear reactors. The fatigue design rules are often too conservative, yet they sometimes fail to prevent early component failure under actual service conditions. In the nuclear industry, unexpected fatigue failures can lead to extensive and costly testing campaigns. These issues partly stem from

an inadequate understanding of the mechanisms of plasticity taking place at the crack tip, which are significantly influenced by exacerbating factors not always accounted for during laboratory tests. Improved management and design of fatigue life could be realized through the development of physically-based numerical models that accurately represent the dominant causes of fatigue damage across a wide range of loading and material conditions.

For example, the nuclear industry has a significant need to prevent fatigue failure in critical components. This type of cracking, which appears either as isolated cracks or networks of cracks, has been frequently observed in auxiliary piping made of austenitic stainless steel (types AISI 304L and 316L) in Pressurized Water Reactors. In a few rare cases, sudden pipe ruptures have been observed. In many cases, the damage directly involves thermal fatigue, which affects cooling line sections that experience strong and fluctuating thermal gradients. Figure 1.1 illustrates a typical issue that occurs at the mixing zones of hot and cold fluids in a cooling system, while Fig. 1.2 helps explain the phenomenon of thermal fatigue.

There is a more recent and challenging case of the divertor of a tokamak fusion reactor. The "divertor" is a critical component designed to manage heat and particle fluxes generated during the fusion process. It serves as an exhaust system that removes waste materials, particularly helium ash and other impurities, from the plasma. The collision between these particles and the plasma-facing unit (PFU) of the divertor captures the heat and energy from the plasma, which is then converted to thermal energy and absorbed by the cooling tube beneath the divertor. Due to the cyclic operation of a tokamak fusion reactor, the divertor and its cooling tube endure substantial fatigue loads.

To improve the efficiency of heat transfer under these conditions, EUROfusion has developed a new material called CuCrZr, a copper-chromium-zirconium alloy noted for its high thermal conductivity high-temperature strength and corrosion resistance, used in the cooling tubes of the reactor. However, estimating the fatigue lifetime of this material requires extensive experimentation to determine its fatigue properties. This task is complicated by factors such as the presence of mean stress, which induces the "ratcheting effect" that accelerates crack initiation (refer to Chapter 4). These complex loading conditions significantly increase the challenges of predicting fatigue life using purely empirical methods.

In alignment with the timeline of EUROfusion's Fusion Power Plants' roadmap, particularly the DEMO construction, it is urgent to assess the fatigue performance of CuCrZr under these specific conditions. The work of this thesis overlaps slightly with the efforts of the MAT group, a part of EUROfusion responsible for material research and development, including compiling a material property handbook and database for future design and construction of

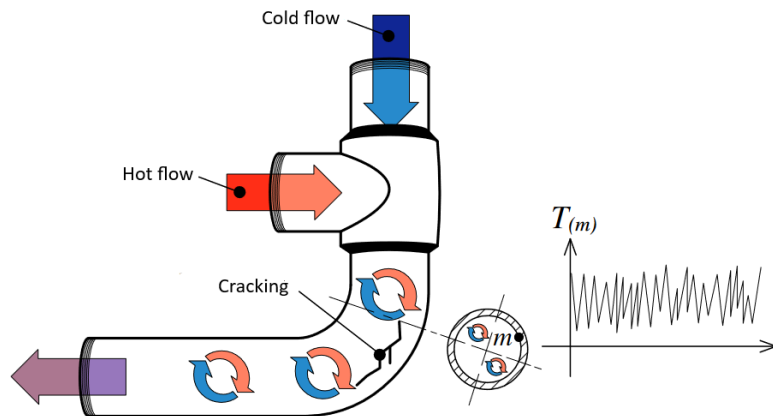


Figure 1.1: Example of cooling line section affected by thermal fatigue damage: mixing tee

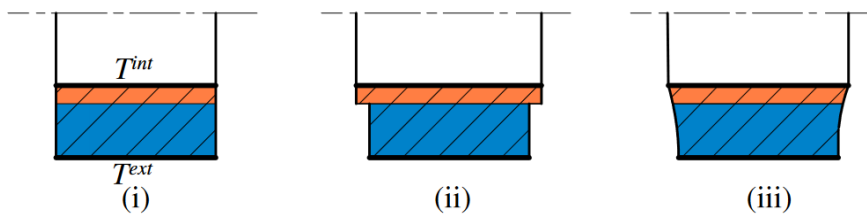


Figure 1.2: Mechanism of thermal-mechanical stress creation: a temperature gradient is established across the thickness of the wall (i). If the hot and cold zones were to expand independently, this would lead to a geometric incompatibility (ii). Compatibility is restored through the creation of thermal-mechanical stress (iii). Since the internal temperature (T^{int}) varies over time, the internal stresses also vary, leading to fatigue loading conditions.

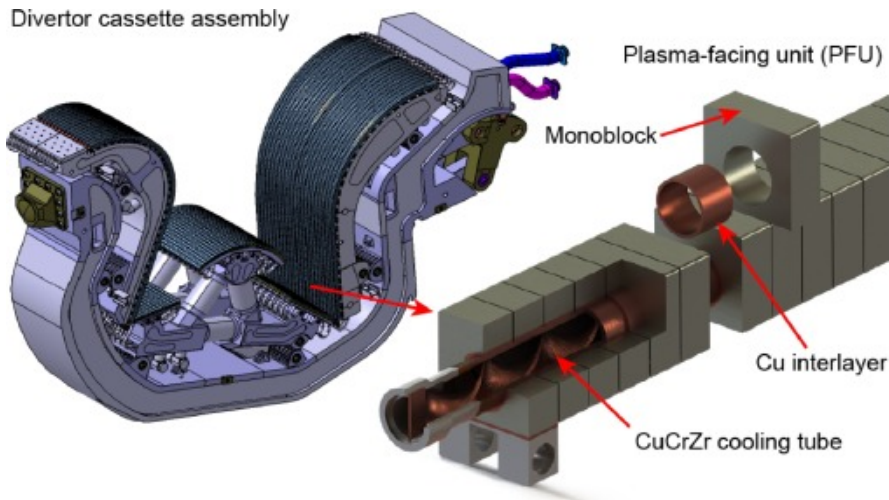


Figure 1.3: The divertor is a critical fusion reactor component transferring a part of the plasma kinetic energy into thermal energy. The divertor plasma facing material is actively cooled by water lines.

the DEMO fusion reactor. This thesis focuses on developing models for fatigue crack propagation and crack initiation, considering mean stress, based on 3D dislocation dynamics simulations. The developed models are based on A316L stainless steel and could be generalized to other materials with an FCC structure, such as CuCrZr.

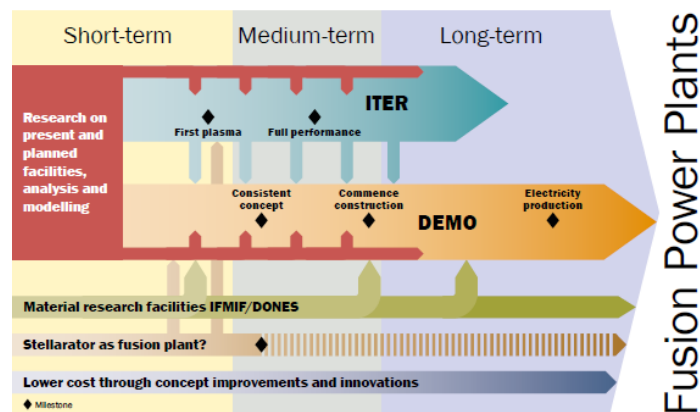


Figure 1.4: Roadmap of Tokamak Fusion Power Plants by EUROfusion

1.2 . Basic concepts of fatigue

Material fatigue refers to the progressive and localized structural damage that occurs in materials subjected to cyclic loading. This phenomenon

is marked by the initiation and growth of cracks within the material due to the repeated application of stress, often significantly lower than the material's ultimate tensile strength. Key concepts of material fatigue include:

- **Cyclic Loading:** Fatigue results from cyclic or repeated loading, where the stress or strain varies over time, in contrast to static loading, which is constant and does not lead to fatigue damage. The loading typically alternates between tension and compression, creating alternating stress conditions. In practice however, a mean stress (or strain) can also be present, influencing many aspects of the fatigue properties.
- **Crack Initiation and Growth:** Fatigue processes start with the initiation of microscopic cracks at stress concentrators, such as surface imperfections, notches, or grain boundaries. These cracks propagate through the material with continued cyclic loading, leading to failure. Crack initiation and growth are the primary stages of the fatigue process. The number of cycles required for crack initiation and from initiation to failure varies greatly depending on the material and loading conditions.
- **Stress-Life Curve (S-N Curve):** This curve depicts the relationship between stress amplitude and the number of cycles to failure, aiding in understanding a material's fatigue life under different stress levels. It is widely used in industry for predicting the fatigue life of components since the stress load is often the first known variable in the design process.
- **Manson-Coffin Curve:** Similar to the S-N curve, the Manson-Coffin curve shows the relationship between strain amplitude (total strain or plastic strain) and the number of cycles to failure. It is particularly useful in low-cycle fatigue analysis and tends to better reflect material behavior in the low-cycle fatigue region than the S-N curve. However, applying this curve can be more challenging as determining the strain load typically requires additional experiments and simulations.

This section introduces only the key concepts guiding this thesis's research. New concepts used for the first time in a section will be defined at the beginning for clearer comprehension. Additionally, all notations and their meanings are listed in the appendix.

1.2.1 . HCF and LCF

Fatigue life in materials such as stainless steel is categorized into low-cycle fatigue (LCF) and high-cycle fatigue (HCF) based on the number of cycles to failure. Each type is influenced by different stress and strain behaviors:

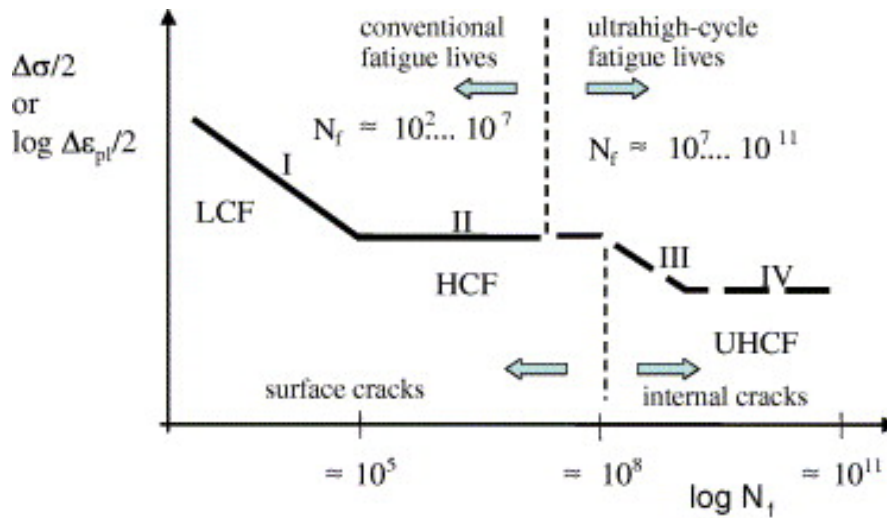


Figure 1.5: Schematic fatigue life diagram showing the different fatigue life-time regimes. [12]

- **Low-Cycle Fatigue (LCF):** LCF is characterized by higher stress levels, which results in bulk plasticity and fewer cycles to failure. For stainless steel, the LCF fatigue life typically ranges from 10^2 to 10^4 cycles. Factors like plasticity, strain aging, and oxidation may significantly influence the LCF duration [10, 11].
- **High-Cycle Fatigue (HCF):** In HCF, the material experiences predominantly elastic behavior with stress levels below the yield strength, which allows for more than 10^4 cycles to failure.
- **Very High Cycle Fatigue (VHCF) and Ultrahigh Cycle Fatigue (UHCF):** These regimes are not covered in this thesis and typically involve 10^7 to 10^8 cycles or more. They are often characterized by the presence of internal cracks rather than surface cracks seen in LCF and HCF.

The transition between LCF and HCF is not always clear-cut, particularly in the transitional region that involves many different influential factors. However, while amplitude, rate of loading, and environmental conditions consistently influence fatigue, certain factors become more pronounced depending on the fatigue type and operational conditions, such as high temperatures.

This thesis presents a structured approach by examining the controlling factors of fatigue life in different stages:

- For LCF, detailed discussions and models are found in Chapter 2.
- For HCF, discussions are centered around crack initiation as detailed in Chapter 4.

Although multiple factors are relevant in transitional regions, it is often possible to identify a dominant stage in the fatigue process, greatly simplifying the prediction of fatigue life. This supports the categorization into LCF and HCF, a concept validated in the conclusion of this thesis (Chapter 5). This organizational approach not only clarifies the different influential mechanisms but also highlights the need for a physical model that simulates fatigue on a smaller scale, integrating the contributions of various physical factors.

1.2.2 . Ramberg-Osgood model

The Ramberg-Osgood expression is a mathematical model used to describe the stress-strain relationship of materials, particularly metals, in the non-linear region beyond the initial elastic behavior. Developed by Warren Ramberg and William Osgood in 1943, this empirical equation characterizes the gradual transition from elastic to plastic deformation. The expression is particularly useful in capturing the behavior of materials under cyclic loading conditions, where traditional linear elastic models fall short.

There are several versions of the Ramberg-Osgood expression though they are mathematically the same expression. The version that we'll use through our projects will be:

$$\frac{\Delta\epsilon}{2} = \frac{\Delta\sigma}{2E} + \left(\frac{\Delta\sigma}{2K'}\right)^{1/n'} \quad (1.1)$$

The version in Wikipedia is:

$$\epsilon = \frac{\sigma}{E} + K\left(\frac{\sigma}{E}\right)^n \quad (1.2)$$

The application of the model is usually in the following ways:

- from $\Delta\epsilon_p$ to $\Delta\sigma$: $\Delta\sigma = 2K' \Delta\epsilon_p^{n'}$
- from $\Delta\sigma$ to $\Delta\epsilon_p$: $\Delta\epsilon_p = 2\left(\frac{\Delta\sigma}{2K'}\right)^{1/n'}$
- from $\Delta\epsilon$ to $\Delta\sigma$: This requires solving the equation of the Ramberg-Osgood model.

Other possible conversions are either too simple or not used in the project.

The parameters of the Ramberg-Osgood model could vary even for the same material under different conditions[13]. This limits the precision of the experimental results and the accuracy of the model. The real parameters will be given in the annex of the thesis.

1.2.3 . Fatigue crack: different stages

The lifespan of metallic materials consists of two main stages: the number of cycles needed to initiate a crack and the cycles required to propagate this

crack to the point of failure. Each of these stages is characterized by unique features.

Initially, except in conditions of Very High Cycle Fatigue (VHCF), fatigue cracks typically initiate at the surface of the material. This initiation is marked by the formation of persistent slip markings (PSMs), including both extrusions and intrusions. Once the criteria for crack initiation are met (as detailed in Chapter 4), an initial crack, known as a stage I crack, emerges. This crack usually propagates within the initial grain and may either be halted by a crystallographic barrier or overcome this barrier to become a stage II crack. Only a few cracks, depending on various factors including the load, evolve into stage II cracks. These cracks then continue to propagate through the material, ultimately leading to the component's failure. The various stages of fatigue are illustrated in Fig. 1.6.

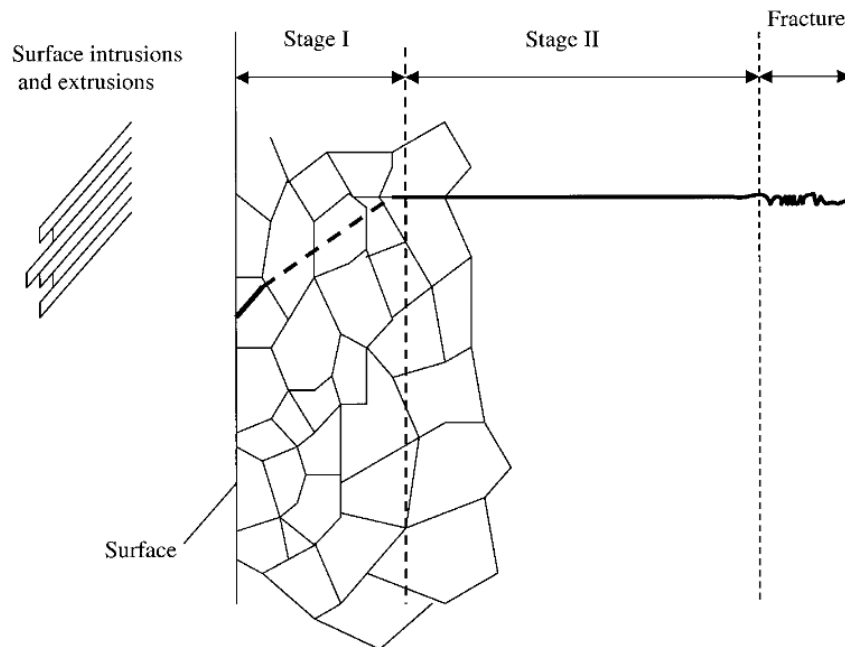


Figure 1.6: Schematic representation of different stages of fatigue in a material from [14].

The concept of fatigue stages was first introduced in [15]. Since then, the notion of fatigue stages has undergone modifications and the particular version used in this thesis employs Arabic numerals for clarity and differentiation; this is a unique representation used solely within this thesis and is not a standard method of depicting fatigue stages. The stages of fatigue, as defined for this research, are as follows:

1. Homogeneous cyclic slip

2. Localized cyclic slip in the form of persistent slip bands (PSBs)
3. Stage I crack initiation (referred to as stage 0)
4. Stage I crack propagation (referred to as stage 1)
5. Stage II crack propagation (referred to as stage 2)
6. Failure

The distinctions between these stages can be clearly identified in ad-hoc experiments and in dislocation dynamics (DD) simulations. As demonstrated in [16] (or see Section 1.5.1), DD simulations reveal the formation of PSBs and the development of extrusions and intrusions. While extrusions are observable through experiments, intrusions remain challenging to detect, even with today's advanced techniques. The simulations and experiments indicate that stages 1 and 2 occur quite rapidly, typically within dozens of cycles. The bulk of a material's fatigue life is usually spent in stages 3, 4, or 5, depending on the type of load considered (LCF or HCF). This understanding has influenced the development of fatigue models from 2004 to the present, which will be discussed in Section 1.5.

1.3 . Basic concepts of dislocation dynamics

One of the following books could be sufficient for the understanding of the basic concepts of dislocation dynamics:

- *Theory of Dislocations* by Hirth and Lothe [17, 18].
- *Introduction to Dislocations* by Hull and Bacon [19].

Over the past two decades, advancements in experimental methods and simulation techniques have provided new insights into dislocation-based plasticity in crystalline materials. The Dislocation Dynamics (DD) technique has emerged as a powerful tool for modeling the behavior of metallic materials at the mesoscale. It incorporates detailed, dislocation-mediated mechanisms into existing plasticity models, proving invaluable for analyzing plastic instabilities, fatigue, nanoindentation, and the growth and deformation of thin films. DD shares similarities with atomistic Molecular Dynamics (MD) simulations, but rather than simulating atomic motions, it models the evolution of dislocation lines. Although these dislocations can theoretically be modeled at the atomic scale, vast dislocation numbers must be represented to assess their impact at the macroscopic level.

DD is founded on the theory of elastic dislocation. The primary entities in DD are discrete dislocation lines gliding within a continuum elastic

medium. These dislocations move by discrete jumps across the underlying lattice, facilitating the incorporation of slip geometries for various crystallographic structures. The elastic properties of dislocations, such as line tension and dislocation-dislocation interactions, as well as the calculation of the effective force on each dislocation segment, are derived directly from classical dislocation theory. Algorithmic parameters such as time step, segment minimum length, and maximum travel distance during a step are fine-tuned to mirror established solutions for typical elastic problems.

In DD simulations, plasticity is achieved through the nucleation, multiplication, and motion of dislocations. The method calculates and tracks dislocation motion, taking into account both short-range and long-range interactions, and evaluates the plastic deformation caused by the collective movement of dislocations. The standard procedure for a DD simulation involves discretizing long dislocation lines into smaller segments connected by discrete nodes, described by either straight lines or parametric curved splines. For each segment, the forces induced by external loads and interactions with other dislocations or defects are calculated. Dislocation mobility laws link these forces to dislocation velocity, which also depends on the crystal structure, material parameters, and temperature. Each dislocation segment's position is then updated based on its velocity and the chosen time increment. The simulation calculates the area slipped by the moving dislocation and the corresponding increment in plastic strain. External loads and displacements are recorded and updated throughout the simulation. Additionally, short-range interactions, such as dislocation junction formation and mutual annihilation of opposite-sign dislocations, require careful management. Thermally activated cross-slip processes are also periodically evaluated. The dislocation network's topology is continually updated to ensure each segment is reasonably discretized, repeating the process until the desired strain or loading condition is achieved.

Over the past three decades, various Dislocation Dynamics (DD) simulation codes have been developed, including the TRIDIS code. Dedicated to studying the mechanical responses of fcc and bcc metals and alloys, TRIDIS—which stands for 3D Discrete Dislocation Dynamics—was initially developed by Verdier et al. [21]. It has been consistently maintained and updated to cater to specific case studies. Resources such as downloadable videos and a comprehensive list of references regarding the simulation and its applications are available on the TRIDIS website, which also introduces a new nodal code, NuMoDis, initially developed by L. Dupuy at CEA.

The selection of this particular DD code represents a balance among computational cost, accuracy and relevance of results, and numerical stability. In TRIDIS simulations, the dislocation microstructure emerges naturally, and the results can be directly compared with transmission electron microscopy (TEM) observations. Dislocation lines in TRIDIS are discretized into pure screw and

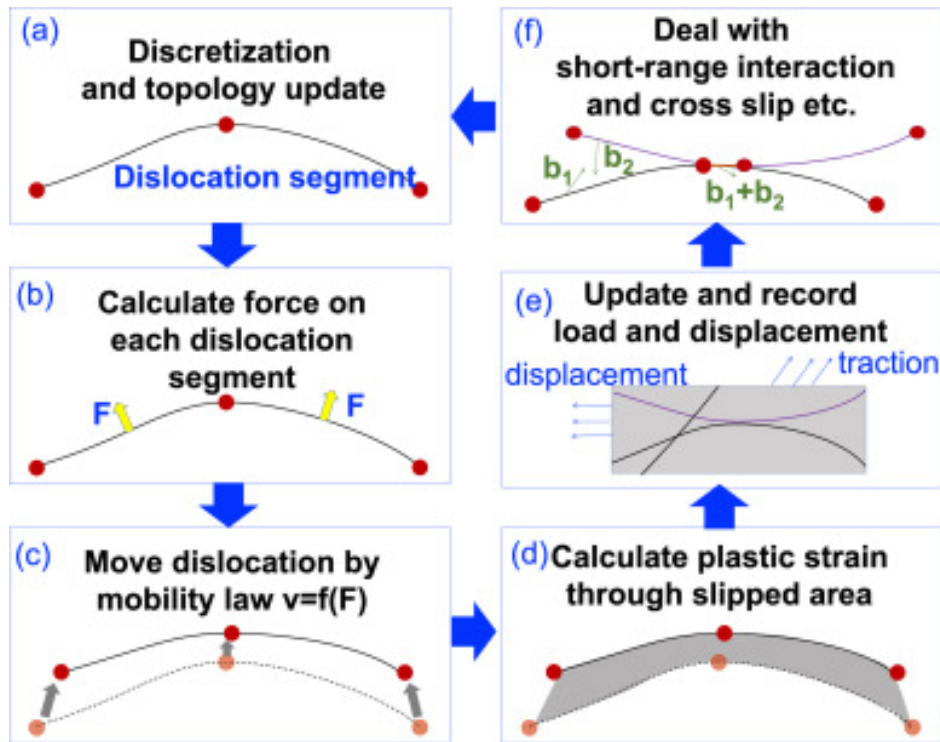


Figure 1.7: The basic process of DD simulation[20]: (a) Discretize dislocation lines into segments and update their topology; (b) Calculate the forces acting on each dislocation segment; (c) Move the dislocation segments according to a mobility law $v = f(F)$; (d) Calculate the plastic strain resulting from the slipped area; (e) Update and record the load and displacement in the material; and (f) Address short-range interactions and phenomena like cross slip.

edge segments that glide in a rigid crystal lattice using a lattice parameter of $10b$. No lattice rotations are considered, and in FCC crystal case, each dislocation segment's velocity is proportional to the effective resolved shear stress, incorporating a drag coefficient that models dislocation-phonon interactions. The simulation algorithm operates as follows: at time t , the velocity field for all discrete segments is computed. These segments are then displaced over a time step δt using an explicit scheme.

The aim of employing DD simulation in studying fatigue phenomena is to comprehend the mesoscopic behavior of materials in a physical manner. This approach facilitates the development of physically-based equations that characterize the fatigue behavior of materials. Such models are crucial for predicting the lifespan of materials under various conditions, which are often challenging to investigate using experimental methods. This is particularly significant in the context of fusion reactor conditions (see Section 1.1), where materials are subjected to variable amplitude loading conditions and other

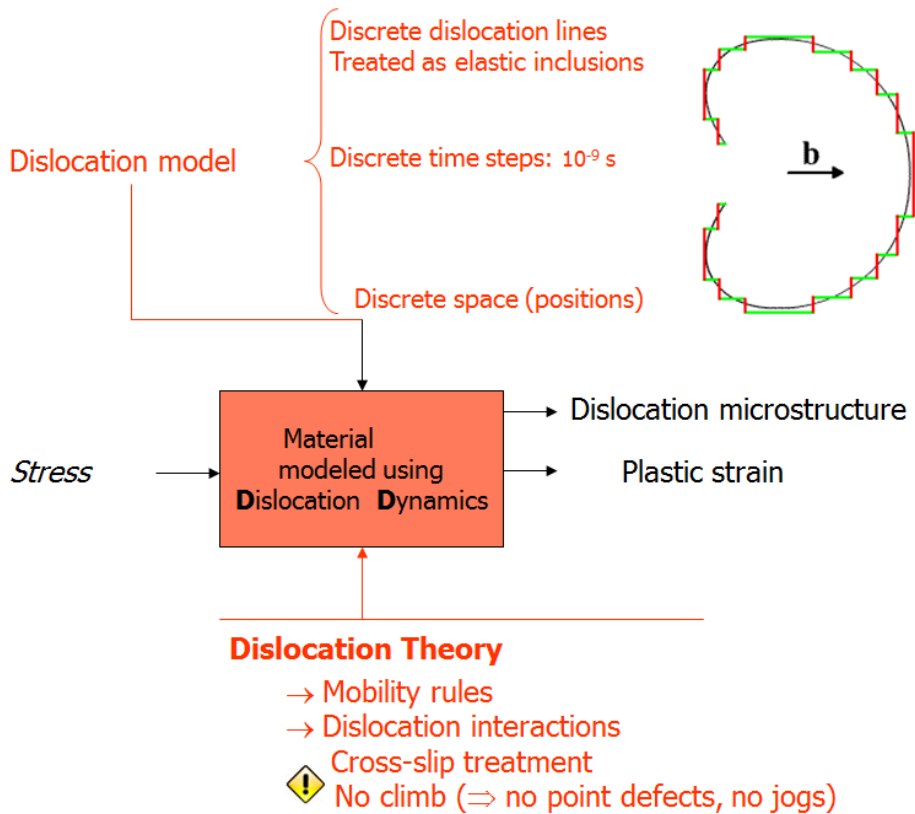


Figure 1.8: Diagram of principles of a DD simulation

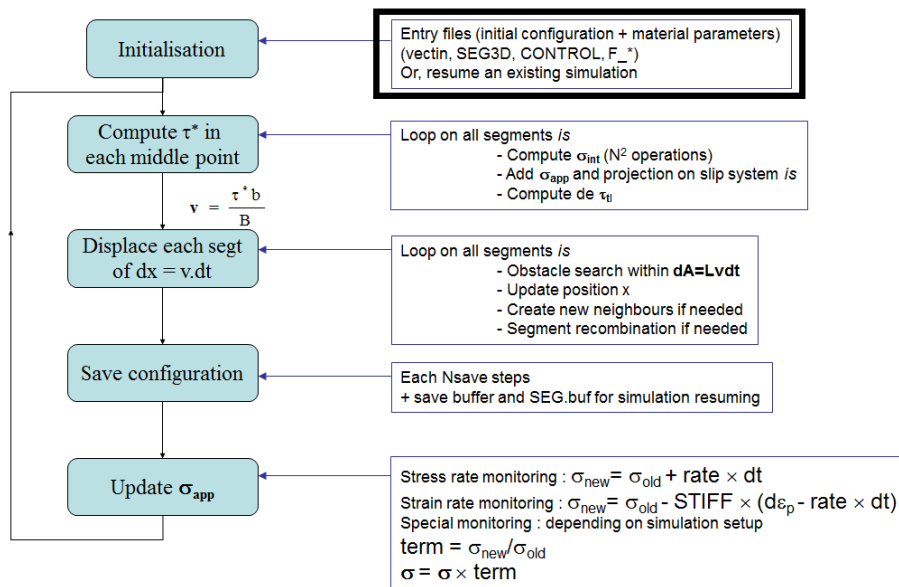


Figure 1.9: Explicit scheme of DD simulation algorithm

complex loading characteristics that significantly influence fatigue behavior and are difficult to address experimentally.

While DD simulations are not conducted in this work, they are the principal source of all the data and equations used in the development of our fatigue crack propagation model. This foundational understanding provides a robust framework for predicting material behavior under operational stresses.

1.4 . Bibliography: Methods of studying and predicting fatigue life

Since the purpose of this thesis is to study a physical base model, traditional empirical fatigue lifetime prediction models will not be introduced here. For a simple review, the reader could refer to [14].

Recent development in machine learning also provides a new way to predict the fatigue lifetime of materials. However, it is also out of scope for our study. For a review of the machine learning models, the reader could refer to [22].

1.4.1 . Dislocation dynamics and fatigue

While existing models can often predict fatigue life effectively in traditional industrial applications, they fall short in providing the physical mechanisms underlying the fatigue process. The parameters within these models typically require extensive and repetitive experimentation for determination, which in some complex cases may even be impractical. Moreover, these models struggle to accurately predict fatigue life under complicated loading conditions, often resulting in conservative estimates that necessitate large safety factors and consequently limit the design life of components.

In response to these challenges, there has been significant effort to develop physical models that can simulate the fatigue process in greater detail. Dislocation Dynamics (DD) simulation stands out as one of the most promising approaches in this regard. DD simulations offer insights into the physical mechanisms of fatigue, providing a basis for developing physically-based fatigue lifetime models. Additionally, DD simulations are particularly valuable for studying fatigue under complex loading conditions that are difficult to replicate experimentally. This capability not only enhances understanding but also aids in the design and evaluation of materials and structures subjected to real-world operational stresses.

For a comprehensive overview, a detailed review is available in [23]. Additionally, some relevant and intriguing work will be summarized and discussed in this subsection.

Generally, Discrete Dislocation Dynamics (DDD) simulations are categorized into two main types: two-dimensional (2D) and three-dimensional (3D)

simulations. Both types are capable of predicting plastic deformation across a variety of materials and crystallographic systems under diverse loading and environmental conditions, including specialized applications such as irradiation effects or material behavior at joints [24]. These simulations are instrumental in advancing our understanding of material behavior under a broad spectrum of operational scenarios, thereby enhancing the reliability and efficiency of engineering designs.

1.5 . Summary of previous works

In this subsection, we summarize the pivotal simulation studies conducted by Robertson and Depres between 2004 and 2020. These investigations are crucial for understanding the context and foundation of the new models and approaches proposed in this thesis. The results of these studies will be organized chronologically and divided according to the stages of fatigue addressed in each work. This structure will ensure clarity and allow readers to navigate the content effectively. To facilitate ease of reference, this subsection will be clearly labeled, enabling readers to optionally skip this part and use hyperlinks to return to it when encountering relevant citations in subsequent chapters. This approach ensures that the foundational research by Robertson and Depres is seamlessly integrated into the thesis, providing a comprehensive backdrop for the new insights and models introduced.

1.5.1 . DDD simulations of fatigue behavior of 316L stainless steel (2004) A 3D DISCRETE DISLOCATION DYNAMICS MODELLING OF THE EARLY FATIGUE CYCLES IN 316L AUSTENITIC STAINLESS STEEL [25]

Pioneering investigations into dislocation behavior in stainless steels (A316L) under fatigue loading include the Ph.D. research of Dr. Déprés [25] and many subsequent research works. These studies form the theoretical basis of the current study. Readers seeking a concise overview of the basis of dislocation simulations may refer to the following papers:

- *Low-strain fatigue in AISI 316L steel surface grains: a three-dimensional discrete dislocation dynamics modeling of the early cycles I. Dislocation microstructures and mechanical behaviour* [16].
- *Low-strain fatigue in 316L steel surface grains: a three-dimensional discrete dislocation dynamics modeling of the early cycles. Part 2: Persistent slip markings and micro-crack nucleation* [26].
- *A dislocation-based model for low-amplitude fatigue behaviour of face-centred cubic single crystals* [27].

Initially, the numerical techniques for Dislocation Dynamics (DD) simulations adapted to fatigue conditions are described in detail. For instance, the production of surface markings by dislocations appearing at the free surface of the simulation volume is simulated using a virtual volume, as illustrated in Fig. 1.10. This feature is crucial because it allows for a quantitative analysis of the characteristics of these surface markings, which plays a significant role in the study of crack initiation discussed in Chapter 4.

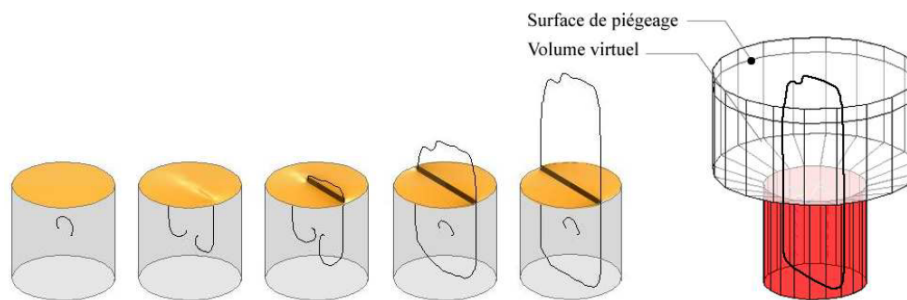


Figure 1.10: Production of surface markings by dislocations escaping through the top free surface of the simulation volume.

Various advanced techniques are detailed in the thesis, encompassing methods that integrate multiple physical phenomena into simulations, as well as the underlying assumptions utilized.

This study replicates and elucidates the phenomena of cyclic hardening and saturation from both microscopic and macroscopic perspectives. For instance, the evolution of dislocation density and shear strain was monitored, particularly in scenarios featuring 12 Frank-Read sources, as depicted in Fig. 1.13. This comprehensive approach not only enhances understanding of the material's fatigue characteristics but also bridges the gap between theoretical predictions and observable physical behaviors.

Various comparisons were conducted between the results from simulations and experimental observations to validate the techniques and hypotheses employed. One notable example is illustrated in Fig. 1.14, which displays the slip lines generated by dislocations in the simulations. These simulated slip lines closely resemble those observed experimentally in copper (see Fig. 1.15), as documented by [28].

Another attempt directly compares the simulated dislocation microstructure with the Transmission Electron Microscopy (TEM) observations from [29], as illustrated in Fig. 1.16. The geometric characteristics of the microstructure can be clearly identified in the simulation.

Yet another comparison can be made by examining the hysteresis loops produced by the simulation alongside the experimental results. Figure 1.17

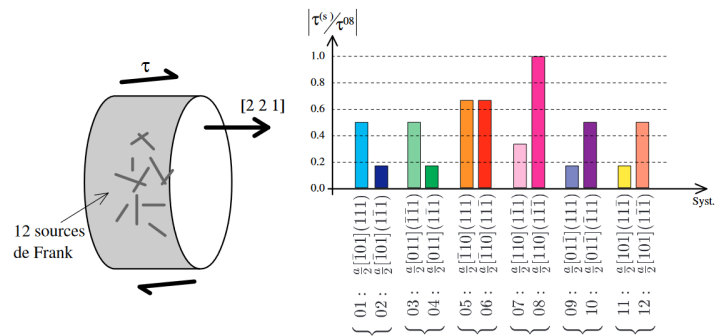


Figure 1.11: Example of a volume with 12 Frank-Read sources and the corresponding resolved stresses. The applied macroscopic shear stress tensor has been visualized in the figure.

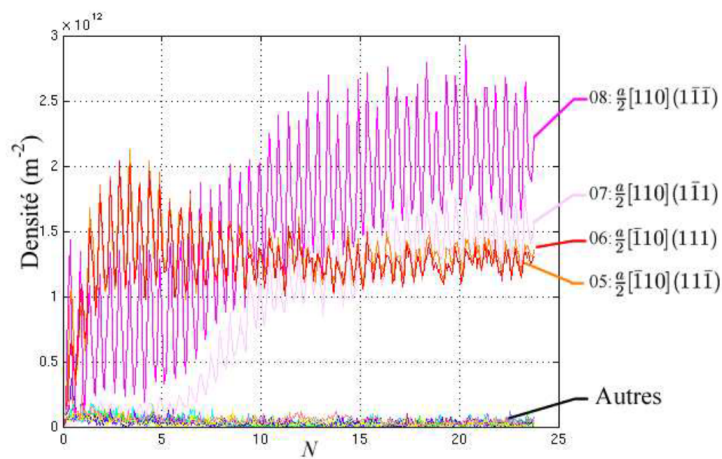


Figure 1.12: Evolution of dislocation density during the first 25 cycles

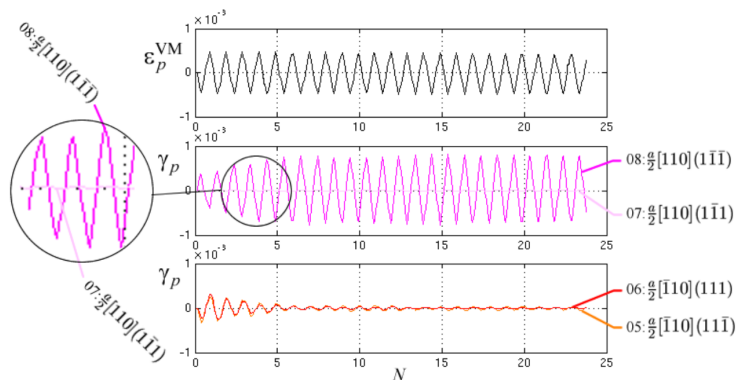


Figure 1.13: Evolution of plastic strains during the first 25 cycles

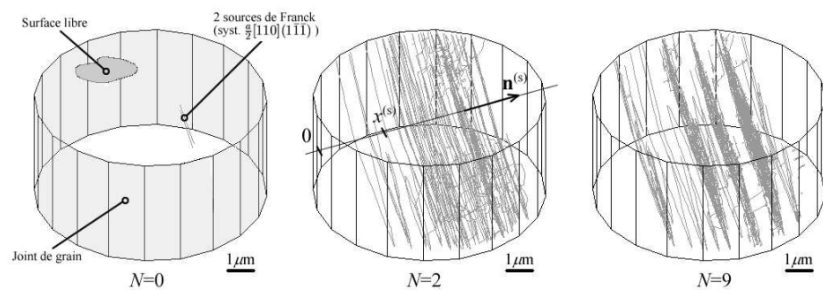
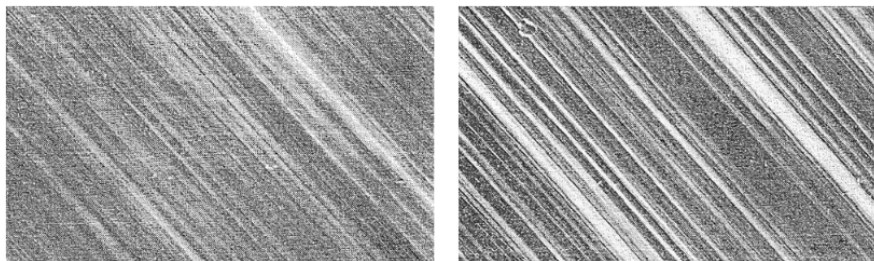


Figure 1.14: Example of a simulation cell loaded in fatigue and initially including 12 Frank-Read sources.



(a) Au cycle n°1.

(b) Au cycle n°25.

Figure 1.15: Experimental observations of surface slip markings in copper by [28]

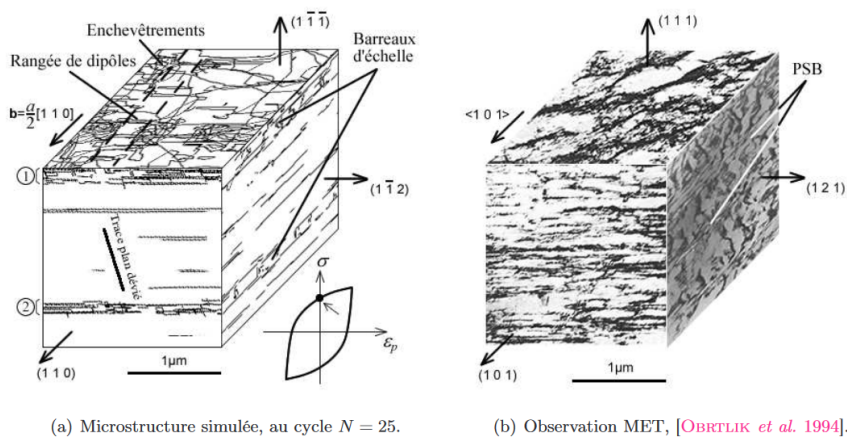


Figure 1.16: Comparison of the dislocation microstructure in DD simulation and the TEM observations of [29] (in the case of 316L steel grain loaded in single slip conditions)

displays the comparison of the hysteresis loops from both the simulation and the experimental data from [30]. Unlike the first two methods, this approach provides a more quantitative analysis.

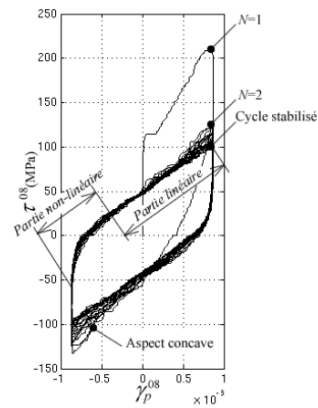
In addition to these microstructural findings, the author proposed two physical models derived from the simulation results. The first is a crack-nucleation model as depicted in Fig. 1.18 [26]. Although the mechanism is clearly described in physical terms, it has not been fully quantified due to the absence of several key pieces of information. This model will be further refined in our study in Chapter 4 with some minor modifications.

An important technique noted in [26] is the method developed for calculating the height of surface extrusions, as illustrated in Fig. 1.19. This technique serves as the basis for the surface height calculation method used in Chapter 4.

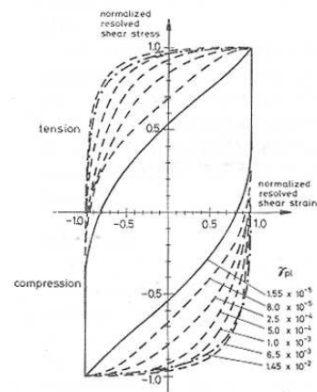
The second model is a general physical cyclic plasticity model that successfully reproduces the hysteresis loops of materials under fatigue loading. This model has been refined and published in [27]. It has been adapted with some minor modifications in our study, as detailed in Chapter 3. A comprehensive explanation of this model will be provided in the corresponding chapter.

The research presented in this thesis examines cyclic plasticity in the surface grains of 316L stainless steel and its connection to crack initiation. Initially driven by an industrial challenge related to thermal fatigue damage prediction, this investigation broadly addresses the fatigue behavior of face-centered cubic structural metals.

A key finding is that dislocation microstructures alone can create permanent surface features such as extrusions and intrusions, similar to those ob-



(a) Cycle contrainte-déformation obtenue en DDD.



(b) A titre indicatif, forme des cycles obtenus dans le cuivre monocristallin par [MUGHRABI 1978].

Figure 1.17: Comparison of the hysteresis loops produced by the simulation and the experimental results[30]

served experimentally. The progression of accumulated irreversible deformation on the surface displays a time-proportional change, culminating in a crack initiation model that aligns with the Manson-Coffin relationship. Furthermore, the energy stored within the microstructure was examined to determine if factors other than surface topography might initiate cracks, indicating that while microstructures tend to minimize distortion energy, they generate localized high-energy zones that are prone to crack formation.

These insights suggest that micro-crack initiation occurs early in the loading cycles and results from micro-cohesions along slip planes. Finally, the results from the simulations supported the initial development of a crystalline model to simulate cyclic plasticity, emphasizing the significant role of different dislocation densities in kinematic hardening, thereby making a substantial contribution to the field of materials science and engineering.

Main findings of this work:

- The research identified that cross-slip and dislocation line recombination together control localization of cyclic plastic deformation.
- Dislocation microstructures were shown to produce irreversible surface topography such as extrusions and intrusions, closely mimicking phenomena observed experimentally.
- The evolution of irreversible deformation on the surface displays a time-dependent evolution, leading to the development of a crack

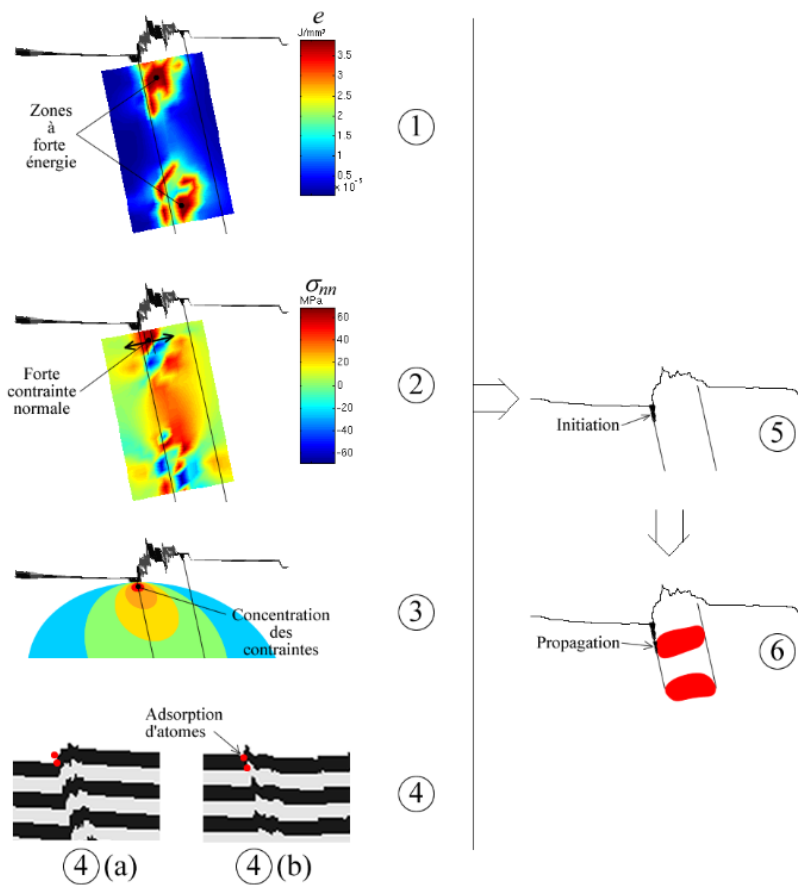


Figure 1.18: Crack nucleation model proposed in [25], and further explained in [26]

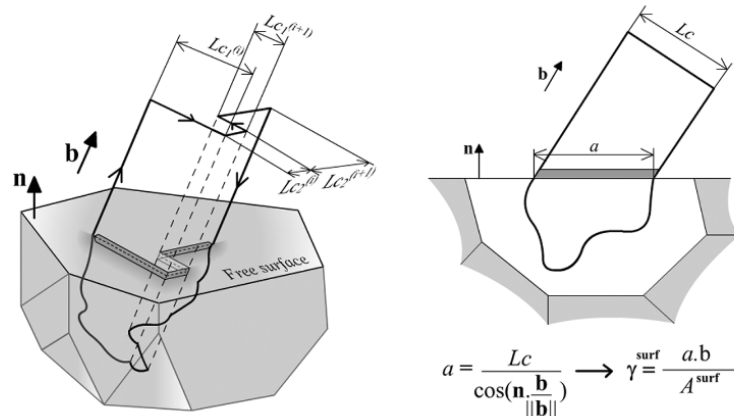


Figure 1.19: Sketch of surface displacement calculation method, including dislocation segments with cross-slipped segments. [26]

initiation model that aligns with the Manson-Coffin relationship.

- Investigations into the energy stored within the PSB dislocation microstructure revealed that while overall distortion energy is minimized, localized high-energy zones are created which are conducive to crack formation.
- Early cycles of micro-crack initiation were found to result from micro-cohesions along slip planes, emphasizing the dynamic nature of microstructural changes in fatigue.
- Simulation results contributed to the preliminary development of a crystalline model that replicates cyclic plasticity, highlighting different dislocation densities and their roles in kinematic hardening.

1.5.2 . Study of the Stage I crack initiation (stage 0)

In this subsection, the use of Discrete Dislocation Dynamics (DDD) simulations to investigate crack initiation in the early stages of fatigue is summarized. This includes a review of the historical development of a crack initiation model and various experimental efforts aimed at understanding the impact of mean stress on crack initiation. The findings from these studies will be incorporated into the development of the crack initiation model presented in Chapter 4.

(2010) Micro-crack initiation in thermal fatigue — an analysis based on experimental and DD simulation results [31]

Experiments to examine the effects of combined cyclic thermal shocks and superimposed static tensile loading (e.g. mean plastic strain) have been carried out, in the context of PWRs cooling line damage prediction. The schematic

representation of one of the many experimental setups utilized is illustrated in Fig. 1.20, and the results of these experiments are plotted in Fig. 1.21.

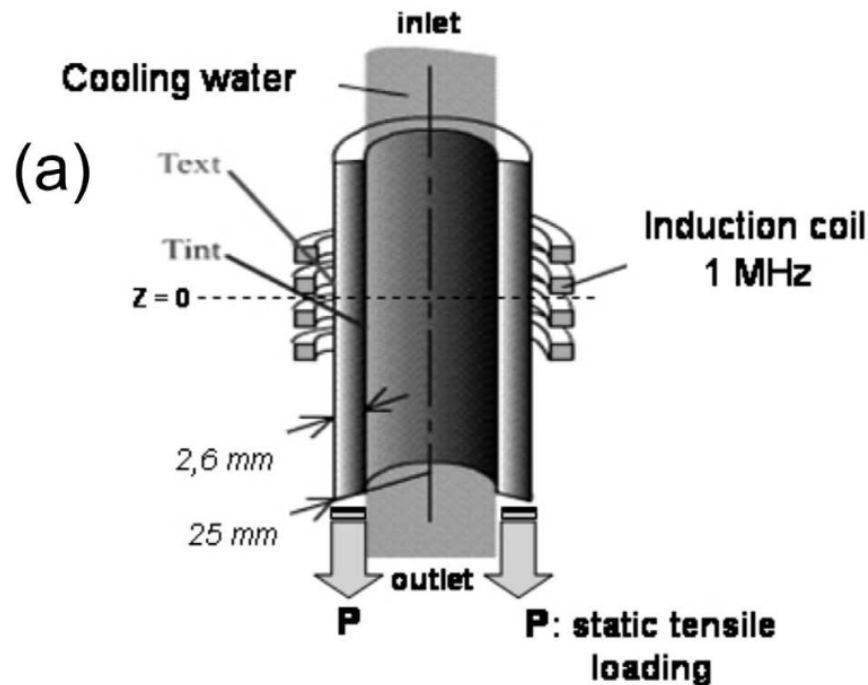


Figure 1.20: Schematic representation of the experimental device used in [31]

In addition to the experimental work, dislocation dynamics (DD) simulations were conducted to investigate the impact of mean plastic strain, as depicted in Fig. 1.22. Although it remains challenging to directly incorporate mean stress into DD simulations, comparisons of stabilized mean stress can be leveraged to align with experimental outcomes. These simulations build upon prior research by incorporating considerations of mean stress. Details of these novel modifications will be further elaborated in Chapter 4.

Further elaboration on this topic will be provided in the aforementioned chapter.

Main findings of this work:

- In thermal fatigue, the number of cycles to crack initiation is 4-5 times faster than in conventional mechanical fatigue.
- In equi-biaxial loading conditions, micro-cracks preferentially initiate in grains having specific surface orientations due to the preferential activation of slip systems having a maximal surface connected volume.

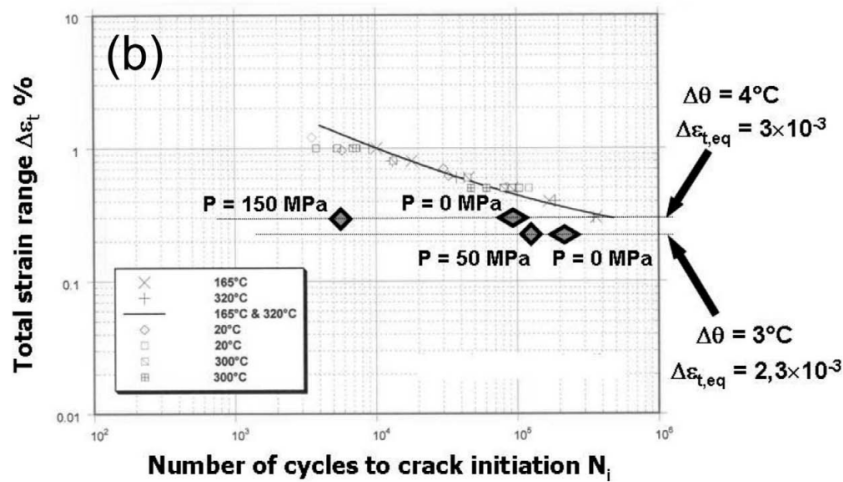


Figure 1.21: Testing results in 304L steel specimens. Full symbols: thermal fatigue testing, open symbols: conventional, mechanical fatigue testing in symmetrical tension/compression. The mechanical testing specimens come from two different heats, both tested at 20°C and 300°C.[31]

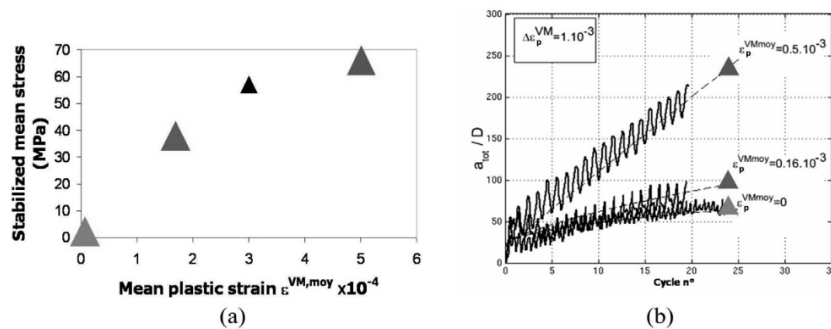


Figure 1.22: Comparison of stabilized mean stress in 304L steel specimens. [31]

- DD simulations reveal that surface slip irreversibility augments with the imposed mean stress.

(2015) 3D Discrete Dislocation Dynamics Investigations of Fatigue Crack Initiation and Propagation [32]

This research builds upon and completes the investigations detailed in [26, 16]. It introduces a quantitative approach to the crack initiation mechanism proposed in those prior studies. The novel aspect of this research is the use of surface shear strain, denoted as γ^{surf} , to measure the irreversibility of defor-

mation. This parameter is calculated as the total length of plastic deformation steps per unit area that remains on the surface. These steps are projected along the normal vector of the surface, thereby providing a measure proportional to the height of material extrusions. The specific formula corresponding to the DD simulation results is as follows:

$$\gamma^{surf}(N) = K \frac{h_g}{D_g} \Delta\epsilon_p \left(1 + 2 \frac{|\bar{\epsilon}|}{\Delta\epsilon_p}\right) \sqrt{N} \quad (1.3)$$

where K is a constant, h_g is the grain depth, D_g is the grain diameter, $\Delta\epsilon_p$ is the plastic strain amplitude, and $\bar{\epsilon}$ is the imposed mean strain. It is worth noting that this result, which is proportional to \sqrt{N} , is different from the one proposed in [33] which is proportional to N and some experimental observations. This has been discussed in [16].

Crack initiation is identified at the point where the surface shear strain attains a critical threshold, as the surface extrusions reach a critical size. This scenario of crack initiation is depicted in Fig. 1.23. Based on this idea, the authors have derived an initial estimate of the number of cycles required for crack initiation, as depicted in Fig. 1.24. This estimation is grounded in the aforementioned definition and provides a foundational measure for further experimental validation and theoretical analysis.

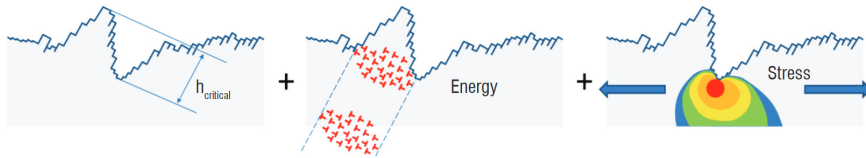


Figure 1.23: Schematic description of a crack initiation scenario consistent with DD simulation findings. The threshold condition is reached when the elastic energy (associated to the multipoles) and the stress concentration (related to the extrusion shape) achieve a critical threshold[32].

The other part of the paper is in fact a summary of the Stage I crack propagation model, the relating results will be presented in the next subsection.

Main findings of this work:

- In practice, crack initiation is defined as the moment when the surface shear strain reaches a critical value, i.e., the moment when the extrusion height reaches a critical size.
- The crack initiation number of cycles is estimated based on the sur-

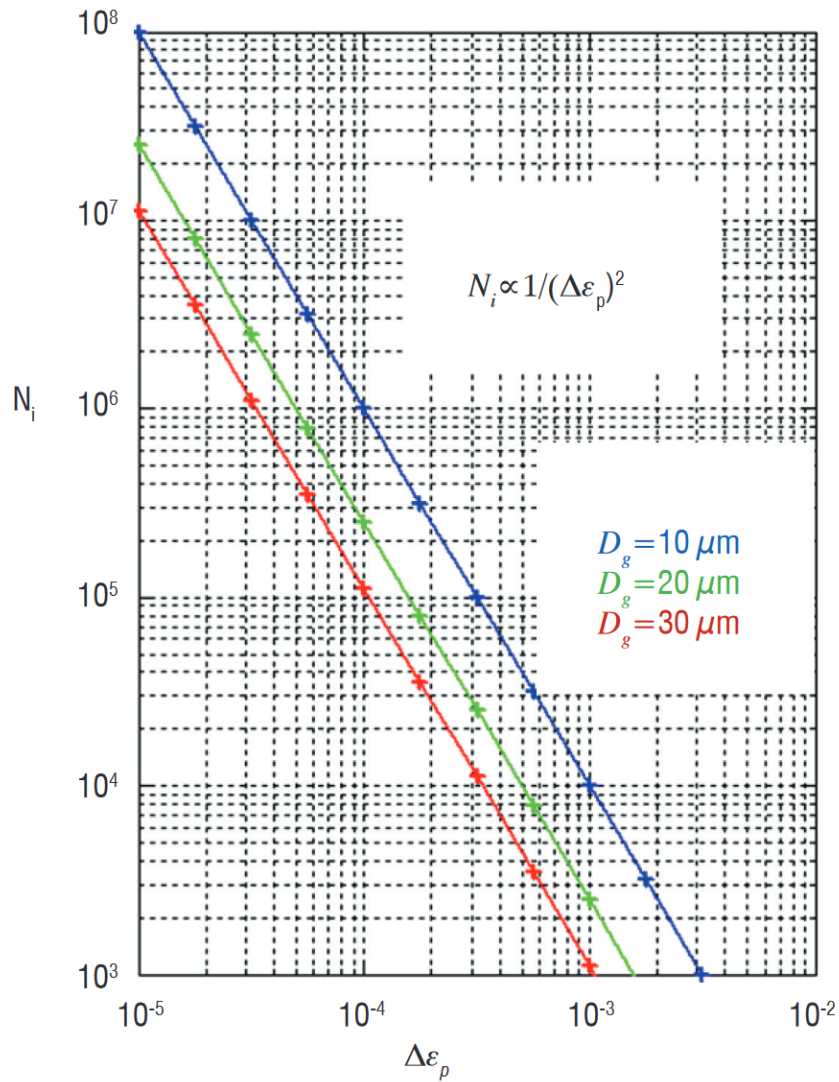


Figure 1.24: Estimation of the number of cycles to crack initiation based on the surface displacement evolutions. [32]

face shear strain and shown be proportional to $\frac{1}{(\Delta\gamma_p)^2}$.

1.5.3 . Study of the Stage I fatigue crack propagation (stage 1)

In this subsection, the use of discrete dislocation dynamics (DDD) simulations to investigate Stage I crack propagation is summarized. This includes a brief overview of the development history of crack propagation models and their subsequent refinements. Although Stage I crack growth is not the central focus of this thesis, the techniques and equations derived from these studies will be instrumental in the development of the Stage II crack propagation

model, to be presented in Chapter 2.

(2013) Effect of Grain Disorientation on Early Fatigue Crack Propagation in FCC Polycrystals [34]

This work is divided into two distinct parts [35, 34]: one focuses on the simulation setups and details [35], while the other addresses the model and experimental validations [34]. The objective of this research is to investigate the impact of grain disorientation on early fatigue crack propagation in FCC polycrystals. This investigation lays the groundwork for the formulation of a comprehensive Stage I fatigue crack propagation model in subsequent studies. The results and methodologies employed in this research offer valuable insights that aid in the development of models within this thesis.

In this study, it is postulated that the propagation of micro-cracks is driven by the development of surface relief in the secondary grain located ahead of the primary crack, with a significant dependency on the disorientation between the two adjacent grains. This situation is depicted in Fig. 1.25. Techniques established in [25] were employed to compute the stress-strain behavior of the slip planes in the secondary grain, thereby estimating the initiation of cracking in the secondary grain. The findings demonstrate a correlation between local shear stress and shear strain at the crack tip, as indicated in Eq. (1.4). Subsequently, various scale transition methods were utilized to articulate the different terms of this equation, ultimately deriving a ratio of local shear strain at the crack site γ_{wc}^{surf} to the local shear strain in the absence of a crack γ_{woc}^{surf} . This ratio, $\frac{\gamma_{wc}}{\gamma_{woc}}$, is then employed to predict the acceleration of the crack. The outcomes are illustrated in Fig. 1.26.

$$\Delta\tau_{local,wc} = \frac{1}{n_B} \left[\frac{1}{S} \frac{\mu}{1-\nu} \right] \Delta\gamma_{local,wc} \quad (1.4)$$

Main findings of this work:

- The presence of a micro crack in a first grain approaching the grain boundary accelerates the extrusion growth in the secondary grain.
- A semi-analytical micro-mechanical model is developed to evaluate the surface evolutions ahead of the primary micro crack.
- The effect of grain disorientation on this micro-crack transmission is quantified and found out that a small disorientation will accelerate this process.

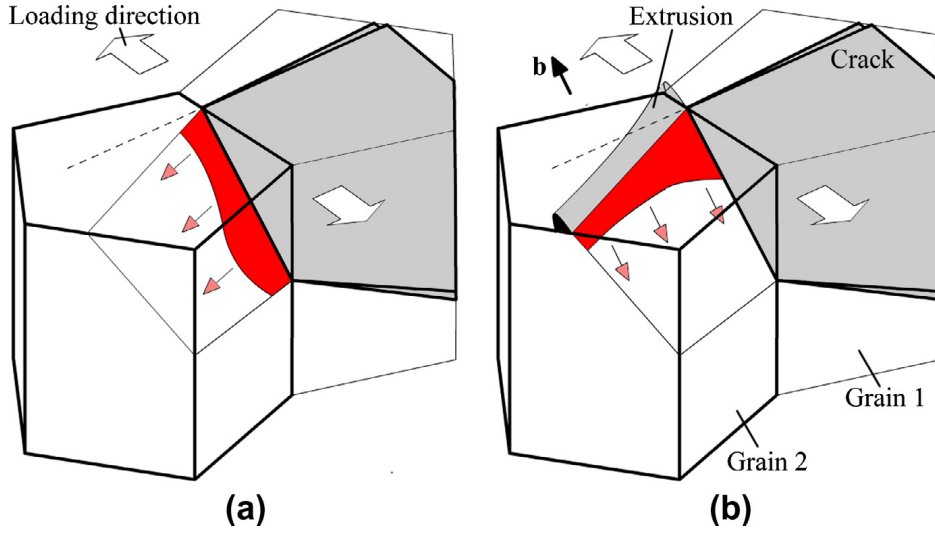


Figure 1.25: Illustration of micro-crack transmission due to surface relief growth in the secondary grain ahead of a primary crack. [35]

(2014) An extensive 3D dislocation dynamics investigation of stage-I fatigue crack propagation [36]

Drawing on previous studies, a comprehensive Stage I fatigue crack propagation model has been developed. This model integrates the influences of pre-existing slip bands and grain disorientation adjacent to the crack. To quantify crack growth, the crack tip slip displacement (CTSD) was analyzed, distinctly separate from the crack tip opening displacement (CTOD) described in Chapter 2. The dependency of CTSD on several variables, such as grain size and crack length, has been established through empirical evidence. A concise overview of the simulations conducted is presented in Fig. 1.27. The formula used to calculate the CTSD is provided in Eq. (1.5):

$$\frac{CTSD}{D_g} \approx \Delta\epsilon_p \left(1 - \exp\left(-\frac{\lambda}{\Delta\epsilon_p} \frac{bd_{gb}}{D_g^2}\right)\right) \quad (1.5)$$

where D_g is the grain size, $\Delta\epsilon_p$ is the imposed plastic strain, λ is a fitting coefficient, b is the Burgers vector, and d_{gb} is the length between crack tip and the grain boundary. The results of the simulations are shown in Fig. 1.27(e).

Building upon the proposed crack propagation mechanism, which involves successive micro-decohesion events, the following equation is employed:

$$\frac{da}{dN} = \frac{\Delta\epsilon_p}{N_i} \left(1 - \exp\left(-\frac{\lambda}{\Delta\epsilon_p} \frac{b}{D_g} \left(1 - \frac{a}{D_g}\right)\right)\right) \quad (1.6)$$

Here, N_i represents the number of cycles required to form a decohesion zone of size equivalent to the CTSD, which has not been precisely evaluated in

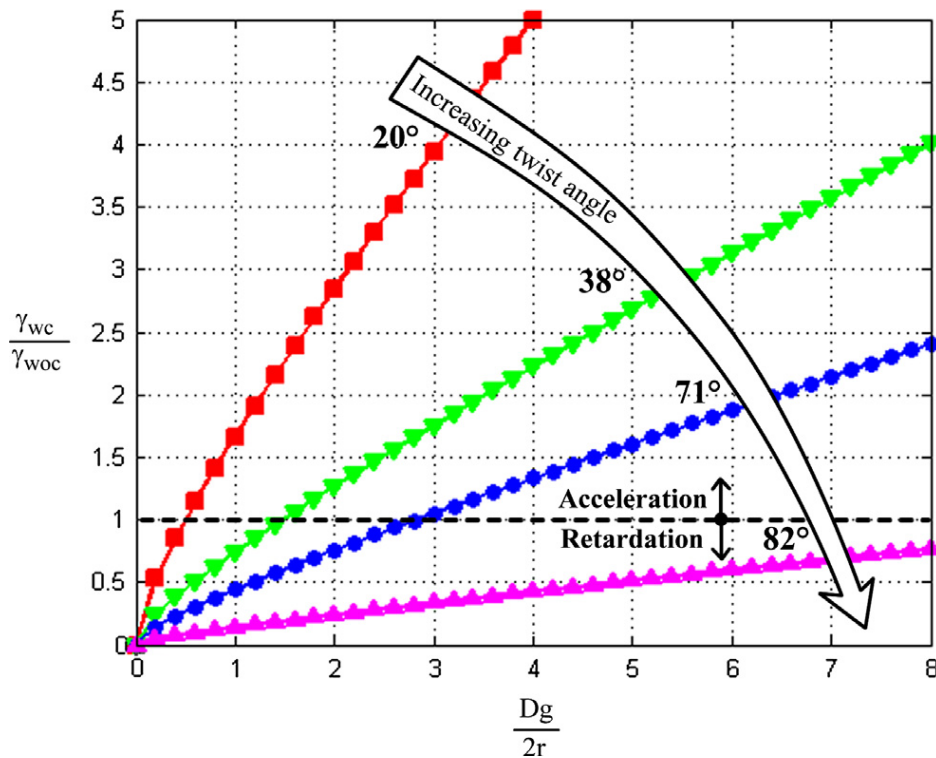


Figure 1.26: Effect of twist angle on micro-crack transmission kinetics towards a secondary grain. The results are normalized with respect to the noncracked case. A slip ratio greater than 1 means extrusion growth acceleration with respect to without-crack conditions; a slip ratio smaller than 1 means extrusion growth retardation with respect to without-crack conditions. [35]

this research. The micro-decohesion mechanism described will also be referenced in the Stage II crack propagation model outlined in Chapter 2. A more detailed evaluation of this mechanism will be provided thereof.

In conjunction with the aforementioned model developments, the influence of image forces and the energy balance during crack propagation were also examined. It was confirmed that the impact of image forces is relatively minor, accounting for approximately 6% of the crack growth driving force. Furthermore, the study of energy balance revealed that smaller crack increments are more favorable than larger ones, aligning with the proposed mechanism. This finding underscores the consistency of the model with observed behaviors in fatigue crack progression.

Main findings of this work:

- A full Stage I fatigue crack propagation model is developed based on the previous works.

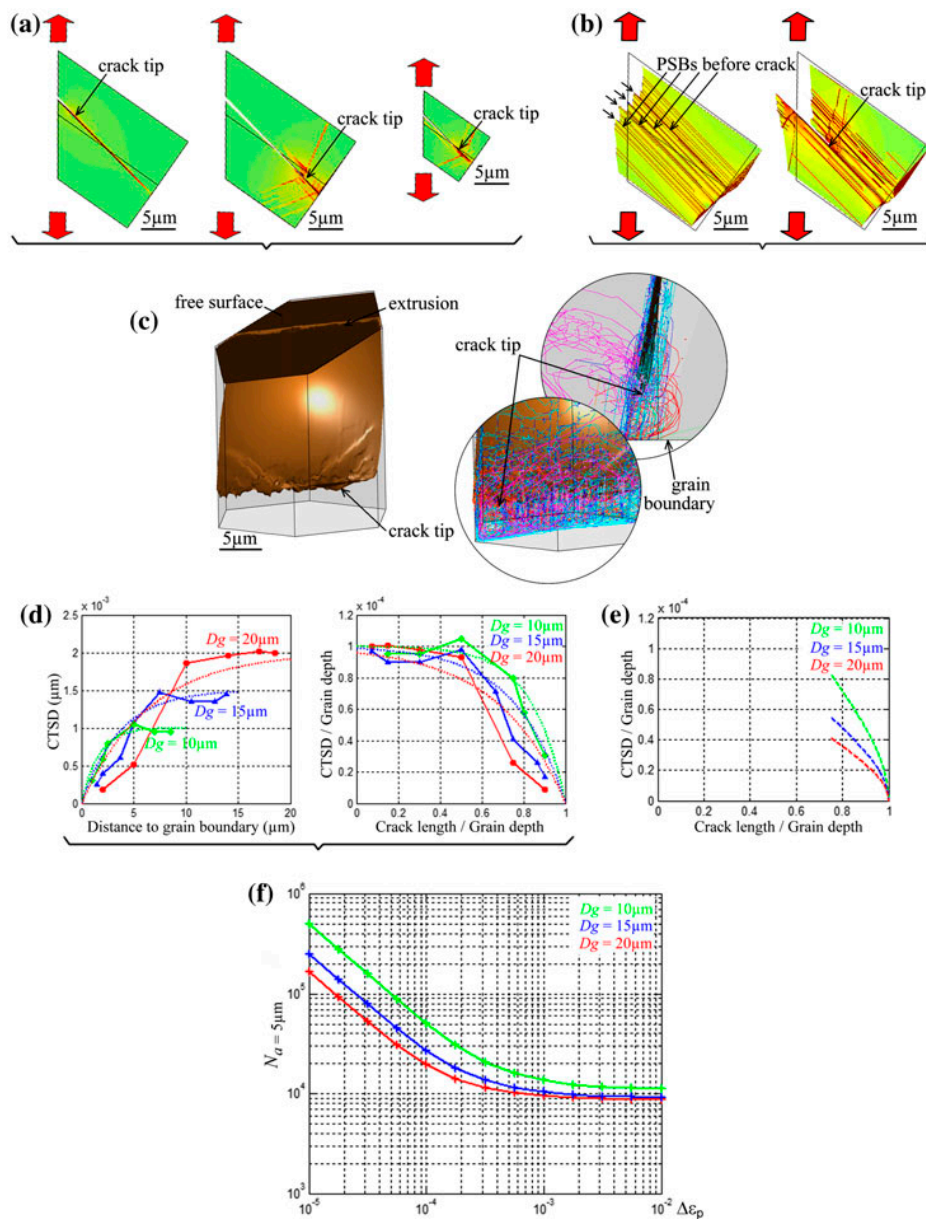


Figure 1.27: (a) Von-Mises strain field for different crack front positions (from the grain boundary) and for 20 and 10 μm grain depths. (b) Von-Mises strain field at higher imposed plastic strain (5×10^{-4}), before and after crack introduction. The displacement field is magnified $\times 30$ for clarity. (c) Crack front morphology and associated dislocation microstructure. (d) CTSD evolution as a function of the crack tip position for the three different grain depths. (e) CTSD evolution as a function of crack tip position for the three tested grain depths. (f) Number of cycle to get a 5 μm length crack. [36]

- The crack tip slip displacement (CTSD) is evaluated quantitatively and found to depend on the grain size, the crack length, etc.
- The number of cycles to get a $5 \mu m$ is evaluated using the equation of CTSD.

(2017) The effect of the location of stage-I fatigue crack across the persistent slip band on its growth rate - A 3D dislocation dynamics study [37]

The research detailed in [37] serves as an extension of the model introduced in earlier work [36]. This subsequent study focuses on the specific impact of the crack's position across the persistent slip band (PSB) on its growth rate. The outcomes of this investigation are illustrated in Fig. 1.28. To quantify this effect, a new factor K has been incorporated into Eq. (1.5):

$$\frac{CTSD}{D_g} \approx \Delta\epsilon_p \left(1 - \exp\left(-\frac{\lambda K}{\Delta\epsilon_p} \frac{bd_{gb}}{D_g^2}\right) \right) \quad (1.7)$$

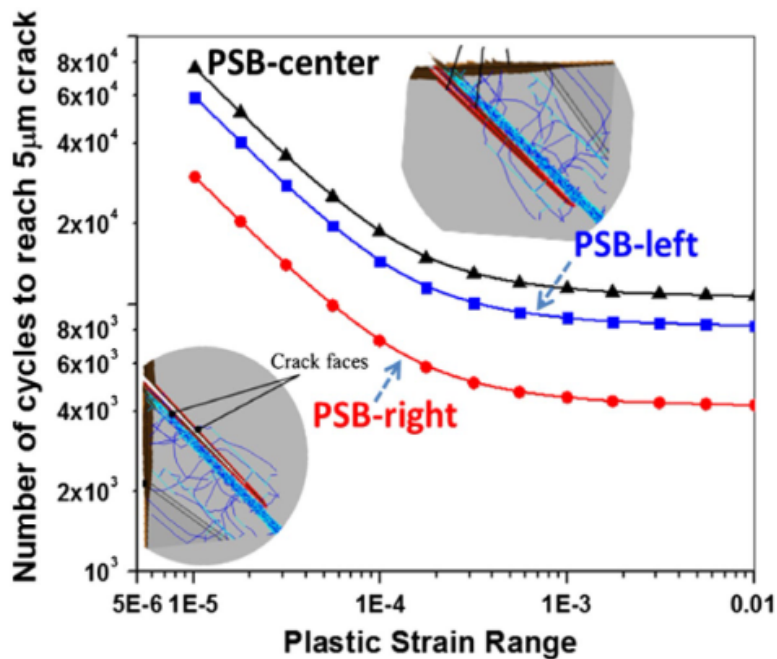


Figure 1.28: The comparison of number of cycles required to reach a crack length of $5 \mu m$ for the three positions of crack across the PSB (i.e. for the crack at PSB center and at both the PSB-matrix interfaces). [37]

Main findings of this work:

- The location of the crack across the persistent slip band has a small effect on the crack growth rate.
- A new factor K is introduced to quantify this effect.

1.5.4 . Conclusion

In addition to the works cited earlier in this section, several other publications, although not directly related to the core thesis, provide also insights and contribute to various equations. These will be cited and elaborated upon in their respective chapters.

The aforementioned studies lay the theoretical groundwork for the models that will be developed in this thesis. Alongside the overview of fatigue stages introduced in Section 1.2.3, these studies are categorized into three stages that are pivotal for predicting fatigue lifetime:

- **Stage 0** (Stage I crack initiation): Stage I crack initiation has been treated in [25, 26, 31, 32]. Notably, [32] proposes a comprehensive crack initiation mechanism and makes an initial attempt at quantification. This thesis will further develop these initial studies by introducing modifications and enhancements in Chapter 4.
- **Stage 1** (Stage I crack propagation): Stage I crack propagation has been treated in [34, 36, 37] which offer valuable insights on crack propagation during Stage I. These results will be summarized and further developed in the form of a comprehensive Stage II crack propagation model.
- **Stage 2** (Stage II crack propagation): Prior to this thesis, the propagation of Stage II cracks has not been extensively explored based on sub-grain, 3D plasticity mechanisms. Methodologies and equations developed in the context of Stage I have been adapted for Stage II, demonstrating the versatility and applicability of these approaches. The developments for this stage will be detailed in Chapter 2.

At the end, as many readers might have noticed, the papers authored by Dr. Polák, Dr. Obtlík and Dr. Man were cited many times in the simulations works and this manuscript [38, 39, 40, 41, 42, 38, 43, 29, 44, 45, 46]. Indeed, their high quality experimental results have proved to be very useful in the validation of the simulation results. They will not be reviewed here but will be cited wherever necessary in the text.

1.6 . Objective of the thesis

The primary objective of this thesis is to develop comprehensive, practical fatigue models adapted to structural materials utilized in nuclear reactors (as discussed in Section 1.1 for the divertor). This study aims to bridge the gap between empirical models and the underlying physical mechanisms under complex cyclic loading conditions. Based on the DDD simulations of FCC material (316L stainless steel), the thesis aims to develop a general fatigue model for the prediction of fatigue life adapted to stages 0 and 2, thus completing the fatigue model system previously developed. A complete structure of the model developed and basic inputs and outputs are given in Fig. 1.29. Additionally, this thesis aims to create a methodology for using this technique to study the fatigue behavior of similar (FCC structure) materials used in the context of fusion reactor technology, including CuCrZr alloys.

An important aspect of this research is to investigate the model's capability to research fatigue under complex loading conditions. This involves studying the effects of mean stress, environment and loading conditions, physical variables which are accessible to experimental validation. The fatigue simulation process will also be highly customizable to allow investigating different loading conditions using minimal supporting empirical data.

While the prediction of the models in this research is usually at the grain scale, multiple scale transition techniques could be employed to predict the behavior of the material at the macroscopic scale: see Section 2.6 in Chapter 2 or [47]. Additional methods used in the context of multiscale investigation of nuclear materials are illustrated in Fig. 1.30.

Industrial objectives:

- Study the fatigue behavior of FCC materials (especially 316L stainless steel and CuCrZr) under complex loadings.
- Predict the fatigue lifetime with better consideration of environmental factors and loading conditions (like ratcheting, step loading etc.).
- Provide material information in the grain scale for the application of larger scale models (like FEM).

Scientific objectives:

- Complete the fatigue crack model system developed in the previous works with DDD simulations.
- Propose physical models that allow a better understanding of the fatigue mechanisms of FCC materials.

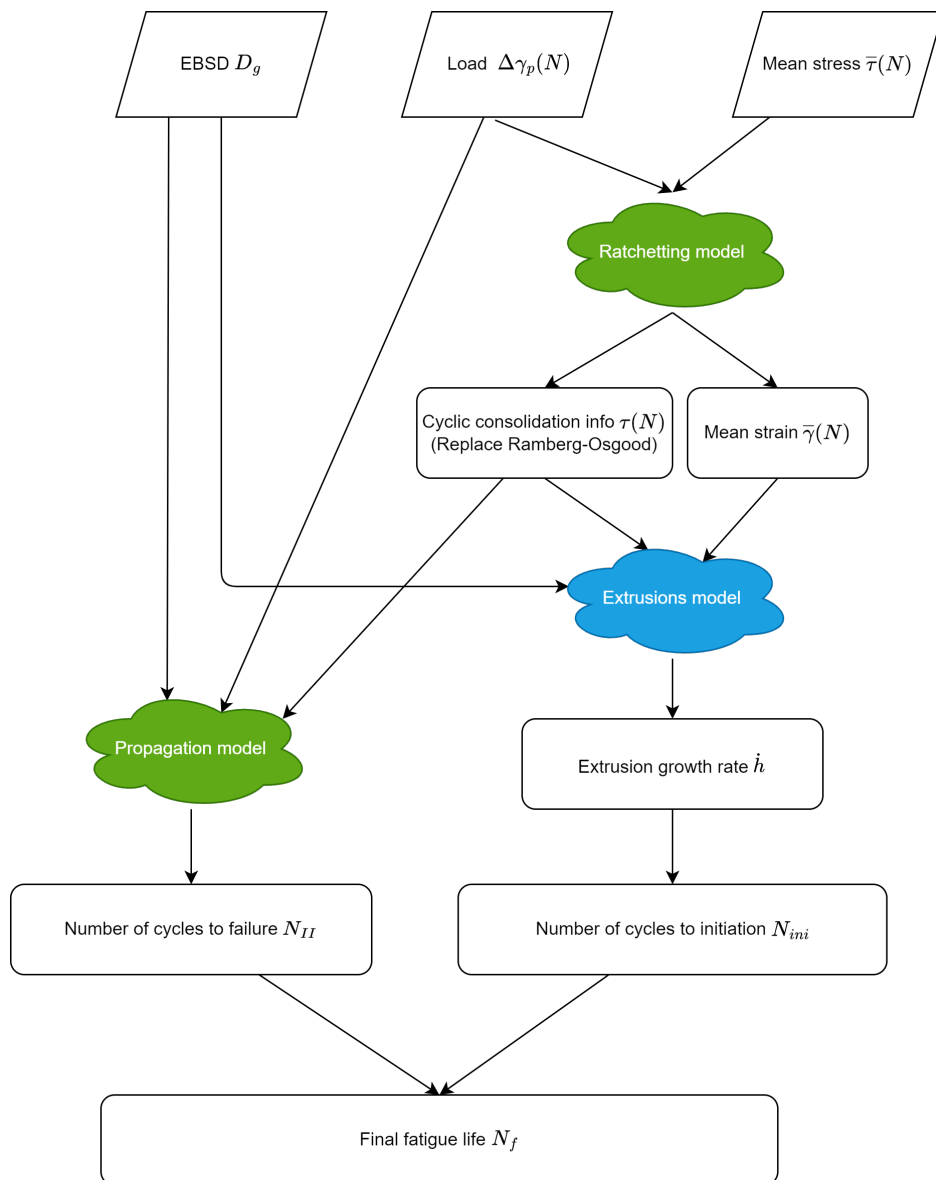


Figure 1.29: Structure and interactions of the models to be developed in this thesis.

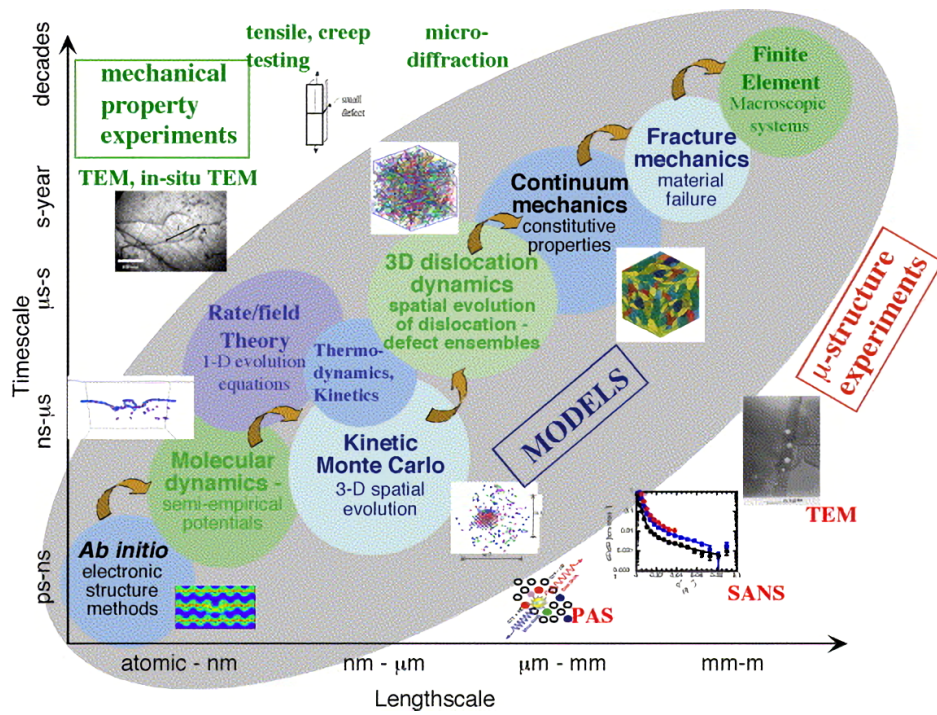


Figure 1.30: Multiscale investigation of nuclear materials [48]

- Verify the capability of DDD simulations in the study of complex fatigue scenarios.

2 - Stage II crack propagation model

The objective of this chapter is to introduce the Stage II crack propagation model, based on the three-dimensional dynamics of dislocation (DDD) simulations [36, 37]. These simulations uncover the mechanisms controlling crack propagation within the Stage II regime, which have been encapsulated into succinct equations mirroring Paris' law. Subsequently, these equations undergo calibration and validation against a broad spectrum of experimental studies, focusing on the crack growth rate and the fatigue life attributable to crack propagation. The culmination of this model is represented by the generation of a crack growth rate figure and the Manson-Coffin curve, elucidating the relationship between crack propagation and fatigue life.

This study is separated into two distinct parts:

1. **The Establishment of the Theoretical Framework and Formulation of the Equations:** This initial part focuses on developing a theoretical framework and deriving the equations that will guide the analysis of Stage II crack propagation (Section 2.3). It involves a detailed investigation of the mechanisms governing the crack tip opening displacement (CTOD) and corresponding crack propagation susceptibility.
2. **The Stochastic Analysis:** The subsequent part is dedicated to applying the formulated equations to practical scenarios, specifically using an Electron Backscatter Diffraction (EBSD) grain aggregate map to evaluate the growth of predetermined crack through macroscopic, polycrystalline grain aggregates. This stochastic type of analysis allows for evaluating the dispersion in crack growth rate and fatigue life.

Two papers have been published (or submitted) corresponding to each of these parts, with graphical abstracts illustrating the core concepts and findings of these studies presented on the subsequent pages (Fig. 2.1 and Fig. 2.2).

Stage-II fatigue crack growth model from 3D dislocation dynamics simulations

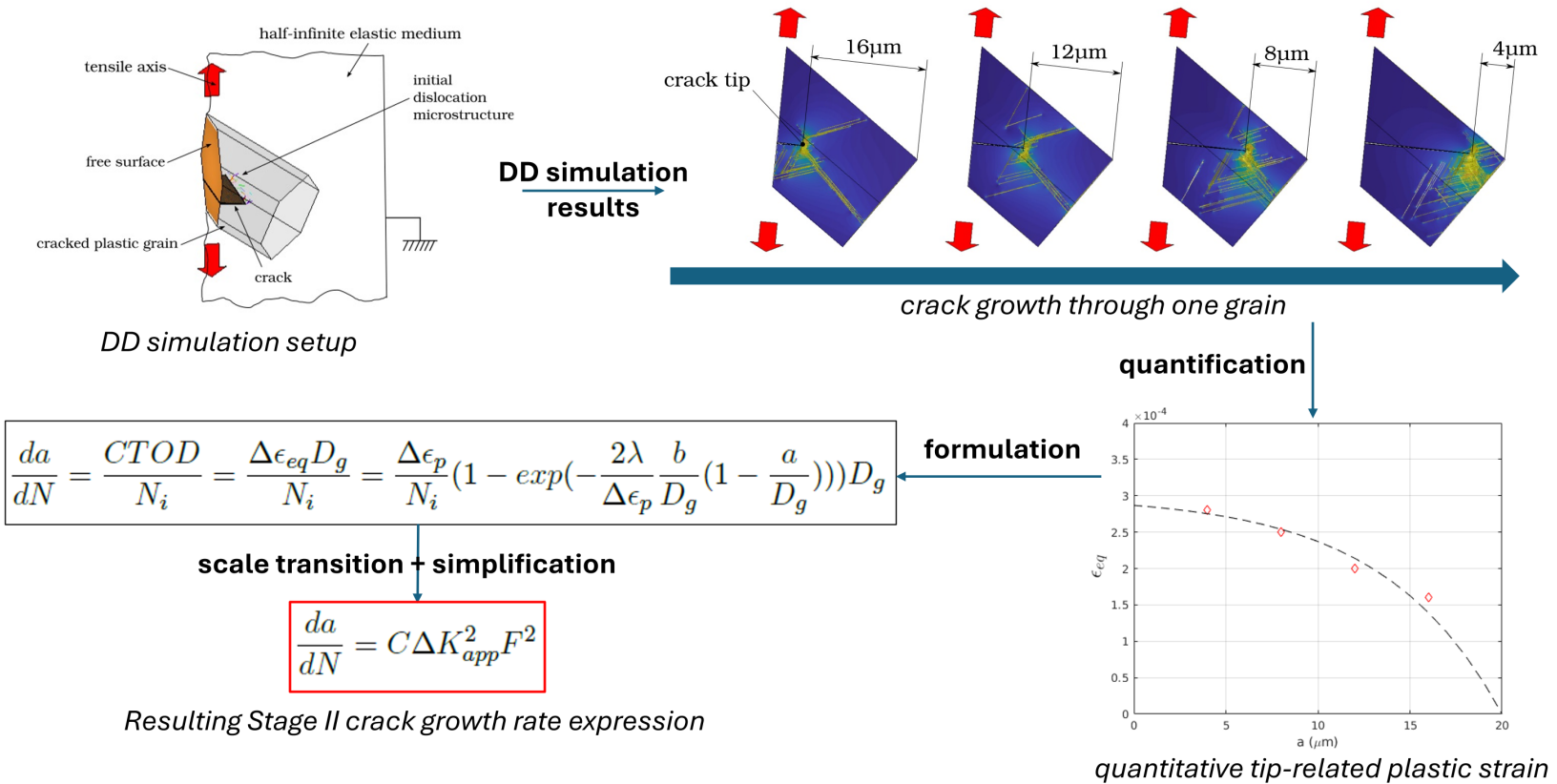


Figure 2.1: Graphical abstract of the Stage II crack propagation model.

Fatigue lifetime prediction using a dislocation-based stage II crack plasticity model

49

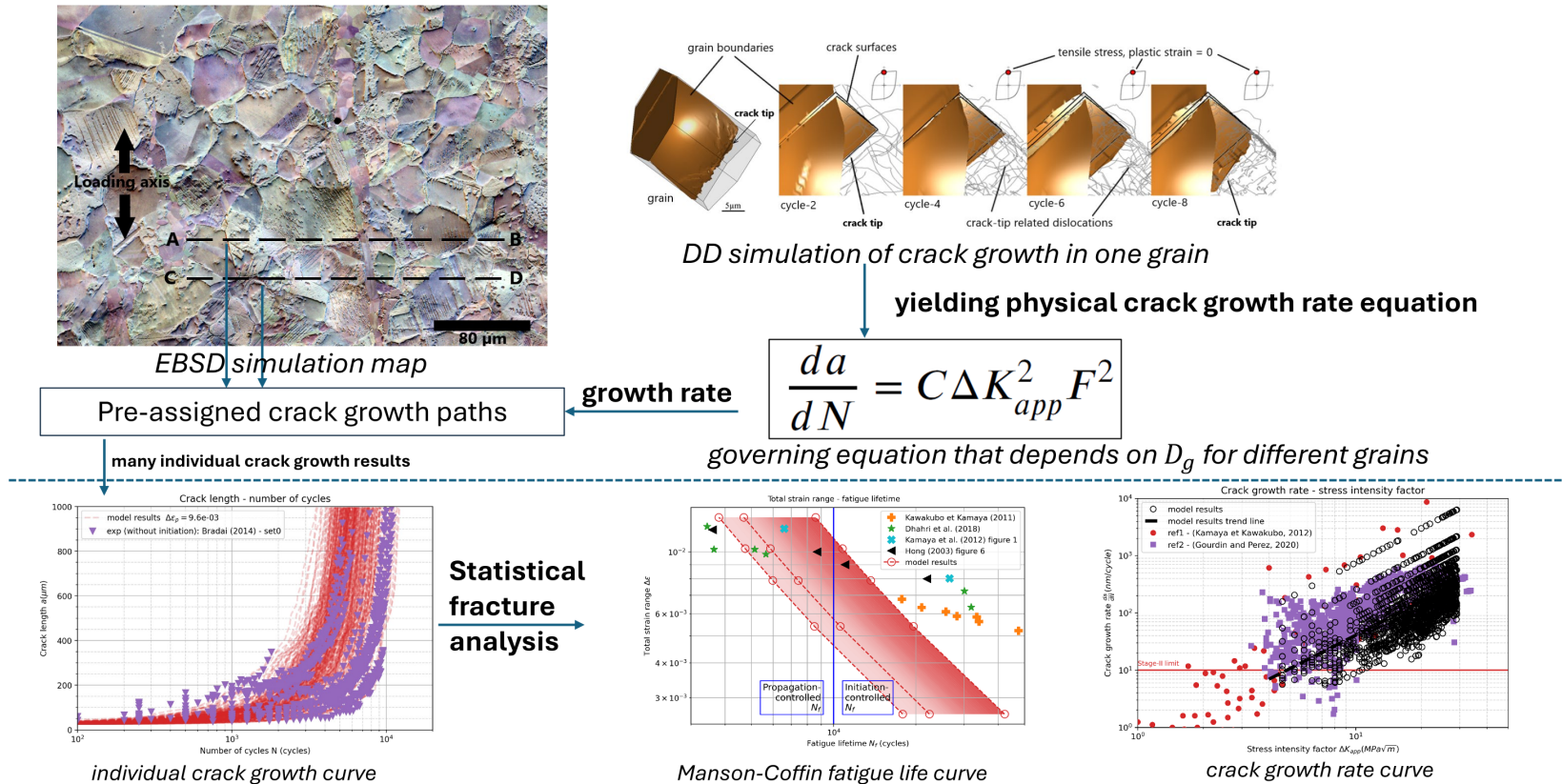


Figure 2.2: Graphical abstract of the Stage II crack propagation model applied to fatigue lifetime prediction of macroscopic, polycrystalline specimens/components.

2.1 . Introduction

As mentioned Chapter 1, structural materials used in nuclear sectors, such as 300 series steels, are frequently exposed to fatigue damage conditions. Initially, cyclic stress leads to concentrated strain in areas known as persistent slip bands (PSBs) [49, 45, 46]. These PSBs then create permanent surface changes referred to as persistent slip markings (PSMs).

PSMs often appear as extrusions that continue to grow during the initial phase, known as Stage 0, until they form nanosized crack-like defects. These early defects then extend and cut through the initial grains during the whole of Stage I, until they encounter a first significant barrier, like a grain boundary. The growth of Stage I cracks mainly happens either at the interface between the PSB and the rest of the material [46, 50, 51] or within the PSB itself [51, 20], following a specific crystallographic slip plane [37]. After overcoming this initial barrier, the cracks enter Stage II, and keep growing until the material ultimately fails.

Stage II fatigue cracks and the accompanying cyclic plasticity mechanisms have been explored in various realistic grain-scale settings through dislocation dynamics (DD) simulations [52]. This study (and its proceeding studies) forms the theoretical basis for our Stage II crack propagation model. The detailed history of these researches is presented in Section 1.5.

In this chapter, we aim to derive an expression for da/dN , reminiscent of Paris' expression, albeit depending on a set of physical variables rather than the usual empirical coefficients (refer to Section 2.3). Subsequently, a statistical analysis of crack growth along pre-assigned crack growth paths allows obtaining a more detailed and realistic examination of the material's behavior under fatigue and facilitates the direct comparison with conventional, macroscopic results for validation (refer to Section 2.6 and [53]).

In this chapter, the organization of the sections is as follows:

- In Section 2.3, the theoretical framework and corresponding Stage II crack propagation model are detailed.
- Section 2.4 will focus on the numerical methods used to solve the equations and other important computational aspects of the model.
- Section 2.5 is dedicated to the model parameter evaluation and calibration, followed by the validation of the computational results.
- The focus of Section 2.6 is on conducting a stochastic analysis for the sake of model comparison with applicable experimental results and validation.
- Finally, Section 2.7 summarizes the chapter, discusses the practical implications of this model for industrial applications, and outlines poten-

tial directions for future research to enhance both the model and the simulations.

2.2 . Literature review of stage II fatigue crack propagation models

During the first studies, Liu found out that the most critical stress parameter influencing the fatigue crack growth rate da/dN is the range of loading (stress range $\Delta\sigma$ or strain range $\Delta\epsilon$), rather than the maximum load (σ_{max} or ϵ_{max}) [54, 55, 56]. Subsequently, Paris and Erdogan [57] introduced the concept of the *stress intensity factor* ΔK in the equation of crack growth rate. During that period, several proposals [58, 59] were made to correlate the crack growth rate with the stress intensity factor, each suggesting different exponents and coefficients.

The most widely recognized version of the Paris-Erdogan law, $\frac{da}{dN} = C(\Delta K)^m$, was formalized in 1963 [59]. However, this equation does not address certain phenomena, such as the effect of the stress ratio on the crack growth rate. To accommodate the stress ratio effect, Forman [60] and Walker [61] each proposed modifications to the Paris-Erdogan law, incorporating the stress ratio R . In contemporary practice, the NASGRO equation [62] is frequently used with a view to better predict crack growth rates for industrial applications. Additionally, there are variations of this equation, like the McClintock equation [63] or the Elber equation [64], which possess similar structures plus specific unique features to each model, which will not be elaborated upon here.

The endeavor to link dislocation behaviors with crack propagation began well after the establishment of the Paris-Erdogan law. In the 1970s, research revealed that the generation of dislocations at the crack tip plays a crucial role in determining whether a material fractures in a ductile or brittle manner [65, 66, 67]. Even before the advent of dislocation simulation capacities, theoretical models of dislocation-based crack propagation were put forward [68, 69]. Some findings from these early models align with discoveries in this research, such as the square relationship between the crack growth rate and the stress intensity factor, and the influence of the shear modulus (G). Nonetheless, the precision in estimating strain distribution in those earlier studies was affected by various limitations. Moreover, these dislocation models did not quantitatively address the impact of grain size and (screw) dislocation cross-slip, which likely play a crucial contribution. Without considering grain size, it generally turned out to be a challenging task to predict the variability of the fatigue crack growth rate observed in various materials.

In modern times, the extensive use of the Finite Element Method (FEM) has prompted researchers to develop models that can predict fatigue crack

growth rates with more accuracy. For instance, Vena et al. studied fatigue crack growth in zirconia, identifying a two-stage growth behavior influenced by stress intensity factors [70] (see Fig. 2.5). This study explores the capability of FEM to predict crack growth rates. Additionally, FEM has been utilized to investigate complex crack behaviors, such as interactions with discontinuities [71]. There have been advancements in FEM techniques specifically for fatigue crack simulation, as demonstrated by Hu et al., who introduced an enriched finite element method to model fatigue crack growth, concentrating

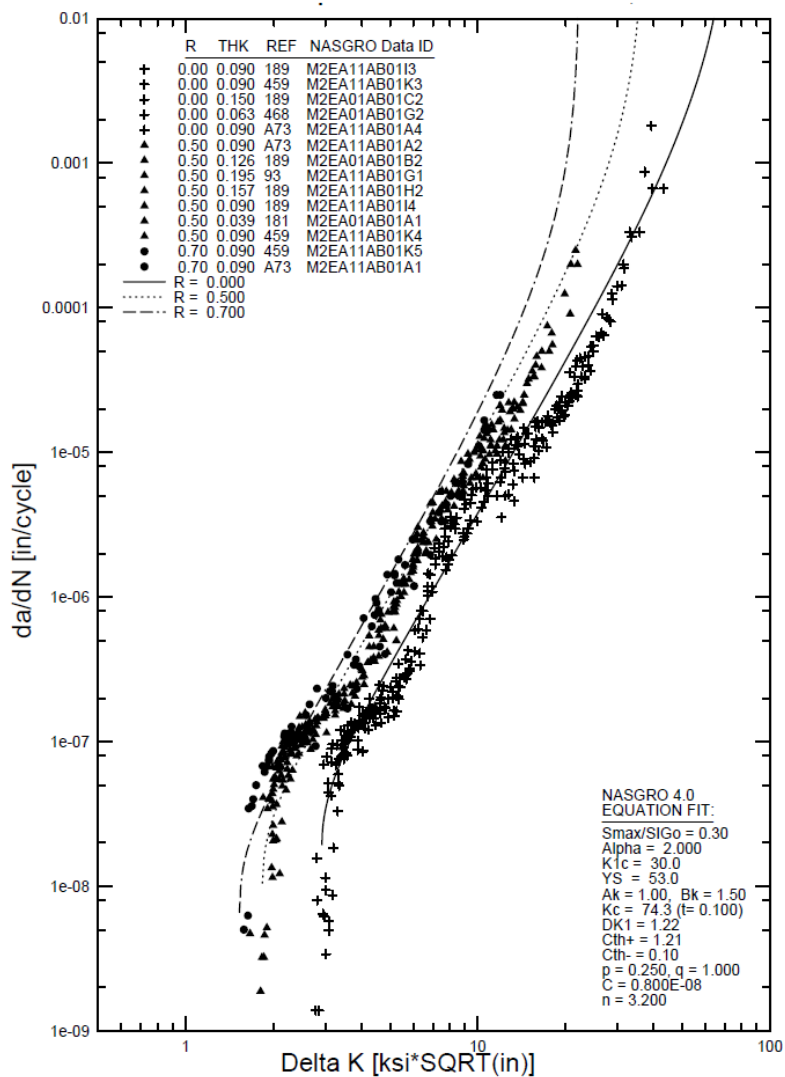


Figure 2.3: The results of the NASGRO equation for the crack growth rate for different stress ratios.

on accurately simulating the displacement and stress fields around crack tips [72] (see Fig. 2.4).

FEM models, however, depend on specific material and load-dependent constitutive rules, to be applied on a specific simulated mesh. These laws are either empirical or physically based and often require investigation at a finer scale, like dislocation dynamics (DD) simulations. Integrating FEM with the model proposed in this thesis could potentially broaden the scope of application, enabling a more comprehensive understanding of fatigue crack growth across different scales.

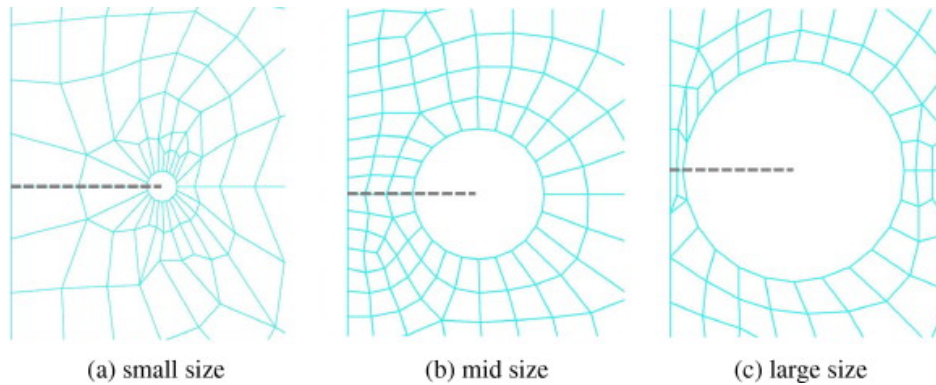


Figure 2.4: An example mesh configuration around the crack tip in a FEM simulation [72].

Compared to the models previously mentioned, the model introduced in this study leverages dislocation dynamics simulations, providing a more precise assessment of strain distribution and the impact of grain sizes. The parameters within this model have a clear physical meaning and can be directly measured through experiments or finer simulations including atomistic simulations. A key advantage of this model is its capability to predict the variability in the fatigue crack growth rate within the material, which is crucial for accurately forecasting the fatigue life of materials. This feature of dispersion prediction distinguishes it from traditional methods, which may not offer such detailed insights, as illustrated in the comparisons with general traditional methods (like those shown in Fig. 2.3 or when comparing Fig. 2.5 with Fig. 2.26).

2.3 . Development of the theoretical equations

The theoretical foundation of the Stage II crack propagation model is rooted in the dislocation dynamics (DDD) simulations utilizing the simulation software TRIDIS [25, 36, 37, 73, 21]. The fundamentals of these DDD simulations and how they were configured are comprehensively discussed in Sec-

tion 1.5. In this section, we briefly revisit the simulation setups and the findings specifically related to Stage II crack propagation.

2.3.1 . Setup of the prior DDD simulations

The simulation setup features a single grain modeled as a hexagonal prism, with a height-to-circumscribed diameter ratio of 1, as shown in Fig. 2.6a. The grain has boundaries impermeable to dislocations, except for one free surface where mobile dislocations can exit and create surface slip markings. The simulated cell functions as an elastic-plastic medium, representing a grain, which is assumed to be embedded within an infinite elastic continuum. This conceptualization is particularly pertinent to the Stage II fatigue regime, where plastic deformation is localized around the crack tip region. Meanwhile, the crystal adjacent to the crack experience partial unloading due to the crack shadowing effect, which reduces the local stress and strain [74, 75, 76].

Inside the simulation environment, a stage II crack is represented as a combination of three elements:

- (i) a set of (two) free surfaces inserted in a grain representing the surrounding, un-cracked grain matrix or medium,
- (ii) a heterogeneous, crack-induced stress field (not shown) [20]. The field

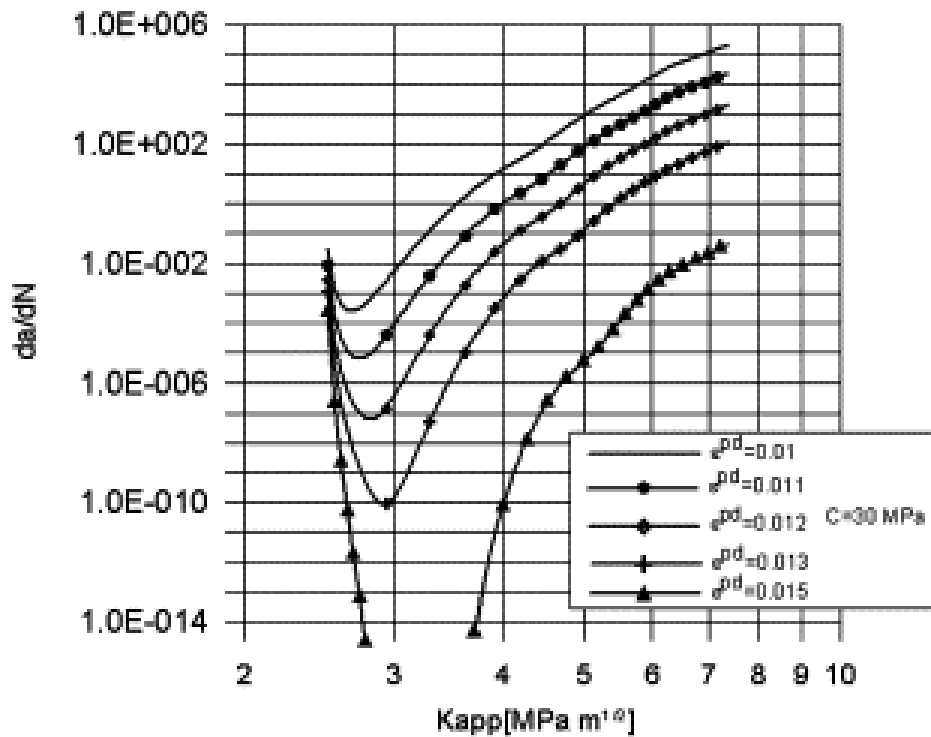
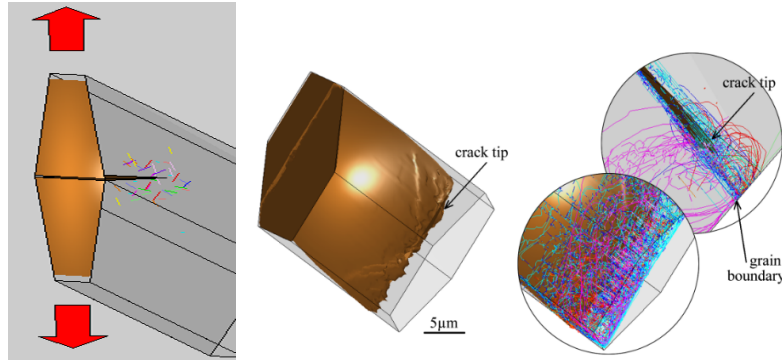


Figure 2.5: The results the crack growth rate for different strain loads [70].



(a) Initial dislocation structures for stage-II, random dislocation sources. (b) Details of dislocation-mediated plasticity mechanisms controlling the crack-tip opening displacements. Out of crack plane plastic strain spreading due to cross-slip mechanism is in evidence, as the tip draws near the grain boundary.

Figure 2.6: Dislocation dynamics simulation cases adapted crack propagation.

is generated in the surrounding cracked grain and can be expressed as:

$$\sigma_{ij}(r, \theta) = \frac{K_I}{\sqrt{2\pi r}} f_{ij}(\theta) + \frac{K_{II}}{\sqrt{2\pi r}} g_{ij}(\theta) + \frac{K_{III}}{\sqrt{2\pi r}} h_{ij}(\theta) \quad (2.1)$$

Since that all the *implemented* cracks are orientated normally to the tensile loading direction, the stress intensity factors $K_{II} = K_{III} = 0$ and $K_I = \sigma\sqrt{\pi a}$ are used. The resulting stress field is then:

$$\sigma_{ij}(r, \theta) = \frac{\sigma\sqrt{\pi a}}{\sqrt{2\pi r}} f_{ij}(\theta) = \sigma\sqrt{\frac{a}{r}} f_{ij}(\theta) \quad (2.2)$$

- (iii) a set of random dislocation sources placed at a short distance ahead of the crack tip surfaces [37] (see Fig. 2.6b). These sources produce plastic strain everywhere in the grain (owing to dislocation multiplication and subsequent glide), including in the crack tip region.

To initiate the corresponding DD simulation, it is essential to position initial dislocation sources within the grain. These sources consist of pinned segments, with at least one segment stting in each possible slip system. Although their lengths are approximately similar, their positions are randomized, yet placed as near as feasible to the crack tip region. The configuration of these initial sources has been empirically verified to exert minimal impact on the microstructure's morphology following sufficient loading cycles [20, 77, 78].

2.3.2 . Basic DD simulation results

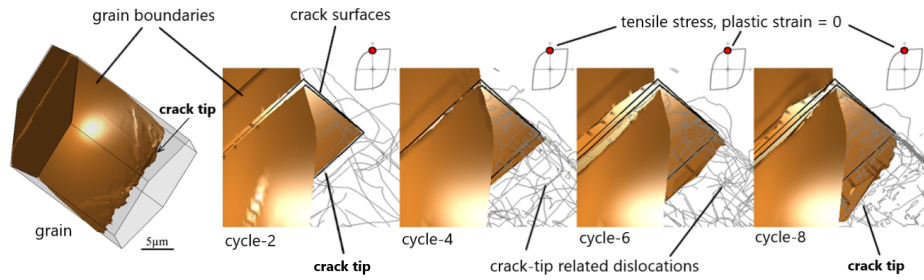
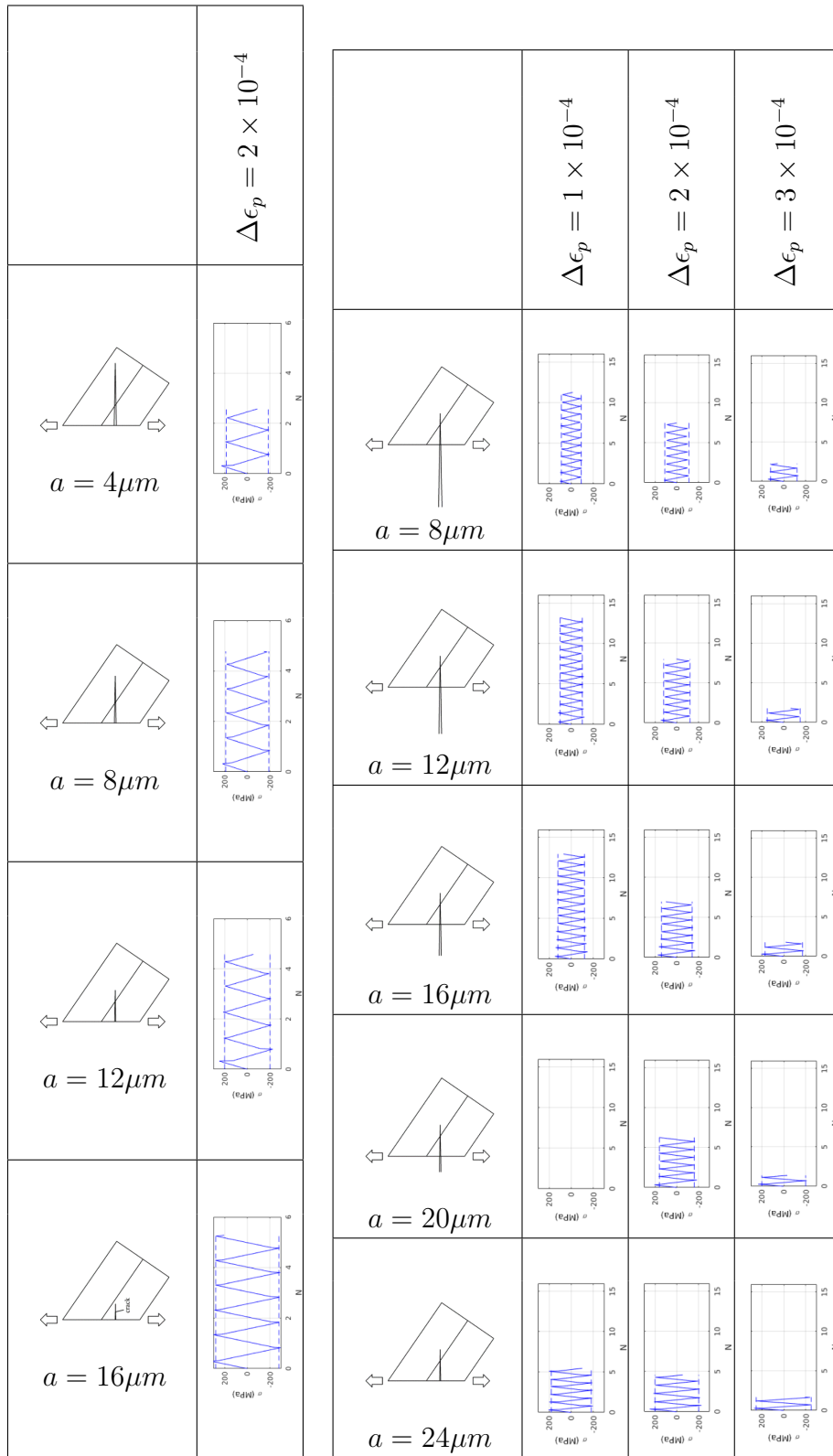


Figure 2.7: Mechanisms of dislocation-mediated cyclic plasticity are pertinent to Stage II crack development. The described simulation setup accurately models the 3D microstructure of a Stage II crack. This simulation is executed under a controlled plastic strain range of $\Delta\epsilon_p = 2 \times 10^{-4}$, utilizing symmetric ($R = -1$) loading conditions. Snapshots are captured at various cycle intervals, all under identical reference plastic strain conditions, to facilitate a precise analysis of the surface displacement over time. These surface displacement maps are instrumental in deriving the Crack Tip Opening Displacement (CTOD) expressions, Eq. (2.3) and Eq. (2.4), as discussed in this study.

The immediate outcomes of the simulations are the local stress and strain responses to cyclic plastic-strain-controlled loading conditions. However, certain results necessitate advanced post-treatment methods, particularly when dealing with substantial dislocation quantities, including the corresponding, highly complex displacement field extraction becomes non-trivial (refer to [79] for details). In the subsequent subsections, these fundamental and direct results of the simulations will be presented. The Crack Tip Opening Displacement (CTOD) calculated based on the local strain response, will also be discussed. This CTOD formula is a crucial element in the development of our principal Stage II crack propagation model.

Local stress response to cyclic plastic-strain-controlled loading

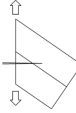
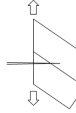
The cyclic stress responses from various simulation scenarios are illustrated in Fig. 2.8 and Table 2.1. Figure 2.8 depicts the cyclic stress response under applied plastic strain and highlights the influence of crack depth. Table 2.1 provides a summary of the stabilized stress levels and the stress intensity factor $K_I = \sigma\sqrt{\pi a}$, which will be utilized in subsequent sections. The findings also confirm that the stress intensity factor is independent of crack depth, aligning with Eq. (2.2). These quantitative outcomes are in agreement with experimental findings cited in [29, 43, 80].

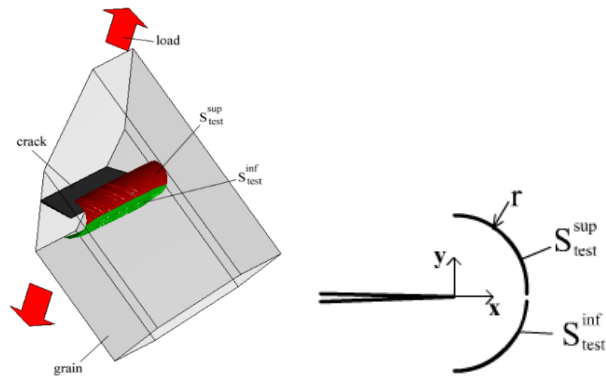


(a) Crack lengths: $a = 4, 8, 12$ and $16 \mu m$. Crack tip stands at $16, 12, 8, 4 \mu m$ off the grain boundary. $\Delta\epsilon_p = 2 \times 10^{-4}$.
 (b) Crack lengths: $a = 8, 12, 16, 20$ and $24 \mu m$. Crack tip stands at $12 \mu m$ off the grain boundary. $\Delta\epsilon_p = 1 \times 10^{-4}, 2 \times 10^{-4}$ and 3×10^{-4} .

Figure 2.8: Applied stress evolutions obtained for different plastic strain ranges and different crack lengths.

Table 2.1: Stress intensity factors calculated based on the result of Fig. 2.8

| |  |  |  |  |  | |
|----------------------|---|---|---|---|--|---------------------------------------|
| $a(\mu m)$ | 8 | 12 | 16 | 20 | 24 | |
| $\Delta\sigma$ (MPa) | 180 | - | 120 | 110 | 100 | $\Delta\epsilon_p = 1 \times 10^{-4}$ |
| K_I (MPa) | 902 | - | 850 | 871 | 868 | |
| $\Delta\sigma$ (MPa) | 200 | 160 | 140 | 120 | 110 | $\Delta\epsilon_p = 2 \times 10^{-4}$ |
| K_I (MPa) | 1002 | 982 | 992 | 951 | 955 | |
| $\Delta\sigma$ (MPa) | 250 | 200 | 170 | 150 | 120 | $\Delta\epsilon_p = 3 \times 10^{-4}$ |
| K_I (MPa) | 1253 | 1227 | 1205 | 1189 | 1128 | |



(a) Half-cylindrical mesh (b) Calculation mesh details, ahead of the crack front. Quantity r is the radius of curvature of the mesh itself.

Figure 2.9: Quantitative CTOD evaluation method.

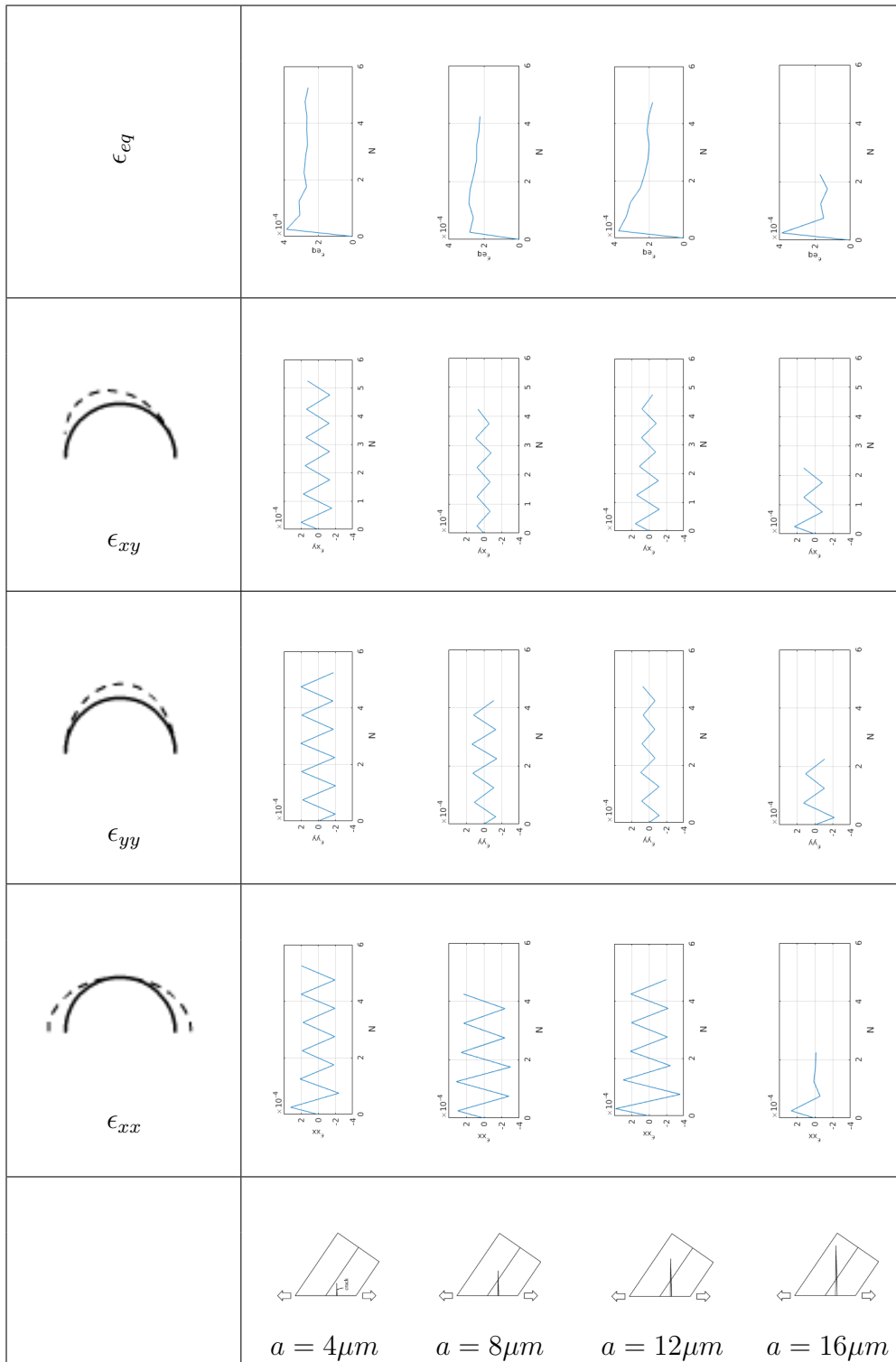


Figure 2.10: Crack-induced plastic strain for different crack lengths. Strain components ϵ_{xx} , ϵ_{yy} , ϵ_{xy} and equivalent strain ϵ_{eq} for applied plastic strain range $\Delta\epsilon_p = 2 \times 10^{-4}$ and different crack lengths: $a = 4, 8, 12$ and $16 \mu m$.

Local strain response to cyclic plastic-strain-controlled loading

The analysis of the local strain response is conducted through a specific post-treatment calculation process, utilizing half-cylinder calculation meshes situated a short distance from the crack tip, as depicted in Fig. 2.9. The strain range induced by the crack tip, denoted as $\Delta\epsilon_{eq}$, is determined by averaging the displacements of the upper and lower meshes, which are affected by dislocations emitted from the tip. Quantitative evaluations of the plastic strain evolution induced by the crack, particularly for Stage II cracks of varying lengths, are presented in Fig. 2.10, assuming a plastic strain increment $\Delta\epsilon_p = 2 \times 10^{-4}$. The components of the plastic strain, ϵ_{xx} , ϵ_{yy} , ϵ_{xy} , and ϵ_{eq} , are defined as follows:

$$\epsilon_{xx} = \frac{((u^{sup} + u^{inf})_x)^{moy}}{r} \quad (2.3)$$

$$\epsilon_{yy} = \frac{((u^{sup} - u^{inf})_y)^{moy}}{2r} \quad (2.4)$$

$$\epsilon_{xy} = \frac{((u^{sup} - u^{inf})_x)^{moy}}{2r} \quad (2.5)$$

$$\epsilon_{eq} = \sqrt{\frac{2}{3}(\epsilon_{xx}^2 + \epsilon_{yy}^2 + 2\epsilon_{xy}^2)} \quad (2.6)$$

where u^{sup} and u^{inf} are the displacements calculated on the superior and inferior meshes as sketched Fig.2.8. Those displacements are projected along x (Eq. (2.3) and Eq. (2.5)) and y (Eq. (2.4)) directions and then averaged out along the whole crack front, i.e. along direction z. The results show that the plastic strain ϵ_{eq} (Eq. (2.6)) developing near the crack tip stabilizes shortly after completion of the first fatigue cycle (see Fig. 2.10). Namely, the local plastic strain level is about $\epsilon_{eq} = 3/2\Delta\epsilon_p$ as long as the crack tip is relatively far-off the grain boundary. The local *stabilized* plastic strain level is plotted in Fig. 2.11 (open symbols), showing the crack tip opening deformation evolution representative of stage II fatigue conditions.

Figure 2.11 evolution can be described using the following, semi-analytical expression:

$$\epsilon_{eq} = K_s \frac{\epsilon_p}{2} [1 - \exp(-\frac{2\lambda}{\Delta\epsilon_p} \frac{b}{D_g} (1 - \frac{a}{D_g}))] \quad (2.7)$$

where K_s is a dimensionless scaling factor, λ is the number of dislocations stored in the crack-tip process zone (averaged out over one complete fatigue cycle), b is the Burgers vector magnitude and D_g the grain size (diameter). Equation (2.7) includes a growth driving term: $K_s\epsilon_p/2$ and a growth mitigation term: $K_s\epsilon_p/2\exp(-2\lambda b/D_g\Delta\epsilon_p(1 - a/D_g))$ that scales with the cross-slip probability (or rate) evolution along the tip-emitted shear bands, as the crack front gradually draws near the grain boundary [36]. Equation (2.7) will be directly used in the crack growth model's equations (see next section Section 2.3.3).

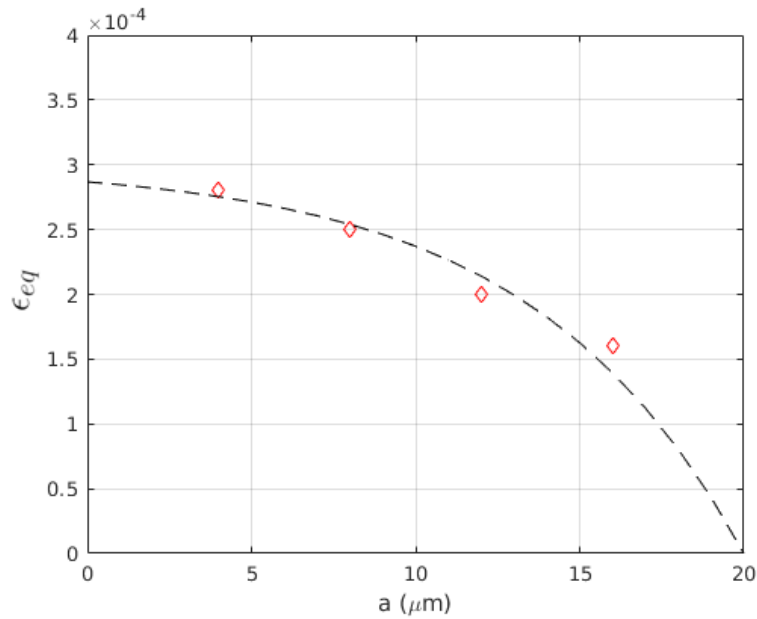


Figure 2.11: Crack-tip strain ϵ_{eq} amplitude for increasing crack length. The analytical curve (dashed line) is plotted using Eq. (2.5) with $\Delta\epsilon = 2 \times 10^{-4}$, $K_s = 3$, $D_g = 20\mu\text{m}$, $b = 2.5 \times 10^{-4}\mu\text{m}$ and $\lambda = 25$ (dimensionless).

2.3.3 . Stage II crack propagation model

As outlined in the literature review chapter, stage II crack growth models are categorized into two primary types:

1. **Slip-induced crack growth:** This model suggests that crack propagation is predominantly governed by dislocation slip mechanisms. The repetitive plastic deformation process facilitates the inception and expansion of cracks along distinct slip planes within the material's crystalline framework. In face-centered cubic (FCC) metals, such as stainless steel, the presence of multiple slip systems allows for crack propagation, given these materials' notable ductility and slip symmetry.
2. **Void formation and growth (nano-cavities):** According to this model, crack growth is characterized by the nucleation and amalgamation of micro-voids or nano-cavities, often accelerated by the material's interaction with its environment, such as in corrosive settings or even in the presence of air, where environmental interactions at the crack tip can promote void formation.

Firstly, the nucleation of quasi-cleavage cavities has been correlated with increased levels of acoustic emission in materials with low stacking fault energy (SFE), as observed in various studies [81]. Secondly, simulations have shown that dislocation-mediated slip within the simulation cell, including at

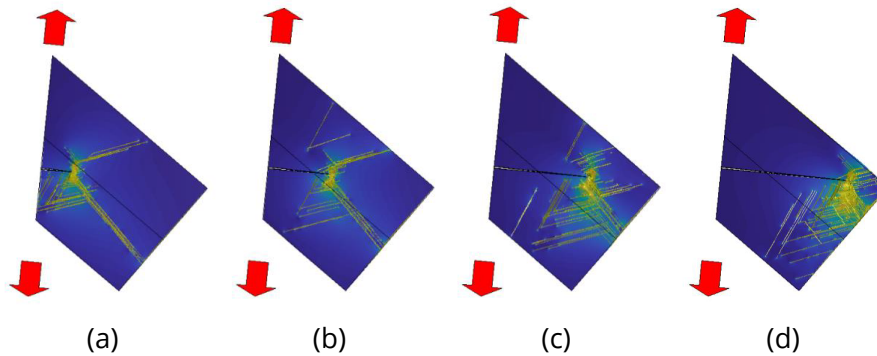


Figure 2.12: Cyclic plasticity mechanisms associated with increasing stage II crack depth. Plastic strain involves multiple slip conditions. Plastic strain confinement depends on the crack tip distance to the microstructural barrier (grain boundary), decreasing from (a) through (d) snapshots.

the crack-tip region, is essentially reversible (refer to Fig. 2.7). This reversibility, as predicted by dislocation dynamics (DD), indicates that the cyclic slip irreversibility is most likely too small to account for the crack growth rates observed in 300-series steels. Furthermore, throughout the discrete dislocation (DD) simulation [36], the nano-cavity model has been identified as the most suitable mechanism for modeling crack growth. This model aligns closely with simulation results and offers a more accurate explanation of the phenomena observed.

A comprehensive mechanism of crack growth is hence delineated. Fig. 2.12 illustrates the plasticity mechanisms linked with stage II cracks, depicting the increase in crack length and the decrease in distance from the crack tip to the grain boundary. Under these circumstances, slip occurs omnidirectionally from the crack tip and activates various non-coplanar slip systems [36].

The dislocation displacements induced by the crack are mostly reversible, alternating with each cycle. This behavior is typical of a wide range of low stacking fault FCC materials. In practice, crack-tip surfaces cyclically interact with the environment, encountering local adsorption of solute elements like O_2 or water vapor, thereby reducing the interfacial energy of the cyclically exposed surfaces. Consequently, fatigue cracks propagate through successive de-cohesion each time fostered by the generation of several (or at least one) nano-cavities along the crack front. In these conditions, the rate of stage-II crack propagation thus directly correlates with the amplitude of the crack tip opening displacement (CTOD).

It is important to note that the crack growth scenario described above aligns with the formation of fatigue striations on the fracture surface, as observed and documented in the literature [82]. This claim is substantiated by the fact that the nano-cavity nucleation rate N_i is significantly greater than

0.25 (one loading stroke) and the nano-cavity size a is considerably smaller than the typical striation width, which typically spans several microns. Under these conditions, the crack tip region undergoes multiple sequences of surface steps moving inward (step-in) and outward (step-out) before any actual permanent crack progression occurs.

The step-out events coincide with the absorption of various molecules like H_2O , N_2 , O_2 , H_2 , etc., from the testing environment (air at room temperature, for instance). Upon load reversal, the subsequent step-in event facilitates the transport of these adsorbed molecules into the crystal, leading to embrittlement of the step-in/step-out region. These reversible sequences continue until a permanent nano-cavity forms somewhere along the crack front, leading to rapid de-cohesion of the adjacent, and much larger brittle region. This process results in a sharp contrast in striations on the fracture surface, often accompanied by the emission of a strong acoustic signal as mentioned at the beginning of this section [81, 83].

That scenario explains the case where sharp, discontinuous striation contrasts are produced alongside continuous, reversible dislocation glide, particularly characteristic of low-SFE metals like the 300 series steels. It is important to clarify that the nano-cavity formation mechanism is not synonymous with the striation formation itself but rather, to striation initiation. This sequence of events is also consistent with observed differences in crack propagation rates between fatigue experiments conducted in air and vacuum [84, 85, 86], highlighting the environmental influence on crack growth behavior.

Based on the previous discussion, our model involves calculating the amplitude of the Crack Tip Opening Displacement (CTOD) and the number of cycles to void nucleation N_i . Then the crack growth rate can be directly evaluated using $da/dN = CTOD/N_i$. The expansion of the CTOD expression and the variable conversion will be detailed in the main model in Section 2.3.3. Following this, the nano-cavity model will be presented in Section 2.3.3 for the calculation of N_i .

Main model

At first, we expand the main model for stage II crack propagation. Based on Eq. (2.7) from the preceding section, we proceed as follows:

$$\frac{da}{dN} = \frac{CTOD}{N_i} = \frac{\Delta\epsilon_{eq}D_g}{N_i} = \frac{\Delta\epsilon_p}{N_i} \left(1 - \exp\left(-\frac{2\lambda}{\Delta\epsilon_p} \frac{b}{D_g} \left(1 - \frac{a}{D_g}\right)\right)\right) D_g \quad (2.8)$$

where $\frac{da}{dN}$ represents the crack growth rate per cycle, $CTOD$ the Crack Tip Opening Displacement from previous section, $\Delta\epsilon_{eq}$ the equivalent plastic strain at the crack tip, $\Delta\epsilon_p$ the applied plastic strain range, D_g the grain size, N_i the number of cycles to void nucleation. Other variables are material constants as defined in Section 6.1.

Application of this model to macroscopic specimens of components entails the transformation of the macro-scale plastic strain range $\Delta\epsilon_{p,macro}$ into the micro-scale local plastic strain range at the cracked grain $\Delta\epsilon_{p,local,wc}$ (*wc* signifying "with crack"). This transformation is imperative for the practical application of the equation, which requires a comparison of the cyclic stress-strain behavior between cracked and uncracked grains, as explored in [35]. Merging expressions (11) and (12) from [35] yields:

$$\Delta\epsilon_{p,local,wc} = \frac{2\Delta K_{app}\sqrt{\frac{1}{2r_0}}}{[\frac{1}{S}\frac{\mu}{1-\nu}](1 + \frac{\bar{\epsilon}_{p,macro}}{\Delta\epsilon_{p,macro}})} \left(1 + \frac{\Delta K_{app}}{\Delta\sigma_{app}}\sqrt{\frac{1}{2r_0}}\right) \quad (2.9)$$

where:

- S is the dimensionless grain shape factor [17], the detailed estimation process can be found in [25].
- r_0 a reference distance to the crack tip scaling with the crack-induced plastic zone size.
- $\Delta K_{app} = \Delta\sigma_{app}\sqrt{\pi a}$ is the aggregate-scale stress intensity factor.
- $\epsilon_{p,macro}$ the macro-scale mean strain amplitude. Although theoretically the mean strain effect can be taken into account, it is generally neglected in the model due to many limitations. In following sections, we will set $\bar{\epsilon}_{p,macro} = 0$.

Inserting Eq. (2.9) in Eq. (2.8) assuming $a \gg D_g$ stage II cracks (therefore $\Delta K_{app}/\Delta\sigma_{app} \gg \sqrt{2r_0}$), makes it (after re-arrangement):

$$\frac{da}{dN} = C\Delta K_{app}^2 F^2 \quad (2.10)$$

Equation (2.10) is similar to the well-known Paris' law for a semi-circular crack front, provided:

$$C = \frac{D_g}{2r_0(\frac{1}{S}\frac{\mu}{1-\nu})\Delta\sigma_{app}N_i} \quad (2.11)$$

and

$$F = \sqrt{1 - \exp\left(-\frac{r_0(\frac{1}{S}\frac{\mu}{1-\nu})\Delta\sigma_{app}}{K_0^2} \frac{\lambda b}{2D_g}\right)} \quad (2.12)$$

putting $(1 - a/D_g)/\Delta K^2 = 1/\Delta K_0^2$ i.e. assuming stable through-grain crack growth; whereas $\Delta K_0 = \Delta\sigma_{app}\sqrt{\pi a_0}$ is related to unit crack length a_0 . *Stable through-grain crack growth* in the j -th grain of a poly-crystal means: $da/dN_j = f(D_{g,j})$ for $a \gg D_g$. This situation contrasts with Fig. 2.11 results, where $da/dN = f(a, D_g)$ for $a < D_g$.

The physical interpretation of the variables appearing in Eq. (2.11) and Eq. (2.12) is as follows:

- C (in MPa^{-2} units) characterizes the material resistance against the crack front extension.
- F is a dimensionless efficiency factor, tuning the local (grain-scale) crack growth rate since $\Delta K_{app}^2 F^2 = \Delta \sigma_{app}^2 \pi a F^2$ is proportional to the elastic energy driving the crack growth.
- $\Delta \epsilon_{p,macro}$ is the applied plastic strain range (tension plus compression)
- $\Delta \sigma_{app}$ is the applied stress range, calculated from the Ramberg-Osgood relation according to $\Delta \epsilon_{p,macro}$.
- D_g is the effective grain size in reference to Section 2.6.1.
- N_i is the time to initiation of a micro-cavity (in cycles) at the tip of the crack from solving Eq. (2.13). Additional qualitative explanations are given in the following paragraphs whereas a thorough quantitative application is presented in [52].

The above-listed variables generally depend on either the loading conditions or the evolution of the grain-scale microstructure. The (invariable) material constants used in the model are listed in Section 6.1.

This concludes the equations of the main model for stage II crack propagation. Now, if furthermore N_i is explicitly determined, the crack growth rate can be directly evaluated using Eq. (2.10). In the next section, the cavity nucleation sub-model will be presented to compute N_i .

Nano-cavity sub-model

In order to obtain quantitatively the number of cycles to void nucleation N_i , the following sub-model is proposed. As discussed at the beginning of this section, the cavity model is chosen to be the mechanism of this crack growth model, in which we assume that crack opening and closing are mostly reversible until the crack surface has formed a cavity that subsequently expands and creates permanent new surfaces along the crack front (interpreted as striations). The number of cycles that lead to the nucleation of a cavity is denoted as N_i (which is used in previous equations). The process governing N_i is influenced by local crystallographic de-cohesion and related to various factors including grain size D_g , load value $\Delta \epsilon_p$ and eventually the interaction between the surface and the environment which is represented by the surface energy term γ_{surf} .

Based on [87, 88, 89] and [26], the following equation can be summarized to describe the cavity nucleation rate:

$$\tau_0 + \left(\frac{d\tau_{int}}{dN}\right)N_i = \tau_{crit}(\gamma_{surf}) \quad (2.13)$$

where $\tau_{crit}(\gamma_{surf})$ is a critical nano-cavity nucleation stress at the crack tip (to be detailed below); $\tau_0 = 0$ is the stress level initially acting at the crack tip scale and $d\tau_{int}/dN$ is the rate of evolution of local, internal stress [90]. We may then write:

$$\frac{d\tau_{int}}{dN} = \frac{d\tau_{int}}{dy} \frac{dy}{dN_{cycle}} \quad (2.14)$$

where $d\tau_{int}/dy$ evolution depends on a simple decay function $\tau_{int} = -\tau_{app} \exp(-2k \frac{|y|}{D_g})$ describing the long-range stress landscape due to individual shear bands (see Fig. 4 of reference [16], for example). We can then rewrite Eq. (2.14) as:

$$\frac{d\tau_{int}}{dy} = -2\tau_{app} \frac{k}{D_g} \exp(-2 \frac{ky_0}{D_g}) \quad (2.15)$$

where the tip-driven plastic zone size $y_0 \leq 1/2\mu\lambda b/\pi(1-\nu)\tau_{MAX}$ i.e. the sub-band dislocation pile-up size. We then obtain:

$$\frac{d\tau_{int}}{dN} = -2\tau_{app} \frac{k}{D_g} \exp(-2 \frac{ky_0}{D_g}) \frac{dy}{dN_{cycle}} \quad (2.16)$$

where dy/dN_{cycle} characterizes (intra)PSB evolution. Quantity $dy/dN_{cycle} \approx 1.5$ to 6 nm/cycle is obtained by solving Eq. (2.16) using $d\tau_{int}/dN_{cycle} \approx 5$ to 12 MPa/cycle from reference [26]. Quantity dy/dN_{cycle} is grain-size and load independent in a broad range of fatigue conditions, as far as crack-related plasticity is controlled by shear band nucleation and activity (glide). We may then estimate the critical crack (or nano-cavity) emission stress $\tau_{crit}(\gamma_{surf})$ in Eq. (2.13) using Griffith's theory of crack stability, where

$$\tau_{crit,0} \approx \sqrt{\mu[\pi/(1-\nu^2)](\gamma_{surf,0}/a_{Griffith,0})} \quad (2.17)$$

is associated with reference surface energy $\gamma_{surf,0}$ and crack/cavity size $a_{Griffith,0}$ [26], in a reference test temperature and chemically inert environment (in vacuum, for example). Further assuming the following energy balance condition:

$$a_{Griffith,0}(\tau_{app} - \tau_{crit,0}) = \gamma_{surf,0} \quad (2.18)$$

allows inserting Eq. (2.17) in Eq. (2.18) and solving the resulting expression for $a_{Griffith,0}$. Stress τ_{crit} is then calculated using:

$$\tau_{crit} \approx \sqrt{\mu[\pi/(1-\nu^2)](\gamma_{surf}/a_{Griffith,0})} \quad (2.19)$$

depending on the actual (environment and temperature-dependent) surface energy γ_{surf} , during a particular test. Stress τ_{crit} from Eq. (2.19) is then inserted in Eq. (2.13), that is subsequently solved for N_i using $\tau_0 = 0$. In the context of this model, τ_0 will always be zero but it is kept in the equation for generality.

Using the equations from Eq. (2.13) to Eq. (2.19), the cavity nucleation rate N_i can be determined. By incorporating this rate into Eq. (2.10), the crack growth rate da/dN is obtained, thus completing the primary model.

2.3.4 . Conclusion of the theory and equation establishment

The above theory and model construction has been published as [52] and can be summarized as follows:

- A theoretical physical model of Stage II fatigue crack growth has been developed, based on supporting dislocation dynamics (DD) simulations that examine crack-induced plasticity in face-centered cubic (FCC) materials with low stacking fault energy. This model features the formation of highly reversible dislocation microstructures, manifested as persistent slip bands. The mechanism for Stage II crack propagation elucidated by this model aligns with the gradual de-cohesion of nano-sized grain regions within the crack tip process zone, highlighting the micro-to-nano scale interactions that contribute to subsequent crack extension.
- Corresponding descriptive equation has been developed to evaluate the crack growth rate per cycle, which hinges on the amplitude of the crack tip opening displacement (CTOD) and the number of cycles to void nucleation N_i . This calculation integrates the quantification of dislocation dynamics (DD) simulations and entails two scale transition descriptions (i-from grain to crack; ii-from polycrystal to crackd grain) derived from prior studies. These elements collectively facilitate a detailed understanding of the crack growth process, bridging microscopic mechanical behaviors with macroscopic fatigue phenomena.
- Through a nano-cavity submodel, the parameter N_i is determined considering the surface energy and the localized stress distribution within individual, tip-associated persistent slip bands.

As with any model, the proposed framework for Stage II fatigue crack growth has its own strengths and limitations. The model's robust theoretical foundation, grounded in dislocation dynamics (DD) simulations and nano-cavity nucleation mechanisms, offers a comprehensive understanding of the crack growth process. However, the model's accuracy and predictive capabilities may be influenced by the assumptions and simplifications made during the theoretical development. These factors underscore the need for further validation and refinement of the model through experimental testing and comparative analysis with existing fatigue data. Without strict verification, the model's applicaiton range is assumed to be $5 \times 10^{-4} < \Delta\epsilon_p 10^{-2}$. Determining this limit is challenging because experimental data that can be directly used to validate the model's results are rather scarce.

In the upcoming sections, we will outline practical steps to solve the equations and determine the crack growth rate, denoted as da/dN , for specific material and loading conditions.

2.4 . Numerical methods and applications

The numerical methods employed in this model are straightforward. However, when dealing with a large number of cracks (exceeding several hundreds) and requiring high precision (with an integration step of approximately 1 μm), the simulation can still take several minutes to complete. Therefore, a minimal level of optimization is necessary to ensure efficiency and manage the computational load effectively.

In the following two sub-sections, the following content will be covered:

1. practical manipulations and simplifications will be presented to solve the equations and obtain the concrete crack growth rate, da/dN .
2. intergration methods and numerical techniques to ensure a fast and accurate calculation of the crack growth rate, da/dN .

2.4.1 . Simplifications and deductions

The main model, during the construction process in Section 2.3, has been satisfactorily optimized so far. However, the equations governing the cavity nucleation (cf. Section 2.3.3) still need some simplification. Note that all the physical quantities mentioned in this section have already been defined in Section 2.3.3 and their physical meanings explained.

Parameter N_i is appraised by solving equation 2.20:

$$\sigma_0 + \left(\frac{d\sigma_{int}}{dN}\right)N_i = \sigma_{crit} \quad (2.20)$$

Calculation of σ_{crit}

σ_{crit} in Eq. 2.20 can be calculated based on Griffith's theory of micro-crack stability criteria, where:

$$\sigma_{crit} = \sqrt{2E\gamma/\pi a_{G0}} \quad (2.21)$$

and

$$a_{G0}(\sigma - \sigma_{crit}) = \gamma \quad (2.22)$$

In order to calculate σ_{crit} , a_{G0} must be obtained first. a_{G0} is calculated using equation 2.21 and 2.22 assuming a reference surface energy $\gamma_0 = 1 J/m^2$. a_{G0} depends then only on σ .

γ is the cohesive surface energy depending on the environment (air, vacuum, liquid) and temperature testing conditions. In principle, γ can be obtained through atomistic simulation of interface failure, in presence of solute atoms or other impurities [91, 92, 93]. In practice however, this quantity is

here evaluated by comparing our fatigue modelling results with relevant experimental observations. This parameter is the most important parameter during the process of model calibration.

Substituting equation 2.21 to 2.22 yields, γ taking the reference value,

$$\begin{aligned} a_{G0}(\sigma - \sqrt{\frac{2E\gamma_0}{\pi a_{G0}}}) &= \gamma_0 \\ -\sqrt{\frac{2E\gamma_0}{\pi a_{G0}}} &= \frac{\gamma_0}{a_{G0}} - \sigma \\ \frac{2E\gamma_0}{\pi a_{G0}} &= (\frac{\gamma_0}{a_{G0}} - \sigma)^2 \end{aligned}$$

Expanding, and multiplying by a_{G0}^2 in both sides,

$$\frac{2E\gamma_0}{\pi} a_{G0} = \gamma_0^2 - 2\gamma_0\sigma a_{G0} + \sigma^2 a_{G0}^2$$

After simplification,

$$\sigma^2 a_{G0}^2 - 2\gamma_0(\frac{E}{\pi} + \sigma)a_{G0} + \gamma_0^2 = 0 \quad (2.23)$$

If $\sigma = 0$,

$$a_{G0} = \frac{\gamma_0\pi}{2E}$$

If $\sigma \neq 0$,

$$\begin{aligned} a_{G0} &= \frac{2\gamma_0(\frac{E}{\pi} + \sigma) \pm \sqrt{4\gamma_0^2(\frac{E}{\pi} + \sigma)^2 - 4\sigma^2\gamma_0^2}}{2\sigma^2} \\ a_{G0} &= \frac{2\gamma_0(\frac{E}{\pi} + \sigma) \pm 2\gamma_0\sqrt{\frac{E^2}{\pi^2} + 2\frac{E\sigma}{\pi} + \sigma^2 - \sigma^2}}{2\sigma^2} \\ a_{G0} &= \frac{\gamma_0(E + \pi\sigma \pm \sqrt{E^2 + 2\pi E\sigma})}{2\pi\sigma^2} \end{aligned}$$

Given the range of a_{G0} should be in 1-3 μm ,

$$a_{G0} = \frac{\gamma_0}{\pi\sigma^2}(E + \pi\sigma + \sqrt{E^2 + 2\pi E\sigma}) \quad (2.24)$$

After that a_{G0} is obtained, σ_{crit} can be calculated using real surface energy and a_{G0} with equation 2.21.

Expression of N_i

Using equation 2.20, with $\sigma_0 = 0$, we have:

$$N_i = \frac{\sigma_{crit}}{\frac{d\sigma_{int}}{dN}} = \frac{\sqrt{2E\gamma/\pi a_{G0}}}{-4\sigma \frac{k}{D_g} \exp(-2\frac{ky_0}{D_g}) \frac{dy}{dN}} \quad (2.25)$$

where a_{G0} is calculated using Eq. (2.24).

N_i will depend on σ and D_g (others are material constants). A reference value of N_i is from 30 to 200 depending on the local grain size and other factors.

2.4.2 . Integration method

The primary numerical methods in this study are utilized to solve equation 2.26. This equation lacks an analytical solution and therefore must be addressed through numerical means.

$$\frac{da}{dN} = C(Dg)\Delta K_{app}^2(a)F^2(a, Dg) \quad (2.26)$$

There are two main categories of methods that can be applied to solve this equation. The first approach involves directly integrating both sides of the equation, as integrating the left side yields the desired solution. The second approach involves solving the differential equation numerically under various assumptions. Compared to the first method, the second approach is more complex due to evolving parameters, where several parameters increase with the grain size.

To address this situation, integration will be performed using two methods: direct integration and reciprocal integration.

Direct integration

The most straightforward approach is direct integration, which involves integrating equation 2.26 without making any modifications. In this method, the term on the left-hand side of the equation will yield a , representing the crack length, while the right-hand side provides the formula needed to evaluate a . This method relies simply on basic discretization and summation techniques.

The original integration,

$$\int_{N_0}^{N_f} \frac{da}{dN} dN = \int_{N_0}^{N_f} C(Dg)\Delta K_{app}^2(a)F^2(a, Dg)dN \quad (2.27)$$

In discretized form, given that $a : N \rightarrow a$ is a continuous and differentiable function, choosing a small δN :

$$\int_{N_0}^{N_f} \frac{da}{dN} dN = \sum_{i=0}^{i_f} C(Dg_i)\Delta K(a_i)F(a_i, Dg_i)\delta N \quad (2.28)$$

where $i_f = \frac{N_f - N_0}{\delta N}$ and for $i \geq 1$,

$$a_i = \sum_{j=0}^{i-1} C(Dg_j)\Delta K(a_j)F(a_j, Dg_j)\delta N \quad (2.29)$$

This method can be straightforwardly implemented in Python or other programming languages. The computation is relatively quick, especially if the step size δN is not too small; a δN value of approximately 10 is considered reasonable. Without requiring any special manipulations of the equation, this approach should yield results with sufficient precision.

Reciprocal integration

In reciprocal integration, the reciprocal of the equation is integrated. δa is set for each time step instead of δN (direct integration), which means:

$$\int_{a_0}^{a_f} \frac{dN}{da} = \int_{a_0}^{a_f} \frac{1}{C(Dg)\Delta K_{app}^2(a)F^2(a, Dg)} da \quad (2.30)$$

Similarly,

$$\int_{a_0}^{a_f} \frac{dN}{da} = \sum_{i=0}^{i_f} \frac{1}{C(Dg_i)\Delta K_{app}^2(a_i)F^2(a_i, Dg_i)} \delta a \quad (2.31)$$

where $i_f = \frac{a_f - a_0}{\delta a}$.

In the reciprocal integration method, all the a_i values (where i denotes the step index) are known prior to integration, as δa (the change in crack length per step) is predetermined ($a_i = a_0 + i \cdot \delta a$). This presents a significant advantage because a_i , being a variable critical to the integration process, is utilized within the integration, unlike N_i which is not. This pre-knowledge of a_i values not only facilitates parallel processing of the integration—contrasting with the sequential nature of direct integration, thereby considerably speeding up the calculations—but also accommodates the adaptation of Dg (grain size) relative to the current crack length, which affects the crack tip's position.

With direct integration, it's challenging to predict post-integration whether the crack tip remains within the same grain (δN represents the integration step in terms of cycles). Essentially, direct integration does not allow for precise control over the 'points of integration' on the material's surface, posing difficulties in managing the spatial parameters of the crack propagation process.

Reciprocal integration addresses this by setting the points on the surface directly, where the distance between points can be constant (and typically smaller than the grain size) or variable, albeit the latter is more challenging to control.

Therefore, the reciprocal integration method is selected for integrating the equation to establish the $a - N$ relationship, due to its advantages in handling variable material properties and enhancing computational efficiency.

2.5 . Parameter sensitivity analysis

In this section, we will explore how different parameters of the model affect the results. The model stability with respect to the integration procedures, including the calculation step magnitude, is also investigated. This examination is crucial for ensuring the model's reliability and accuracy and shall help the calculation comparison with experimental data for validation.

The examination of the impact of various parameters is initially conducted using both direct and reciprocal integration methods (cf. Section 2.4.2). In the following result figures (Fig. 2.13 to Fig. 2.16), ourcomes derived from direct integration are illustrated with dashed lines, whereas those from indirect integration are depicted using solid lines. For preliminary comparison, some experimental results are presented as distinct data points. If the increments dN and da are sufficiently small, the results from both integration methods should appear virtually indistinguishable.

2.5.1 . Effect of changable parameters

The study will explore parameters such as γ_{surf} , λ , N_i , D_g , $\Delta\epsilon_p$, and dN (or da in the context of reciprocal integration). Notably, the formulas for N_i are comprehensively integrated into the analysis to ascertain the direct effect of this crucial intermediate quantity on the ultimate outcomes.

Plots of the results are shown below (Figure 2.13, 2.14, 2.15, 2.16).

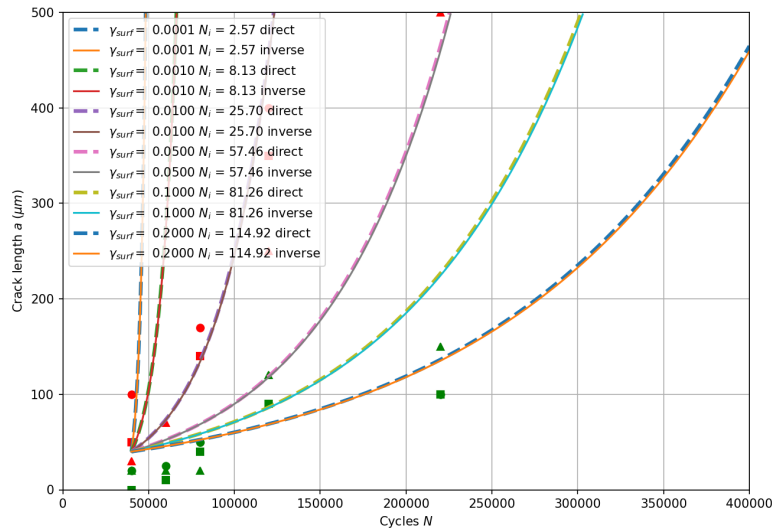


Figure 2.13: Influence of the cohesive energy parameter γ_{surf}

The cohesive surface energy parameter, γ_{surf} , plays a crucial role in the propagation of the crack through its impact on quantity N_i . A higher γ_{surf} value leads to an increased N_i , resulting in slower crack propagation because more cycles are needed for the crack to advance "one step" (refer to section 2.3.3). This parameter is not easily accessible to experimental validation and is here estimated by fitting the model.

The parameter λ , which ranges from 25 to 100 based on comparable dislocation dynamics (DD) simulation results, significantly affects the outcomes

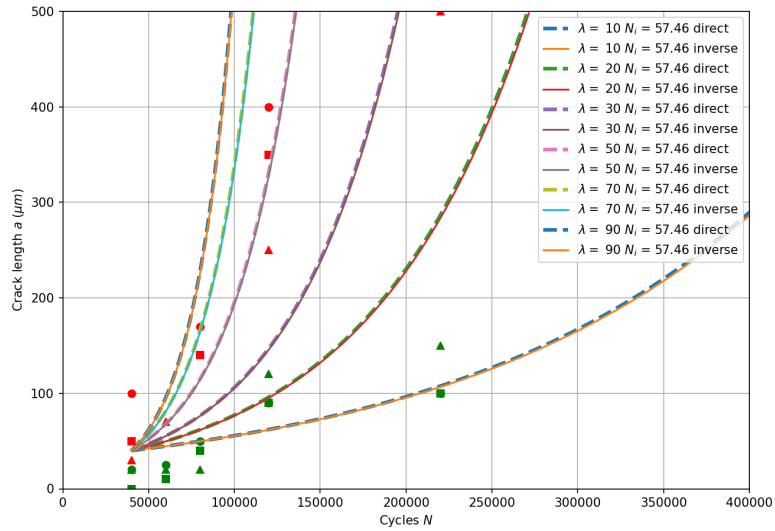


Figure 2.14: Influence of plastic zone size parameter λ

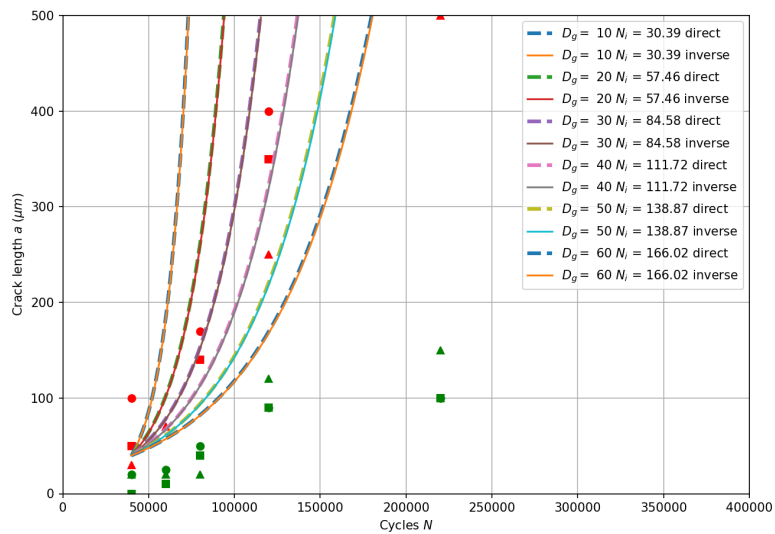


Figure 2.15: Influence of effective grain size parameter D_g

of the model. The distance between the crack tip and the grain boundaries, is another critical factor influencing crack propagation. For this and other reasons, larger grain sizes tend to slow down the crack growth rate.

The plastic strain range, $\Delta\epsilon_p$, also has a direct effect on the propagation rate. The number of cycles required for a crack to reach a certain length typ-

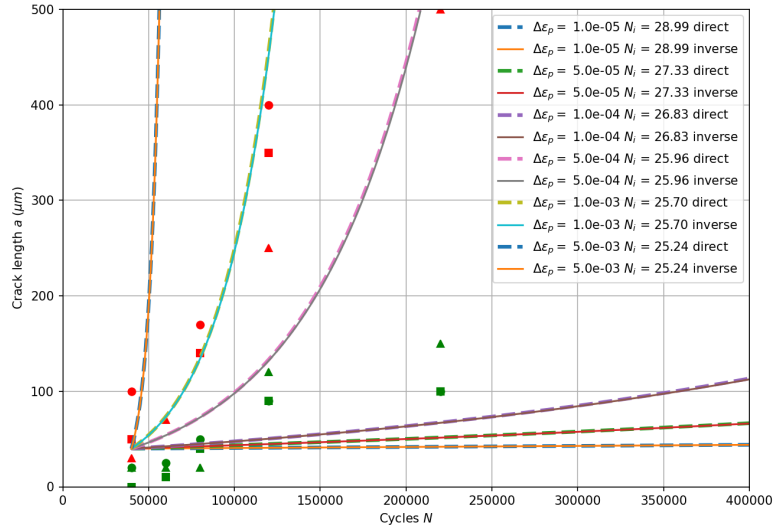


Figure 2.16: Influence of $\Delta\epsilon_p$

ically has an exponential relationship with the applied load (refer to section 2.6.3). Additionally, $\Delta\epsilon_p$ slightly alters the value of N_i as it influences the crack tip opening displacement.

These four parameters are identified as principal factors affecting crack propagation, as illustrated in the figures.

To study the direct influence of N_i , N_i is intentionally fixed to different levels in figure 2.17.

Conversely, another intermediate value, r_0 , appears to exert negligible influence on a , the crack length. r_0 is included in the expressions for C and F . It has been observed that F is significantly related to r_0 at lower cycle counts ($N < 10^5$). However, since C is inversely correlated with r_0 , this relationship tends to neutralize its impact in the equation (refer to Eq. 2.10). Consequently, although there is a connection between da , the crack growth increment, and r_0 , this influence has a relatively minor impact on the associated crack growth rate.

2.5.2 . Influence of integration step size

The integration step size, denoted as dN and da , plays a crucial role in determining the numerical precision of the model. Inherent limitations in the numerical methods used mean that errors introduced at each step of the integration process accumulate over the simulation period. If the step size is too large, the cumulative error by the end of the simulation cycle becomes a significant factor.

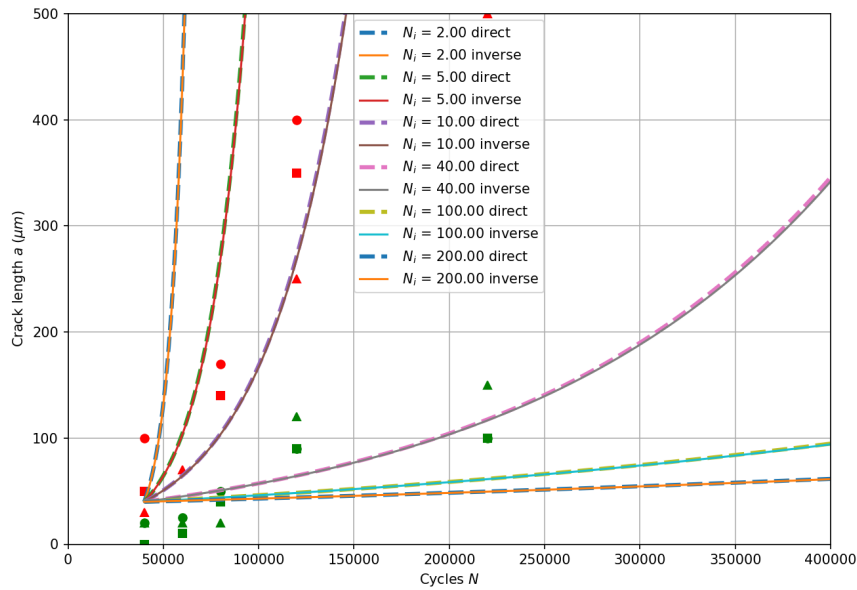


Figure 2.17: Influence of N_i

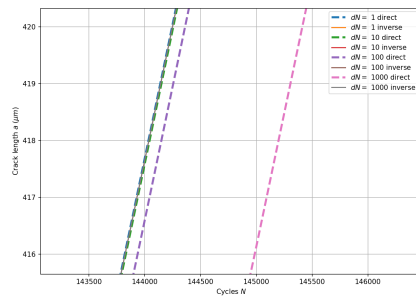
Conversely, the integration step size also affects the computational load. In complex models like the multi-grain analysis model, which employs stochastic evaluation involving numerous calculations, a very small step size can excessively prolong the time required to obtain results. Therefore, finding an optimal step size is crucial to balance precision and computational efficiency.

Comparative analyses of various step sizes in both direct and reciprocal integration methods are conducted, with the findings presented in figures 2.18. To ensure a fair comparison of the integration methods, the step size for one method is set to the smallest value utilized in the other method, facilitating an effective assessment of their respective impacts on the model's performance.

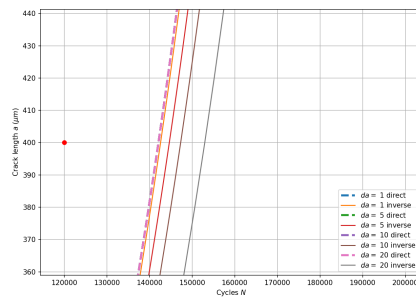
In both integration methods, a large integration step size can result in an underestimation of the crack length. If the chosen step size is inappropriate, the discrepancy between the simulation results and the reference values can be substantial, as illustrated in figure 2.18b. According to the comparative analysis, a step size of $dN = 10$ and $da = 1\mu m$ yields simulation results that are considered acceptable. This balance ensures that the model provides a reliable representation of the physical phenomenon without incurring excessive computational time or significant errors in the simulation outcomes.

2.5.3 . Conclusion

In this section, the influence of various parameters on the crack propagation is studied. The results are summarized as follows (in terms of crack



(a) Influence of dN , zoomed around (150000, 474)



(b) Influence of da , zoomed around (150000, 400)

Figure 2.18: Influence of integration steps in both direct integration and reciprocal integration

length a after a same number of cycles):

- γ_{surf} : negatively correlated. $\gamma_{surf} \nearrow \rightarrow a \searrow$
- λ : positively correlated. $\lambda \nearrow \rightarrow a \nearrow$
- D_g : negatively correlated. $D_g \nearrow \rightarrow a \searrow$
- $\Delta\epsilon_p$: positively correlated. $\Delta\epsilon_p \nearrow \rightarrow a \nearrow$

Furthermore, the stability of the model has been analyzed, with findings indicating that accurate results can be achieved using both direct and reciprocal integration methods, providing an appropriate selection of the integration step size. To achieve results with acceptable precision, the step size should be within the following range:

- $dN < 10$ for direct integration.
- $da < 1\mu m$ for reciprocal integration.

The comparison with experimental results presented in this section is quite preliminary. Only a few data points have been included in the figures to demonstrate that the simulated crack length values do not significantly deviate from the experimental data. In the next section, a more detailed comparison with experimental results will be conducted. This will encompass comparisons of crack growth rate, crack length, and fatigue life, providing a comprehensive assessment of the model's accuracy and reliability in replicating observed behaviors in practical scenarios.

2.6. Evaluation of the macro-scale fatigue lifetime using stochastic analysis

Previous sections have established a model of Stage II fatigue crack growth with uniform grain size. That model will be referred as the *single-grain model* in this section to distinguish from the *multi-grain model*. Using this single-grain model, the influences of each parameter have been studied separately, depending on the grain size change. This assumption helped also evaluate the two proposed integration methods because all the grains have the same size, both direct and reciprocal integration could be applied.

In actual polycrystalline materials, grain sizes vary from one grain to another, affecting how a crack propagates through the material. This variability leads to changes in the crack growth rate, making the crack growth curve not a smooth continuous line but rather a segmented one, with each segment representing the passage of the crack through a different grain. This effect and its impact on the fatigue lifetime scattering can be evaluated by analyzing the

propagation of a large number of cracks, following arbitrary or pre-assigned growth paths (like paths AB and CD in Fig. 2.20).

In this context, the grain size D_g is determined based on the span of the grain along the crack growth direction. As emphasized in the theoretical section (Section 2.3.4), this specific grain size quantity is more relevant than an average grain size, such as one derived from converting the grain aggregate into a circle and calculating its average radius. Moreover, directly assessing the grain span along the crack growth path from the EBSD result file simplifies the extraction process, making it more practical.

It's assumed here that the crack moves in a straight line through the grains without deviating or encountering obstacles, a scenario well-adapted to crack spanning more than two or three grains. Therefore, even within the same material, grain sizes and the consequent crack growth rates will differ along each (arbitrary or pre-assigned) crack path. This variability leads to different fatigue lives, meaning the number of cycles until a crack reaches a certain length (a_f), for each path. A stochastic model, therefore, can be developed by simulating numerous cracks following these defined paths, to understand and predict the variation in crack growth and fatigue life. A detailed calculation algorithm is presented in Fig. 2.19

In this section, this stochastic model will be developed and applied to the A316L stainless steel material. The organization of this section is as follows:

1. **EBSD result file reading:** This section details the process of reading Electron Backscatter Diffraction (EBSD) data files to map grain structures of A316L stainless steel. It explains the methodology for extracting crucial parameters from EBSD scans, such as grain boundary characteristics, misorientation angles, and phase identification. These parameters are essential for setting the initial conditions in the stochastic crack growth model, providing insights into the material's microstructural characteristics that influence crack propagation.
2. **Integration techniques:** This part explores the numerical methods used to integrate the crack growth rate across the heterogeneous grain structure as revealed by EBSD data.
3. **Results and calibration:** The outcomes of the stochastic simulations are presented here, with a focus on the variability in crack growth rates and fatigue life for A316L stainless steel. The section discusses the alignment of the model's predictions with experimental data and the calibration processes needed for model validation. The results will be compared thoroughly with experimental data not only in terms of fatigue life (in the form of Manson-Coffin curves) but also in terms of crack growth rate and crack length.

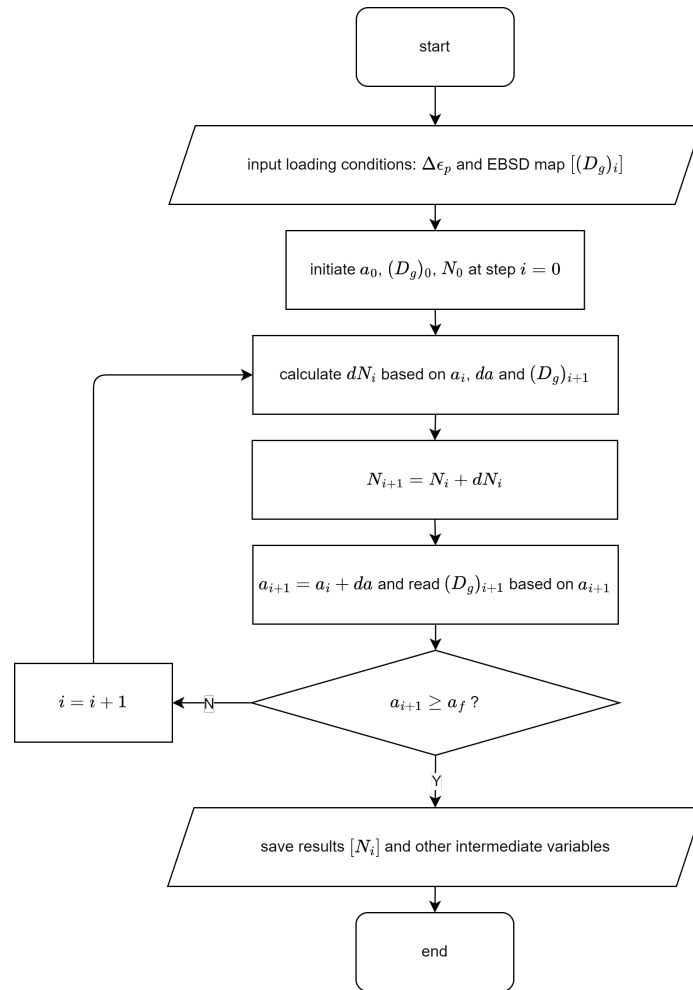


Figure 2.19: Detailed calculation procedure allowing the simulation of a macroscopic fatigue damage in polycrystalline grain aggregates. This procedure is repeated for a large number of pre-assigned crack path in an attempt to simulation the crack growth rate variability of macro-scale specimens. Note that the calculation step is not based on the number of cycles increment dN but on the crack length increment da .

2.6.1 . EBSD result file reading

Electron Backscatter Diffraction (EBSD) raw data, typically in binary format, contains patterns from diffracted electrons that have interacted with a material's crystalline structure, aiding in identifying the crystallographic orientation of each grain within a macroscopic, polycrystalline grain aggregate. For the sake of simplicity in this study, we will employ a processed EBSD result file in plain text format. This EBSD data comes in a .csv file, containing plain text entries that represent the crystal orientation at each measurement point, as illustrated in figure 2.20.

The main goal of using an EBSD scan in this context is to evaluate the effective size assigned to each grain within the sample. Traditional tools for EBSD visualization or analysis, however, do not typically offer capabilities to directly derive grain size information. In the subsequent subsections, we will elaborate on the methodology for interpreting EBSD data and extracting detailed information about grain sizes.

EBSD data visualisation

The Electron Backscatter Diffraction (EBSD) data, corresponding to SEM micrograph shown in Fig. 2.20 and extracted from an actual fatigue test specimen of A316L stainless steel, presented in Fig. 2.21a. Fig. 2.20 offers detailed view of the grain structure within the material. In this visualization, grain boundaries are prominently outlined. However, this visualization alone does not provide direct information on the grain boundary positions. Therefore, in the subsequent section, an algorithm will be introduced to locate the grain boundary (size) information from the EBSD data.

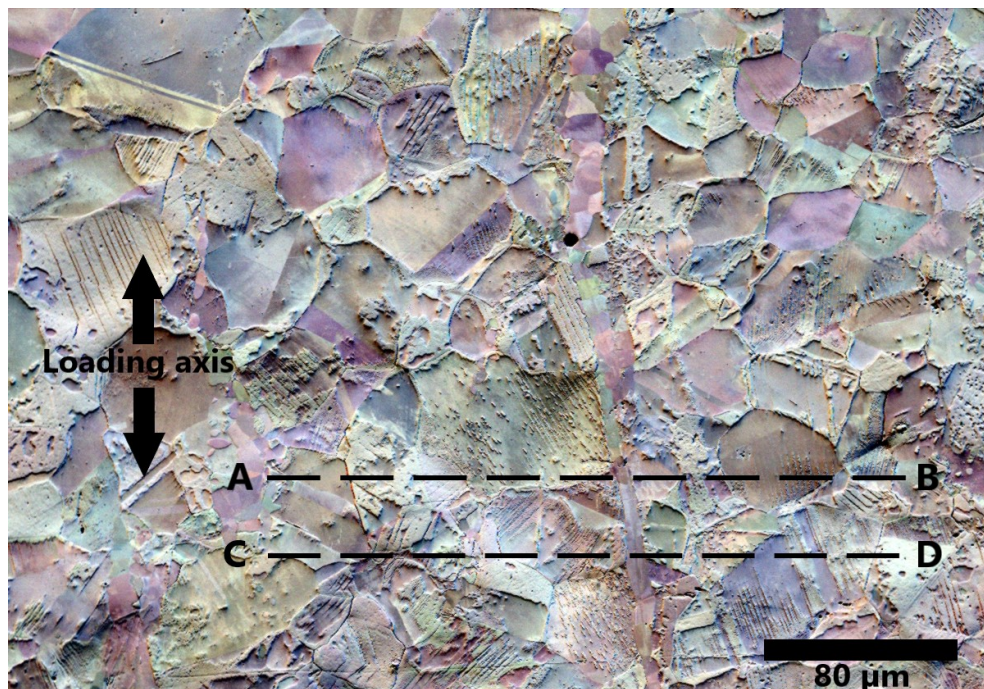
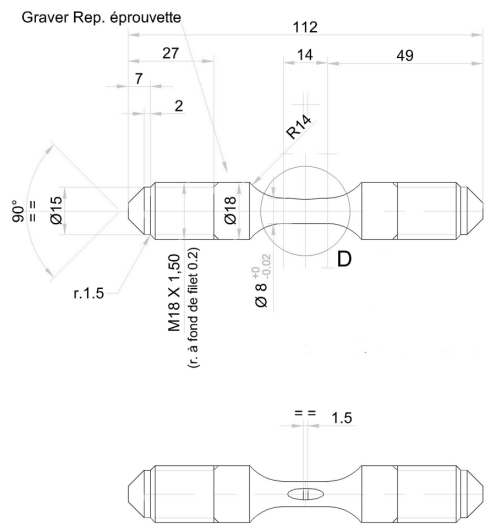


Figure 2.20: Typical surface grains aggregate of a grade 300 austenitic steel specimen (SEM micrograph). Markers A-B and C-D show two possible crack propagation paths, consistent with the loading axis indicated.



(a) The A316L stainless steel specimen used for the EBSD scan.



(b) Detailed geometry information of the specimen used for the EBSD scan.

Figure 2.21: The A316L stainless steel specimen used for the EBSD scan shown in Fig. 2.20.

Criteria for different grains

The EBSD results provide information on the crystal structure (e.g., FCC), the position coordinates (x, y) , and the Euler angles (ϕ_1, ϕ_2, ϕ_3) that represent the grain's orientation. Each grain is distinguished by its unique Euler angles.

To differentiate between grains, the Euler angles can be used through simple methods such as:

1. Calculating the sum of absolute changes in angles, $\sum |\Delta\phi|$, and defining a critical value, $\Delta\phi_0$, above which points are considered to belong to different grains.
2. Determining the maximum absolute change in angles, $\max(|\Delta\phi|)$, and setting a critical value, $\Delta\phi_0$, beyond which the grains are deemed separate.

The first method is more computationally efficient, while the second offers stricter criteria for grain differentiation. In this study, given the lack of necessity for a precise threshold, the sum of the absolute changes in angles, $\sum |\Delta\phi|$, is preferred for distinguishing between grains.

Defects and invalid points

In this study, a *defect* is identified as a point within a grain that exhibits different angular values, possibly due to persistent slip markings (PSMs), polishing errors, or precipitations, among other factors. When tallying points in a grain, it's crucial to recognize and filter out these defects. A point is categorized as a defect if the valid points immediately preceding and following it share the same orientation. While these defects are noted, they are not considered as indicators of grain boundaries.

The methodology employed here may not identify all actual defects, particularly those that affect multiple measurement points in the scanning direction. Nevertheless, this approximation is deemed sufficient for the purposes of this research. Developing a more accurate defect recognition algorithm falls outside the scope of this study.

An *invalid point* refers to a location where EBSD indexing has been unsuccessful, resulting in a lack of data. These points are excluded from the analysis, as they provide no useful information regarding the material's crystallographic orientation or structure.

Results

Building on the principles above, an algorithm for processing EBSD results has been developed. The algorithm operates by reading the EBSD result file

line by line, replicating the line-by-line scanning of the material's surface. As it reads, the algorithm stores the grain orientation information and applies the previously described criteria to identify grain boundaries and defects. When a boundary is detected, its specific position coordinates are recorded in a separate file. By comparing the coordinates of this boundary with the previous one along the same scan line, the algorithm calculates the grain size depending on the number of measurement points in between. The specific details and workflow of this algorithm are illustrated in figure 2.22, providing a visual representation of the process used to analyze the EBSD data systematically.

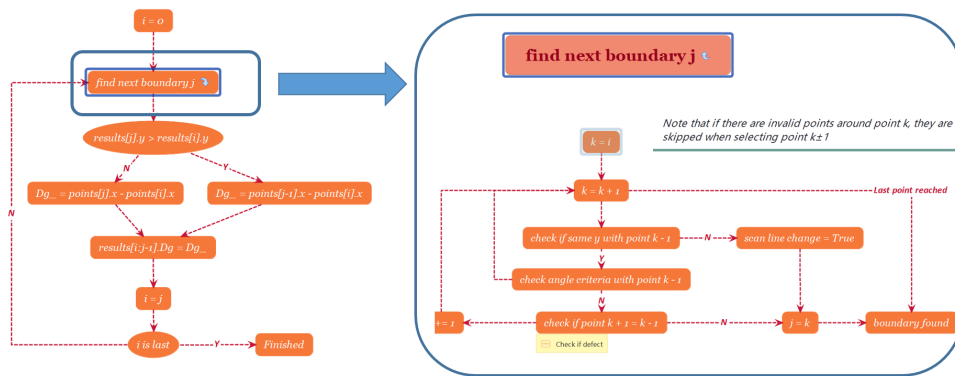


Figure 2.22: Algorithm of identification of grain boundaries in EBSD results

The grain boundaries are shown in figure 2.23 (blue points). The red points are the defects detected.

Data from lower y values will be prioritized for analysis to circumvent regions like around (1200, 800), which are known to have a high density of defects due to poor EBSD indexation. The detailed distribution of grain sizes, as depicted in figure 2.24, indicates that the most prevalent grain size is approximately $20 \mu m$. The distribution pattern (it's like a log-normal distribution which is believed to be a reasonable assumption) of these sizes is influenced by the material's fabrication process.

It is important to clarify, as mentioned at the beginning of this section, that the grain sizes determined through this method represent the effective grain size along a selected crack path, following predefined crack propagation directions, rather than the actual "size" of the grains. This effective grain size serves as a reasonable estimate for the actual dislocation gliding distance within various sub-grain locations, providing a useful metric for analyzing the stochastic behavior of crack propagation.

2.6.2 . Integration algorithm

The complete algorithm for the stochastic analysis of polycrystalline grain aggregates can be summarized as follows: Based on the EBSD reading results,

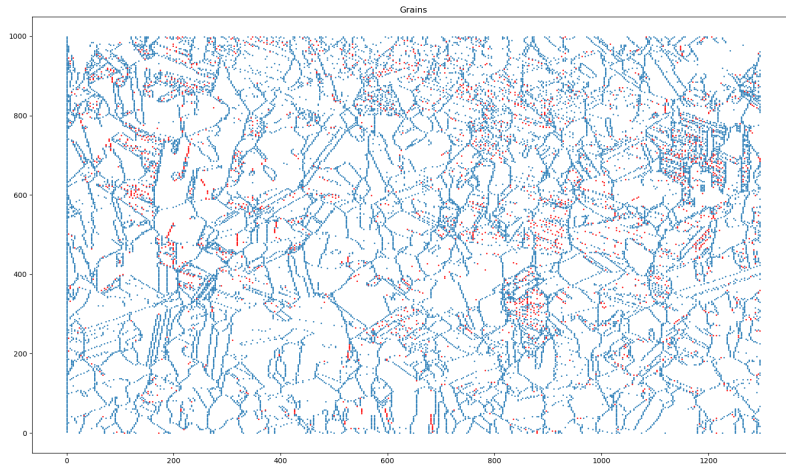


Figure 2.23: Grains identified from EBSD results

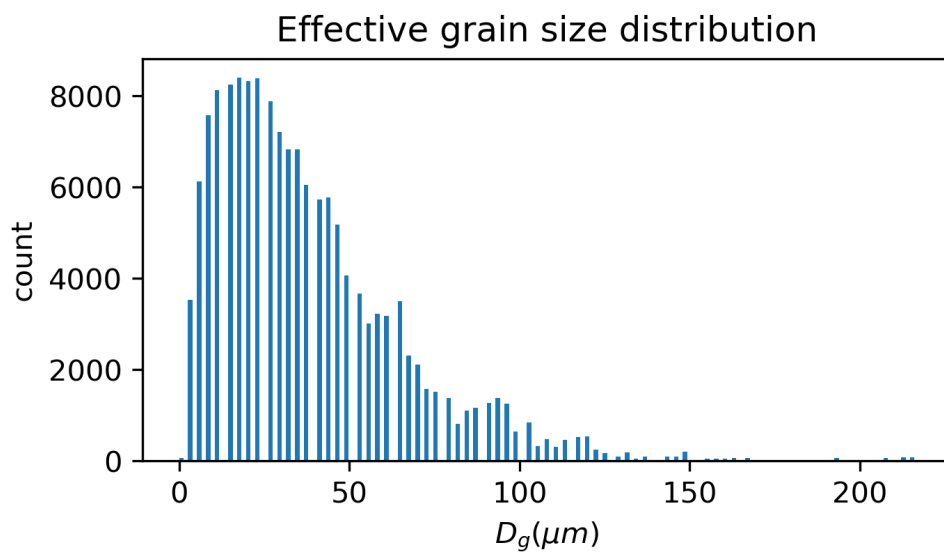


Figure 2.24: Distribution of effective grain sizes, each count corresponds to a data point of the EBSD scan

a (x, y, D_g) mesh table is created, where D_g is the effective grain size at each measurement point. On the (x, y, D_g) mesh, M imaginary crack paths are selected along the axis y (such as the AB and CD in Fig. 2.20). Along each of these paths, a crack propagation rate calculation is performed. The crack is assumed to have an initial length a_0 . At each step, the crack length grows by $\frac{\delta}{D}$ where δ is the EBSD measurement step length and D is the parameter to set

the integration step size.¹ The number of cycles required for this growth dN is calculated using the equation Eq. (2.30). The steps continue until a critical crack length $a_f = 1000 \mu m$ is reached. The integration equation is thus given by:

$$N_f = \int_{a_0}^{a_f} \frac{dN}{da} da = \int_{a_0}^{a_f} \frac{1}{C(D_g)\Delta K_{app}^2(a)F^2(a, D_g)} da \quad (2.32)$$

The direct result out of each single crack simulation is the fatigue lifetime N_f along this selected crack path. For L levels of loading amplitude, M paths are calculated, resulting in a $L \times M$ matrix of N_f . Other information, such as the crack growth rate, the crack length at each step and the quantity N_i of the nano-cavity model, are also recorded in separate files for further analysis.

As outlined in Section 2.4, the reciprocal integration method is employed to perform integration along the crack path. For each integration step, the number of cycles required for crack propagation is determined using this integration approach. The spacing between measurement points is set at $dx_0 = 2.92 \mu m$. Although this is a suitable average distance for da (yielding approximately 100 – 200 data points over a 500 μm crack length), we could actually use a smaller da by selecting a fraction of dx_0 . This is essential because every data point needs to be an integration point to ensure we have detailed information about the grain size at each step.

To achieve more accurate data integration, we can adopt $da = dx_0/4 = 0.73 \mu m$, in consistence with the guidelines mentioned in Section 2.5.3. The formulas and equations for the integration remain consistent, except that the grain size parameter, D_g , changes for different integration points.

For the stochastic assessment, around 200 to 300 lines ($M = 200$ – 300) are utilized to simulate crack propagation. These lines, equally spaced along the x direction and parallel to the y direction, serve to model the behavior of cracks as they traverse different grains. Throughout each crack's progression, the grain size data obtained from the previously mentioned algorithm will be employed to replicate the changes in grain size that a crack would experience while cutting through actual materials. The outcomes of this simulation will be elaborated upon in the subsequent subsection.

2.6.3 . Results and analysis

In this section, the outcomes of the stochastic crack propagation simulations are detailed, emphasizing the variability in crack growth rates and fatigue life for A316L stainless steel. These results are compared with experimental findings, addressing not only fatigue life (via Manson-Coffin curves) but also crack growth rates and lengths.

The subsections will be arranged as follows:

¹ D has to be an integer to ensure that at each step, the grain size D_g is well defined.

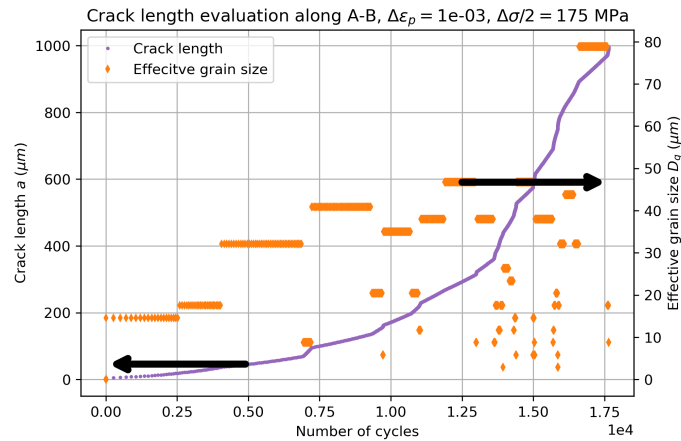
1. **Individual Crack Path Results:** This subsection will showcase the results from two specific stochastic simulations of individual crack paths, illustrating the differences in crack growth rates. It will particularly emphasize how variations in crack size impact these rates.
2. **Crack Growth Rate Distribution:** Here, the focus shifts to examining the spread of crack growth rates across a variety of crack paths. This analysis will provide a deeper understanding of the crack growth rate variability. The findings will be displayed in a graph correlating growth rates with stress intensity factors, including a comparison to experimental data.
3. **Dispersion of Crack Lengths:** This part will compare the real-time evolution of crack lengths with corresponding experimental data under identical load conditions. The comparison will be depicted in a chart showing crack length against fatigue cycles.
4. **Fatigue Life Distribution:** In the context of low cycle fatigue (LCF), where crack propagation significantly influences fatigue life, the simulated results will be aligned with experimental fatigue life data. This comparison will be represented through a Manson-Coffin curve, providing a statistical view of the fatigue life expectancy.

Individual crack growth results

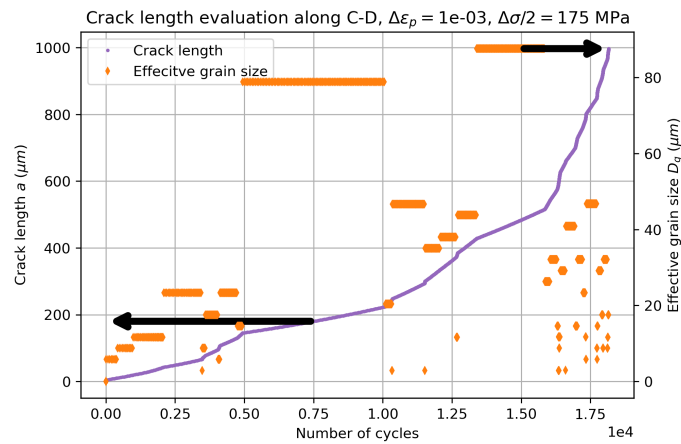
Figure 2.25 presents two outcomes of stochastic simulations for distinct crack paths, labeled A-B and C-D, as depicted in Fig. 2.20 (arbitrary location). The solid orange markers indicate the grain size intersected by the crack tip after a certain number of cycles, while the solid purple curve shows the corresponding crack length at the same cycle count. An interesting observation is the relationship between changes in grain size and notable fluctuations in the crack growth rates. Specifically, Stage II cracks tend to expand more slowly in areas with larger effective grain sizes and, conversely, progress more slowly in regions where the active or resisting grain size is smaller (as illustrated in Figs. 2.25a and 2.25b). This finding aligns with the conclusions drawn from the parameter study in Section 2.5.3.

Crack growth rate distribution

The crack growth rate $\frac{da}{dN}$ data for all cracks, as depicted in Fig. 2.25, are aggregated and illustrated in Fig. 2.26, where only a selected percentage of average data points are plotted for the sake of clarity. The crack growth rate is graphed against the stress intensity factor ΔK , comparing the outcomes of the stochastic simulations with experimental findings. Primary experimental



(a)



(b)

Figure 2.25: The solid orange symbols indicate the size of the grain being cut by the crack tip, at a given number of cycles. The solid purple curve indicates the corresponding crack length, at the same number of cycles. It is interesting to note the correlation between the grain size changes and the significant corresponding crack growth rate variations. a Crack length evolution along individual crack path A-B shown in Fig. 2.20. b Crack length evolution along individual crack path C-D shown in Fig. 2.20.

results are drawn from studies conducted in a strain control model, deemed more compatible with this model [94, 95].

The model furnishes accurate absolute crack growth rates and also the distribution of these rates, aligning well with the experimental observations. Notably, the model's trend line (depicted as a dashed line) intersects with the Stage II crack growth threshold at $4 - 5 \text{ MPa}\sqrt{m}$, consistent with the established stress intensity factor threshold for Stage II crack growth in series 300 steels. The analysis identifies distinct "groups" of rates, represent-

ing the variability of crack growth rates within the same grain but at differing crack lengths. The calculation results are generally conservative, especially for $K > 10 \text{ MPa}\sqrt{\text{m}}$ as shown in Fig. 2.26.

These simulation findings underscore the model's ability to predict stochastic probabilities of crack growth, demonstrating an advancement over conventional models that rely on Paris' law or Walker's law, as discussed in Section 2.2.

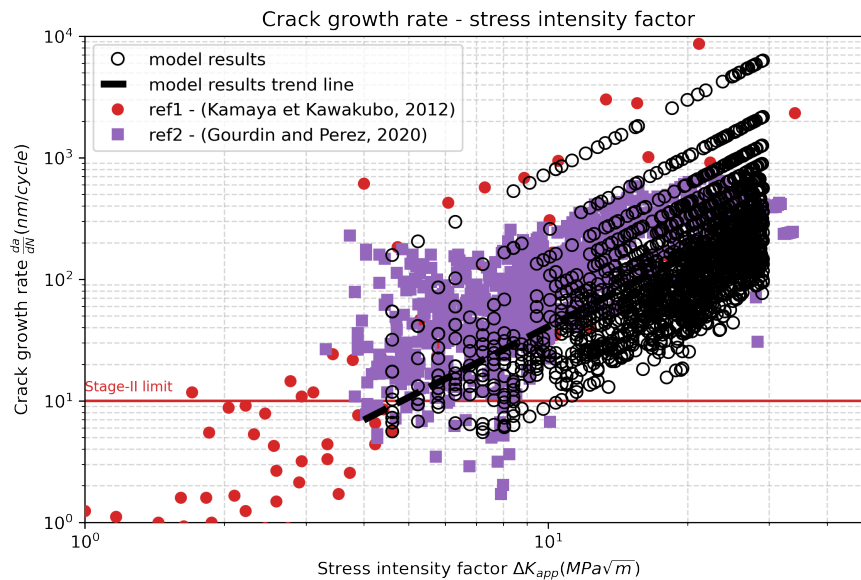


Figure 2.26: Stage II crack growth rate versus stress intensity factor. The open symbols are modeling results; the solid symbols represent two distinct sets of experimental results [94, 95]. The dashed line corresponds to the average, modeling trend curve. The model allows predicting both the average crack growth rate and scattering, in consistency with corresponding experimental evidence. The modeling trend curve (dashed line) cuts the Stage II limit at $4-5 \text{ MPa}\sqrt{\text{m}}$ in agreement with the stress intensity factor threshold of Stage II crack growth of series 300 steels. The result shows "groups" of rates that are in fact the crack growth rates in the same grain but at different crack lengths.

Dispersion of crack lengths

One crack size a versus N evolution example considering every potential crack propagation path (or EBSD data line) is shown in Fig. 2.27. The thin dashed lines correspond to individual crack-path propagation cases. The simulation results are plotted half-transparent and so wherever the color is darker, the more simulation lines are overlapping meaning more cracks are propagating along this situation. The calculation results are consistent with the experimen-

tal FABIME results [96] where the initiation cycles have been removed make the comparison more coherent. It can be observed that the crack growth rate during the crack growth and the dispersion caused by the different grain sizes are well captured by the model.

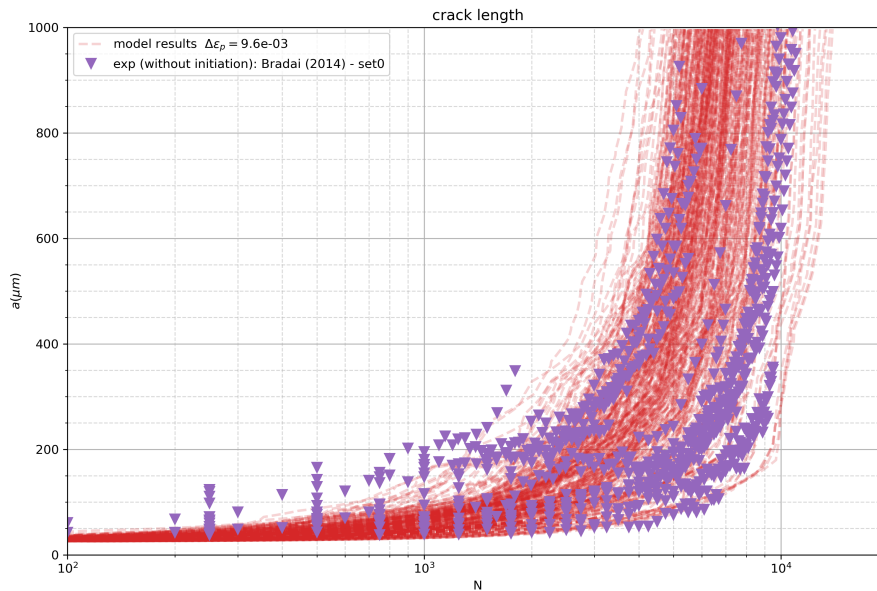


Figure 2.27: The crack depth versus the number of cycles along different crack paths. The thin dashed lines correspond to individual crack-path propagation cases. The calculation results are consistent with the experimental FABIME results [96].

The main fatigue data validation set shown in Fig. 2.26 (main part of it) and Fig. 2.27 is obtained using the "FABIME" testing device [96], which utilizes quasi-structural disk specimens (diameter = 170 mm, 2 mm thickness in central gauge region) subjected to alternating bending displacements (e.g. total imposed strain conditions). The present FABIME tests are carried out at room temperature using an optically transparent and chemically inert oil as a working fluid. Symmetrical disk bending displacement amplitudes up to 2.75 mm are applied, with corresponding strain ratio $R = -1$ and $\Delta\epsilon_p = 9.6 \times 10^{-3}$. The tests were interrupted every 500 cycles for the evaluation of the surface crack length a (resolution limit is 50 μm). The test ran up to 19680 applied cycles yielding multiple crack development, in the specimen gauge section [94].

Fatigue life distribution

The above calculation results (c.f. Fig. 2.27) provide a way to estimate the fatigue lifetime associated with Stage II crack propagation. Here, the fatigue

lifetime is defined as the number of cycles required to reach a crack propagation of $1000 \mu m$, noting that this value is somewhat arbitrary, it can however be shown that choosing a larger a_{crit} value results in minimal change to the fatigue lifetime. The calculated fatigue lifetimes are plotted against different levels of total applied strain range and compared with relevant datasets [97, 98, 95, 99], as shown in Fig. 2.28.

It is observed that the fatigue lifetime related to Stage II and its variability significantly increase with lower loading levels, especially when considering the logarithmic scale used. This trend reflects the non-linear impact of grain size and orientation as indicated by Eq. (2.10). The theoretical results from Fig. 2.28 align with experimental data for loading amplitudes above a critical threshold ($N_f < 10^4$ cycles or $\Delta\epsilon_p > 7 \times 10^{-3}$, with a 50

From these observations, we deduce that the fatigue lifetime, in the context of laboratory test specimens, is governed by crack propagation for $\Delta\epsilon_p > 7 \times 10^{-3}$ and by crack initiation for $\Delta\epsilon_p < 7 \times 10^{-3}$. Thus, the results in Fig. 2.28 highlights a significant load-dependent transition effect that could greatly affect fatigue design procedures. For components with initial crack-like defects (such as machining marks), the contribution from Stage 0 and 1 (crack initiation) is essentially negligible. In these instances, the fatigue lifetime is predominantly controlled by crack propagation, aligning with the simulation results depicted in Fig. 2.28 with open red symbols, rather than the typical fatigue data represented by solid symbols.

2.7 . Conclusions

In this chapter, we presented a detailed model for Stage II crack propagation, emphasizing the physical mechanisms involved and utilizing 3D dislocation dynamics (DDD) simulations. Here are the main points and contributions of our study:

1. **Theoretical Foundation:** Our model is based on in-depth DDD simulations that shed light on the microstructural behaviors affecting crack propagation. We have developed equations that accurately represent the physical processes observed, ensuring our model is both empirically sound and theoretically robust.
2. **Model Calibration and Validation:** We validated and each time necessary calibrated our model parameters by comparison with a broad range of experimental data to ensure it accurately reflects the observed crack growth rates and fatigue lives. This validation is essential for proving our model's reliability and its practical application in industry.
3. **Stochastic Analysis:** We also carried out a stochastic analysis of our modelling results with a view to adress the micro to macro scale tran-

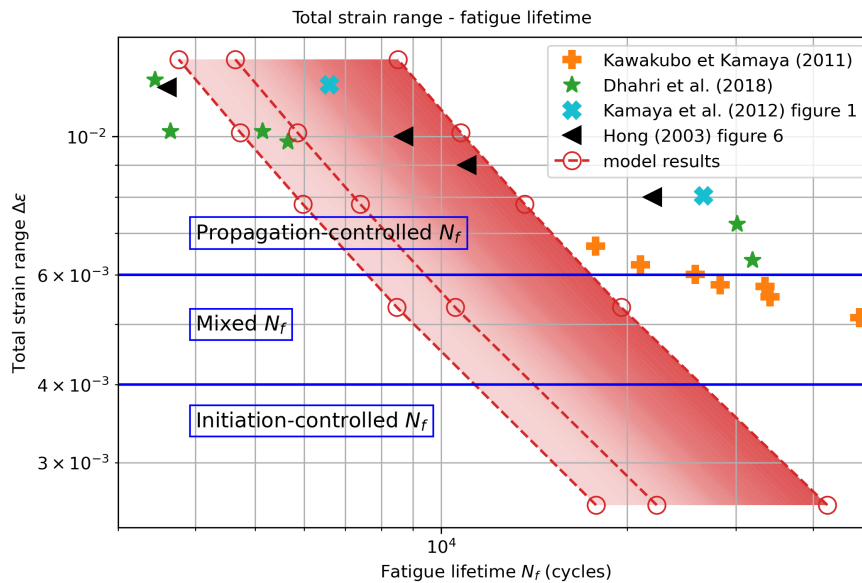


Figure 2.28: Stage II related contribution to fatigue lifetime versus total strain range in a poly-crystalline series 300 steel. The three represented curves are associated with 1%, 10% and 90% failure probability respectively. The color radiant from darker to lighter represents the decreasing failure probability. The solid symbols correspond to experimental measurements from macroscopic fatigue tests in [97, 98, 95, 99].

sition, considering the variability in material properties and microstructural configurations. This recognizes the random nature of crack propagation paths through different grains and offers a more detailed prediction of fatigue life.

- 4. Advantages over Traditional Models:** Our model provides several benefits compared to traditional fatigue crack growth models. By using physical variables directly from microstructural observations and simulations, our approach avoids the empirical adjustments often needed in conventional models, improving predictive accuracy and enhancing our understanding of crack propagation mechanisms.

In summary, this chapter introduces a new method for predicting Stage II fatigue crack propagation that is physically informed and theoretically robust. It proposes a realistic and comprehensive mechanism together with equations that describe this mechanism. The simulated crack growth rate and length have been calibrated and validated against experimental data, yielding promising results.

However, multiple improvements can be made to enhance the model's connection with the material's microscopic properties. For example, the phys-

ical simulation of the surface energy will provide a better understanding and quantification of the cavity model. These enhancements could be explored in the future with better simulation tools and more powerful computational capabilities.

In addition, it's important to recognize that fatigue life is not only about the Stage II period (as shown in Fig. 2.28). Crack initiation also plays a significant role, especially under low loading conditions (HCF). A model addressing crack initiation will be discussed in Chapter 4. Integrating both models will lead to a more comprehensive prediction of fatigue life.

3 - General fatigue model and investigation of the ratcheting effect

The aim of this chapter is to present a comprehensive fatigue model designed to replicate the low-amplitude fatigue behavior of the same 316L material investigated in the previous chapters. While the fatigue stress-strain response of this material is not the primary focus of this work, the present modelling developments are nonetheless crucially dependent on this property. This section pertains to the crack initiation model in Chapter 4.

The present model leverages the outcomes of Discrete Dislocation Dynamics (DDD) simulations to establish a correlation between the distribution of dislocation dipoles and the overall dislocation density. Based on this distribution, the model can then predict localized strain and stress, thereby replicating the material's fatigue response. This modeling step includes detailed simulation of the hysteresis loops on a cycle-by-cycle basis, incorporating the effects of kinematic hardening.

Our particular model is capable of predicting the ratcheting effect in the material, as it inherently incorporates kinematic hardening. By integrating mean stress through a straightforward negative feedback loop, the model effectively forecasts the ratcheting strain as a function of the number of fatigue cycles.

The predictive accuracy of this model is satisfactory in various scenarios including under applied mean strain is applied and mean stress conditions, or during step loading.

3.1 . Introduction

The industrial context of this research focuses on studying the impact of ratcheting phenomena on fatigue crack initiation. As indicated in Chapter 1, the DEMO reactor's cooling tube experiences mean stress during the fatigue process, which can induce a ratcheting effect thereof. This effect must be accurately evaluated, for the sake of matching the fatigue design target set to 1%. Therefore, accurate prediction of this ratcheting strain is critical for estimating the component's lifespan. Moreover, since this design rule is not entirely based on theoretical grounds, this physical study will also contribute valuable insights for the foundation of this limitation.

However, the complexity of the ratcheting effect necessitates dividing the current undertaking into two distinct studies. The first study aims to develop a model capable of simulating the material's fatigue behavior (stress response, cyclic stress-strain curve, etc.), including in the presence of a significant ratch-

eting effect. The second study focuses on developing a crack initiation model that incorporates the ratcheting effect, integrating the findings from the first study to enhance predictive accuracy.

From a physical perspective, these two investigations contribute to the completion of a comprehensive dislocation-based fatigue lifetime prediction approach. The complete approach encompasses Stage II propagation, Stage I propagation, and Stage I initiation, as indicated in Chapter 1. The findings from this chapter will be utilized in the subsequent chapter for predicting Stage I crack initiation.

The ratcheting effect is characterized as the directional progressive accumulation of plastic deformation in a material when subjected to a primary load in conjunction with a secondary cyclic load. Figure 3.1 illustrates various cyclic load types and their definitions. In the conventional understanding of the ratcheting effect, the study should employ a stress-controlled load type. Nonetheless, the theoretical foundation of the dislocation fatigue system is based on plastic-strain-controlled Discrete Dislocation Dynamics (DDD) simulations. Stress-controlled conditions are generally impossible due to convergence issues [16]. Furthermore, it has been observed that plastic-strain-controlled studies more accurately reflect the actual physical behavior and damage of the material during the fatigue process [52]. Consequently, the stress-controlled ratcheting effect will be examined using the plastic-strain-controlled model. The methodology for applying mean stress through a feedback system will be detailed in the subsequent sections.

To analyze the ratcheting effect, or more specifically, to predict the ratcheting strain as a function of fatigue cycles, it is imperative to develop a general fatigue material model beyond empirical descriptions. This model should not only predict the hysteresis loops of each cycle but also quantitatively forecast kinematic hardening using fully defined parameters that hold a clear physical interpretation. Fortunately, a foundation for such a model exists, having been previously developed by the research group through Discrete Dislocation Dynamics (DDD) simulations [27]. Nevertheless, this preliminary study did not extend sufficiently to explore the ratcheting effect or to yield the crucial data necessary for a crack initiation model. The expansion and refinement of this model to include these aspects will be the focus of this chapter and the next one.

For this chapter, which focuses on the general model and prediction of the ratcheting effect, the structure will be organized as follows:

1. **Literature Review of Fatigue Ratcheting Models:** This section will examine existing models that describe the ratcheting effect of materials, outlining their key features and limitations.
2. **Theory and Construction of the Equations:** Here, the theoretical

framework and the formulation of the equations for the general fatigue model will be discussed. Detailed explanations of all the main model equations will be provided. This section will also cover the numerical methods employed to solve these equations and the algorithm used to apply mean stress for the study of the ratcheting effect.

3. **Study of the Parameters and Sensitivity Analysis:** This section will explore the parameters and their corresponding impacts on the model's outcomes.
4. **Results and Discussion:** The findings from the general fatigue model will be presented in this section, along with comparisons to experimental data and a discussion of the implications and significance of these results.

3.2 . Brief review of ratcheting models

The advancements in observation and constitutive modeling of the ratcheting phenomenon up to 1997 were comprehensively reviewed by Ohno [101]. Subsequent models developed after this period were similarly reviewed in [102]. However, the models outlined in these reviews are predominantly constitutive in nature. They do not delve into the microscopic mechanisms underlying the ratcheting effect, focusing instead on replicating macroscopic mechanical behaviors. These models are readily applicable in finite element analysis (FEA) to simulate the ratcheting effect, proving extremely useful in industrial settings. Nonetheless, they do not facilitate a deeper understanding of the mechanisms driving ratcheting.

For the advancements of experimental studies on the ratcheting effect (not limited to the stainless steels), the review of the paper [100] is recommended. It is found that the study of the ratcheting effect using *true stress* is more accurate than using engineering stress [103, 104]. Another important experimental conclusion is that the ratcheting strain evolution is generally reversible which means that the tensile and compressive ratcheting strain can be compensated by each other.

Generally, three possible types of ratcheting behavior are observed in the experiments. They are listed below and illustrated in Fig. 3.2.

- *decreasing ratcheting strain:* This type of ratcheting behavior is characterized by a continuous decrease in the ratcheting rate with the number of cycles, commonly observed in severely hardened materials [100].
- *constant ratcheting strain:* This behavior is characterized by a constant ratcheting rate which leads to early fatigue crack initiation and propagation.

- *increasing ratcheting strain*: The ratcheting rate increases with the number of cycles, then keeps constant and at last diverges. It is believed that in most cases in the experiments, this is due to the cross-sectional area reduction caused by the ratcheting elongation. The model cannot predict this behavior yet but theoretically, it can be combined with FEM to simulate this behavior.

Two competitive physical mechanisms exist in the ratcheting process. The first one is the cyclic hardening which will cause the ratcheting rate to decrease gradually [104, 105, 106]. This mechanism dominates the starting period of a fatigue test when the total ratcheting strain is relatively low. The second one is the cross-sectional area reduction due to the total elongation of the specimen. Most fatigue tests are stress-controlled so at this stage, the true stress reacting upon the central area of the specimen will be higher than the total stress. This creates a phenomenon called *geometrical softening* which will cause the ratcheting rate to increase [103, 107]. The competition between these two mechanisms will determine the final ratcheting behavior divided into three zones as illustrated in Fig. 3.3.

3.3 . Theory and construction of the equations

The current study employs the cyclic plasticity model described in [27], which is based on a physical representation of dislocation microstructures through a statistical distribution of dislocation dipoles acting as effective obstacles to (cyclic) plastic slip. Throughout the fatigue process, dislocations on the primary slip plane multiply and accumulate, forming edge dipoles as a result of the mutual trapping of opposite sign dislocations. This accumulation of primary dislocations is often considered heterogeneous, leading to the formation of networks of edge dislocations typically known as dislocation tangles and/or veins.

To predict mechanical behavior in FCC crystals, the model constructs a strain-hardening framework derived from the local mechanisms active during plastic deformation. The strength of a dipole is given by the formula $s = \frac{Gb}{8\pi(1-\nu)h}$, where G represents the shear modulus, b is the Burgers vector, h is the height of the dipole, and ν is the Poisson ratio. The initial quantification of dipole heights in this model was proposed to be done through Dislocation Dynamics (DD) simulations. Subsequent simulations cited in [16, 25] determined that the dipole height h is random and normally distributed, as illustrated in Fig. 3.4).

The distribution has a mean value \bar{s} that increases during cycling, namely while dislocation density ρ increases:

$$\bar{s} = \int_0^{\infty} s \cdot f(s) ds = \tau_0 + \alpha Gb\sqrt{\rho} \quad (3.1)$$

Based on the DDD simulations [16, 25] with the validation of certain experimental observation in [108], the variance of the distribution σ_s is found to be proportional to the mean value \bar{s} :

$$\sigma_s = \sqrt{\int_0^{\infty} (s - \bar{s})^2 \cdot f(s) ds} = \lambda \cdot \bar{s} \quad (3.2)$$

The above two equations contain three parameters related to the distribution of dipole heights: τ_0 , α , and λ . These values are material specific so in the case of stainless steel, they will be calibrated accordingly. However, τ_0 is the well-known lattice friction stress that can not be adjusted freely. For the material stainless steel, τ_0 is about 50 MPa.

When destabilized under the local resolved shear stress, any dipolar obstacle of strength s is supposed to accommodate the same local shear strain at a rate $\dot{\gamma}_s$. This local strain contributes with its fraction $f(s)$ to the global strain rate $\dot{\gamma}$. This yields the following equation of strain rate $\dot{\gamma}$ by integrating the whole distribution of dipole strengths s with their corresponding local strain rates $f(s)\dot{\gamma}_s$:

$$\dot{\gamma} = \int_0^{\infty} \dot{\gamma}_s \cdot f(s) ds \quad (3.3)$$

The flow law governing the local strain rate $\dot{\gamma}_s$ is derived from the thermal activation glide theory [109, 110]. It is classically expressed as:

$$\dot{\gamma}_s = \dot{\gamma}_0 \left| \frac{\tau - X_s}{s} \right|^{1/m} \text{sign}(\tau - X_s) \quad (3.4)$$

In this expression, τ represents the resolved shear stress and X_s denotes the internal long-range stress. The parameter m in the equation is a very small value, typically set as $1/m = 20$, indicating that the equation is highly sensitive to the value of $\tau - X_s$. Consequently, the value of $\tau - X_s$ must be kept very close to zero to avoid fast divergent evolutions.

The determination of the expression for X_s presents considerable complexity. A detailed explanation is available in the work of Depres et al. [27]; however, this will not be discussed further in this context. The expression for X_s is defined as follows: $X_s = MG(\gamma_s - \gamma)$, where M represents a material-dependent coupling parameter, G denotes the shear modulus, γ_s is the average strain of the dipole, and γ is the average strain of the material. The parameter M is a phenomenological coefficient that encapsulates the average impact of the dislocation dipole distributions on the actual kinematic stress level. This includes the actual configurations of polarized loops and their average radius relative to the dimensions of the volume. In the case of copper, the value of M has been determined to be 2, as estimated by dislocation dynamics (DD) simulations. For stainless steel, the value of M will be adjusted based on empirical calibration.

The last equation required is the evolution of the dislocation density ρ based on [111, 109]:

$$\dot{\rho} = \frac{1}{b} \left(\frac{\sqrt{\rho}}{K} - 2y_c \rho \right) |\dot{\gamma}| \quad (3.5)$$

where K is the mean free path of dislocations, y_c is the critical annihilation distance. This is a classical equation of equilibrium between the creation and annihilation of dislocations. The saturation density is $\rho_{sat} = \frac{1}{4y_c^2 K^2}$.

This set of five constitutive equations constitutes the mathematical framework for the mechanisms previously described. Numerous sources for the model's development are cited in the study by Depres et al. [27], details of which are omitted here for brevity. All parameters pertinent to the model will be presented in the material property given in Chapter 6. General parameters are included in the general section, while those specific to this model are listed in the model-specific section.

Although the constitutive equations are clearly defined, solving these equations entails various computational challenges. The subsequent section will provide an algorithm for solving these models. Additionally, it will describe the method for applying mean stress to induce the ratcheting effect.

3.3.1 . Model construction and calculation

As outlined in Section 3.3, the utilization of the model necessitates solving a coupled system of five nonlinear differential equations, which lack an analytical solution and must therefore be resolved through explicit numerical methods. The principal input for the model is the plastic shear strain, which can be specified by the user either directly or through the plastic shear strain rate, given their equivalence. The output from the model is the stress evolution. All these values are defined at each time step. This means that the model is general, applicable to all types of loading conditions and thus does not inherently account for the fatigue process.

The core of the final equation, addressed via numerical methods, is detailed in Eq. (3.3). The terms within this equation are expressed through the equations listed in Eq. (3.4), Eq. (3.1), and Eq. (3.2). Additionally, Eq. (3.5) is utilized to compute the rate of change in the dislocation density ρ and to update ρ at each time step. These equations are presented in their fundamental physical formulations.

Firstly, Eq. (3.1) and Eq. (3.2) are the equations of the distribution of s . The definite form of s in the numerical method is $f(s)$ which is the probability density function of s . It can be expressed as:

$$f(s) = \frac{1}{\sigma_s \sqrt{2\pi}} \exp \left(- \frac{(s - \bar{s})^2}{2\sigma_s^2} \right) \quad (3.6)$$

Since the distribution of s depends on ρ which evolves during the simulation, the distribution of s is also a function of time step i . In addition, the distri-

bution of s has to be discretized to calculate the integration in Eq. (3.3). This creates a second index j for the discretized distribution of s_j . So the final equation of the distribution of s in Eq. (3.3) is:

$$f^i(s_j) = \frac{1}{(\tau_0 + \alpha Gb\sqrt{\rho^i})\sqrt{2\pi}} \exp\left(-\frac{(s_j - \lambda(\tau_0 + \alpha Gb\sqrt{\rho^i}))^2}{2(\tau_0 + \alpha Gb\sqrt{\rho^i})^2}\right) \quad (3.7)$$

Then substituting equation Eq. (3.4) to the main equation Eq. (3.3), the principle equation becomes:

$$\frac{\dot{\gamma}^i}{\dot{\gamma}_0} = \sum_{j=0}^{N_s} f^i(s_j) \left| \frac{\tau - MG(\gamma_{s_j}^i - \gamma^i)}{s_j} \right|^{1/m} \text{sign}(\tau - MG(\gamma_{s_j}^i - \gamma^i)) \quad (3.8)$$

where i is the index of the time step, j is the index of discretized distribution of s , N_s is the number of discretized points of s_j , and $f^i(s_j)$ is the probability density function of s_j at time step i .

3.3.2 . Numerical methods

Equation (3.8) utilizes the plastic shear strain rate $\dot{\gamma}$ as an input, whereas the unknown variable in the equation being the shear stress τ . The resolution of this equation employs the optimization methods provided by *SciPy*, specifically, the *scipy.optimize.brentq* function, which is cited for its optimal performance and stability [112]. This solving process must be repeated at each time step.

Given that all variations in this study are cycle-wide, it is judicious to regulate the precision using the number of points per cycle N_{pp} , rather than the time step dt , to avoid any influence of period T . Using a higher number of points per cycle enhances both the precision and stability of the solution. Should issues arise in achieving a successful solution, increasing N_{pp} may be considered.

During the simulation steps, many values have to be updated with their time derivatives. This can be done with the trivial formula given their derivative:

$$x^{i+1} = x^i + \dot{x}^i dt \quad (3.9)$$

If the plastic shear strain rate $\dot{\gamma}$ is selected as the input, the following solving procedure is employed:

Initially, the plastic shear strain γ is derived directly from $\dot{\gamma}$ using Eq. (3.9). It is assumed that the initial values for all $\gamma_{s_j}^i$ are set to 0. The time step dt is then determined based on the number of integration points per cycle N_{pp} and the strain rate $\dot{\gamma}$, calculated as $dt = \frac{2\Delta\gamma_p}{\dot{\gamma}_p N_{pp}}$. Depending on the specific loading conditions or the method employed for solving, N_{pp} may typically range from 500 to 5000.

The procedure continues cycle by cycle until the predetermined number of cycles N_c is achieved. Within each iteration, the following steps are executed:

1. The value of τ^i is determined using the *SciPy* optimization methods previously described, particularly through the function referenced in Eq. (3.8).
2. The values of ρ^i and ρ^{i+1} are computed in accordance with Eq. (3.5) and Eq. (3.9), respectively.
3. The updates for $\dot{\gamma}_{s_j}^i$ and $\dot{\gamma}_{s_j}^{i+1}$ are conducted utilizing Eq. (3.4) and Eq. (3.9).
4. The process advances to the next cycle.

The algorithm of the solution above is shown in the area named *Single cycle calculation* in Fig. 3.7 which shows the solution of a single cycle. Multi-cycle simulations are carried out by repeating the same process for as long as requested.

3.3.3 . Application of the mean stress

In our model, the nonlinear kinematic hardening is explicitly calculated based on the density and distribution of dislocation dipoles obtained from DD simulations. The ratcheting strain accumulation thus becomes a natural outcome of the model. In this section, the method of using the model to predict the ratcheting effect is described.

The general model can be resolved using the aforementioned method to predict the mechanical behavior of the material under any given arbitrary plastic shear strain load γ . However, the model encounters numerical constraints that prevent the direct application of mean stress (similar to the constraints in discrete dislocation dynamics (DDD) simulations, where stress cannot be directly inputted). To circumvent this limitation, a feedback control system has been implemented. This procedure manages the application of mean stress by controlling the plastic shear strain rate $\dot{\gamma}$.

At the beginning of each simulation, an array of target mean stress values ($\bar{\tau}_0^{ii}$) is given. Here ii is the current cycle number, it is different from the index i which is the time step (integration point). Each cycle ii contains N_{pp} time steps i . The plastic shear strain rate is adjusted multiple times at each cycle to reach the target mean stress, as shown in Fig. 3.5.

Methods of setting $\dot{\gamma}$

There are several ways of fixing a plastic strain range $\Delta\epsilon_p$. The most straightforward method is to set a corresponding simulation period. Once the period

is fixed, equal-length steps can be generated. The load control method may be applied according to one of the two following possibilities:

1. Change t_+ and t_- . (Period of extension and compression) This method has a disadvantage. The mean strain level $\bar{\gamma}$ is limited to a fourth of the plastic strain amplitude. This value is too small to be considered effective.
2. Change $\dot{\gamma}_+$ and $\dot{\gamma}_-$ (deformation rate). This is the main method used in the calculations. In the case of ratcheting simulation, this method is more reasonable as practically, the period of extension and compression is fixed. The deformation rate is the main parameter that would change during the tests. Usually, we would shift the deformation rate of extension and compression with the same absolute value which should be the case in practical situations. This is also a limit of the mean deformation $\bar{\gamma}$ but this limit is much higher than the first method and can cover most of the usage cases.
3. Add independent extension and compression periods to create the mean deformation. This method can be practical in the case of applying a mean strain. However, it lacks practical correspondence with real experiments and doesn't fit well in the framework of fatigue tests.

The illustration of the two first methods can be found in Fig. 3.6.

In experimental plastic-strain-controlled fatigue tests, particularly when investigating the ratcheting effect, the use of this procedure is indispensable. Typically, many experiments maintain a fixed plastic shear strain rate $\dot{\gamma}$ because the deformation rate influences numerous other material properties, such as temperature. Consequently, altering the period of extension and compression becomes essential to modify the mean deformation ratio.

All these two methods could correctly create the desired mean stress, but they differ in terms of numerical stability. The forthcoming study will demonstrate that in simulation scenarios, the difference between maintaining a constant $\dot{\gamma}$ and varying the extension/compression periods is negligible. Using the latter method is shown to improve numerical stability significantly.

In real practical applications, there are multiple cases of the mean stress (which is more common than the mean strain). For example, mean stress could be applied directly during the first cycle to full amplitude. This is theoretically possible to be simulated with the above model but numerically impossible for the moment. The mean stress could also be applied gradually during the cycles and it may be varying during the entire test. In addition, during the operation pause, the mean stress could be reduced to zero and then increased again with a frequency much lower than the fatigue frequency. All these cases could be studied with the above model but for simplicity, in our

research we will just simulate a constant mean stress that is gradually applied during the first cycles as a representation. The other cases could be studied in the future.

Definition of number of apply cycles

The number of applied cycles N_{apply} (N_a for short) represents the number of fatigue cycles during which the mean stress is progressively applied. This gradual application is critical; attempting to apply the mean stress abruptly would overwhelm the feedback system. The number of apply cycles N_{apply} significantly influences the initial evolution of stress and strain in the material.

It is crucial to incrementally apply the mean stress and strain until the selected number of apply cycles N_{apply} is reached. Beyond this point, the applied mean stress (and mean strain) remains constant, matching the desired target value. Therefore, if the objective is to apply a mean stress $\bar{\tau}_0$ over N_{apply} cycles, the relationship of the applied mean stress $\bar{\tau}$ to fatigue cycles N will be characterized as follows:

$$\bar{\tau}(N) = \begin{cases} N \times \frac{\bar{\tau}_0}{N_{apply}} & N < N_{apply} \\ \bar{\tau}_0 & N > N_{apply} \end{cases}$$

However, it has been observed that a linear increment in stress can lead to abrupt stress evolutions (jumps) in the first few cycles. Consequently, a sigmoid function has been selected as a more appropriate alternative to the linear increment approach. The sigmoid function facilitates a smooth transition in stress values both at the onset and upon reaching saturation levels. Thus, the applied mean stress $\bar{\tau}$ will evolve as follows:

$$\bar{\tau}(N) = \begin{cases} \frac{\bar{\tau}_0}{1 + e^{\frac{12N}{N_{apply}} - 6}} & N < N_{apply} \\ \bar{\tau}_0 & N > N_{apply} \end{cases}$$

The $\bar{\tau}_0$ is the target mean stress at the end of the simulation, assuming that constant mean stress is simulated. N_{apply} is the number of cycles to reach the target mean stress. The model can apply the mean stress of various forms. It does not have to be a constant. However, this *buffer zone* is necessary to avoid any calculation instability.

Here, Fig. 3.7 illustrates the algorithm of the feedback system, which is controlled by the modulation of the plastic strain rate. The entire simulation, encompassing N_c cycles, is divided into N_c blocks, each containing N_{pp} time steps. Within each block, the outlined algorithm for solving the equation is rigorously adhered to, as indicated in the upper right corner of the algorithm diagram.

After completing each cycle (block), the mean stress $\overline{\tau^{ii}}$ is calculated and assessed against the target mean stress $\overline{\tau_0^{ii}}$. A precision coefficient $[\eta^{ii}]$ is pre-determined for each cycle, generally ranging from 1% to 0.1%. It is noteworthy that this coefficient may vary across different cycles, typically being higher in the initial cycles to aid in achieving convergence.

The criterion for equality is defined by the equation $\Delta\tau = \left| \overline{\tau^{ii}} - \overline{\tau_0^{ii}} \right| \leq \eta^{ii} \overline{\tau_0^{ii}}$. If this criterion is not met, the strain value $[\gamma^i]$ is adjusted by incorporating a correction value $\Delta\gamma^i$, which is calculated using the following formula:

$$\Delta\gamma^i = -\frac{\alpha^{ii} * \Delta\tau}{4MG} \quad (3.10)$$

where α^{ii} represents a sensitivity coefficient. Initially set to a uniform value, α^{ii} may be adjusted during the simulation to mitigate oscillations or prevent any computational instabilities. The operative criterion involves comparing the absolute value of the current iteration's $\Delta\tau$ to that of the previous one. If the current $\Delta\tau$ exceeds the previous value, α^{ii} is reduced by half to curtail potential divergence. This adjustment occurs individually within each cycle and is effective only if the criterion is satisfied during that cycle. The initial value of α^{ii} is consistent across all cycles, typically set at $\alpha_{init}^{ii} = 0.7$.

The results of the model will be shown in the following section.

3.4 . Results and discussion

In this section, the results of various studies around the model will be discussed, including the model's output and interpretation, the study of parameters, complex loadings and the quantitative calibration of the model based on the experimental data and the calibrated representative ratcheting rate results.

3.4.1 . Model output and interpretation

At first, the model effectively reproduced the ratcheting forms and associated hysteresis loops. A comprehensive summary of the model's outcomes with non-calibrated parameters is depicted in Fig. 3.9. This summary figure, which encapsulates all essential information of the results, is referred to as the *nine-fold grid*.

The model primarily generates hysteresis loops as a function of the applied plastic shear strain *at each time step*. The presence of kinematic hardening is evident in the model's outputs. It is important to acknowledge that this hardening effect is not governed by an empirical hardening rule, which typically depends on the number of fatigue cycles. Instead, the model operates independently of the fatigue cycles, receiving only the applied plastic shear strain at each time step as its input. A more precise comparison focusing on kinematic hardening is depicted in Figure 3.24.

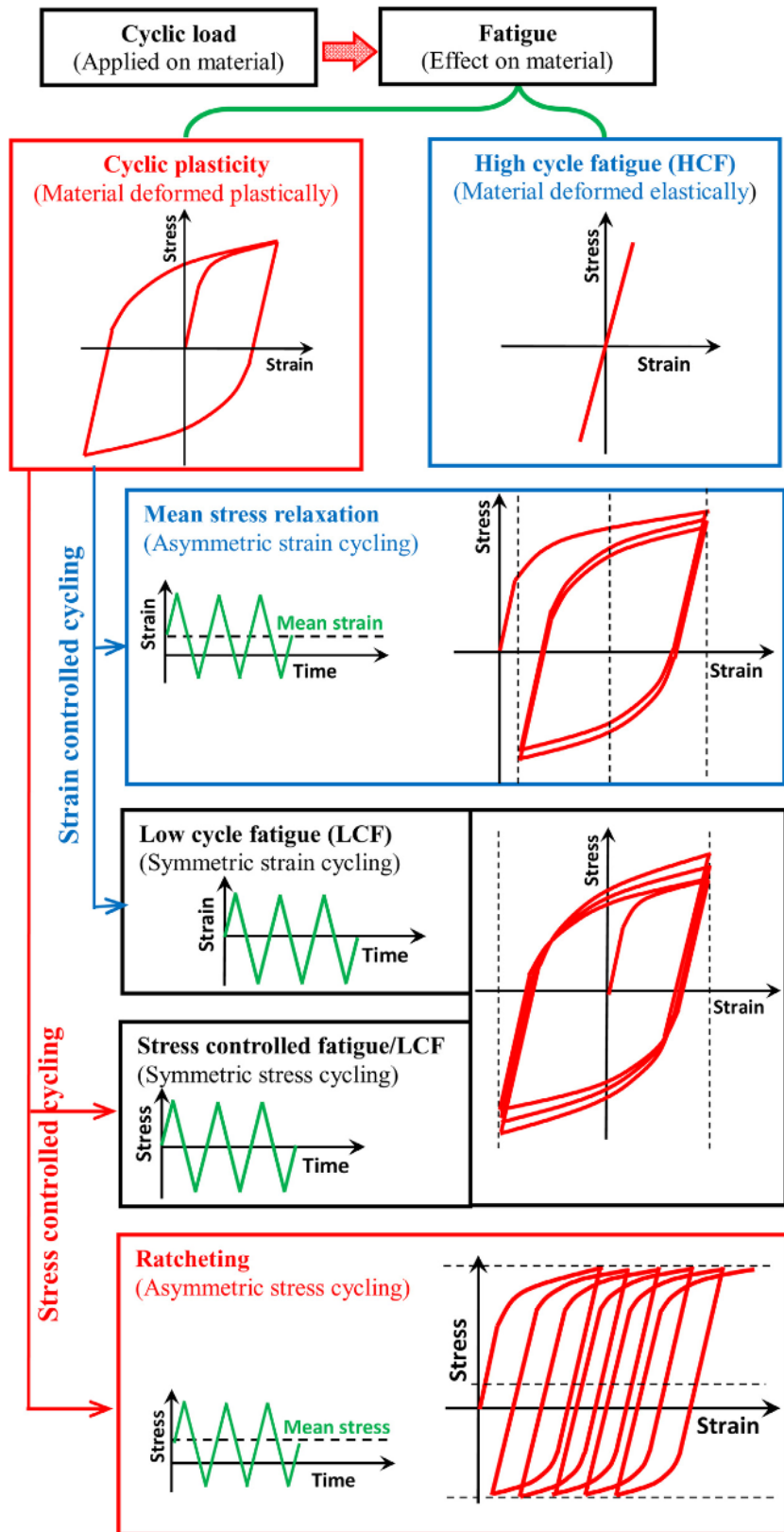


Figure 3.1: Different types of cyclic loading and corresponding material response[100].

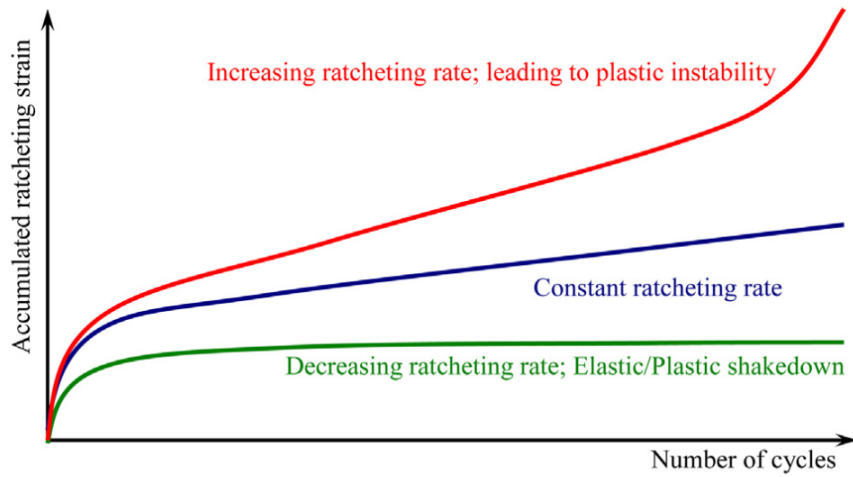


Figure 3.2: Different types of ratcheting [100].

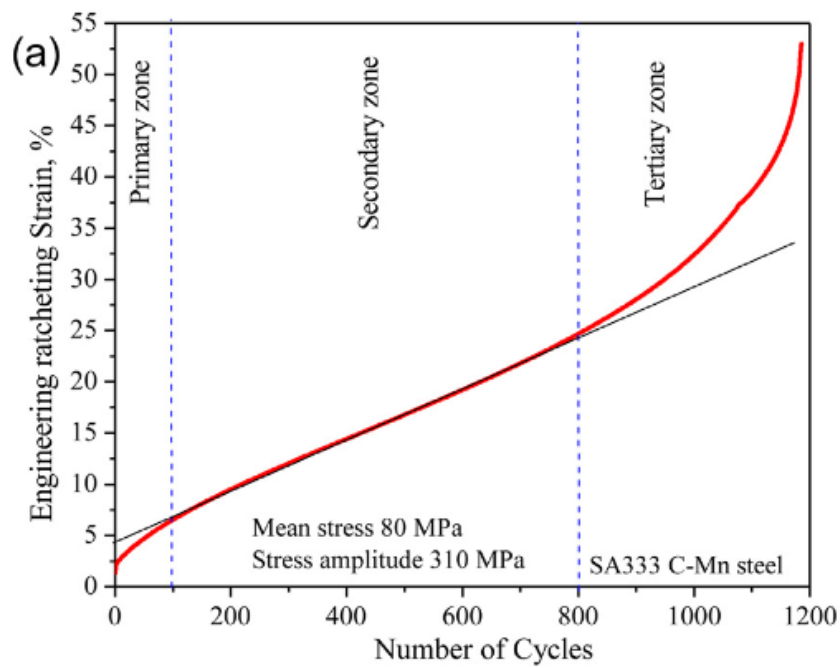


Figure 3.3: Three ratcheting zones as determined by the two competitive mechanisms [100].

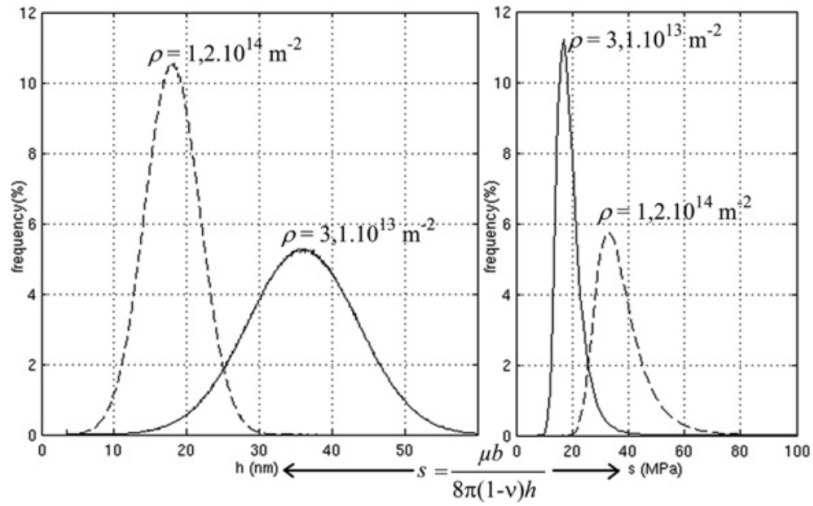


Figure 3.4: Distribution of dipole heights in a copper crystal for two different dislocation densities [27].

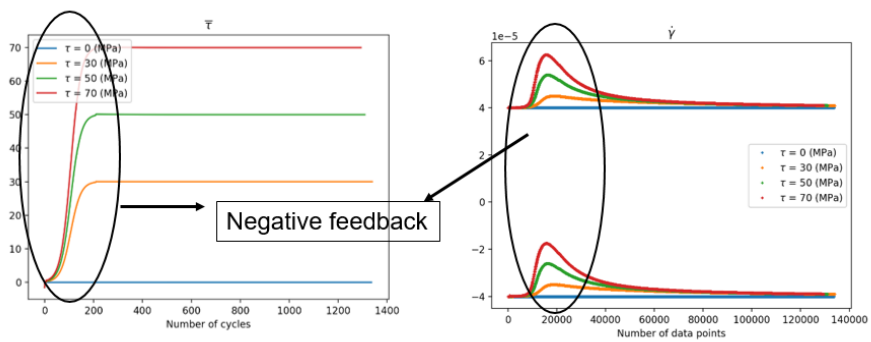
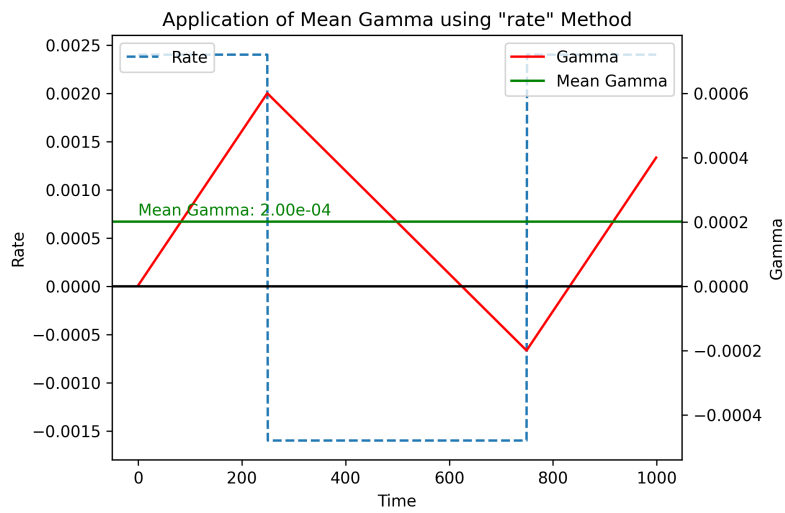
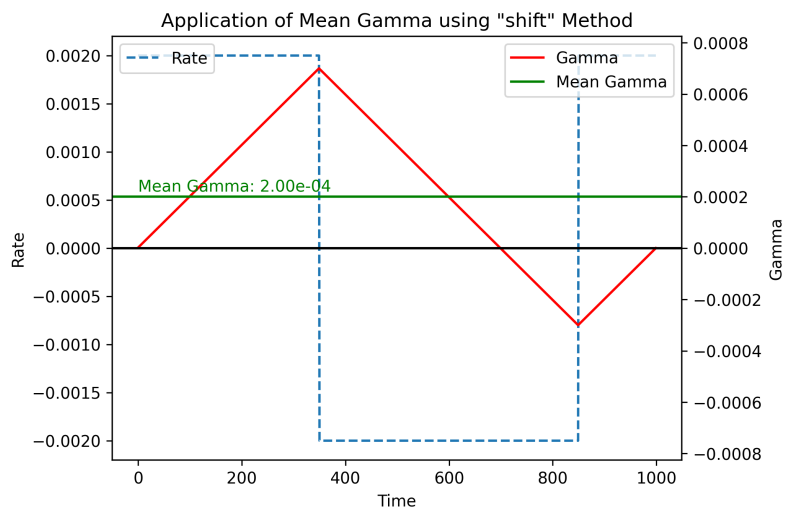


Figure 3.5: The feedback system to apply the mean stress. The plastic strain rate is adjusted as the figure at right to produce the mean stress at left.



(a) Applying the mean strain by changing the deformation rate.



(b) Applying the mean strain by shifting the fatigue cycles

Figure 3.6: Different methods of applying the mean strain.

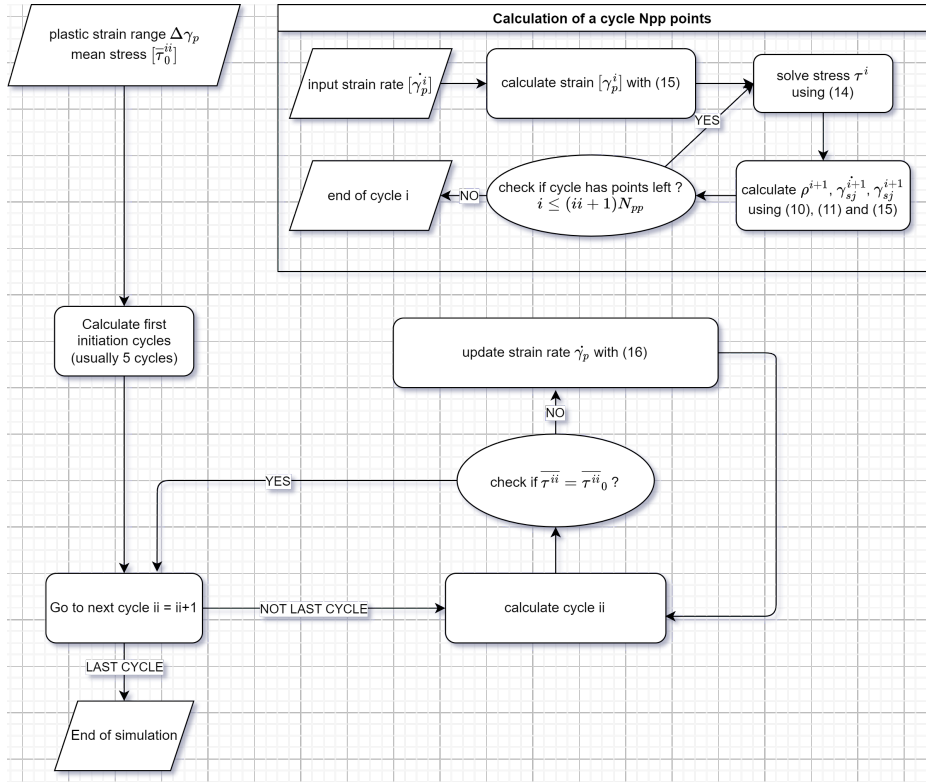


Figure 3.7: Algorithm of the feedback system piloted by the altitude of plastic strain rate.

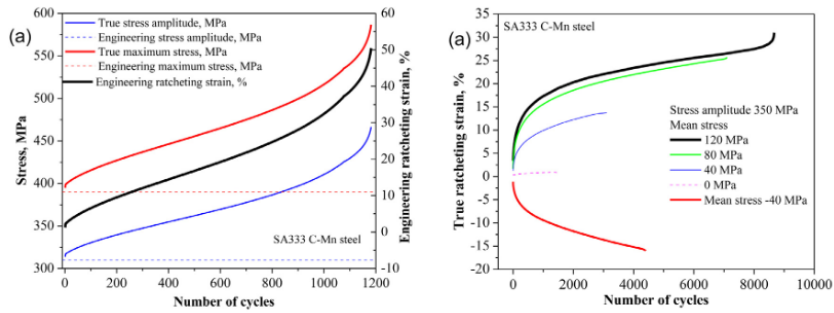


Figure 3.8: (a) Comparison between the engineering stress, strain and the true stress, strain. (b) The true ratcheting strain.

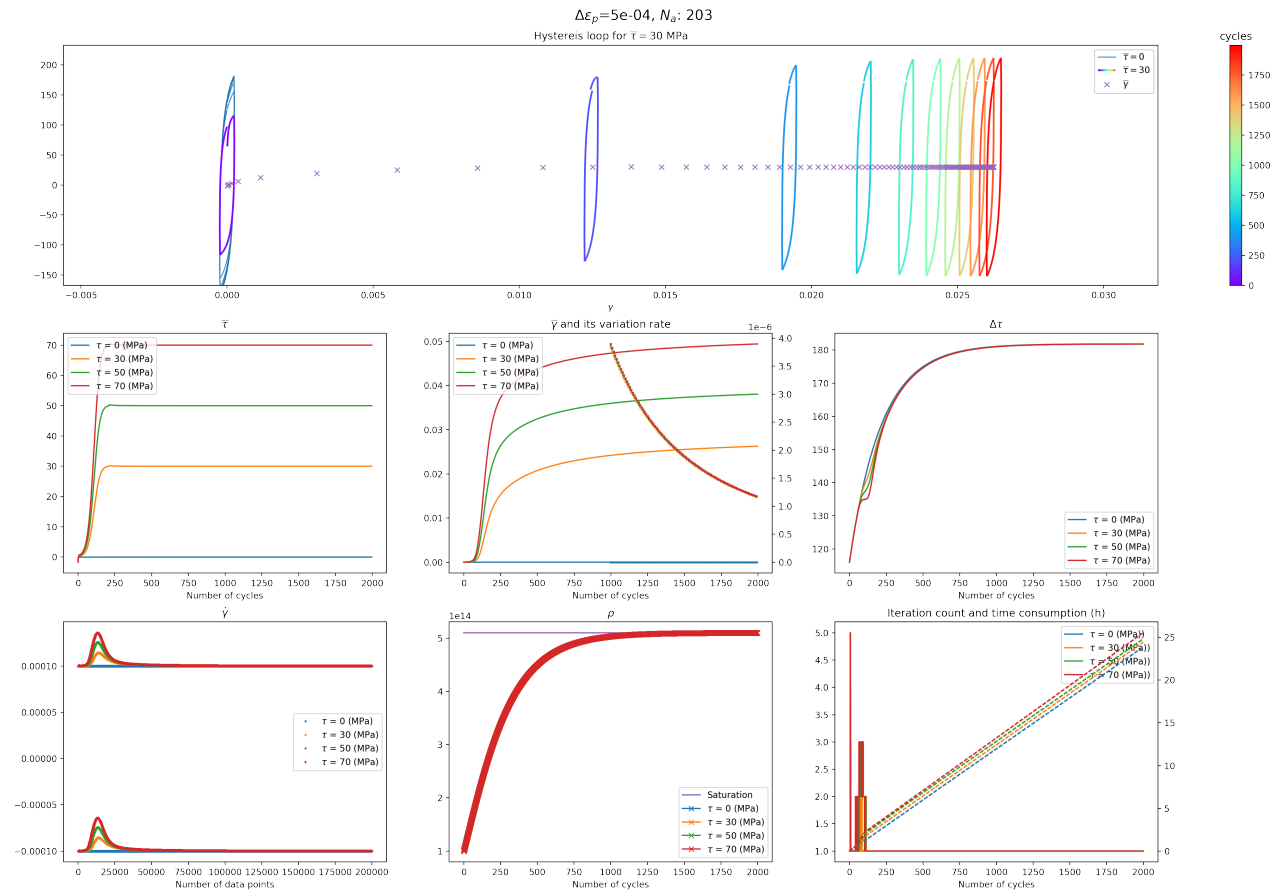


Figure 3.9: A complete set of figures monitoring the results of the model. They are (listed by row number):

1. hysteresis loops, the ratcheting strain is much more important than the applied cyclic strain range. The color changes indicate the number of the cycle evolution.
2. from left to right, 1) the evolution of the mean stress, 2) the evolution of ratcheting strain and its variation rate, 3) the evolution of stress range
3. from left to right, 1) plastic strain rate (which is the result of the feedback system), 2) the evolution of the dislocation density, 3) computational time consumption and the number of iterations performed before convergence

Figure 3.9 presents all outcomes from the model, detailing the evolution of critical physical parameters throughout the simulation. The process requires approximately 20 hours to simulate 1500 cycles. Subsequent cycles continue to exhibit a decreasing ratcheting rate, which does not stabilize at a constant value or go down to zero. As mentioned in Section 3.2, experimental observations typically show a stabilization of the ratcheting rate after a certain number of cycles. This discrepancy arises due to the interplay between cyclic hardening and the reduction of the cross-sectional area, as discussed in [100]. The reduction in cross-sectional area is a structural effect that is not accounted for in the current model. While it is possible to investigate this effect using the finite element method, such analysis is beyond the scope of this study. Figure 3.8 displays experimental data utilizing true strain, which is more appropriate for comparison with the theoretical model.

3.4.2 . Study of the parameters and sensitivity analysis

Numerous parameters within the ratcheting model have yet to be defined for stainless steel, as the original study was based on discrete dislocation (DD) simulations for copper. Given the extensive time required for these simulations—often spanning several months and necessitating a dedicated study. These parameters will be analyzed for their impact on the ratcheting strain and stress range and subsequently calibrated against experimental results.

Since the effects of individual parameters are not independent, a machine-learning model has been developed to improve the parameter calibration process. For the purposes of this section and to facilitate physical interpretation, the influence of each parameter will be examined separately, with all other parameters held constant at typical values.

In this section, two specific ratcheting rates will be examined to show the material's influence on the ratcheting effect. The early (initial) ratcheting rate, $\dot{\gamma}_{160}$, observed at cycle number 160, is utilized to demonstrate the parameter's impact during the initial phase of ratcheting. The later rate, $\dot{\gamma}_{10000}$, observed at cycle number 10000, is used to assess the parameter's effect during the stabilized ratcheting stage.

Additionally, the stress range $\Delta\tau$ will be investigated to explore how the parameters influence the stress range across different ratcheting stages. This analysis aims to provide a comprehensive understanding of each parameter's role in the material's ratcheting response.

Parameter 1: $\dot{\gamma}_0$

$\dot{\gamma}_0 = 10^{-10} \text{ s}^{-1}$ in the flow law equation corresponding to Eq. (3.4). This reference value is influenced by temperature, as discussed in [110]. From a mathematical perspective, it ensures the dimensional compatibility of both sides

of the equation. Simulation outcomes indicate that the magnitude of this parameter has a direct impact on the absolute value of the mean strain $\bar{\gamma}$, as demonstrated in Fig. 3.10. Its effect is limited.

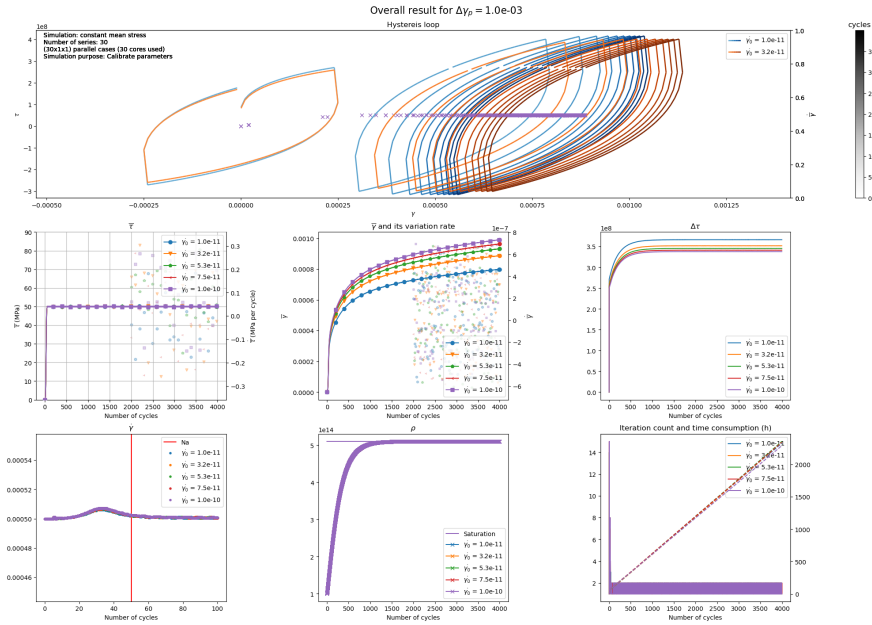


Figure 3.10: Results of ratcheting model with different γ_0

The ratcheting strain exhibits a different behavior compared to the stress range. Specifically, as the value of γ_0 increases, there is a corresponding increase in the ratcheting strain, whereas the stress range decreases.

In this comparison figure, only the three figures in the middle (mean stress, ratcheting strain and stress range) are important in the identification of the parameter's influence. The other figures are not necessary for the interpretation of the parameter's influence. In the analysis of the following parameters, only the three figures in the middle will be shown.

Table 3.1: γ_0 effect

| α | $\bar{\gamma}_{160}$ | $\bar{\gamma}_{10000}$ | $\Delta\tau$ |
|----------|----------------------|------------------------|--------------|
| 1e-11 | 7.59e-7 | 1.47e-8 | 720 |
| 3.2e-10 | 1.08e-6 | 1.94e-8 | 650 |
| 6.6e-10 | 1.16e-6 | 2.70e-8 | 630 |
| 1.0e-9 | 1.20e-6 | 2.31e-8 | 610 |

Parameter 2: M

The parameter M , defined in the equation Eq. (3.4), is incorporated in the formulation of the long-range internal stress. According to [27], the parameter M is a parameter linked to the dislocation microstructure effect on the kinematic stress evolutions. Consequently, its value is not fixed and is expected to be material-dependent.

The initial value recommended by [27] for copper is $M = 2$. For stainless steel, it is hypothesized that this value fluctuates between 1 and 10, and 30 different, evenly distributed values within this range are selected to examine the parameter's influence.

The findings are partially depicted in Fig. 3.11. It is observed that at elevated values of M , the rate of variation approaches zero. A more comprehensive plot for $M \leq 4$ is presented in Fig. 3.12.

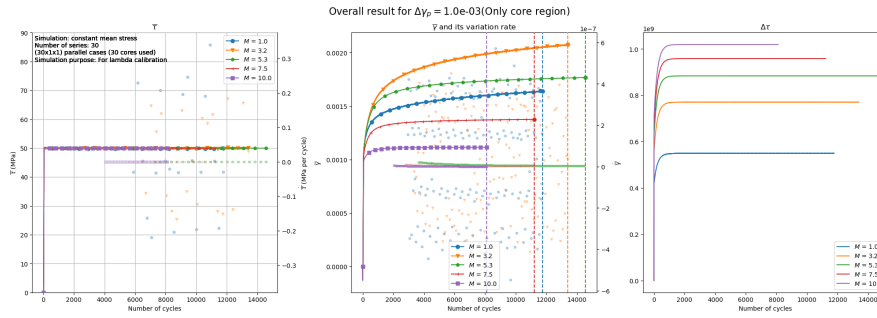


Figure 3.11: Results of ratcheting model with different M varying from 1 to 10

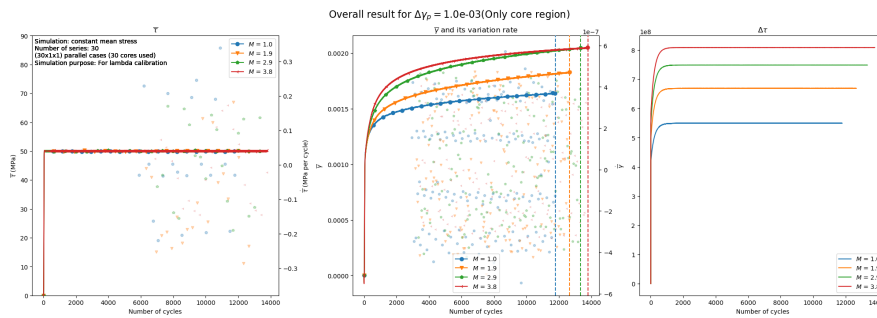


Figure 3.12: Results of ratcheting model with different M varying from 1 to 4

The outcomes associated with this parameter are summarized in Table 3.2. It can be concluded that:

- An increase in M corresponds to an increase in $\Delta\tau$. Specifically, as M increases from 1 to 10, $\Delta\tau$ rises by approximately 500 MPa (from 500 to 1000 MPa).

- Initially, an increase in M yields a higher $\bar{\gamma}$ level but subsequently leads to its reduction. Regarding the variation rate $\dot{\bar{\gamma}}$, an escalation in M results in a decreased variation rate, indicating that the second derivative of the function representing $\bar{\gamma}$ with respect to M is negative.

These results underscore the critical role of the parameter M in the calibration of the model. It significantly influences the contour of the ratcheting strain by affecting the second derivative of the function representing $\bar{\gamma}$ in terms of M .

The impact of M on the stress range is substantial compared to other parameters. This effect can be understood through equation Eq. (3.4), where the internal stress is directly proportional to M , and the macroscopic stress should approximate this value as closely as possible.

Table 3.2: M effect

| α | $\dot{\bar{\gamma}}_{160}$ | $\dot{\bar{\gamma}}_{10000}$ | $\Delta\tau$ |
|----------|----------------------------|------------------------------|--------------|
| 1.0 | 7.88e-7 | 1.12e-8 | 550 |
| 3.8 | 1.20e-6 | 1.87e-8 | 800 |
| 6.9 | 7.16e-7 | 2.34e-9 | 910 |
| 10.0 | 2.67e-7 | | 1050 |

Parameter 3: λ

From this subsection, the focus will be on three parameters that pertain to the distribution of the dipoles, as referenced in Section 3.3. These parameters can typically be derived from Dislocation Dynamics (DDD) simulations. However, DDD simulations applicable to stainless steel are unavailable for this study. Consequently, the calibration of these parameters will rely on experimental results. In the following three subsections, an analysis will be conducted on how these parameters influence the ratcheting strain and stress range, thereby aiding the calibration process.

The parameter λ is defined in Eq. (3.2) within the study by [27]. It describes the linear relationship between the mean value of the dipole strength and the variance of the dipole strength. This correlation is derived from Dislocation Dynamics (DDD) simulations, indicating that λ should be a material-specific quantity. This is also applicable to the other two parameters, α and τ_0 .

The range of values chosen in this simulation is from $\lambda = 0.5$ to $\lambda = 1.5$ while the recommended value for copper is $\lambda_{Cu} = 0.8$. The results are shown in Fig. 3.13. When $\lambda \geq 0.8$, the influence on $\bar{\gamma}$ is not significant. A more detailed plot of $\lambda \leq 0.8$ is shown in Fig. 3.14.

Similarly to the analysis of M in Section 3.4.2, the variation of λ will affect the two parameters $\Delta\tau$ and $\bar{\gamma}$.

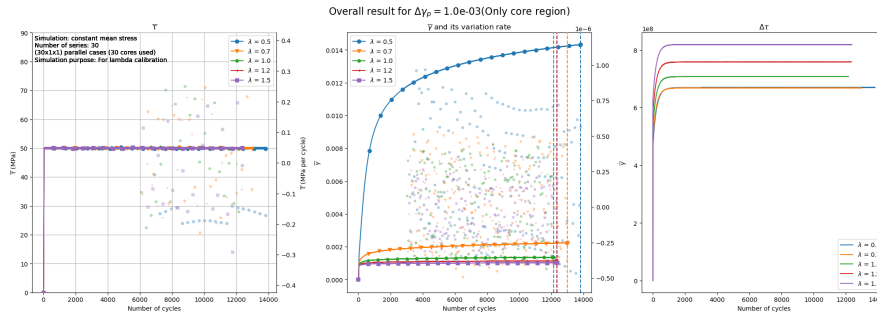


Figure 3.13: Results of ratcheting model with different λ

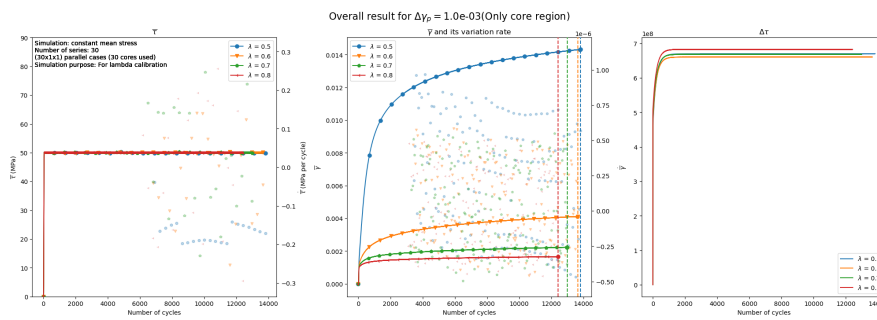


Figure 3.14: Results of ratcheting model with different $\lambda \leq 0.8$

Table 3.3: λ effect on important points

| λ | $\bar{\gamma}_{160}$ | $\bar{\gamma}_{10000}$ | $\Delta\tau$ |
|-----------|----------------------|------------------------|--------------|
| 0.5 | 1.34e-5 | 1.46e-7 | 670 |
| 0.8 | 9.11e-7 | 1.05e-8 | 680 |
| 1.2 | 3.82e-7 | 5.09e-9 | 720 |
| 1.5 | 2.40e-7 | 3.13e-9 | 810 |

- $\Delta\tau$ increases with increasing λ , but the phenomenon is only relatively important for $\lambda \geq 1.0$. The increment of $\Delta\tau$ is not as significant as that due to M evolution and comparable to that due to $\dot{\gamma}_0$.
- $\bar{\gamma}$ is greatly affected by λ when $\lambda \leq 0.7$ while at this value the influence on $\Delta\tau$ is negligible.

In conclusion, λ variations have a strong influence on the total mean strain $\bar{\gamma}$. It has the potential to substantially alter the value of $\bar{\gamma}$ while leaving the value of $\Delta\tau$ almost unaffected. The reasons for this observation are not immediately apparent. The significant impact on the ratcheting strain could stem from the direct correlation between dipole strength and local shear strain. Conversely, the stress range is not directly linked to this distribution but is influenced indirectly by the difference between local shear strain and macro-

scopic strain.

Parameter 4: α

Similar to λ , the parameter α is associated with the distribution function of dipoles and is defined within the expression for the mean dipole strength, as specified in Eq. (3.1). It characterizes the linear correlation between the mean value of the dipole strength and the dislocation density value.

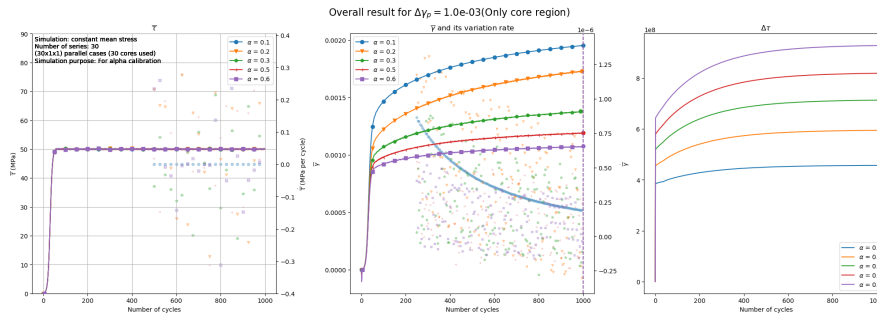


Figure 3.15: Results of ratcheting model with different α

Results indicate that an increase in α leads to a reduction in mean strain $\bar{\gamma}$ and a corresponding rise of the stress range $\Delta\tau$. This effect is similar to those observed with γ_0 and λ , as noted in the previous subsection. Additionally, α plays a crucial role in the kinematic hardening effect, as it correlates the dislocation density ρ with the distribution of dipoles. A higher value of α enhances the kinematic hardening effect, which may also account for its substantial impact on the stress range.

Table 3.4: α effect

| α | $\bar{\gamma}_{160}$ | $\bar{\gamma}_{10000}$ | $\Delta\tau$ |
|----------|----------------------|------------------------|--------------|
| 0.1 | 1.74e-6 | 2.42e-8 | 370 |
| 0.3 | 1.03e-6 | 1.60e-8 | 500 |
| 0.4 | 6.32e-7 | 6.55e-9 | 610 |
| 0.6 | 4.56e-7 | 4.41e-9 | 710 |

Parameter 5: τ_0

τ_0 appears the expression of mean dipole strength expression Eq. (3.1). Its value for 316 steel is $40 \text{ MPa} < \tau_0 < 50 \text{ MPa}$ and the value recommended for copper is much lower, i.e. $\tau_{0Cu} = 4 \text{ MPa}$. The effect of τ_0 is shown in Fig. 3.16.

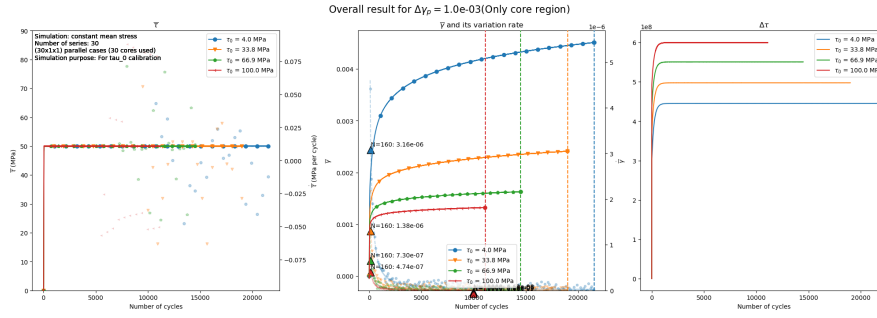


Figure 3.16: Results of ratcheting model with different τ_0

The impact of varying τ_0 is indeed significant, aligning with observations made thus far: parameters associated with the distribution of dipoles profoundly influence the outcomes. Alterations in τ_0 result in substantial changes in both $\dot{\gamma}_{160}$ and $\dot{\gamma}_{10000}$, reflecting its critical role in the mechanical behavior of the material. However, the stress range $\Delta\tau$ does not exhibit as much sensitivity to changes in τ_0 as might have been expected. Although both τ_0 and $\Delta\tau$ are measures of stress, they do not have a direct relationship in the equations. The stress range remains most sensitive to the parameter M .

Table 3.5: Table caption

| τ_0 (MPa) | $\dot{\gamma}_{160}$ | $\dot{\gamma}_{10000}$ |
|----------------|----------------------|------------------------|
| 4 | 3.16e-6 | 4.62e-8 |
| 33.8 | 1.38e-6 | 2.19e-8 |
| 66.9 | 7.03e-7 | 9.26e-9 |
| 100 | 4.74e-7 | 6.68e-9 |

It is important to recognize that the value of τ_0 cannot be extensively modified. The dipole strength, which τ_0 represents, is a well-defined physical quantity linked with the lattice friction stress of the material. Although the precise distribution of dipoles in stainless steel, and consequently the exact value of τ_0 , remains unknown, it is still possible to estimate a reasonable range for this parameter. For instance, a value of 100 MPa for τ_0 would be excessively high. A more plausible range would be between 30 and 60 MPa, which better aligns with the known characteristics of stainless steel.

Parameter 6: m

m is the power factor in the expression of local strain rate $\dot{\gamma}_s$ which is derived from the thermal activation theory.

In the case of the parameter m , the model exhibits significant instability. The majority of the simulation attempts fail to converge. Among the 30 val-

ues selected within the range from $\frac{1}{15}$ to $\frac{1}{30}$, only two values successfully converged, and the results are presented in Fig. 3.17. The outcomes for these two values are nearly identical, which can be anticipated considering that this power coefficient acts as an error amplifier within the equations. Its function is to maintain $\tau - MG(\gamma_{sj} - \gamma)$ as close to zero as possible while allowing for a slight variance. For the final model configuration, a default value of $m = \frac{1}{20}$ will be used.

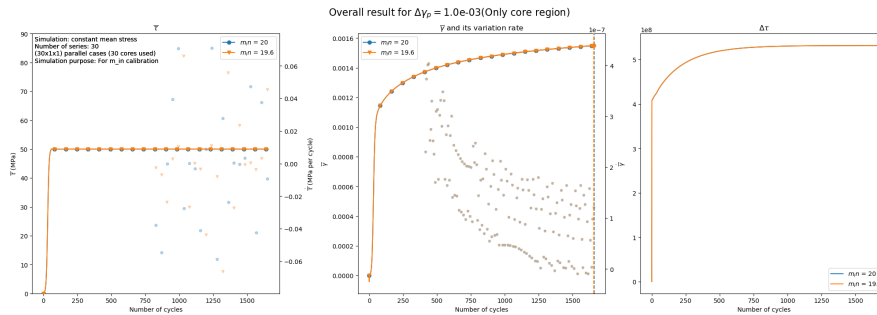


Figure 3.17: Results of ratcheting model with different m

3.4.3 . Step load tests

In this subsection, the model's capacity to simulate complex loads is tested with step loading, both for the change of mean stress and the change of applied shear strain range. In addition, the comparison between time control and rate control is also performed to verify the influence of different control methods as introduced in Section 3.3.3.

The experimental results for this kind of step loading are not available in the literature for stainless steel. However the behavior of the material can be qualitatively compared to some other similar ductile materials. Some experimental results using true stress and true strain could be found [113]. They will be shown beside the simulation results for comparison in the following paragraphs.

Comparison for different mean stress

Step tests are performed for both increasing and decreasing mean stresses. The plastic shear strain ranges $\Delta\gamma_p$ considered are $(0.1e - 3, 0.3e - 3, 1e - 3, 1.5e - 3, 2e - 3, 2.5e - 3, 3e - 3)$. With a control group, it takes $6 \times 7 = 42$ tests.

The results are not consistently favorable due to the delicate nature of convergence. It proves challenging to adjust the parameters in a manner that enhances stability and addresses the oscillation issue, even when employing a small PID controller.

Nevertheless, a complete comparison at $\Delta\gamma_p = 1.5 \times 10^{-3}$ for decreasing mean stress scheme is possible as shown below in fig 3.18. The two types of control result in the same variation in both mean strain and $\Delta\tau$. However, time control shows more oscillations in iterations which indicates lower computational stability. This conclusion will be confirmed in other results as well.

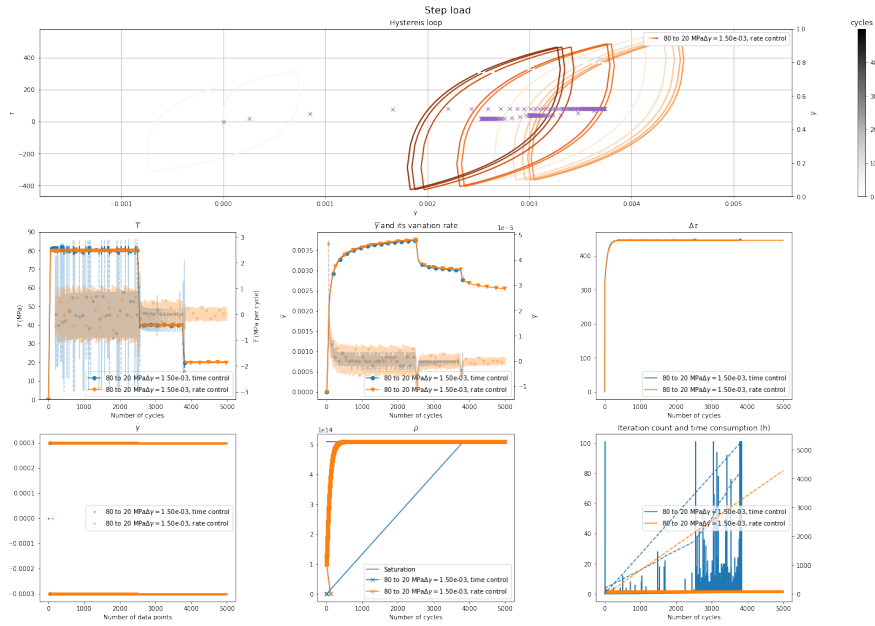


Figure 3.18: Material response comparative results for different time control and rate control procedures for $\Delta\gamma_p = 1.5 \times 10^{-3}$ and downstep loading conditions

All cases for increasing mean stress scheme failed to converge in time control. Severe oscillation problems are found from the early stages of the simulation which lead to the failure of the simulation. The rate control, however, shows a good convergence and the results are shown in fig 3.19.

Comparison for different applied plastic shear strain range

In the downstep loading scheme, experimental results show that the ratcheting strain will not decrease even if we decrease the applied mean stress, as shown in figure 3.20. However, in the simulation results, the ratcheting strain will decrease.

This phenomenon indicates that when mean stress decreases, in Eq. (3.3), mean γ_s should follow and increase. When mean stress decreases, to maintain a constant mean strain γ_s should increase with the same quantity as the original mean strain. Mathematically, this is not easy to achieve because the

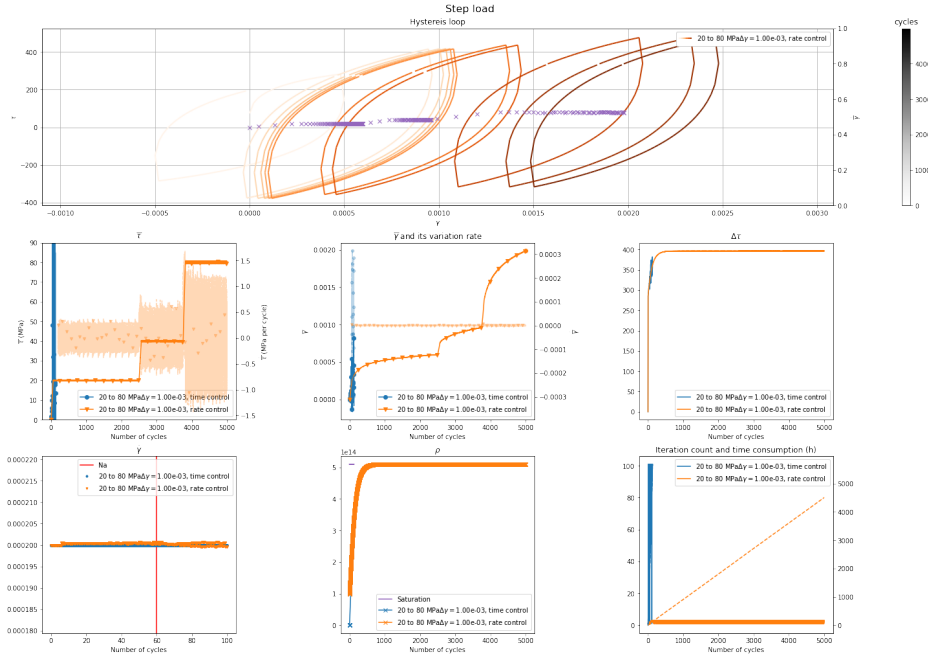


Figure 3.19: Material response comparative results for different time control and rate control procedures for $\Delta\gamma_p = 1.0 \times 10^{-3}$ and upstep loading conditions

equation is not cycle-wide, which means it is explicitly mean-stress dependent.

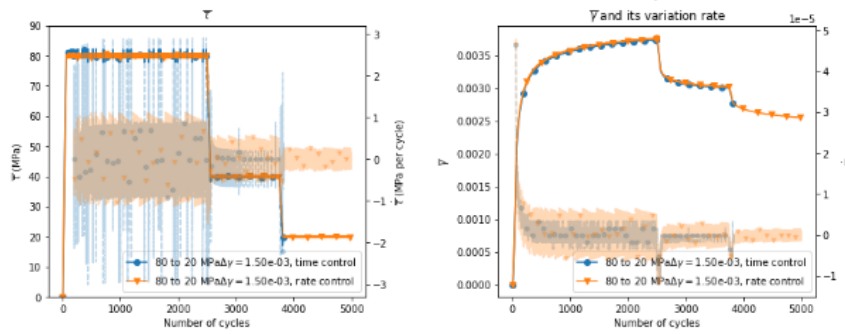
$$\frac{\dot{\gamma}}{\dot{\gamma}_0} = \sum_{j=0}^M f^i(s_j) \left| \frac{\tau - MG(\gamma_{s_j}^i - \gamma)}{s_j} \right|^{1/m} \text{sign}(\tau - MG(\gamma_{s_j}^i - \gamma)) \quad (3.11)$$

In the upstep scheme, the simulation results are quite consistent with their experimental counterparts.

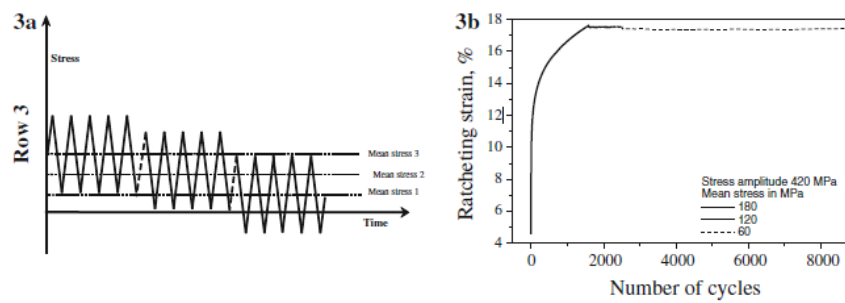
3.4.4 . Calibration of the ratcheting model

Upon analyzing the impacts of various parameters, we shall now explain how our model can be calibrated to achieve a given, experimentally informed outcome, using a given load-control procedure. Precise ratcheting experiments were conducted in 2010 on 304L stainless steel, a material that exhibits nearly identical fatigue performance to 316 stainless steel. The experimental protocol consisted of plastic strain-controlled tests, maintaining a constant plastic strain amplitude of 10^{-3} and a mean stress of 50 MPa .

To facilitate the manual calibration process, some characteristic values are defined for easier comparison. They are the stress range, the ratcheting strain rate at the initiation stage of ratcheting and the ratcheting rate at the stabilized stage of ratcheting. At the reference load ($\bar{\sigma} = 50 \text{ MPa}$, $\Delta\epsilon_p = 10^{-3}$), the desired values are:



(a) Comparative simulation results for downstep loading conditions



(b) Experimental results for downstep loading conditions [113]

Figure 3.20: Comparative simulation results for downstep loading

- $\Delta\tau = 500 \text{ MPa}$
- $\dot{\gamma}_p = 5 \times 10^{-7} / \text{cycle}$ at $N = 110(160) \text{ cycles}$
- $\dot{\gamma}_p = 2.5 \times 10^{-8} / \text{cycle}$ at $N = 40000 - 50000 \text{ cycles}$

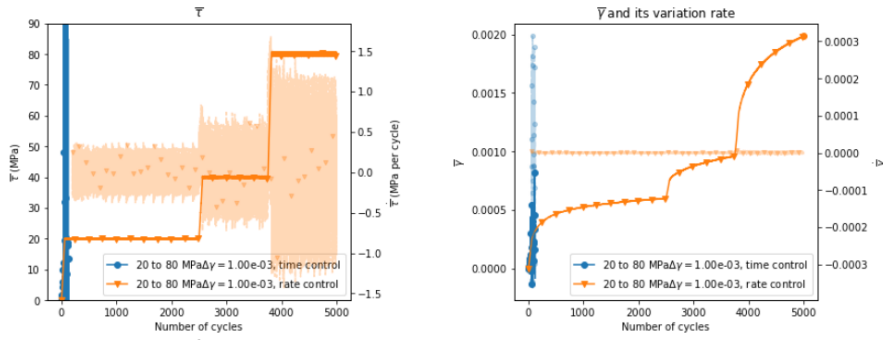
We shall evaluate the optimal model parameters using simulations up to $N = 10000$.

- $\dot{\gamma}_p = 4 - 5 \times 10^{-8} / \text{cycle}$ at $N = 10000 \text{ cycles}$

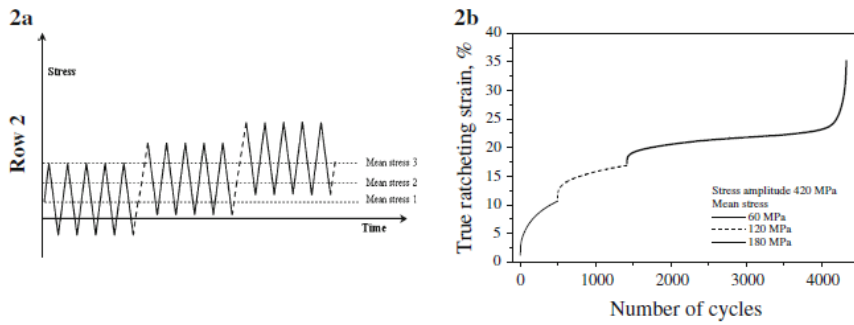
The default number of cycles to apply the mean stress is $N_a = 50$, the cycle number (110) to calibrate should be adjusted accordingly (160). Careful comparison at the first 100 cycles shows that with the sigmoid function, a proper adjustment is to put the initial cycle of experimental data at $N = 25$.

Calculation of the ratcheting rate

Before computing the ratcheting rate, a specific load control procedure is implemented in an attempt to minimize the computational instabilities and obtain an average ratcheting strain response. This load control procedure involves convolving the ratcheting strain data with a basic kernel, specifically



(a) Simulation results for upstep loading scheme



(b) Experimental results for upstep loading scheme[113]

Figure 3.21: Comparative material response for upstep loading conditions

$\frac{1}{N_{con}}$, where N_{con} represents the convolution cycle number, set to 50 for simplicity. This convolution is executed using the *convolve* function from the *scipy* library. Following this, the ratcheting rate is determined by calculating the gradient of the smoothed ratcheting strain.

It is worth noting that in formal application of the model, this calibration process will not include so many parameters. The DD simulation after proper post-processing will provide the value for the parameters concerning the distribution of dipoles (including λ , α , τ_0). The parameters $\dot{\gamma}_0$ and m are constants. The only parameter that should be calibrated is the parameter M whose correlation with the material properties (or the output of simulation) is not well-known.

However, in this research, due to the lack of DD simulation results, we have to calibrate all the parameters including the distribution of dipoles. From [27] we have the data for copper but for stainless steel the values are very different.

Calibration results

After several manual attempts, the following parameters are chosen:

- $\dot{\gamma}_0 = 10^{-10} \text{ s}^{-1}$
- $M = 2.0$ (comparison parameter in the following figure)
- $\lambda = 0.5$
- $\alpha = 0.3$
- $m = \frac{1}{20}$
- $\tau_0 = 50 \text{ MPa}$

This set of parameters yields the following results:

Manual parameter tuning is limited in precision (c.f. Fig. 3.23) and highlights the need for a better calibration method. In the following section, we will introduce a machine-learning calibration procedure to address this issue.

Machine learning calibration procedure

Machine learning (ML) is a subset of artificial intelligence (AI) that involves the use of algorithms and statistical models to enable computers to perform tasks without explicit instructions. By learning from and making predictions based on data, ML can identify patterns, make decisions, and improve over time. ML

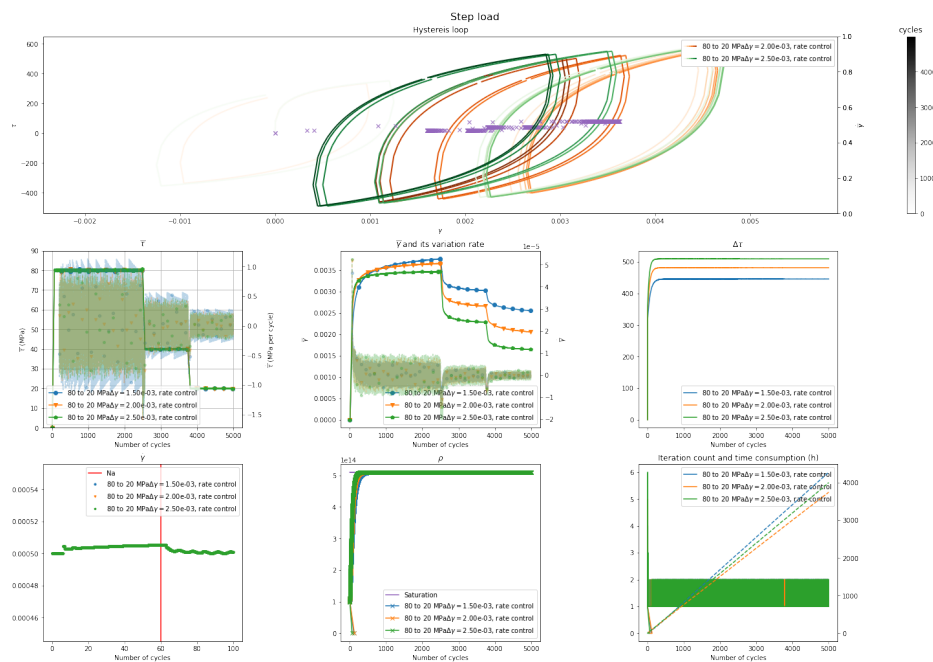


Figure 3.22: Material response comparative results for different $\Delta\gamma_p$ loading levels

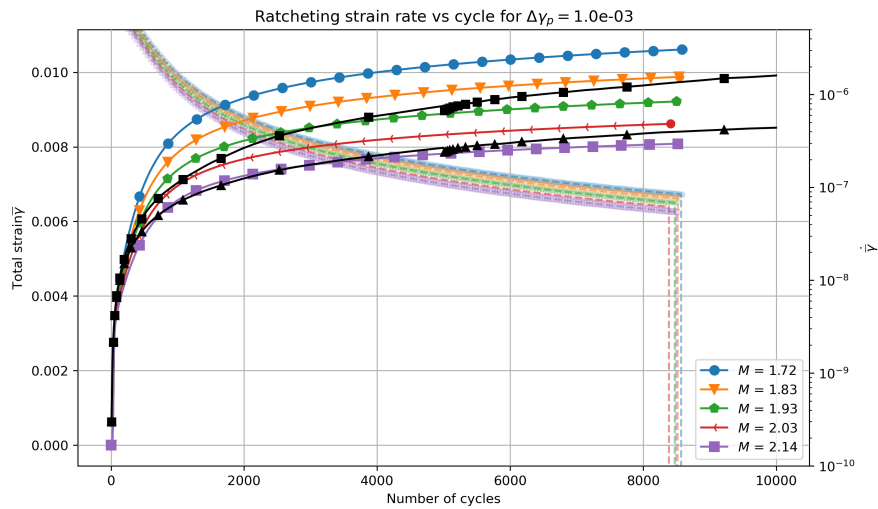


Figure 3.23: Ratcheting model results obtained with different sets of simulation parameters (M)

encompasses a variety of techniques, including supervised learning, unsupervised learning, and reinforcement learning, each suited to different types of tasks and data structures.

One of the significant applications of machine learning is in the determination and calibration of parameters in physical models. Traditionally, this calibration process can be labor-intensive and computationally expensive, relying on expert knowledge and iterative experimentation like what is done in the previous subsection. Machine learning offers an alternative approach that can streamline the calibration process, reduce the labor burden, and potentially improve the accuracy of the model.

Machine learning offers an efficient and automated approach to parameter calibration by leveraging large datasets and advanced algorithms. ML models can *learn* the complex relationships between input parameters and observed outcomes, providing more accurate and quicker calibration than traditional methods. This approach can significantly enhance the precision and efficiency of physical models in various fields, such as climate modeling, structural engineering, and fluid dynamics such as in the present case.

To implement this calibration procedure, we initially formulated the whole issue as a minimization problem. This includes the definition of an objective function that quantifies the discrepancy between the simulation and experimental results. The determination of several weight factors to prioritize the importance of different results of simulation, etc.

Then we performed a set of simulations to prepare the data for the machine learning model, by selecting representative parameters and running the model for a range of input values. Using the objective function, a dataset of

parameters-error pairs was generated, which was then used to train the machine learning model. The model can thus learn the relationship between the input parameters and the error, enabling it to predict the optimal parameters for the desired outcome.

The details of the algorithm and methods will be given and detailed in annex Section 6.2. The result of this calibration method is:

- $\dot{\gamma}_0 = 8.9 \times 10^{-10} \text{ s}^{-1}$
- $M = 3.5$
- $\rho_0 = 2.9 \times 10^{13} \text{ m}^{-3}$
- $\lambda = 0.38$
- $\alpha = 0.18$
- $\tau_0 = 29 \text{ MPa}$

3.4.5 . Cyclic stress-strain results

Since the output of the model includes the hysteresis loops, the stress range during each cycle naturally emerges as an output of the model. It is feasible to compare the defined stress range, which is the stabilized difference ($\tau_{max} - \tau_{min}$), with experimental data. This comparison is illustrated in Fig. 3.24. The model itself does not inherently conceptualize the stress or strain range and works for a broad range of applied loading levels.

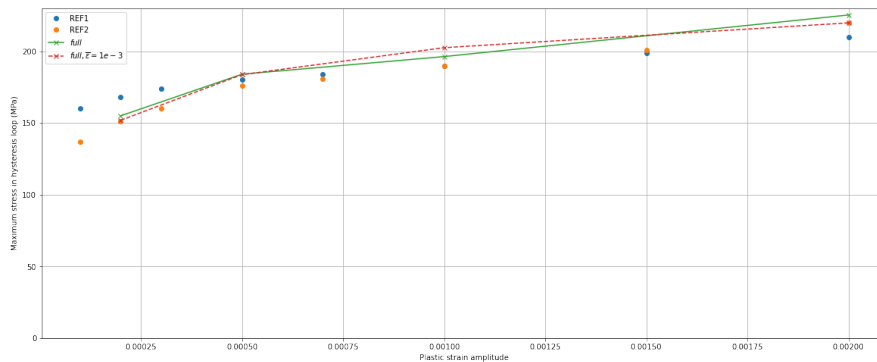


Figure 3.24: The cyclic stress-strain curve, comparison with the experimental results.

3.4.6 . Representative ratcheting rate (*Abacus*)

The representative ratcheting rate, a concept that will be utilized in subsequent chapters for the study of fatigue crack initiation, is a measure indicative of the ratcheting rate at a specific cycle number. It is characterized as the maximum average ratcheting rate observed during the simulation, which typically

occurs at the beginning of the fatigue lifetime. This value is crucial as it provides a benchmark for the ratcheting effect on the crack initiation process.

To thoroughly examine the distribution of the representative ratcheting rate, a graphical representation, or *abacus*, is employed. This is constructed by plotting the plastic strain range on the x-axis against the maximum average ratcheting strain rate on the y-axis presented in figure 3.25.

The rationale behind selecting the maximum average ratcheting strain rate as a significant metric is predicated on the understanding that ratcheting exerts a notable "history" effect on crack initiation, implying that the maximum damage is most significant and should be taken into account. Such a history effect can also be observed in the downstep loading scenario in Section 3.4.3 where accelerated damage accumulation persists long after the load level is decreased. Typically, the ratcheting rate diminishes considerably after the initiation stage, failing to adequately account for the substantial changes observed during the crack initiation process.

From an industrial perspective, the proposed *abacus* serves as a valuable tool for estimating the impact of ratcheting on crack initiation for specific materials under various loading conditions.

3.5 . Conclusions

In this chapter, a comprehensive model has been developed and evaluated to simulate the ratcheting effect under diverse loading conditions. The model amalgamates results from Discrete Dislocation Dynamics simulations, providing an intricate prediction of localized strain and stress through the cycle-by-cycle simulation of hysteresis loops, and incorporates the kinematic hardening phenomena characteristic of the material. Dubbed the "general model," it generates a wealth of data pertinent to the fatigue process and will supply crucial insights for the study of fatigue crack initiation in the subsequent chapter, particularly in the context of the ratcheting effect.

Extensive validation efforts have been undertaken to ascertain the model's predictive accuracy across various scenarios, including mean strain applications, mean stress conditions, and step loading. These evaluations have underscored a specific limitation in the model's capability to forecast changes in the cyclic stress-strain curve influenced by mean stress, pointing to a potential area for enhancement in future investigations.

The calibration of the model, achieved through both manual techniques and machine learning methods to fine-tune parameter estimates based on empirical data, has demonstrated a favorable alignment with experimental results. Despite this success, challenges persist in attaining optimal variation rates of the ratcheting strain, though the resultant ratcheting strain curve has aligned with experimental data more accurately than initially expected. In

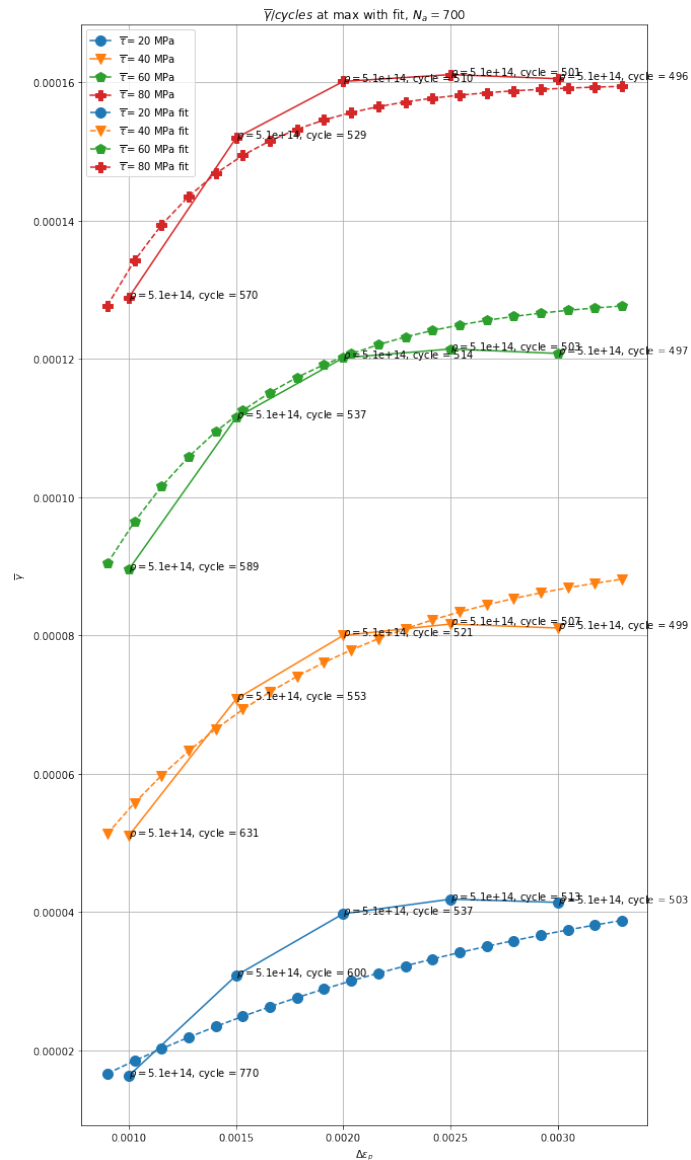


Figure 3.25: Abaqe figure

addition, one phenomenon that the model does not yet accurately predict is the alteration in the cyclic stress-strain curve resulting from the application of mean stress. Addressing this limitation remains a subject for future research.

In the forthcoming chapter, the focus will shift to introducing the crack initiation model, which will leverage the representative ratcheting rate derived from the current chapter's findings. This model will be applied to actual fatigue lifetime prediction processes.

Key findings:

- A general fatigue mechanical behavior model is implemented based on previous research using DDD simulation [27]. The model takes the plastic shear strain rate as input and outputs the stress at each time step and thus the hysteresis loop, stress range, ratcheting strain rate, etc. information.
- The model can predict the material's behavior under various loading conditions, including mean strain, mean stress, and step loading.
- After calibration on the five key parameters in the model, the ratcheting rate, as well as the stress range, match excellently with the experimental results.

4 - Crack initiation model in HCF loading conditions

The objective of this chapter is to develop a model for predicting micro-crack initiation under high-cycle fatigue (HCF) conditions. The model is based on the concept of persistent slip markings (PSMs) and extrusions, which are precursors to fatigue crack initiation in crystalline materials. The predicted number of cycles to crack initiation is based on the evolution of PSMs and extrusions during the fatigue process. The extrusion growth is described using a physically-based approach which equates micro-crack initiation with the realization of a critical extrusion size, in a given grain.

To suit industrial application cases, the model incorporates the results from the previous chapter to account for the effect of ratcheting phenomena on the crack initiation process. The ratcheting effect has long been known to significantly shorten fatigue lifetime as it promotes surface extrusion growth, which critically influences the number of cycles to micro-crack initiation.

The model is validated using various experimental data under diverse loading conditions. It is validated not only for the final number of cycles to crack initiation but also for intermediate parameters, such as slip band thickness and spacing.

4.1 . Micro-crack initiation: general ideas and concepts

The quest for engineering materials capable of withstanding extreme conditions in nuclear and aerospace domains underscores the critical importance of understanding fatigue crack initiation. Particularly in the context of fusion energy which is the industrial basis of this study, the integrity of materials is essential, not just for operational efficiency but for safety. Fatigue crack initiation thus represents a fundamental concern.

A critical gap in the current understanding of fatigue crack initiation is the absence of a comprehensive, physically-based model that can accurately predict the initiation and early growth of cracks under diverse operating conditions. Existing models often rely on empirical data and phenomenological approaches, which, while useful, lack the universality and predictive power needed for the broad range of materials and conditions encountered in nuclear fusion and aerospace applications. This gap not only hinders the development of more resilient materials but also limits the ability to predict and extend the lifespan of critical components.

By integrating the previous DD simulation research with the newly developed model and experimental data, our goal in this work is to understand the

microscopic mechanisms controlling micro-crack initiation and subsequent crack growth.

The structure of this chapter will be as follows:

1. **Literature review of existing crack initiation models:** This section will provide an overview of the current state of research on fatigue crack initiation in crystalline metallic materials. It will summarize the key findings and models proposed by previous studies and highlight the gaps and limitations of the existing approaches and concepts.
2. **Proposed crack initiation scheme and equations:** This section will introduce a new model for fatigue crack initiation based on the latest research in material science and computational modeling. It will present the theoretical framework, equations, and assumptions underlying the proposed model.
3. **Estimation of the number of slip bands:** This section will describe the submodel for estimating the number of slip bands in the proposed model. It will explain the theoretical basis for this estimation and provide a step-by-step guide to calculating this important intermediate parameter. The results of the estimation will be validated against experimental data.
4. **Estimation of the extrusion width:** Similar to the band number submodel, another equation will be proposed to estimate the width of the slip bands. The results will also be validated using experimental data.
5. **Results and discussion:** This section will present the results of the model validation and discuss the implications of the findings. It will compare the model predictions with experimental data and highlight the strengths and limitations of the proposed model.
6. **Conclusion:** This section will summarize the key findings of the study, discuss the implications for future research, and propose recommendations for further development of the model.

4.2 . Literature review of existing crack initiation models

Crack initiation in crystalline materials is a complex process influenced by multiple factors, including material properties, microstructure, loading conditions, and environment. The study of this phenomenon began about 100 years ago when it was discovered that cyclic loading could lead to the formation of surface relief [7] through optical microscopy. The inhomogeneous distribution of this surface damage was identified as a precursor to crack initiation. The concept of persistent slip bands (PSBs) was subsequently proposed,

revealing that cracks initiate along the border or within the PSBs [8, 9] (see Fig. 4.1). The localization of strain in PSBs is now accepted as a fundamental feature representing the initial signs of fatigue damage. The sharp surface markings, termed persistent slip markings (PSMs), develop at emerging PSBs and become the crack initiation sites [114, 42, 115, 64]. The PSMs consist of intrusions and extrusions, which have been identified both in experiments [43] and simulations (enabled by advancements in computational power and dislocation dynamics theories) [16, 26].

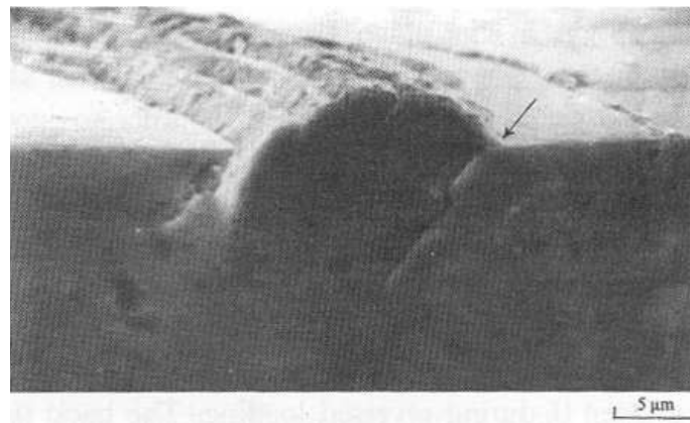


Figure 4.1: Initiation of a crack along a PSB [9]

There is no universally accepted model that dominates the crack initiation mechanisms, although the concentration of dislocations inside PSBs is considered to be a possible cause. Other causes, such as point defect accumulation, are considered by a few authors [116, 117]. In fact, the mechanisms of crack initiation vary under different environmental and loading conditions, as well as for different materials, and can generally not be described based on a single mechanism (or model). For example, temperature can be an important factor in determining whether point defects contribute to crack initiation [117].

In this study, grade 300 stainless steel was chosen as the target material, focusing on uniaxial fatigue conditions with a fixed plastic strain load, consistent with the previous fatigue crack propagation model. The initiation of fatigue cracks in this material has been extensively studied by various researchers [43], and comprehensive experimental observations of surface relief evolution can be found in [45, 44, 46].

Several early models were proposed for crack initiation in metals, notably the studies of Mura and Tanaka [90, 118, 119]. These models are energy-based and involve corresponding dislocation mechanisms. In these models, the definition of initiation is the critical number of cycles N_0 at which the free energy is maximized, leading to mechanical instability and subsequent micro-

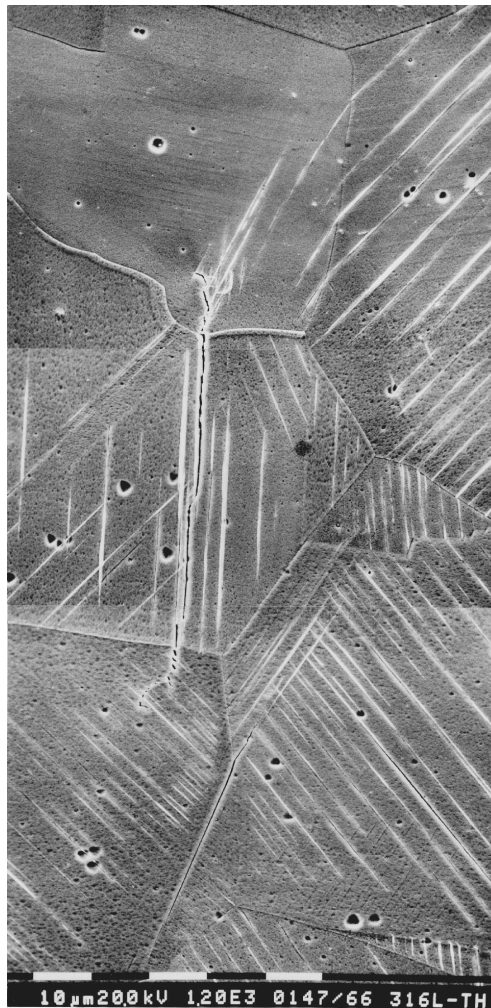


Figure 4.2: Surface relief with cracks initiated along PSBs in a specimen cycled with $\Delta\epsilon_p = 10^{-3}$ and $N = 20\%N_f$ [43]. Loading axis is horizontal

crack initiation. By estimating an expression for the Gibbs free energy, the critical number of cycles can be calculated using its derivative. However, due to the limitations of experimental techniques and computational power at that time, these models could not be fully validated either experimentally or numerically. A recent extension of these models to the variable amplitude loading cases can be found in [120].

A detailed review of newer models can be found in [121] where detailed information on existing fatigue crack initiation models is provided along with their theoretical basis and experimental background. The microstructure models of crack initiation have been divided into two categories: micromechanical models and crystal plasticity models. They use multiple different simulation methods (Monte-Carlo [122] or finite element-crystal plasticity (FE-CP)

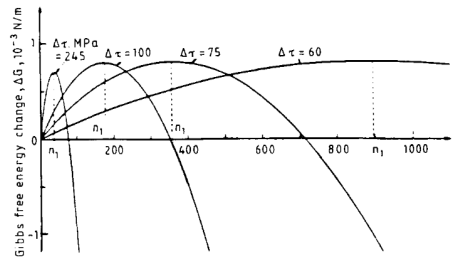


Fig. 8. Variation in the Gibbs free energy change ΔG with the number of loading cycles showing that the maximum point is retarded by the decrease in the applied stress range $\Delta \tau$.

Figure 4.3: The Gibbs free energy as a function of the number of cycles

[123]).

In this study, the crack initiation scheme characterized by the extrusion growth of the surface relief is favored [124, 125, 32]. This approach is pragmatic, and well supported by observations and recent advances in computational modeling. The observation of the surface relief of the material, along with quantitative measurements of the extrusions and intrusions, has enabled experimental validation of the model. In the next subsection, these observations will be presented.

Description of the surface relief evolution in fatigued stainless steel

As mentioned in the previous section, it is crucial to understand the changes occurring on the material's surface during the fatigue process in order to correctly predict the micro-crack initiation time (or number of cycles). However, this study heavily relies on experimental observations. Using optical microscopy, surface relief is only observable as an inhomogeneous distribution of markers indicative of fatigue damage. With the development of atomic force microscopy (AFM), surface relief can now be observed at high resolution and in real space.

In this subsection, the most recent experimental results regarding the surface relief of fatigued stainless steel will be presented in chronological order. It should be noted that, in the original papers, the load value is typically provided in terms of total strain amplitude. However, for the sake of consistency with our study, all values have been converted to the plastic strain range.

In 2003, constant plastic strain controlled fatigue tests were performed on polycrystalline 316L stainless steel [44]. The characteristics of the PSMs and extrusions were studied by AFM. The plastic strain range in this study is $\Delta \epsilon_p = 4.0 \times 10^{-3}$. The AFM micrographs obtained can be found in Fig. 4.4.

This study found that during most of the fatigue life, the extrusion height

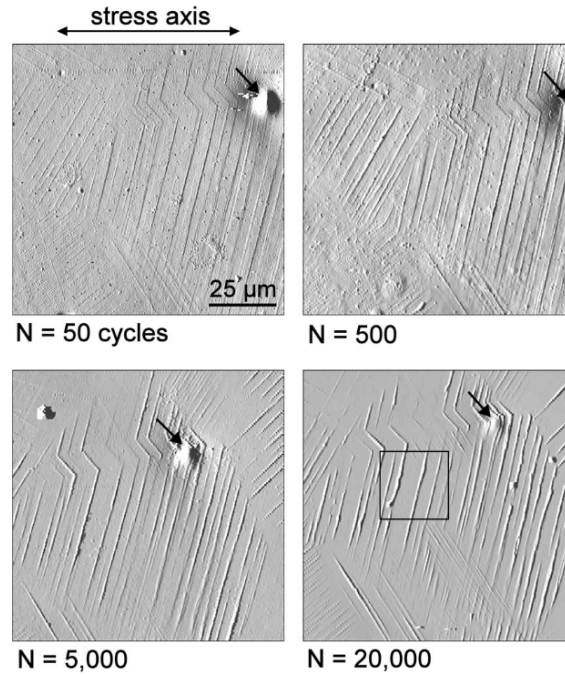


Figure 4.4: AFM micrographs of the surface relief with a grain of 316L steel cycled with constant plastic strain range $\Delta\epsilon_p = 4.0 \times 10^{-3}$ for different numbers of cycles. The scale of all micrographs is identical. [44]

varies linearly with the number of cycles (about 0.025 nm/cycle for $\Delta\epsilon_p = 4.0 \times 10^{-3}$, see Fig. 4.5). However, the figure also shows a non-linear increment at the beginning of cycles which supports the modeling results presented in the next section.

In 2013, a study examining the surface relief shape of 316L stainless steel was conducted, utilizing scanning electron microscopy (SEM) and focused ion beam (FIB) techniques [39]. The primary objective of this investigation was to determine the presence of intrusions, which were challenging to observe and had been a topic of debate. The load type in this study was a total strain range with a value of $\Delta\epsilon = 5 \times 10^{-3}$. The converted plastic strain range was $\Delta\epsilon_p = 3.1 \times 10^{-3}$, while the measured value reported in the paper was $\Delta\epsilon_p = 2.8 \times 10^{-3}$. An image of the surface relief captured by SEM is shown in Fig. 4.6. The width of the extrusion identified at this early stage of fatigue varied from $e_B = 0.5 \mu\text{m}$ to $e_B = 1.0 \mu\text{m}$.

These experimental studies focused on surface relief observations, leading to several important conclusions:

1. Fatigue induces surface relief deformations on the material's surface, rapidly forming lines of concentration identified as persistent slip markings (PSMs).

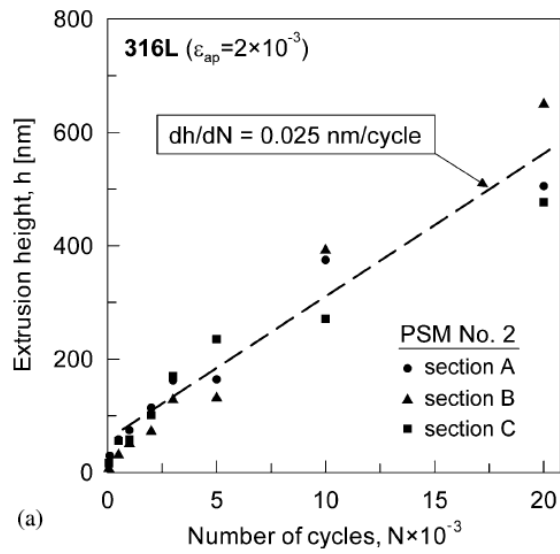


Figure 4.5: Extrusion height h vs. number of cycles N for 316L steel cycled with constant plastic strain range $\Delta\epsilon_p = 4.0 \times 10^{-3}$. Linear increment is found during most of the fatigue life but decreasing increment speed can be identified at the first cycles.

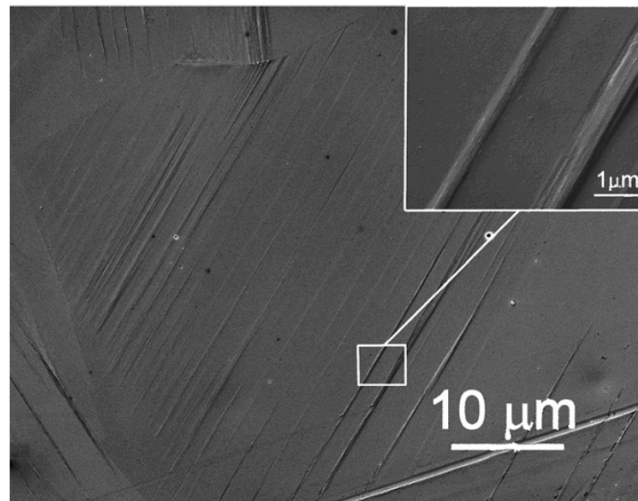


Figure 4.6: Characteristic surface relief of the grain with parallel PSMs (316L steel cycled with total strain range $\Delta\epsilon = 5 \times 10^{-3}$ for 500 cycles) from [39]

2. The PSMs are characterized by both extrusions and intrusions (for volume conservation). The height and width of the extrusions are related to loading conditions, while the intrusions remain challenging to observe.

3. Crack initiation occurs along the intrusions, but the criteria for initiation are still unclear.

In 1987, Polák proposed a crack initiation scenario involving the transport of point defects [116]. This scenario effectively explains crack initiation at higher loads and accurately predicts the observations obtained in subsequent studies [45, 44].

However, Cretegnny et al. and Risbet et al. introduced a new criterion for crack initiation based on surface deformation [124, 125], which aligns more closely with the outcomes of dislocation dynamics (DD) simulations discussed in Section 1.5. Another crack nucleation scenario, which involves nucleation along grain boundaries, will not be addressed in this study (we assume that it typically occurs at high load amplitudes where crack initiation does not constitute a significant portion of the fatigue lifetime).

Depres et al. [16, 26, 32] proposed a crack initiation scheme entirely based on dislocation-induced irreversibility. For details of these studies, refer to Section 1.5.2. Thanks to the additional DD simulations, the crack initiation mechanism is described in much more detail. This crack initiation scenario will be explained in the next section.

4.3 . Proposed crack initiation scenario and corresponding governing equations

Different researchers have proposed a basic framework for a new crack initiation scheme grounded in the theory of dislocations (c.f. Section 1.5). Investigation of persistent slip bands (PSBs) and persistent slip markings (PSMs) evolutions can be found in [16, 26]. Building on these studies, a comprehensive crack initiation scenario is proposed hereinafter.

Initially, during the first cycles of fatigue, PSMs form on the surface of the material, as observed in experiments (refer to the previous section) and in simulations (refer to Fig. 4.7). These PSMs then develop into extrusions and intrusions, with their height and depth increasing with the number of fatigue cycles (as shown in Fig. 4.5).

During this process, elastic energy and stress concentration accumulate inside the intrusions. This energy accumulation is concurrent with irreversible slip accumulation in the grain surface, which is characterized by quantity γ_{surf} , which is defined as the total length per unit area of the plastic steps left on the free surface and projected along the surface normal vector. This projection accounts for the extrusions that are typically not perpendicular to the surface due to the grain's crystallographic orientation.

Crack initiation occurs when critical distortion elastic energy and stress concentration coincide, as depicted in Fig. 4.8 (rightmost snapshot). This can be characterized by the extrusion height h , which is easier to interpret than

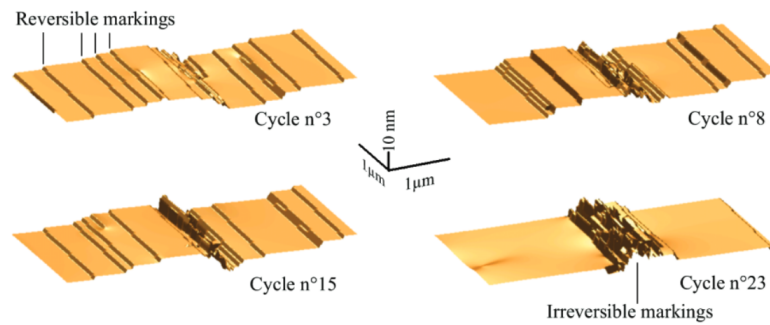


Figure 4.7: Surface slip marking evolution during the first 20 cycles of simulation. [26]

γ_{surf} quantity. The extrusion height is defined as the distance between the tip of the extrusion and the material's surface. The extrusion height is equivalent to surface deformation, with the conversion method provided in equation 1 of [26].

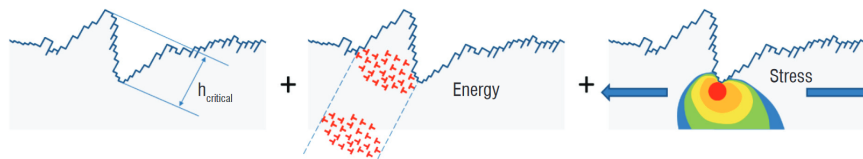


Figure 4.8: Schematic description of the crack initiation scenario. The threshold condition is reached when the elastic energy (associated to the multipoles) and the stress concentration (related to the extrusion shape) coincide. [32]

The choice of extrusion height as the final criterion is justified for several reasons. Firstly, it is the simplest quantity that can be directly compared with experimental observations. Additionally, using extrusion height as a criterion eliminates dependence on grain size. Moreover, as cited in [124], reaching a critical surface deformation does not always guarantee crack initiation. This situation is accounted for by calculating an average extrusion height. For 316L stainless steel at room temperature, the critical extrusion height is estimated to be $h_{crit} = 250 \text{ nm}$.

In the simulations, the extrusion height and width for different slip bands are typically uniform (at the single grain scale). However, in actual experimental observations, slight deviations always exist (see Fig. 4.9). The spacing between the slip bands is not strictly uniform either. In the model, it is assumed, as observed in the simulations, that the slip bands are uniformly distributed and that the extrusion height and width are consistent across all slip bands.

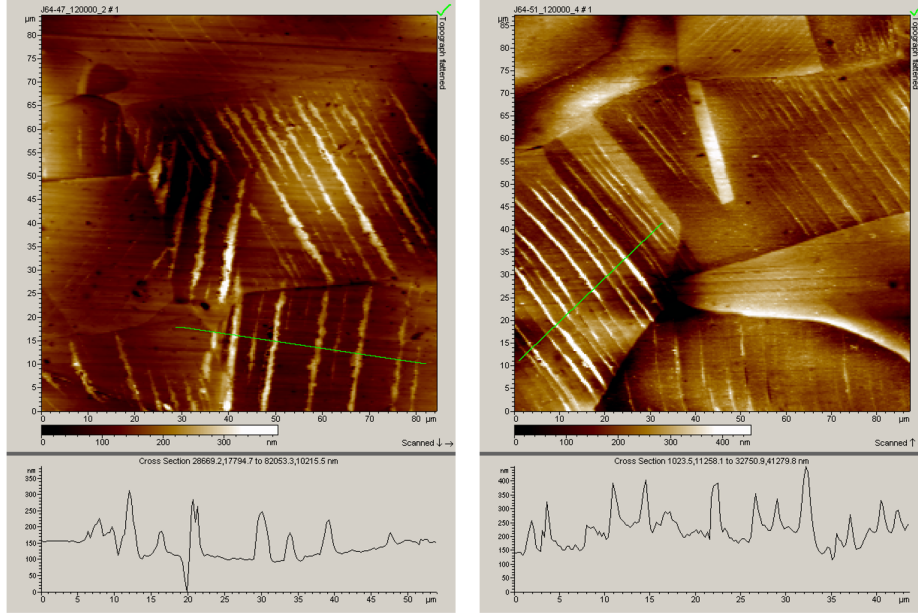


Figure 4.9: Extrusion height as obtained from AFM measurements of the slip bands. CEA (unpublished results)

The first version of the crack initiation equation is defined in [32] as:

$$\gamma_{surf}(N) = K \frac{h_g}{D_g} \Delta\epsilon_p \left(1 + 2 \frac{|\bar{\epsilon}|}{\Delta\epsilon_p}\right) \sqrt{N} \quad (4.1)$$

where K is a constant, h_g is the grain height, D_g is the grain size, $\Delta\epsilon_p$ is the plastic strain range, $\bar{\epsilon}$ is the mean strain, and N is the number of cycles.

This equation characterizes an extrusion height that grows with the square root of the number of cycles, which typically holds true at the beginning of the fatigue stage before crack initiation. After crack initiation, the extrusion height grows linearly with the number of cycles, as depicted in Fig. 4.5.

Despite the initial utility of this equation, it has been found to have multiple issues during the recent development of the crack initiation model. Firstly, the grain height is a parameter that is difficult to measure. Additionally, the mean strain introduced in this equation has been shown to inadequately predict the ratcheting effect. Lastly, the equation lacks a parameter for the number of slip bands, which has later been found to be crucial for estimating the extrusion height. A new equation is proposed in this study to address these problems:

$$\gamma_{surf} = k D_g \frac{\Delta\epsilon_p}{n_B} \left(1 + 2 \frac{\bar{\gamma}_p}{N} \Big|_{sat}\right) \sqrt{N} \quad (4.2)$$

where k is still a constant, n_B is the number of slip bands, $\frac{\bar{\gamma}_p}{N} \Big|_{sat}$ is the representative ratcheting rate obtained in the previous chapter. The conversion

between the extrusion height h and the surface deformation γ_{surf} is given by: $\gamma_{surf} = \frac{h}{e_B}$ where small e_B is the width of the slip bands (which is supposed to be uniform [126]). This leads to the final equation to estimate the number of cycles to crack initiation:

$$\frac{h}{e_B} = kD_g \frac{\Delta\epsilon_p}{n_B} \left(1 + 2 \frac{\overline{\gamma_p}|_{sat}}{\Delta\epsilon_p} \right) \sqrt{N} \quad (4.3)$$

and then:

$$N_{ini} = \frac{h_{crit} n_B}{e_B k D_g \Delta\epsilon_p \left(1 + 2 \frac{\overline{\gamma_p}|_{sat}}{\Delta\epsilon_p} \right)}^2 \quad (4.4)$$

In the following sections, the method for calculating all the intermediate parameters in this equation will be provided. This presentation includes the approach for estimating the number of slip bands n_B and the width of the slip bands e_B . After determining the values for the parameters under different load conditions, the number of cycles to crack initiation can be directly calculated using Eq. (4.4).

It is worth noting that the effect of a mean stress, which is a critical factor in the development of this model, is introduced into the model through the representative ratcheting rate $\overline{\gamma_p}|_{sat}$ and changes in the cyclic stress-strain relation. The influence of mean stress is highly significant, as will be demonstrated in Section 4.6.

4.4 . Estimation of the number of slip bands (in single grains)

The initial studies on the number of slip bands were conducted by Depres in [26], where detailed information about the simulations and the formulation of the equations was provided comprehensively. However, during the subsequent application of these results, the equations have been utilized and simplified in various other contexts [127, 128]. In this study, the version from [127] is employed.

The fundamental concept behind calculating the number of slip bands is the equilibrium of the stress generated by the slip bands and the overall stress field acting on each slip band. Initially, during the first dislocation dynamics (DD) simulations, the shear stress field generated by a single slip band (denoted as τ_i) is given by [25] (see Fig. 4.10):

$$\tau_i = -\tau_{app} \exp\left(-k_B \frac{|x|}{l}\right) \quad (4.5)$$

where τ_{app} is the applied shear stress, k_B is a constant, x , z are coordinates of the measurement point for the stress as shown in Fig. 4.10, l is the length of the slip band.

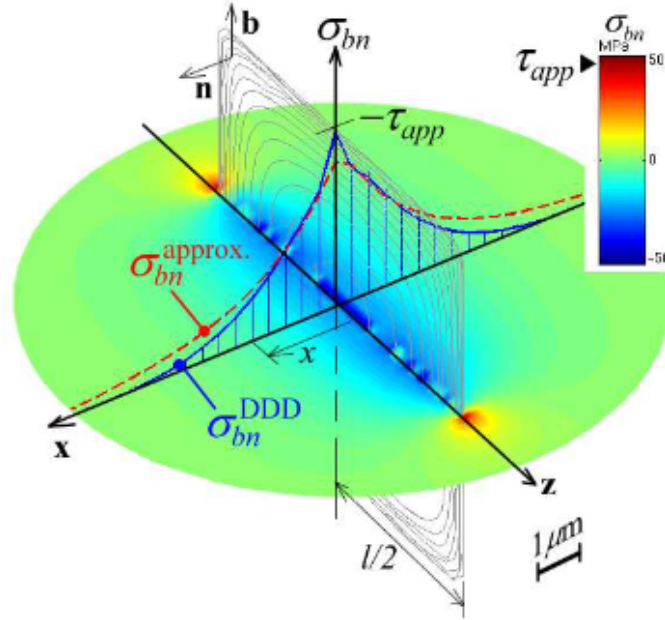


Figure 4.10: Stress field generated by a single pile up. The stress field of a slip band is in similar shape based on the superposition of the stress field of each slip band. [25]

Using Eq. (4.5), the stress of one slip band i to another slip band j is given by:

$$\Delta\tau_{j \rightarrow i} = -\Delta\tau_j \exp\left(-k_B \frac{|j-i|\lambda}{l}\right) \quad (4.6)$$

where $|j-i|\lambda$ is the distance between the two slip bands and λ is the distance between slip bands (which is supposed to be constant for different bands). This forms the first part of the system of equations.

The second part is the back stress of every slip band, which can be expressed as [129, 18]:

$$\Delta\tau_{app} = \frac{1}{S} \frac{\mu}{1-\nu} \gamma \quad (4.7)$$

The parameters in this equation are the same as in the previous chapters.

The last part is the self line tension of the slip band which is given by:

$$\Delta\tau_{LT_i} = 2 \frac{\mu b}{D_g} \quad (4.8)$$

This leads to the final system of equations:

$$\Delta\tau_{app} + \sum_{j=1}^{n_B} \Delta\tau_{j \rightarrow i} + \Delta\tau_{LT_i} = 0 \quad (4.9)$$

This system is linear and its matrix form is: (let $E_{ij} = \Delta\tau_{j \rightarrow i}$, $Y_0 = -\Delta\tau_{app} - \Delta\tau_{LT}$)

$$\begin{bmatrix} 1 & E_{1j} \\ & \ddots \\ E_{ij} & 1 \end{bmatrix} \begin{bmatrix} \Delta\tau_1 \\ \vdots \\ \Delta\tau_{n_B} \end{bmatrix} = \begin{bmatrix} Y_0 \\ \vdots \\ Y_0 \end{bmatrix} \quad (4.10)$$

or simpler:

$$[E_{ij}][\Delta\tau_i] = [Y_i] \quad (4.11)$$

4.4.1 . Analytical solution of the system

Before the solution of the system, a simple simplification can be done for the line tension, as general the line tension is very much inferior to the applied stress. It can be directly omitted in the system.

The solution is straightforward and can be done manually when $n_B = 2$.

- Equation: $\Delta\tau_1 + \Delta\tau_2 \exp(-k \frac{\lambda}{D_g}) = \Delta\tau_{app}$ and exchange 1 and 2.
- Solution: $\Delta\tau_1 = \Delta\tau_2 = \frac{1}{1 + \exp(-k \frac{\lambda}{D_g})} \Delta\tau_{app}$

And we'll have:

$$\Delta\tau_1 + \Delta\tau_2 \exp(-k \frac{\lambda}{D_g}) = \frac{1}{1 + \exp(-k \frac{\lambda}{D_g})} \Delta\tau_{app} + \frac{1}{1 + \exp(-k \frac{\lambda}{D_g})} \exp(-k \frac{\lambda}{D_g}) \Delta\tau_{app} \quad (4.12)$$

$$= \Delta\tau_{app} \quad (4.13)$$

The solution of the system when $n_B > 2$ is not straightforward. But it can be done with the help of Wolfram Alpha. However, Wolfram Alpha can only solve the system with a fixed number of n_B . So we decide to try to solve for different number of slip bands and then try to find a pattern.

The code used is:

```

1  n = 2; (*set the number of dimension*)
2  k = Symbol["k"];
3  u = Symbol["u"];
4  l = Symbol["l"];
5  y0 = Symbol["y0"];
6  X = Array[Symbol["X" <> ToString[#]] &, n];
7  M = Table[Exp[-k Abs[j - i] u/l], {i, n}, {j, n}];
8  IN = IdentityMatrix[n];
9  equations = Table[Sum[M[[i, j]] X[[j]], {j, n}] ==
10     y0, {i, n}];
11  solution = Solve[equations, X];
    simplifiedSolution = Simplify[solution]
```

The result for the case $n_B = 2$ is:

- $\Delta\tau_1 = \frac{\exp(k \frac{\lambda}{D_g})}{1 + \exp(k \frac{\lambda}{D_g})} \Delta\tau_{app}$
- $\Delta\tau_2 = \frac{\exp(k \frac{\lambda}{D_g})}{1 + \exp(k \frac{\lambda}{D_g})} \Delta\tau_{app}$

This solution offered by Wolfram Alpha is the same but in a different form than the solution provided above.

Increasing n_B to 4 gives:

- $\Delta\tau_1 = \Delta\tau_4 = \frac{\exp(k \frac{\lambda}{D_g})}{1 + \exp(k \frac{\lambda}{D_g})} \Delta\tau_{app}$
- $\Delta\tau_2 = \Delta\tau_3 = \frac{-1 + \exp(k \frac{\lambda}{D_g})}{1 + \exp(k \frac{\lambda}{D_g})} \Delta\tau_{app}$

Further increasing n_B to 6 or other numbers (including odd numbers), we could conclude that:

- $\Delta\tau_1 = \Delta\tau_N = \frac{\exp(k \frac{\lambda}{D_g})}{1 + \exp(k \frac{\lambda}{D_g})} \Delta\tau_{app}$
- $\Delta\tau_i = \frac{-1 + \exp(k \frac{\lambda}{D_g})}{1 + \exp(k \frac{\lambda}{D_g})} \Delta\tau_{app}$ for $i = 2, 3, \dots, n_B - 1$

Summing up the above solution gives:

$$\sum_{i=1}^{n_B} \Delta\tau_i = 2 \times \frac{1}{1 + \exp(-k \frac{\lambda}{D_g})} \Delta\tau_{app} + (n_B - 2) \times \frac{1 - \exp(-k \frac{\lambda}{D_g})}{1 + \exp(-k \frac{\lambda}{D_g})} \Delta\tau_{app} \quad (4.14)$$

$$= \frac{2 + (n_B - 2)\exp(-k \frac{\lambda}{D_g})}{1 + \exp(-k \frac{\lambda}{D_g})} \Delta\tau_{app} \quad (4.15)$$

Then we suppose (as obtained in the simulation or illustrated in Fig. 4.9) that the slip bands will be uniformly distributed along the full length of the grain and the dislocation density is also uniform in all bands [128, 130]. This gives $\lambda/D_g = D_g/(n_B \sqrt{bD_g/\Delta\gamma_p})$

$$\sum_{i=1}^{n_B} \Delta\tau_i = \frac{2 + (n_B - 2)\exp(-k \frac{D_g}{n_B \sqrt{bD_g/\Delta\gamma_p}})}{1 + \exp(-k \frac{D_g}{n_B \sqrt{bD_g/\Delta\gamma_p}})} \Delta\tau_{app} \quad (4.16)$$

Subscribing the equation of the back stress to the stress Eq. (4.7) of each slip band.

$$\sum_{i=1}^{n_B} \frac{1}{S} \frac{\mu}{1 - \nu} \Delta\gamma_p^i = \frac{2 + (n_B - 2)\exp(-k \frac{D_g}{n_B \sqrt{bD_g/\Delta\gamma_p}})}{1 + \exp(-k \frac{D_g}{n_B \sqrt{bD_g/\Delta\gamma_p}})} \Delta\tau_{app} \quad (4.17)$$

Now apply the principle of superposition on the strain component, we have:

$$\frac{1}{S} \frac{\mu}{1-\nu} \Delta\gamma_p = \frac{2 + (n_B - 2) \exp\left(-k \frac{D_g}{n_B \sqrt{bD_g/\Delta\gamma_p}}\right)}{1 + \exp\left(-k \frac{D_g}{n_B \sqrt{bD_g/\Delta\gamma_p}}\right)} \Delta\tau_{app} \quad (4.18)$$

After rearrangement, we have the final form which will be used to solve the number of slip bands:

$$\frac{\Delta\tau_{app}}{\Delta\gamma_p} = \frac{\mu}{S(1-\nu)} \frac{1 + \exp\left(-k \frac{D_g}{n_B \sqrt{bD_g/\Delta\gamma_p}}\right)}{2 + (n_B - 2) \exp\left(-k \frac{D_g}{n_B \sqrt{bD_g/\Delta\gamma_p}}\right)} \quad (4.19)$$

The numerical solution of this equation present several difficulties, due to a singularity point in the equation that causes significant instability during the solution process. The detailed methods and numerical analysis of this aspect will be provided in the appendix for completeness.

4.4.2 . Experimental calibration of the number of slip bands

The above equation, for instance, is a theoretical deduction without robust experimental verification. Furthermore, the exact values of S and k have yet to be determined. In this subsection, some experimental results from various observations have been collected (from CEA reports) and compared with calculation results for validation.

Investigation of the grain size dependent evolutions

Several results from CEA technique reports are collected and the number of slip bands are counted manually. The process is shown in Fig. 4.11.

Information extraction from Fig. 4.11 micrograph turned out to be a challenging undertaking. The slip bands are not always clearly defined or uniformly formed indeed. The bands can be transgranular, penetrate multiple grains, and sometimes appear as a polyline instead of a straight line. Additionally, the size, length, and spacing of the bands vary considerably more than initially anticipated.

The results read from Fig. 4.11 are shown in Fig. 4.12 Interestingly, the results show a rather weak dependence of band number on grain size. The number of bands, within the margin of error, doesn't change significantly with the grain size. The experimental results collected appear consistent with model prediction using $k > 2$.

Simulation results at the same load are shown in Fig. 4.13 and Fig. 4.13. The dashed lines depict the simulation results.

Calculations using $S' = 7S'_{origin}$ and $S' = 10S'_{origin}$ yield the best comparative results. These results fit the experimental results rather well within the

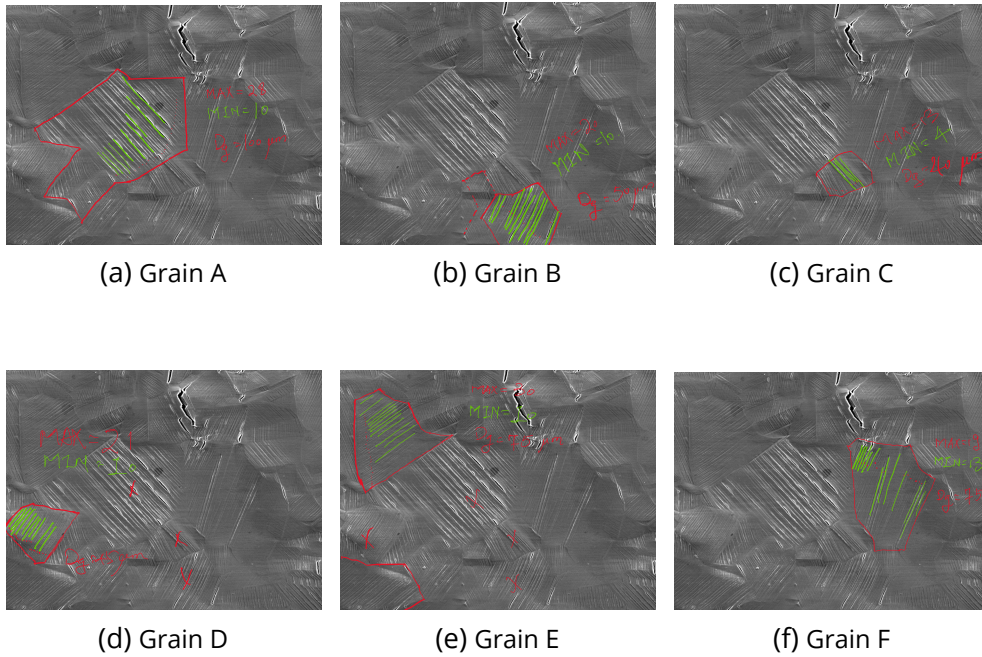


Figure 4.11: Grain images at load $\Delta\gamma_p = 4 \times 10^{-3}$

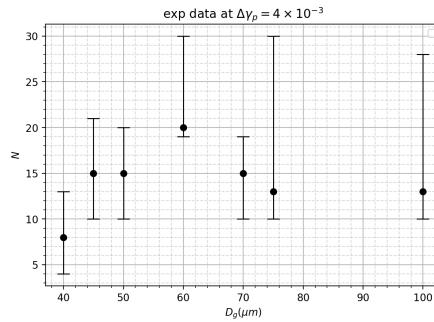


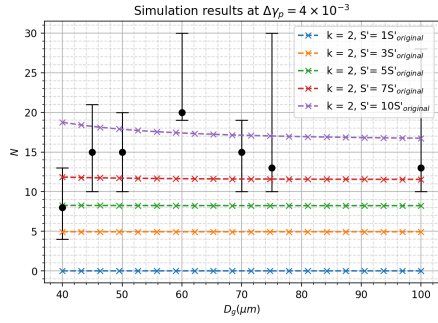
Figure 4.12: Experimental data read from Fig. 4.11

margin of error. When $k = 2$ and $S' = S'_{origin}$, the simulation results show a weak dependence on the grain size D_g .

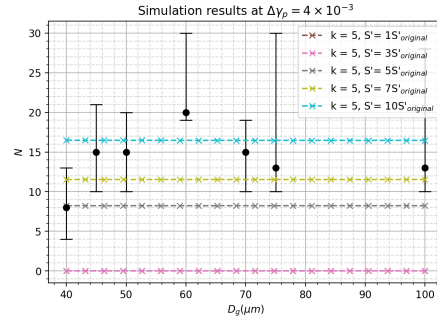
Based on Fig. 4.14, the value of k doesn't affect the absolute value of N . Dependence on D_g is only clear when $k = 1$.

Estimation of the applied load dependent evolutions

Experimental data exist for two values of $\Delta\gamma_p$ in the reports, 1×10^{-3} and 4×10^{-3} . The grains extracted from the images are shown in Fig. 4.15. The grain sizes are similar in these two micrographs shown. In Fig. 4.15c and Fig. 4.15d, the mean stress is $\bar{\tau} = 50 \text{ MPa}$.

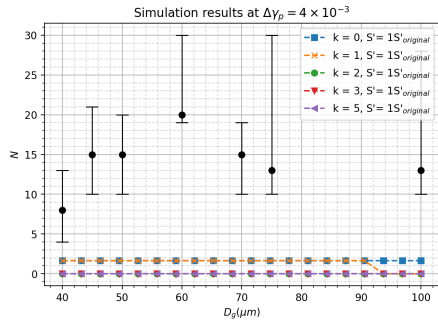


(a) Simulation results with experimental data using $k = 2$

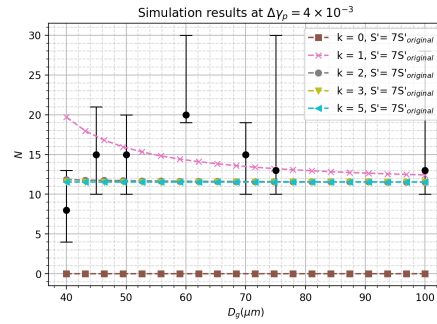


(b) Simulation results with experimental data using $k = 5$

Figure 4.13: Simulation results with experimental data for different S' at $k = 2$ and $k = 5$



(a) Simulation results with experimental data using $S' = S'_{origin}$



(b) Simulation results with experimental data using $S' = 10S'_{origin}$

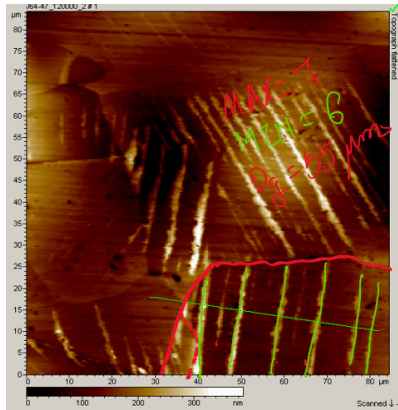
Figure 4.14: Simulation results with experimental data for different k using $S' = S'_{origin}$ and $S' = 10S'_{origin}$

Combined with the data for $\Delta\gamma_p = 4 \times 10^{-3}$ in Fig. 4.12, the results are presented in Fig. 4.16. The grains chosen to be displayed here have a grain size around $60 \mu m$ ($50 \mu m \leq D_g \leq 70 \mu m$).

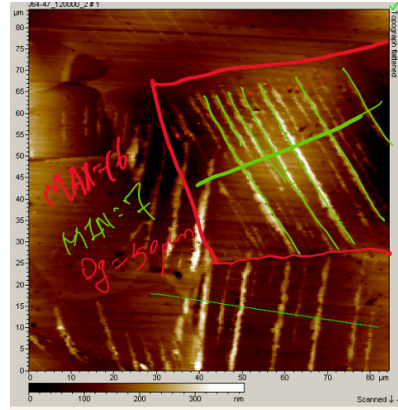
At last, we could add the simulation results with respect to $\Delta\gamma_p$ evolutions (x axis). The first one compares results for different values of k for two values of S' and the second one compares results for different values of S' choosing two values of k .

In conclusion, the simulation results fit best the experimental data when $k \in [2, 5]$ and $S' \in [7, 10]S'_{origin}$. The dependence on D_g is quite weak as regards both the experimental results and simulation results. The dependence on $\Delta\gamma_p$ fits well for the two values available in the experimental data.

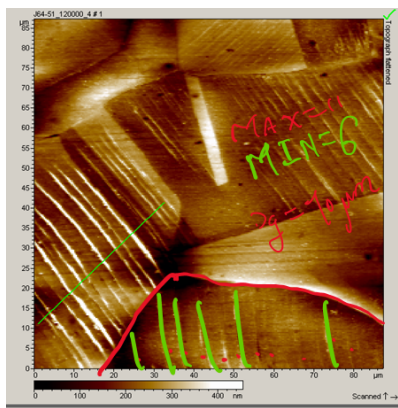
The results of the number of slip bands increase linearly with the applied load, which is coherent with the estimation in [26] where the conclusion was made even before the systems of equations were proposed. This holds true



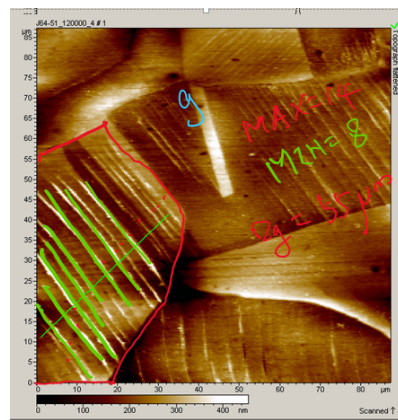
(a) Grain A with $\bar{\tau} = 0 \text{ MPa}$



(b) Grain B with $\bar{\tau} = 0 \text{ MPa}$



(c) Grain C with $\bar{\tau} = 50 \text{ MPa}$



(d) Grain D with $\bar{\tau} = 50 \text{ MPa}$

Figure 4.15: Grain images at load $\Delta\gamma_p = 1 \times 10^{-3}$, note that grain C and D have a mean stress of $\bar{\tau} = 50 \text{ MPa}$

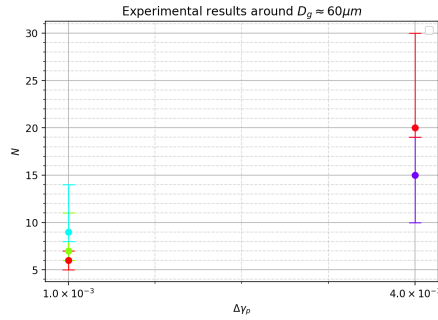
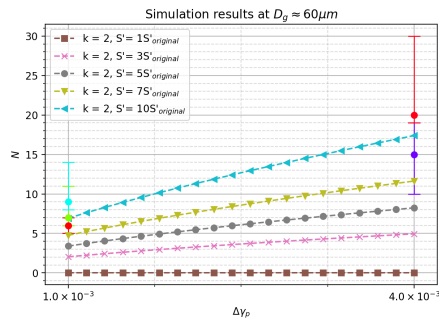
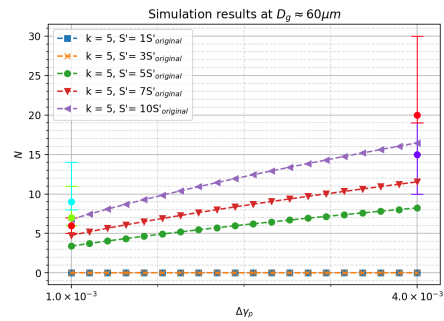


Figure 4.16: Experimentals for different values of $\Delta\gamma_p$ for grains with $50 \mu\text{m} \leq D_g \leq 70 \mu\text{m}$

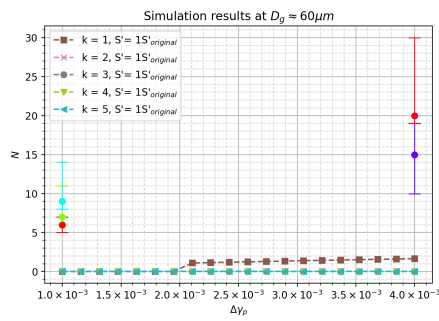


(a) Simulation results with experimental data at $k = 2$

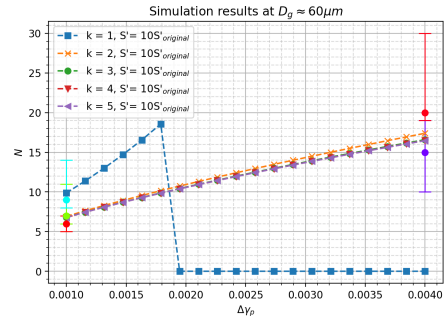


(b) Simulation results with experimental data at $k = 5$

Figure 4.17: Simulation results with experimental data for different S' at $k = 2$ and $k = 5$



(a) Simulation results with experimental data at $S' = S'_{origin}$



(b) Simulation results with experimental data at $S' = 7S'_{origin}$

Figure 4.18: Simulation results with experimental data for different k at $S' = S'_{origin}$ and $S' = 7S'_{origin}$

for the experimental data as well and verifies the coherence of the model. The following section treats the extrusion width evolutions.

4.5 . Estimation of the extrusion width evolutions

The extrusion width, which is supposed to equal the slip band width and uniform for all slip bands in the same grain, has been preliminarily given a form in [126] as per:

$$e_B = \frac{2d}{k(x)} \ln\left(\frac{\sigma_{defect} + \frac{1}{2}S\sigma_{app}}{S\sigma_{app}}\right) \quad (4.20)$$

However, this equation was originally used for irradiation cases instead of fatigue study. The equation can be modified to:

$$e_B = \frac{2d}{k} \ln\left(1 + \frac{\tau_{III}}{f_B + m\Delta\sigma_{app}}\right) \quad (4.21)$$

where m is the Schmid factor, f_B is a band width factor constant.

However, this expression will create a e_B that decreases as $\Delta\sigma_{app}$ increases. The result of N_0 using this expression will be incorrect and the corresponding e_B is not consistent with the experimental observations in the literature of fatigue tests [45, 44, 39]. After modification, the final band width estimation equation to be used in the model writes:

$$e_B = \frac{0.1d}{k} \ln\left(1 + \frac{m\Delta\sigma_{app}}{\tau_{III}}\right) \quad (4.22)$$

where d is the space between slip bands, k is a material constant that can be obtained from DD simulations (this is the same k as used in Chapter 2), τ_{III} is critical cross-slip stress.

Band width, similar to the band number, can be easily compared with experimental data for validation. The comparison of the result of the above equation with experimental results obtained from literature is shown in Fig. 4.19. The experimental results show a large error bar as this quantity is affected by a significant experimental scattering.

4.6 . Results and discussion

After determining the band number n_B and band width e_B , inserting the results into Eq. (4.4) directly yields the estimated number of fatigue cycles required for crack initiation. However, there are parameters that need to be calibrated. The calibration process is analogous to the previous models in Chapter 2 and Chapter 3, and will not be detailed here.

The calibrated result is displayed in Fig. 4.20. The symbols used thereof are explained in the figure caption. In this figure, only the results from [31, 45] represent the actual number of cycles to crack initiation. The other results pertain to the fatigue lifetime.

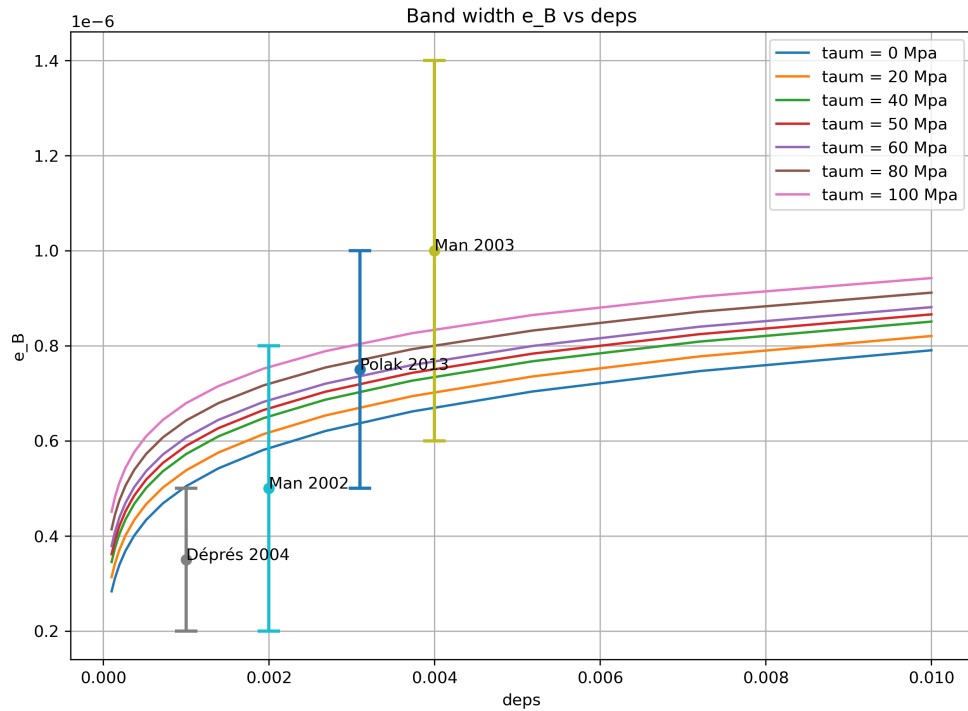


Figure 4.19: Band thickness evolution with the applied plastic strain range. Solid lines: calculation results using Eq. (4.22); solid symbols: corresponding experimental results from [45, 44, 26, 39].

In high-cycle fatigue (HCF), crack initiation accounts for nearly the entire fatigue life. The small difference existing between the actual fatigue lifetime and the initiation-based calculation results can explain the small model/experiment discrepancy visible in Fig. 4.20. The aforesaid discrepancy increases with increasing load values, as the higher the load, the smaller the fraction of the fatigue lifetime represented by the number of cycles to crack initiation. For this reason, the maximum applicable range of this model is chosen to be $\Delta\gamma < 5 \times 10^{-3}$.

Comparing the simulation results with experimental data in the presence of mean stress reveals that the model somewhat underestimates the number of cycles to crack initiation. However, there is no detailed experimental study on the effect of mean stress focusing on crack initiation and its impact on fatigue lifetime. It is possible that mean stress could reduce this fraction and promote crack initiation more than it does on crack propagation.

Nevertheless, the accurate estimation of the changes in fatigue lifetime under the influence of mean stress validates the theoretical assumptions regarding this effect. Fatigue crack initiation will be accelerated by mean stress because it enhances extrusion growth during the fatigue process. This causes the extrusion height to reach the critical value more rapidly, thereby expedit-

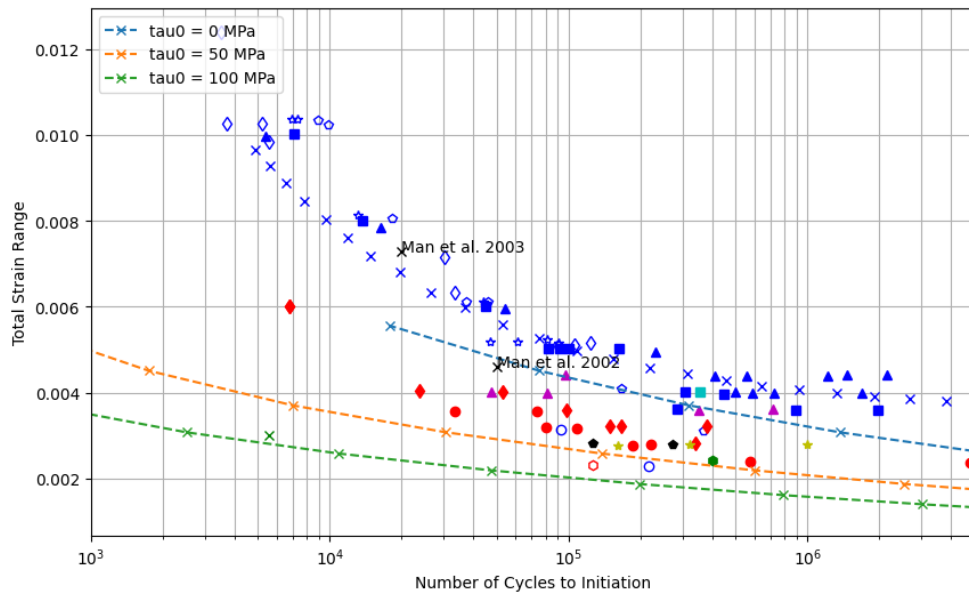


Figure 4.20: The result of crack initiation for different mean stress applied. The dashed lines are the simulation results and the solid symbols are experimental results. The colors in the experiments indicate the mean stress applied (both for simulation results and for experiments), blue indicates zero mean stress, red indicates a mean stress of 50 MPa, green indicates a mean stress of more than 100 MPa. The experimental results come from [31, 131, 45, 44] and several technique reports from CEA.

ing crack initiation.

In industrial applications where crack initiation should be avoided, this suggests that experiments should focus more on the effect of mean stress on crack initiation, rather than solely examining the fatigue lifetime. Crack initiation might be more significantly influenced by mean stress. This is an important conclusion, as it aligns with the industrial context of this study. The design code for the fusion reactor DEMO (introduced in Chapter 1) has established a very strict ratcheting strain allowance for the cooling tube of the divertor. This study justifies this strict requirement and indicates that crack initiation could be more impacted by mean stress than initially anticipated.

4.7 . Conclusion

In this chapter, a new model for estimating the number of cycles to crack initiation in high-cycle fatigue (HCF) was developed. The model is based on the theory of extrusion growth and accounts for the applied means stress effect on extrusion growth. The model was validated with experimental data, and the results demonstrate that it accurately predicts the number of cycles

to crack initiation in a broad range of loading conditions. The results indicate that mean stress accelerates the crack initiation process. This model can be utilized to estimate the number of cycles to crack initiation in HCF and to optimize the design of components subjected to HCF loading.

The proposed model includes a submodel predicting the number of persistent slip bands at the scale of individual grains. That submodel is based on a stress balance expression involving stress generated by the slip bands and the overall stress field on each slip band. This submodel was validated using applicable experimental data. The results indicate that the number of slip bands is weakly dependent on grain size whereas the number of slip bands increases with the applied load level. The results of the submodel align with both the literature and the experimental data.

The model developed in this chapter completes the fatigue lifetime study system proposed in the context of Chapter 1. It is used to estimate the fatigue cycles spent in stage 0, as detailed in Section 1.2.3, which typically constitutes the majority of the fatigue lifetime in HCF conditions. It is worth noting that, although the fatigue lifetime is divided into different stages depending on the applied load range considered, usually only one stage will dominate the fatigue lifetime. This will be elaborated in the next conclusion chapter, where the results of this chapter will be combined with Chapter 2 to produce a final fatigue lifetime estimation across all load values.

There remain several limitations and potential improvements for this model. For instance, the estimation of extrusion width has not been thoroughly theoretically verified. Several parameters could be studied more thoroughly using discrete dislocation (DD) simulations. Theoretically, the results of this model could be applied to other FCC materials by simply calibrating a new set of parameters. These aspects could be explored in future works.

Key finding:

- A new model for the estimation of the number of cycles to crack initiation in HCF was developed. The model is based on the theory of the extrusion growth and the effect of mean stress on the extrusion growth.
- After integration with several submodels and calibration, the model is able to predict the number of cycles to crack initiation with a good accuracy while correctly capturing the effect of mean stress on fatigue crack initiation.
- This model completes the fatigue lifetime study system proposed in the context chapter Chapter 1 and is used to estimate the fatigue cycles spent in the stage 0 as in Section 1.2.3.

5 - Conclusion

In this final chapter, we'll conclude the thesis by summarizing the main models and results obtained in the previous chapters. We'll point out the applications and contributions of the models in both the scientific and industrial aspects. We'll also discuss the limitations of the models and the possible extensions of the work.

5.1 . Summary of the thesis

At the beginning of the thesis, we've separated the fatigue lifetime into three stages (c.f. Section 1.2.3) contributing to the fatigue lifetime:

1. Stage I crack initiation (referred to as stage 0)
2. Stage I crack propagation (referred to as stage 1)
3. Stage II crack propagation (referred to as stage 2)

Based on the previous studies using the DD simulations, we've proposed new models that could predict the fatigue lifetime spent in stage 0 (c.f. Chapter 4) and stage 2 (c.f. Chapter 2). The combination of these two models could predict the fatigue lifetime given the load range $2.0 \times 10^{-3} \leq \Delta\epsilon_p \leq 1.0 \times 10^{-2}$ (c.f. Fig. 5.1).

In Fig. 5.1, the combined use of Chapter 2 and Chapter 4 models demonstrates effective fatigue lifetime predictions within the load range $2.0 \times 10^{-3} \leq \Delta\epsilon_p \leq 1.0 \times 10^{-2}$. Specifically, for $\Delta\epsilon_p \leq 4.0 \times 10^{-3}$, stage 0 (Stage I crack initiation) predominantly influences the fatigue lifetime. Conversely, for $\Delta\epsilon_p \geq 6.0 \times 10^{-3}$, the fatigue lifetime is primarily governed by stage 2 (Stage II crack propagation). The fatigue lifetime in the intermediate load range is influenced by both stages.

However, the models fail to predict the fatigue lifetime for $\Delta\epsilon_p \geq 1.0 \times 10^{-2}$. At these higher strain amplitudes, the stage 2 model, which solely considers crack propagation, is insufficient because crack coalescence and intergranular crack propagation, which typically become significant at these levels, are not accounted for. These factors influence fatigue lifetime differently than transgranular cracks do.

Moreover, accurately predicting the fatigue lifetime for very low strain amplitudes ($\Delta\epsilon_p \leq 2.0 \times 10^{-3}$) is also challenging. At such low load levels, cracks may propagate beyond the first grain boundaries, resulting in an almost indefinite fatigue life, rendering predictions irrelevant in absence of additional modeling developments. Modeling addressing this situation however exist [35] and could be incorporated in the present studies.

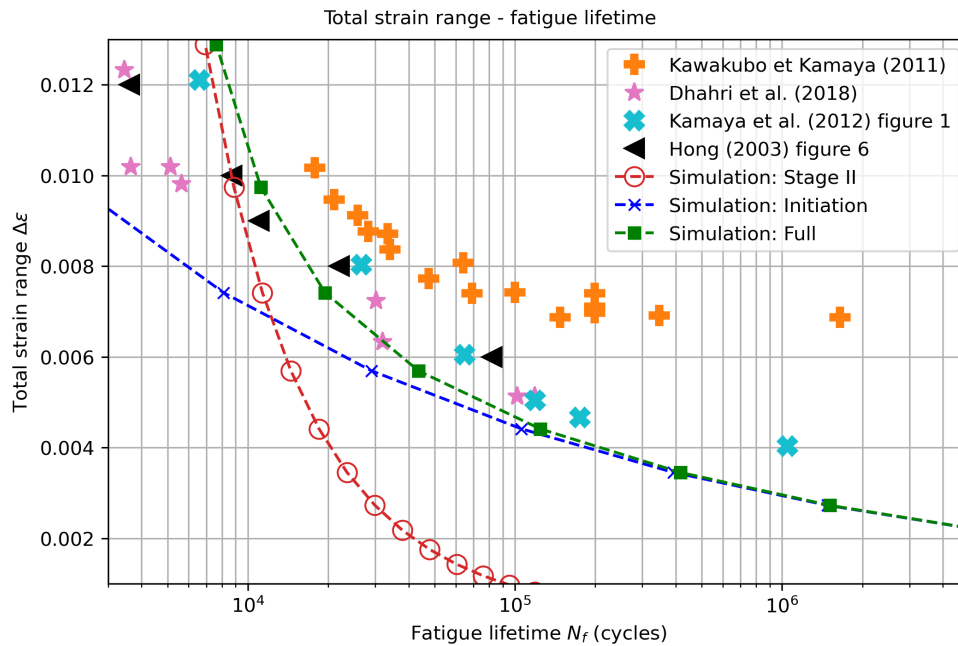


Figure 5.1: The result of fatigue lifetime as a function of applied total strain range. The dashed lines are the simulation results (of stage 2 and stage 0 and combined full prediction) and the solid symbols are the experimental results. The original data is on plastic strain range, conversion is performed using the Ramberg-Osgood correlation.

There is a consistent underestimation of fatigue lifetime across various phases, likely due to the omission of stage 1 (Stage I crack propagation) in these predictions. The complexities associated with stage 1 and transitions to stage 2 present significant challenges that warrant further investigation [36, 25].

The models however address a broad spectrum of fatigue lifetime prediction scenarios. With further refinement to address the identified deficiencies, a comprehensive fatigue lifetime prediction framework could be developed, thereby achieving all the scientific objectives outlined in Section 1.6.

In industrial contexts, the models may be employed individually to address the demands of particular scenarios. For instance, the stage 2 model is adept at forecasting the progression of fatigue cracks, effectively isolating the crack initiation phase. This proves especially useful in predicting the fatigue life of components that are designed with pre-existing crack-like defects, as noted in [132].

Regarding the stage 0 model, its applicability could be broader. It is primarily utilized to calculate the number of fatigue cycles leading to the initiation of micro-cracks, which is critical in scenarios where the presence of ini-

tial crack-like defects in components is not allowed. An example includes the cooling tubes in the diverter of the DEMO fusion reactor, currently under development (see Chapter 1). Moreover, the stage 0 model incorporates considerations for the ratcheting effect, accounting for the cumulative history of mean stress and offering predictions of ratcheting strain under nearly arbitrary loading sequences. Should this model undergo thorough validation and calibration through dedicated experimental studies across these various scenarios, its utility in accurately predicting and documenting fatigue crack initiation is highly promising.

5.2 . Future work

There are three main areas for practical improvement applicable to the models developed in this work:

1. Although the models developed have shown promising capabilities, they still have limitations that need addressing. A critical step is to complete and validate them by comparison with dedicated experimental results. Currently, research resources have not allowed for comprehensive experimental testing for unique applications of the models (like understanding the effects of step loading on ratcheting and tracking crack initiation accurately), except for the FABIME tests referenced in Section 2.6.3. Many of the model parameters were estimated through a calibration process instead of being directly measured or simulated. Conducting focused experiments, although expensive and time-consuming, is essential to fully validate the models and address any possible shortcomings.
2. The second goal is to broaden the practical uses of the models. So far, Discrete Dislocation (DD) simulations have mostly been done on individual grains. Transition techniques to larger scales were introduced in the stage 2 model, as mentioned in Section 2.6, by incorporating an Electron Backscatter Diffraction (EBSD) datasets representative of macroscopic grain aggregate. It could be insightful to connect these single-grain models to Finite Element Method (FEM) models through an explicit scaling method, provided FEM description successfully described the fatigue-induced strain localization effect.
3. It is possible to apply the model to a broad range of environmental conditions, most importantly, for different temperatures. Such fatigue data exist already and have been used to calibrate the Stage II crack propagation model developed in Chapter 2 (not included in this thesis). Some preliminary results have been obtained and are promising, at least up to 600°C. Detailed studies could be carried out to accurately correlated

the model's parameters to the temperature and a similar study could be carried out for the Stage 0 model.

In addition to the two main improvement paths, numerous smaller studies could be conducted focusing on certain assumptions in the models, as mentioned in the relevant chapters. An example of such a study is the dipole density verification conducted for the general model, detailed in Chapter 3. These focused studies would be instrumental in enhancing the precision and reliability of the models, ensuring they provide utilizable predictions.

6 - Appendix

6.1 . Material details

The material used in this research is stainless steel AISI 316L, a largely used FCC material in the nuclear industry thanks to its high performance in extreme operating conditions. The chemical composition of the material is given in Table 6.1. It is important to note that this composition is for the material for the experiments used in the laboratory for the validations. The material under the same name could have slight differences in both chemical composition and mechanical properties due to the manufacturing process. The mechanical properties of the material are given in Table 6.2.

Table 6.1: Chemical composition of AISI 316L stainless steel

| C | Mn | Si | P | S | Cr | Ni |
|------|------|------|-------|------|-------|-------|
| 0.03 | 2.00 | 1.00 | 0.045 | 0.03 | 16.00 | 14.00 |

Table 6.2: Material constants for fatigue life prediction in grade 300 austenitic steel.

| Parameter | Value | Physical meaning |
|-----------|-------------------------|------------------|
| μ | $8.4 \times 10^{10} Pa$ | Shear modulus |
| ν | 0.3 | Poisson's ratio |
| b | $2.5 \times 10^{-10} m$ | Burgers vector |
| ρ_v | $7870 kg/m^{-3}$ | Density |

The parameters for the fatigue models introduced in previous chapters will be given below, in the form of a list instead of a table. Generally, all values are given in the SI unit system. Based on the parameter's determination method, it can be general divided into three categories:

- **Parameters obtained from the experiments:** These parameters are obtained from the experiments conducted in the laboratory or collected from literature. They are specific to the material and are used for the material.
- **Parameters obtained with calibration:** These parameters are obtained with a calibration process using the experimental data though they can in fact be obtained from the simulations. The simulations to obtain these parameters are too costly to be conducted in the context of this thesis.

- **Parameters obtained from the simulations:** These parameters are obtained from the DD simulations or derived indirectly from other compatible physical theories. The values of these parameters are not related to any experiments.

These parameters will be colorized in the following list to provide a better understanding of the origin of the parameters.

Common parameters for all models:

- **S : Geometry parameter: 0.66**, a dimensional parameter that depends on the shape of the grains and the PSB distribution in the grain. Can be determined using DD simulations for each grain but could be estimated to be 0.66 for general cases. The determination process of this parameter can be found in the annex of [25].
- **K : Mean free path of dislocations: 19.7**, the mean free path of dislocations in the material related to the accumulation of dislocations by the trapping against dipolar obstacles. The calculation method is referenced from [27, 111].
- **y_c : Mean annihilation distance: 1.12 nm**, a characteristic length that describes the annihilation of dislocations. The calculation method is the same as previous parameter.
- **K' : Romberg-Osgood parameter: 2.55 GPa**, a parameter that describes the stress-strain behavior of the material.
- **n' : Romberg-Osgood exponent: 0.39**, the exponent that describes the stress-strain behavior of the material.

Stage II crack propagation model:

- **λ : Number of dislocations in the crack tip area: 25**, the dimensionless count of dislocations in the crack tip area, can vary from 25 to 100 depending on the crack. The value comes from DD simulations presented in [52].
- **γ_{surf} : Surface energy: $1.3 \times 10^{-3} J/m^2$** , the surface energy of the crack tip, can be obtained with the help of molecular dynamics simulations. The current value is calibrated based on the experimental data.
- **k : PSB stress decay factor: 5**: the stress decay factor for the PSB stress field, can be obtained from the dislocation dynamics simulations. It depends mostly on the crystal structure of the material. The value is given in [52].

- dy/dn : **PSB evolution rate:** $16.5 \times 10^{-9} m/cycle$, characterizes (intra) PSB evolution. It is independent of the grain size or the load level. The value is solved with a dedicated model presented in [52].

General model:

- τ_0 : **Lattice friction:** $50 MPa$: the lattice friction of the material. The current value is based on the experimental results of the material and the calibration.
- α : **Dipole strength distribution parameter: 0.3**, the parameter that defines the distribution of the dipole strength in the material. It is a dimensionless parameter that can be obtained from the dislocation dynamics simulations. In this research, the value is determined by calibration
- λ : **Proportionality coefficient of the standard deviation: 0.5**, the proportionality coefficient of the standard deviation of the dipole strength distribution. It is a dimensionless parameter that can be obtained from the dislocation dynamics simulations. In this research, the value is determined by calibration.
- M : **Long-range stress factor: 2**, a phenomenological coefficient that encapsulates the average impact of the dislocation dipole distributions on the actual kinematic stress level. However, the connection between the simulation result and this parameter is not completely clear. The calibration method is the only option to determine this parameter at the moment.
- m : **Strain rate sensitivity exponent: 0.05**, the strain rate sensitivity exponent of the material. It is a small value that enlarges the effect of stress equilibrium on the dislocation dynamics. The value is from an equation in [27] and the origin is from [110].
- $\dot{\gamma}_0$: **Reference strain rate:** $10^{-10} s^{-1}$: a reference strain rate and the value is fixed in the original development [27].

Stage I micro-crack initiation model:

- S' : **Linear correction factor: 10**, a linear correction factor to fit the band number equations, fixed by the calibration process.
- h_{crit} : **Critical extrusion height:** $300 nm$, the critical extrusion height for the micro-crack initiation. This value is fixed based on the previous experimental and simulation studies in the laboratory.

- k_{surf} : **Extrusion growth factor:** $2.7 \times 10^6 \text{ m}^{-1}$, the extrusion growth factor for the micro-crack initiation, can be obtained from DD simulations.
- τ_{III} : **Critical cross-slip stress:** 52 MPa , the critical cross-slip stress, used for the estimation of extrusion width. The value is fixed based on the experimental results.

6.2 . Machine learning calibration process

In this section, details about the machine learning (ML) algorithm used to evaluate the error of a certain parameter set will be given. In Chapter 3, there are 6 parameters to be determined by calibration in the study. The comparison between the experimental data and the simulation manually is very complex because the effects of the parameters are not independent. On this occasion, ML provides powerful predictive functionality that is in principal superior to manual adjustment.

This sub-study can be divided into two parts: the first one is to run a certain number (several hundred should be enough) of simulations with different parameters and calculate an error value for each simulation case to prepare the training data. The second part is to train a machine learning model to predict the error associated with a certain parameter set and try to minimize the error with a certain minimization algorithm.

At first, the problem must be formulated as a mathematical problem. The objective is to minimize the difference between the simulated ratcheting strain and the experimental ratcheting strain. This can be formulated as a minimization problem where we should first define an objective function that quantifies the difference between the simulated results and the experimental results.

This difference can be quantified by the sum of the differences between the respective results corresponding to each cycle. This approach also accounts for the difference between the stress range value with the experimental result.

However, different types of results hold different importance, some weight factors must be defined as well. The first weight parameter would be the weight of the overall ratcheting strain error η_1 and the second weight parameter would be the weight of the stress range η_2 . For the ratcheting strain error calculation, there should also be a weight for each cycle. The weight of the cycle i can be defined as:

$$w(i) = \begin{cases} 0 & \text{if } n \leq 100 \\ 0.3 & \text{if } 100 < n \leq 1000 \\ 1.0 & \text{if } n > 1000 \end{cases} \quad (6.1)$$

Then the error of the ratcheting strain can be calculated as follows:

$$f_{strain} = \frac{\sum_{i=1}^{N_{max}} w(i)(\bar{\gamma}_{sim}(i) - \bar{\gamma}_{exp}(i))}{\sum_{i=1}^{N_{max}} w(i)} \quad (6.2)$$

where N_{max} is the maximum number of fatigue cycles where the comparison is made, $\bar{\gamma}_{sim}(i)$ is the simulated ratcheting strain at cycle i , and $\bar{\gamma}_{exp}(i)$ is the experimental ratcheting strain at cycle i .

For the stress range, a simplified comparison method can be used. In the stabilized stage, the stress range is almost constant. We defined a stabilized stress range value $\Delta\tau_{stab}$ as the average stress range of the last 30% of the cycles (for the experiments, the exceeding part that doesn't exist in the simulation will be removed before choosing these cycles). Thus:

$$f_{stress} = \Delta\tau_{stab,sim} - \Delta\tau_{stab,exp} \quad (6.3)$$

The objective function f will then be:

$$f = \frac{\eta_1 f_{strain} + \text{sign}(f_{strain})|\eta_2 f_{stress}|}{\eta_1 + \eta_2} \quad (6.4)$$

f here is a function of the parameters to calibrate. For simplicity, we've also chosen $\eta_1 = \eta_2 = 1$. $\text{sign}(f_{strain})$ is the sign of the f_{strain} value, this prevents the cancelation of two errors if they have opposite signs while conserving the sign of the strain error in the final result. Thus $f : \mathbb{R}^6 \rightarrow \mathbb{R}$ is in the following form (with the parameters to calibrate $\dot{\gamma}_0, \rho_0, M, \lambda, \alpha, \tau_0$):

$$f = f(\dot{\gamma}_0, \rho_0, M, \lambda, \alpha, \tau_0) \quad (6.5)$$

Following the problem's formulation, the next step is to prepare the data to feed the machine learning algorithm. Specifically, the data consists of the error calculated with the above objective function for various parameter sets. The data is organized into a matrix formatted as $(N_{data}, 7)$, where N_{data} represents the total number of data entries, and the number 7 denotes 6 parameters plus the resultant error value.

Typically, the dataset is divided into two segments: the training set and the testing set. The training set, which generally comprises 80% of the data, is employed to train the model. Conversely, the testing set, accounting for the remaining 20%, is utilized to evaluate the model's performance.

For a standard ratcheting simulation where $N_{max} = 10000$ and $N_{pp} = 3000$ (representing the number of data points per cycle), the process typically requires approximately two days to complete. Utilizing parallel computing, a dataset comprising 1000 simulations can be generated within approximately one month. This volume of data is generally sufficient for training a machine learning model. Nevertheless, to conduct an effective analysis of each parameter, it is advisable to consider between 7 to 10 values per parameter (except

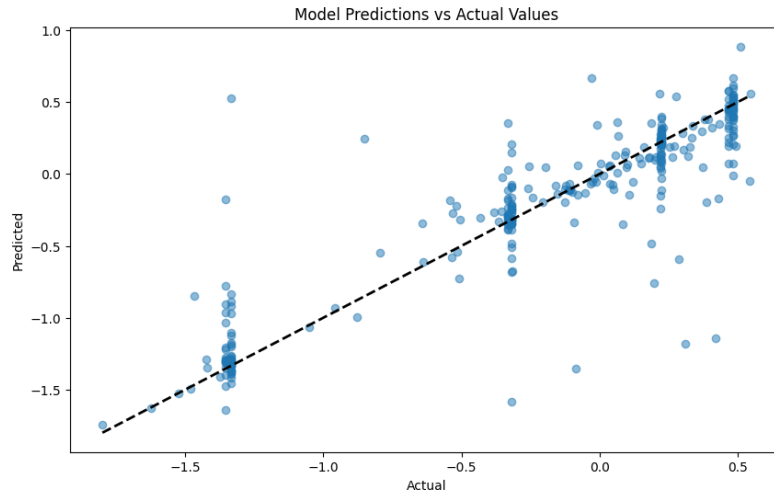


Figure 6.1: Machine learning model prediction evaluation

perhaps for $\dot{\gamma}_0$ which requires only 3 to 4 values), which implies that the total number of simulations required would be around $4 \times 5^{10} = 39062500$. This number of simulations is impossible to carry out in practice.

To solve this computational load issue, a *factorial design* approach is employed to scientifically select the values of parameters for the simulations. Using the Python library *pyDOE*, the number of necessary simulations can be efficiently reduced to approximately 1000.

After the data preparation and quantification using the objective model, the next step is to train the machine learning model. In this study, we choose the *Multilayer Perceptron* neural network method for the prediction of this highly complex physical correlation. There are several reasons for choosing this model, such as its ability to model highly non-linear relationships, its robustness against noise and its easy implementation using the *Keras* library.

The most critical part of this study is the tuning of this neural network, which requires a lot of settings, such as the number of neurons, the number of layers, the sensitivity etc. After optimization, the model's prediction versus actual results is shown in Fig. 6.1.

This result is quite promising as the prediction is close to the actual results. After the training of the model, the next step is to use the model to find the optimal parameter set. In this study, the *Differential Evolution* optimization method is used. This method is robust to non-smooth functions and can effectively search the parameter space. The result yields:

- $\dot{\gamma}_0 = 8.9 \times 10^{-10} \text{ s}^{-1}$
- $M = 3.5$
- $\rho_0 = 2.9 \times 10^{13} \text{ m}^{-3}$

- $\lambda = 0.38$
- $\alpha = 0.18$
- $\tau_0 = 29 \text{ MPa}$

The predicted error associated with this parameter set is approximately -5×10^{-7} . However, actual validation, achieved by comparing the simulation outcomes of this parameter set with experimental data, reveals that the error is substantially larger, at 1.5×10^{-2} . Such a difference is to be expected, given the inherent imperfections in experimental data, which inherently limit the achievable accuracy of simulation predictions.

However, the counterpart of this study is that, during the data preparation, the selection mechanism happens to have selected several very good candidates for the calibration result. These randomly selected parameter sets yield results within the acceptable range as shown in Fig. 6.2 that are comparable to manual calibration and the result of ML calibration.

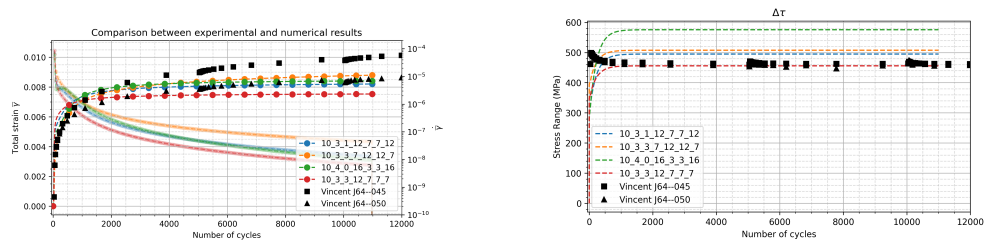
This proves that multiple candidates actually exist for calibrating based on ratcheting strain and stress range. The calibration process is not unique with only the data for one load (one applied plastic strain range and one applied mean stress). It is thus concluded that if we wish to find out the real parameter set, we should consider acquiring more data for different loads to further calibrate the model.

It is also a better option to fix several parameters that could be obtained physically and calibrate only the parameters that are too costly to obtain. This will reduce the number of parameters to calibrate and make the calibration process more efficient. For example, the parameter α , λ , τ_0 can be obtained using DD simulations (though the amount of work is quite significant) and the initial dislocation density ρ_0 can be fixed when comparing the simulation results with a specific experimental result that has the initial dislocation density data for its specimens.

In conclusion, ML algorithms still are a good candidate for obtaining suitable parameter values when the experimental data for the material studied is limited. The calibration process will not provide exact values for the material, but it will indeed create a set of parameters that permit the model to predict the material's behavior under applicable conditions with a certain level of accuracy.

6.3 . Dipole strength distribution investigation

In this section, a separate study is conducted to investigate whether the precision of the dipole strength is good enough to be used in the general model in Chapter 3. This concern comes from a phenomenon of unsymmetry



(a) Total mean strain comparison for several simulations versus the experimental data.

(b) Stress range comparison for several simulations versus the experimental data.

Figure 6.2: Results of several simulations versus the experimental data. The labels are the index of the parameters used during data preparation.

from [133]. During the formation process of a dislocation dipole, due to the different dislocation types (edge and screw) and the different shear direction, there are in total four possible dipole configurations as shown in Fig. 6.3.

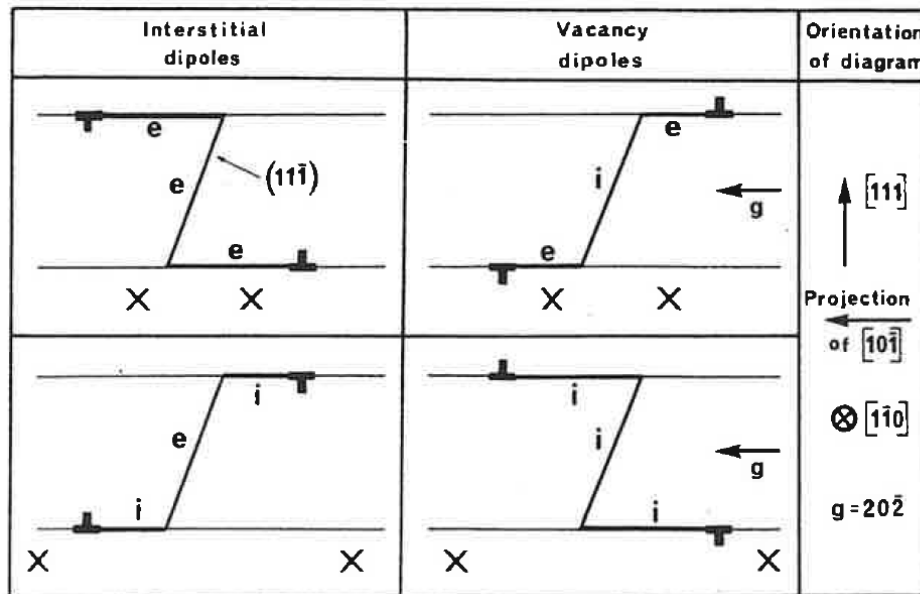


Figure 6.3: The four possible configurations for a faulted dipole parallel to the $[1\bar{1}0]$ direction.

In previous simulations, all these four types of dipoles are supposed to have same strength. However, whether the unsymmetry will affect the dipole strength is still unknown. Therefore, we've done some simulations with the DD simulation software NuMoDis to investigate the dipole strength distribution.

6.3.1 . Simulation setup

NuMoDis takes several input files as the simulation setup, they include the geometry file, the material file, the loading file and an initiation file that contains the initial dislocation information in the geometry. These definition files are in *.xml* format.

The geometry is set to a simple cube with a size of 50000^3\AA^3 . After defining this, it is also important to correlate the directions of the axis of the cartesian coordinate system to the crystallographic directions of the material. In our simulation, we denote $x = [10\bar{1}]$, $z = [111]$. After defining the geometry, the material file is set to the material properties of the material we are interested in. In this case, we use the material properties of the FCC acier with properties shown in Table 6.2. And finally, we put two Frank-Read sources in front of each other in a proper distance. They must contain a "vertical" height difference in order to form dipole. This vertical height difference h is the *dipole height* which is the only configurable factor that determines the dipole strength. The formula of calculation is $s = \frac{Gb}{8\pi(1-\nu)h}$ where s is the dipole strength, G is the shear modulus, b is the Burgers vector, and ν is the Poisson ratio.

The slip direction and the load direction are configured based on Fig. 6.3. This leads to the topology shown in Fig. 6.4.

The load is a gradually increasing shear stress in the configured direction. During the increment, dislocations will be generated by the Frank-Read sources and the dipole will be formed (shown in Fig. 6.5). The strength of the dipole is defined as the stress when the dipole is separated. The simulation is stopped when the dipole is separated. The strength of the dipole is recorded for later analysis.

6.3.2 . Simulation results

Eight simulations are conducted with the same setup as described in Section 6.3.1, using different configurations of the Frank-Read sources and loading direction, all four types of dipoles are covered in these simulations. The results show that there are indeed no significant differences in the dipole strength for the four types of dipoles as shown in Fig. 6.7. Simulations are also carried out with different configurations of the Frank-Read sources (different length and distance) and the results are the same.

The dispersion of the simulation results are due to the fact that the separation of dipoles must be observed manually, which leads to a certain degree of uncertainty. The simulated values are a bit higher than the theoretical value which is also normal as the observation of the dipole separation is not instantaneous. There is also the effect of time step which amplifies this uncertainty. However, the results are still acceptable to conclude that all four types of dipole have the same strength.

6.3.3 . Conclusion

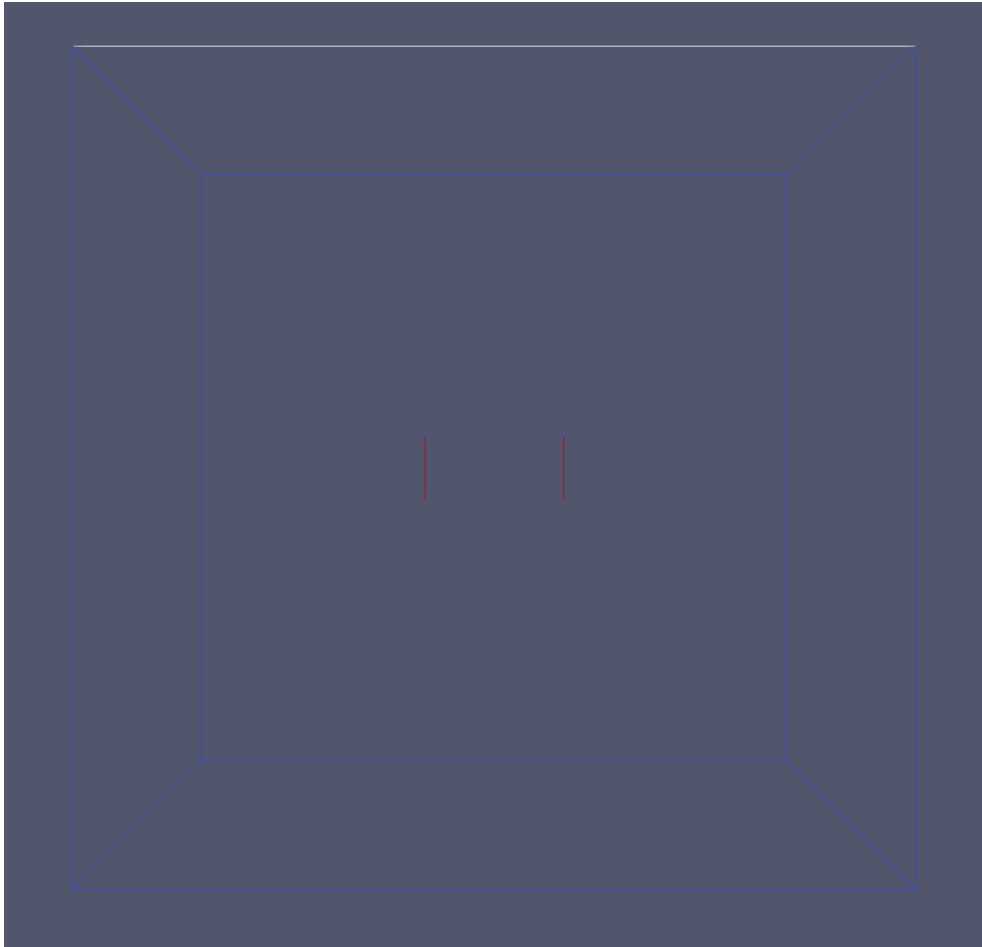


Figure 6.4: The topology of the dipole simulation

The dipole strength distribution is investigated in this section. The results show that the dipole strength is not affected by the dipole configuration. This means that the dipole strength can be used in the general model in Chapter 3 without any modification. The dipole strength is a good approximation for the general model.

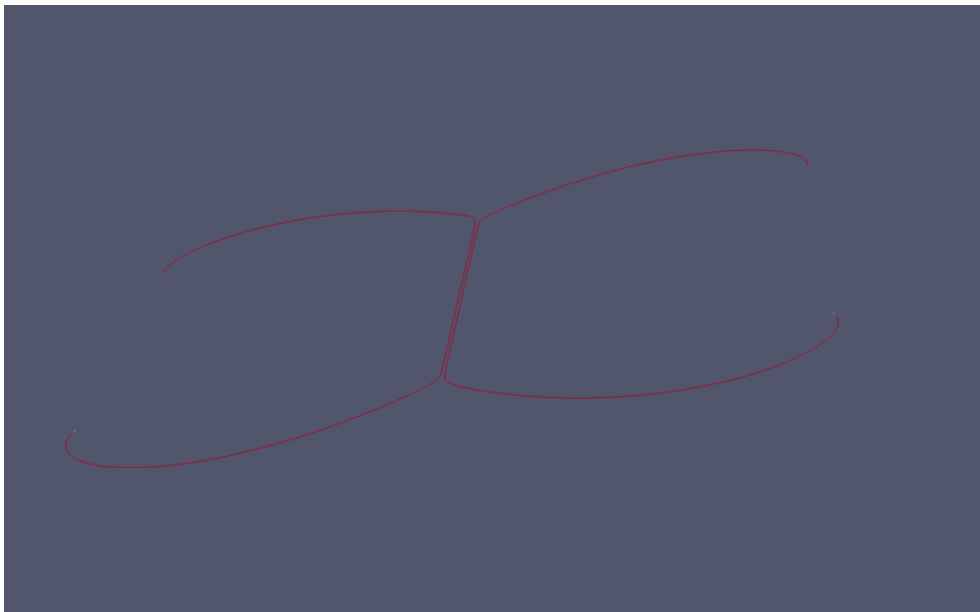


Figure 6.5: The formation of a dipole



Figure 6.6: The separation of a dipole (shown in the yellow rectangle), the shear stress applied at this moment is the strength of the dipole

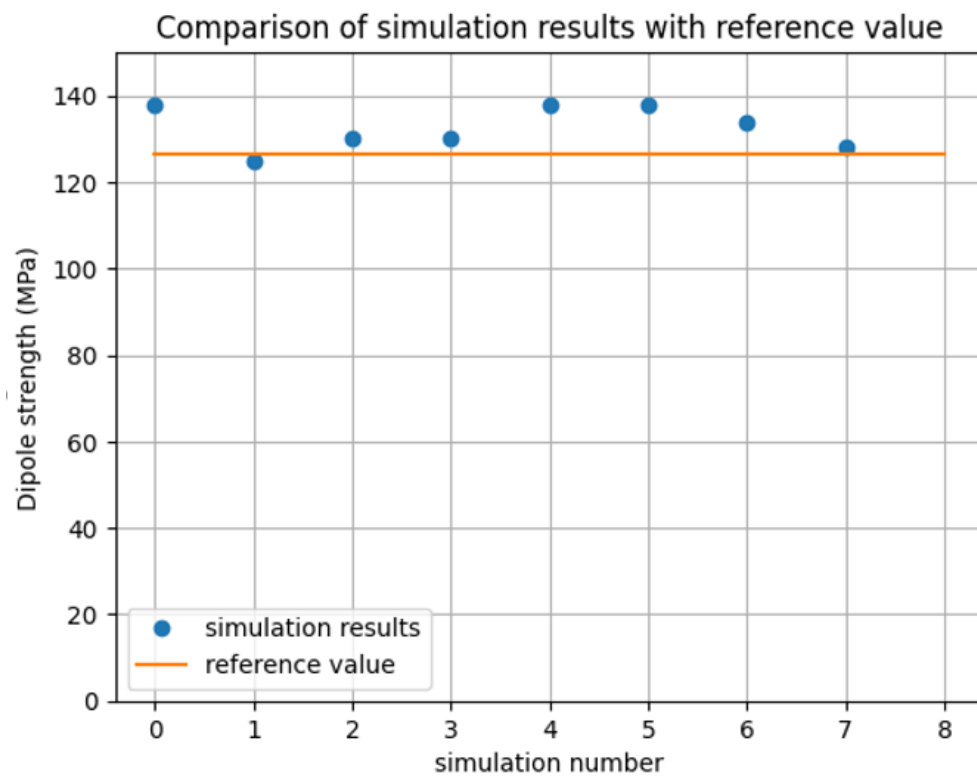


Figure 6.7: The dipole strength result compared to the theoretical value, calculated by $s = \frac{Gb}{8\pi(1-\nu)h}$ where h is the dipole height.

Bibliography

- [1] Ann MacLachlan. Dealing with cracking in the French nuclear fleet - Nuclear Engineering International, 2023.
- [2] S. K. Bhaumik, M. Sujata, and M. A. Venkataswamy. Fatigue failure of aircraft components. *Engineering Failure Analysis*, 15(6):675–694, September 2008.
- [3] R. C. Alderliesten. Critical review on the assessment of fatigue and fracture in composite materials and structures. *Engineering Failure Analysis*, 35:370–379, December 2013.
- [4] S. Beretta and S. Romano. A comparison of fatigue strength sensitivity to defects for materials manufactured by AM or traditional processes. *International Journal of Fatigue*, 94:178–191, January 2017.
- [5] PeiYong Chen, Chanho Lee, Shao-Yu Wang, Mohsen Seifi, John J. Lewandowski, Karin A. Dahmen, HaoLing Jia, Xie Xie, BiLin Chen, Jien-Wei Yeh, Che-Wei Tsai, Tao Yuan, and Peter K. Liaw. Fatigue behavior of high-entropy alloys: A review. *Science China Technological Sciences*, 61(2):168–178, February 2018.
- [6] Nima Shamsaei and Ali Fatemi. Small fatigue crack growth under multi-axial stresses. *International Journal of Fatigue*, 58:126–135, January 2014.
- [7] James Alfred Ewing and J. C. W. Humfrey. VI. The fracture of metals under repeated alternations of stress. *Philosophical Transactions of the Royal Society of London. Series A, Containing Papers of a Mathematical or Physical Character*, 200(321-330):241–250, January 1903. Publisher: Royal Society.
- [8] N. Thompson, N. Wadsworth, and N. Louat. Xi. The origin of fatigue fracture in copper. *The Philosophical Magazine: A Journal of Theoretical Experimental and Applied Physics*, 1(2):113–126, February 1956. Publisher: Taylor & Francis _eprint: <https://doi.org/10.1080/14786435608238086>.
- [9] Bao-Tong Ma and C. Laird. Overview of fatigue behavior in copper single crystals. III. Interpretation of crack growth kinetics and a new approach to predict fatigue life based on crack population density in specimens cycled at constant strain amplitude. *Acta metall.*, 37(2):349–355, 1989. ISBN: 0001-6160.
- [10] Vani Shankar, M. Valsan, K. Bhanu Sankara Rao, R. Kannan, S. L. Manan, and S. D. Pathak. Low cycle fatigue behavior and microstructural

- evolution of modified 9Cr–1Mo ferritic steel. *Materials Science and Engineering: A*, 437(2):413–422, November 2006.
- [11] S. L. Mannan and M. Valsan. High-temperature low cycle fatigue, creep-fatigue and thermomechanical fatigue of steels and their welds. *International Journal of Mechanical Sciences*, 48(2):160–175, February 2006.
- [12] Hael Mughrabi. Specific features and mechanisms of fatigue in the ultrahigh-cycle regime. *International Journal of Fatigue*, 28(11):1501–1508, November 2006.
- [13] S. Sajith, S.S. Shukla, K.S.R.K. Murthy, and P.S. Robi. Mixed mode fatigue crack growth studies in AISI 316 stainless steel. *European Journal of Mechanics - A/Solids*, 80:103898, March 2020.
- [14] Weicheng Cui. A state-of-the-art review on fatigue life prediction methods for metal structures. *Journal of Marine Science and Technology*, 7(1):43–56, June 2002.
- [15] Peter Joseph Edward Forsyth. The physical basis of metal fatigue. (*No Title*).
- [16] C. Déprés, C. F. Robertson *, and M. C. Fivel. Low-strain fatigue in AISI 316L steel surface grains: a three-dimensional discrete dislocation dynamics modelling of the early cycles I. Dislocation microstructures and mechanical behaviour. *Philosophical Magazine*, 84(22):2257–2275, August 2004.
- [17] John Price Hirth and Jens Lothe. *Theory of dislocations*. Wiley, New York, 2nd ed edition, 1982.
- [18] Peter M. Anderson, John Price Hirth, and Jens Lothe. *Theory of dislocations*. Cambridge University Press, Cambridge, 2017 edition edition, 2017.
- [19] D. Hull and D. J. Bacon. Chapter 10 - Strength of Crystalline Solids. In D. Hull and D. J. Bacon, editors, *Introduction to Dislocations (Fifth Edition)*, pages 205–249. Butterworth-Heinemann, Oxford, January 2011.
- [20] K. Katagiri, A. Omura, K. Koyanagi, J. Awatani, T. Shiraishi, and H. Kaneshiro. Early stage crack tip dislocation morphology in fatigued copper. *Metallurgical Transactions A*, 8(11):1769–1773, November 1977.
- [21] M. Verdier, M. Fivel, and I. Groma. Mesoscopic scale simulation of dislocation dynamics in fcc metals: Principles and applications. *Modelling and Simulation in Materials Science and Engineering*, 6(6):755–770, November 1998. Publisher: IOP Publishing.

- [22] Jie Chen and Yongming Liu. Fatigue modeling using neural networks: A comprehensive review. *Fatigue & Fracture of Engineering Materials & Structures*, 45(4):945–979, April 2022.
- [23] Steven Lavenstein and Jaafar A. El-Awady. Micro-scale fatigue mechanisms in metals: Insights gained from small-scale experiments and discrete dislocation dynamics simulations. *Current Opinion in Solid State and Materials Science*, 23(5):100765, October 2019.
- [24] Jaafar A. El-Awady, Haidong Fan, and Ahmed M. Hussein. Advances in Discrete Dislocation Dynamics Modeling of Size-Affected Plasticity. In Christopher R. Weinberger and Garritt J. Tucker, editors, *Multiscale Materials Modeling for Nanomechanics*, pages 337–371. Springer International Publishing, Cham, 2016.
- [25] C. Déprés. *MODÉLISATION PHYSIQUE DES STADES PRÉCURSEURS DE L'ENDOMMAGEMENT EN FATIGUE DANS L'ACIER INOXYDABLE AUSTÉNITIQUE 316L*. PhD thesis, INSTITUT NATIONAL POLYTECHNIQUE DE GRENOBLE, Grenoble, 2004.
- [26] C. Déprés, C. F. Robertson, and M. C. Fivel. Low-strain fatigue in 316L steel surface grains: a three dimension discrete dislocation dynamics modelling of the early cycles. Part 2: Persistent slip markings and micro-crack nucleation. *Philosophical Magazine*, 86(1):79–97, January 2006. Publisher: Taylor & Francis _eprint: <https://doi.org/10.1080/14786430500341250>.
- [27] C. Déprés, M. Fivel, and L. Tabourot. A dislocation-based model for low-amplitude fatigue behaviour of face-centred cubic single crystals. *Scripta Materialia*, 58(12):1086–1089, June 2008. Number: 12.
- [28] S. J. Basinski, Z. S. Basinski, and A. Howie. Early stages of fatigue in copper single crystals. *The Philosophical Magazine: A Journal of Theoretical Experimental and Applied Physics*, 19(161):899–924, May 1969. Publisher: Taylor & Francis _eprint: <https://doi.org/10.1080/14786436908225856>.
- [29] Karel Obřtlík, Tomášš Kruml, and Jaroslav Polák. Dislocation structures in 316L stainless steel cycled with plastic strain amplitudes over a wide interval. *Materials Science and Engineering: A*, 187(1):1–9, October 1994.
- [30] H. Mughrabi. The cyclic hardening and saturation behaviour of copper single crystals. *Materials Science and Engineering*, 33(2):207–223, May 1978.
- [31] C. F. Robertson, C. Déprés, and M. C. Fivel. Micro-crack initiation in thermal fatigue — an analysis based on experimental and DD simulation re-

- sults. *Transactions of the Indian Institute of Metals*, 63(2-3):529–533, April 2010.
- [32] Christophe Depres, Christian Robertson, and Marc Fivel. 3D Discrete Dislocation Dynamics Investigations of Fatigue Crack Initiation and Propagation. *AerospaceLab Journal*, Issue 9:8 pages, 2015. Artwork Size: 8 pages Medium: PDF Publisher: [object Object].
- [33] Ahmed M. Hussein and Jaafar A. El-Awady. Surface roughness evolution during early stages of mechanical cyclic loading. *International Journal of Fatigue*, 87:339–350, June 2016.
- [34] C. Robertson, G. V. Prasad Reddy, C. Déprés, and M. Fivel. Effect of Grain Disorientation on Early Fatigue Crack Propagation in FCC Polycrystals: Dislocation Dynamics Simulations and Corresponding Experimental Validation. *Transactions of the Indian Institute of Metals*, 69(2):477–481, March 2016.
- [35] G. V. Prasad Reddy, C. Robertson, C. Déprés, and M. Fivel. Effect of grain disorientation on early fatigue crack propagation in face-centred-cubic polycrystals: A three-dimensional dislocation dynamics investigation. *Acta Materialia*, 61(14):5300–5310, August 2013.
- [36] C. Déprés, G.V. Prasad Reddy, C. Robertson, and M. Fivel. An extensive 3D dislocation dynamics investigation of stage-I fatigue crack propagation. *Philosophical Magazine*, 94(36):4115–4137, December 2014. Publisher: Taylor & Francis _eprint: <https://doi.org/10.1080/14786435.2014.978830>.
- [37] G. V. Prasad Reddy, R. Sandhya, K. Laha, C. Depres, C. Robertson, and A. K. Bhaduri. The effect of the location of stage-I fatigue crack across the persistent slip band on its growth rate – A 3D dislocation dynamics study. *Philosophical Magazine*, 97(16):1265–1280, June 2017.
- [38] J. Polák, M. Klesnil, and P. Lukáš. On the cyclic stress-strain curve evaluation in low cycle fatigue. *Materials Science and Engineering*, 28(1):109–117, April 1977. Number: 1.
- [39] J. Polák, I. Kuběna, and J. Man. The shape of early persistent slip markings in fatigued 316L steel. *Materials Science and Engineering: A*, 564:8–12, March 2013.
- [40] J. Polák and P. Liškutían. Nucleation and Short Crack Growth in Fatigued Polycrystalline Copper. *Fatigue & Fracture of Engineering Materials & Structures*, 13(2):119–133, 1990. _eprint: <https://onlinelibrary.wiley.com/doi/pdf/10.1111/j.1460-2695.1990.tb00584.x>.

- [41] J. Polák, K. Obrtlík, and M. Hájek. CYCLIC PLASTICITY IN TYPE 316L AUSTENITIC STAINLESS STEEL. *Fatigue & Fracture of Engineering Materials and Structures*, 17(7):773–782, July 1994. Number: 7.
- [42] Jaroslav Polák. *Cyclic plasticity and low cycle fatigue life of metals*. Number 63 in Materials science monographs. Elsevier, Amsterdam ; New York, 1991.
- [43] K. Obrtlík, J. Polák, M. Hájek, and A. Vašek. Short fatigue crack behaviour in 316L stainless steel. *International Journal of Fatigue*, 19(6):471–475, August 1997. Number: 6.
- [44] J Man, K Obrtlík, and J Polák. Study of surface relief evolution in fatigued 316L austenitic stainless steel by AFM. *Materials Science and Engineering: A*, 351(1):123–132, June 2003.
- [45] J. Man, K. Obrtlík, C. Blochwitz, and J. Polák. Atomic force microscopy of surface relief in individual grains of fatigued 316L austenitic stainless steel. *Acta Materialia*, 50(15):3767–3780, September 2002.
- [46] J. Man, T. Vystavěl, A. Weidner, I. Kuběna, M. Petrenec, T. Kruml, and J. Polák. Study of cyclic strain localization and fatigue crack initiation using FIB technique. *International Journal of Fatigue*, 39:44–53, June 2012.
- [47] Bo Xiao, Richard O’Leary, Anthony Gachagan, Wenqi Li, and Timothy Burnett. Accurate finite element model of equiaxed-grain engineering material for ultrasonic inspection. In *2014 IEEE International Ultrasonics Symposium*, pages 1364–1367, September 2014. ISSN: 1051-0117.
- [48] B. D Wirth, G. R Odette, J Marian, L Ventelon, J. A Young-Vandersall, and L. A Zepeda-Ruiz. Multiscale modeling of radiation damage in Fe-based alloys in the fusion environment. *Journal of Nuclear Materials*, 329-333:103–111, August 2004.
- [49] T. Kruml, J. Polák, K. Obrtlík, and S. Degallaix. Dislocation structures in the bands of localised cyclic plastic strain in austenitic 316L and austenitic-ferritic duplex stainless steels. *Acta Materialia*, 45(12):5145–5151, December 1997.
- [50] Ma Bao-Tong and C. Laird. Overview of fatigue behavior in copper single crystals—I. Surface morphology and stage I crack initiation sites for tests at constant strain amplitude. *Acta Metallurgica*, 37(2):325–336, February 1989.
- [51] J. Ahmed, A. J. Wilkinson, and S. G. Roberts. Electron channelling contrast imaging characterization of dislocation struc-

- tures associated with extrusion and intrusion systems and fatigue cracks in copper single crystals. *Philosophical Magazine A*, 81(6):1473–1488, June 2001. Publisher: Taylor & Francis _eprint: <https://doi.org/10.1080/01418610108214358>.
- [52] C. Déprés, Z. Yang, and C. Robertson. Stage-II fatigue crack growth model from 3D dislocation dynamics simulations. *Philosophical Magazine*, 102(6):504–521, March 2022. Publisher: Taylor & Francis _eprint: <https://doi.org/10.1080/14786435.2021.2009135>.
- [53] Z Yang, C Robertson, X Ma, and C Déprés. Fatigue lifetime prediction based on the stochastic evaluation of a dislocation-mediated stage II crack plasticity model. page 16.
- [54] A.K. Head. XCVIII. The growth of fatigue cracks. *The London, Edinburgh, and Dublin Philosophical Magazine and Journal of Science*, 44(356):925–938, September 1953. Publisher: Taylor & Francis _eprint: <https://doi.org/10.1080/14786440908521062>.
- [55] N. E. Frost and D. S. Dugdale. The propagation of fatigue cracks in sheet specimens. *Journal of the Mechanics and Physics of Solids*, 6(2):92–110, January 1958.
- [56] H. W. Liu. Crack Propagation in Thin Metal Sheet Under Repeated Loading. *Journal of Basic Engineering*, 83(1):23–31, March 1961.
- [57] P. Paris. A rational analytic theory of fatigue. *Trends Engin*, 13:9–14, 1961.
- [58] H. W. Liu. Fatigue Crack Propagation and Applied Stress Range—An Energy Approach. *Journal of Basic Engineering*, 85(1):116–120, March 1963.
- [59] P. Paris and F. Erdogan. A Critical Analysis of Crack Propagation Laws. *Journal of Basic Engineering*, 85(4):528–533, December 1963.
- [60] R. G. Forman, V. E. Kearney, and R. M. Engle. Numerical Analysis of Crack Propagation in Cyclic-Loaded Structures. *Journal of Basic Engineering*, 89(3):459–463, September 1967.
- [61] K. Walker. The Effect of Stress Ratio During Crack Propagation and Fatigue for 2024-T3 and 7075-T6 Aluminum. January 1970.
- [62] R.G. Forman. Fatigue Crack Growth Database for Damage Tolerance Analysis, 2005.

- [63] R.O. Ritchie. Mechanisms of fatigue-crack propagation in ductile and brittle solids. *International Journal of Fracture*, 100(1):55–83, November 1999.
- [64] S. Suresh. *Fatigue of Materials*. Cambridge University Press, October 1998. Google-Books-ID: j4w6frFAiQcC.
- [65] James R. Rice and Robb Thomson. Ductile versus brittle behaviour of crystals. *The Philosophical Magazine: A Journal of Theoretical Experimental and Applied Physics*, January 1974. Publisher: Taylor & Francis Group.
- [66] P. Neumann, H. Fuhlrott, and H. Vehoff. Experiments Concerning Brittle, Ductile, and Environmentally Controlled Fatigue Crack Growth. In *Fatigue Mechanisms*, pages 371–395. ASTM International.
- [67] H. Vehoff and P. Neumann. Crack propagation and cleavage initiation in Fe-2.6%-Si single crystals under controlled plastic crack tip opening rate in various gaseous environments. *Acta Metallurgica*, 28(3):265–272, March 1980.
- [68] R. W. Lardner. A dislocation model for fatigue crack growth in metals. *The Philosophical Magazine: A Journal of Theoretical Experimental and Applied Physics*, 17(145):71–82, January 1968. Publisher: Taylor & Francis _eprint: <https://doi.org/10.1080/14786436808218181>.
- [69] P. K. Mazumdar. Dislocation mechanism based model for stage II fatigue crack propagation rate. *Acta Metallurgica*, 34(12):2487–2492, December 1986.
- [70] P. Vena, D. Gastaldi, R. Contro, and L. Petrini. Finite element analysis of the fatigue crack growth rate in transformation toughening ceramics. *International Journal of Plasticity*, 22(5):895–920, May 2006.
- [71] I. V. Singh, B. K. Mishra, S. Bhattacharya, and R. U. Patil. The numerical simulation of fatigue crack growth using extended finite element method. *International Journal of Fatigue*, 36(1):109–119, March 2012.
- [72] X. F. Hu and W. A. Yao. A new enriched finite element for fatigue crack growth. *International Journal of Fatigue*, 48:247–256, March 2013.
- [73] C Robertson, M.C Fivel, and A Fissolo. Dislocation substructure in 316L stainless steel under thermal fatigue up to 650 K. *Materials Science and Engineering: A*, 315(1-2):47–57, September 2001. Number: 1-2.
- [74] J. Rupil, L. Vincent, F. Hild, and Stephane Roux. IDENTIFICATION AND PROBABILISTIC MODELING OF MESOCRACK INITIATIONS IN 304L STAINLESS STEEL. *International Journal for Multiscale Computational Engineering*, 9(4), 2011. Publisher: Begel House Inc.

- [75] J. Rupil. Multi-cracking in uniaxial and biaxial fatigue of 304L stainless steel; Multifissuration en fatigue uniaxiale et biaxiale de l'acier inoxydable 304L. September 2012.
- [76] N. Malesys. Probabilistic modeling of crack networks in thermal fatigue; Modelisation probabiliste de formation de reseaux de fissures de fatigue thermique. November 2007.
- [77] J. Ahmed, A. J. Wilkinson, and S. G. Roberts. Study of dislocation structures near fatigue cracks using electron channelling contrast imaging technique (ECCI). *Journal of Microscopy*, 195(3):197–203, 1999. _eprint: <https://onlinelibrary.wiley.com/doi/pdf/10.1046/j.1365-2818.1999.00574.x>.
- [78] M. C Fivel, C. F Robertson, G. R Canova, and L Boulanger. Three-dimensional modeling of indent-induced plastic zone at a mesoscale1. *Acta Materialia*, 46(17):6183–6194, November 1998.
- [79] Marc Fivel and Christophe Déprés. An easy implementation of displacement calculations in 3D discrete dislocation dynamics codes. *Philosophical Magazine*, 94:3206–3214, September 2014.
- [80] Jaroslav Polák, Karel Obrtlík, and Alois Vašek. Short crack growth kinetics and fatigue life of materials. *Materials Science and Engineering: A*, 234-236:970–973, August 1997.
- [81] D. O. Harris and H. L. Dunegan. Continuous monitoring of fatigue-crack growth by acoustic-emission techniques: Purpose of this investigation was to further explore the relationship between crack-growth characteristics and acoustic-emission variables such as instrumentation gain and sensor frequency. The threshold conditions for crack detection were also investigated. *Experimental Mechanics*, 14(2):71–81, February 1974. Number: 2.
- [82] R. Pippan and A. Hohenwarter. Fatigue crack closure: a review of the physical phenomena. *Fatigue & Fracture of Engineering Materials & Structures*, 40(4):471–495, 2017. _eprint: <https://onlinelibrary.wiley.com/doi/pdf/10.1111/ffe.12578>.
- [83] V. Moorthy, T. Jayakumar, and Baldev Raj. Influence of micro structure on acoustic emission behavior during stage 2 fatigue crack growth in solution annealed, thermally aged and weld specimens of AISI type 316 stainless steel. *Materials Science and Engineering: A*, 212(2):273–280, July 1996. Number: 2.

- [84] Laurent De Baglion and José Mendez. Low cycle fatigue behavior of a type 304L austenitic stainless steel in air or in vacuum, at 20 °C or at 300 °C: Relative effect of strain rate and environment. *Procedia Engineering*, 2(1):2171–2179, April 2010.
- [85] T. Takeda, Y. Shindo, and F. Narita. Vacuum crack growth behavior of austenitic stainless steel under fatigue loading. *Strength of Materials*, 43(5):532–536, September 2011.
- [86] R. Alain, P. Violan, and J. Mendez. Low cycle fatigue behavior in vacuum of a 316L type austenitic stainless steel between 20 and 600°C Part I: Fatigue resistance and cyclic behavior. *Materials Science and Engineering: A*, 229(1):87–94, June 1997. Number: 1.
- [87] A Van der Ven. The thermodynamics of decohesion. *Acta Materialia*, 52(5):1223–1235, March 2004.
- [88] C. P. Blankenship Jr and E. A. Starke Jr. THE FATIGUE CRACK GROWTH BEHAVIOR OF THE Al—Cu—Li ALLOY WELDALITE 049. *Fatigue & Fracture of Engineering Materials & Structures*, 14(1):103–114, 1991. _eprint: <https://onlinelibrary.wiley.com/doi/pdf/10.1111/j.1460-2695.1991.tb00646.x>.
- [89] J. R. Rice and D. C. Drucker. Energy changes in stressed bodies due to void and crack growth. *International Journal of Fracture Mechanics*, 3(1):19–27, March 1967.
- [90] T. Mura. A theory of fatigue crack initiation. *Materials Science and Engineering: A*, 176(1):61–70, March 1994. Number: 1.
- [91] M Rieth, B Dafferner, and H. D Röhrig. Embrittlement behaviour of different international low activation alloys after neutron irradiation. *Journal of Nuclear Materials*, 258-263:1147–1152, October 1998.
- [92] Ken-ichi Ebihara, Tomoaki Suzudo, Masatake Yamaguchi, and Yutaka Nishiyama. Introduction of vacancy drag effect to first-principles-based rate theory model for irradiation-induced grain-boundary phosphorus segregation. *Journal of Nuclear Materials*, 440(1):627–632, September 2013.
- [93] Masatake Yamaguchi. First-Principles Study on the Grain Boundary Embrittlement of Metals by Solute Segregation: Part I. Iron (Fe)-Solute (B, C, P, and S) Systems. *Metallurgical and Materials Transactions A*, 42(2):319–329, February 2011.

- [94] Cédric Gourdin and Grégory Perez. Réalisation d'Essais de Fatigue Equibiaxiaux dans le cadre de l'action DDC-IC 2020. Technical report, 2020.
- [95] Masayuki Kamaya and Masahiro Kawakubo. Strain-based modeling of fatigue crack growth – An experimental approach for stainless steel. *International Journal of Fatigue*, 44:131–140, November 2012.
- [96] S. Bradaï, C. Gourdin, and C. Gardin. Study of Crack Propagation Under Fatigue Equibiaxial Loading. In *Volume 5: High-Pressure Technology; ASME NDE Division; 22nd Scavuzzo Student Paper Symposium and Competition*, page V005T11A013, Anaheim, California, USA, July 2014. American Society of Mechanical Engineers.
- [97] Masahiro Kawakubo and Masayuki Kamaya. Fatigue Life Prediction of Stainless Steel under Variable Loading (Damage Factors Determining Fatigue Life and Damage Evaluation for Two-Step Test). *Journal of the Society of Materials Science, Japan*, 60(10):871–878, 2011. Number: 10.
- [98] Hager Dhahri, Cédric Gourdin, Grégory Perez, Stéphan Courtin, Jean-Christophe Le Roux, and Habibou Maitournam. PWR EFFECT ON CRACK INITIATION UNDER EQUI-BIAXIAL LOADING: DEVELOPMENT OF THE EXPERIMENT. *Procedia Engineering*, 213:571–580, 2018.
- [99] Seong-Gu Hong, Samson Yoon, and Soon-Bok Lee. The effect of temperature on low-cycle fatigue behavior of prior cold worked 316L stainless steel. *International Journal of Fatigue*, 25(9):1293–1300, September 2003. Number: 9.
- [100] Surajit Kumar Paul. A critical review of experimental aspects in ratcheting fatigue: microstructure to specimen to component. *Journal of Materials Research and Technology*, 8(5):4894–4914, September 2019. Number: 5.
- [101] Nobutada Ohno. Recent Progress in Constitutive Modeling for Ratcheting. *II*, 46(3Appendix):1–9, 1997.
- [102] Guozheng Kang. Ratchetting: Recent progresses in phenomenon observation, constitutive modeling and application. *International Journal of Fatigue*, 30(8):1448–1472, August 2008.
- [103] Surajit Kumar Paul, S. Sivaprasad, S. Dhar, and S. Tarafder. Key issues in cyclic plastic deformation: Experimentation. *Mechanics of Materials*, 43(11):705–720, November 2011. Number: 11.

- [104] Surajit Kumar Paul, S. Sivaprasad, S. Dhar, and S. Tarafder. True stress control asymmetric cyclic plastic behavior in SA333 C-Mn steel. *International Journal of Pressure Vessels and Piping*, 87(8):440–446, August 2010. Number: 8.
- [105] Surajit Kumar Paul, S. Sivaprasad, S. Dhar, and S. Tarafder. Ratcheting and low cycle fatigue behavior of SA333 steel and their life prediction. *Journal of Nuclear Materials*, 401(1):17–24, June 2010.
- [106] Yanyao Jiang and Jixi Zhang. Benchmark experiments and characteristic cyclic plasticity deformation. *International Journal of Plasticity*, 24(9):1481–1515, September 2008. Number: 9.
- [107] Surajit Kumar Paul, S. Sivaprasad, S. Dhar, and S. Tarafder. Cyclic plastic deformation behavior in SA333 Gr. 6 C-Mn steel. *Materials Science and Engineering: A*, 528(24):7341–7349, September 2011. Number: 24.
- [108] X. Feaugas and H. Haddou. Effects of grain size on dislocation organization and internal stresses developed under tensile loading in fcc metals. *Philosophical Magazine*, 87(7):989–1018, March 2007. Publisher: Taylor & Francis _eprint: <https://doi.org/10.1080/14786430601019441>.
- [109] L. Tabourot, M. Fivel, and E. Rauch. Generalised constitutive laws for f.c.c. single crystals. *Materials Science and Engineering: A*, 234-236:639–642, 1997.
- [110] C. Teodosiu and F. Sidoroff. A theory of finite elastoviscoplasticity of single crystals. *International Journal of Engineering Science*, 14(2):165–176, January 1976.
- [111] U. Essmann and H. Mughrabi. Annihilation of dislocations during tensile and cyclic deformation and limits of dislocation densities. *Philosophical Magazine A*, 40(6):731–756, 1979. Number: 6 Publisher: Taylor & Francis _eprint: <https://doi.org/10.1080/01418617908234871>.
- [112] Pauli Virtanen, Ralf Gommers, Travis E. Oliphant, Matt Haberland, Tyler Reddy, David Cournapeau, Evgeni Burovski, Pearu Peterson, Warren Weckesser, Jonathan Bright, Stéfan J. van der Walt, Matthew Brett, Joshua Wilson, K. Jarrod Millman, Nikolay Mayorov, Andrew R. J. Nelson, Eric Jones, Robert Kern, Eric Larson, C. J. Carey, İlhan Polat, Yu Feng, Eric W. Moore, Jake VanderPlas, Denis Laxalde, Josef Perktold, Robert Cimrman, Ian Henriksen, E. A. Quintero, Charles R. Harris, Anne M. Archibald, Antônio H. Ribeiro, Fabian Pedregosa, and Paul van Mulbregt. SciPy 1.0: fundamental algorithms for scientific computing in Python. *Nature Methods*, 17(3):261–272, March 2020. Number: 3 Publisher: Nature Publishing Group.

- [113] Surajit Kumar Paul, S. Sivaprasad, S. Dhar, and S. Tarafder. True stress-controlled ratcheting behavior of 304LN stainless steel. *Journal of Materials Science*, 47(11):4660–4672, June 2012. Number: 11.
- [114] H. Mughrabi. *Dislocations and properties of real materials*. 1985.
- [115] Petr Lukáš. Fatigue Crack Nucleation and Microstructure. January 1996.
- [116] J. Polák. On the role of point defects in fatigue crack initiation. *Materials Science and Engineering*, 92:71–80, August 1987.
- [117] U. Essmann, U. Gösele, and H. Mughrabi. A model of extrusions and intrusions in fatigued metals I. Point-defect production and the growth of extrusions. *Philosophical Magazine A*, 44(2):405–426, August 1981. Publisher: Taylor & Francis _eprint: <https://doi.org/10.1080/01418618108239541>.
- [118] K. Tanaka and T. Mura. A theory of fatigue crack initiation at inclusions. *Metallurgical Transactions A*, 13(1):117–123, January 1982.
- [119] T. Mura and Y. Nakasone. A Theory of Fatigue Crack Initiation in Solids. *Journal of Applied Mechanics*, 57(1):1–6, March 1990.
- [120] Yahiya Ahmed Kedir and Hirpa G. Lemu. Prediction of Fatigue Crack Initiation under Variable Amplitude Loading: Literature Review. *Metals*, 13(3):487, March 2023. Number: 3 Publisher: Multidisciplinary Digital Publishing Institute.
- [121] Michael D. Sangid. The physics of fatigue crack initiation. *International Journal of Fatigue*, 57:58–72, December 2013.
- [122] Michael D. Sangid, Hans J. Maier, and Huseyin Sehitoglu. An energy-based microstructure model to account for fatigue scatter in polycrystals. *Journal of the Mechanics and Physics of Solids*, 59(3):595–609, March 2011.
- [123] A. Manonukul and F. P. E. Dunne. High- and low-cycle fatigue crack initiation using polycrystal plasticity. *Proceedings of the Royal Society of London. Series A: Mathematical, Physical and Engineering Sciences*, 460(2047):1881–1903, July 2004. Publisher: Royal Society.
- [124] L. Cretegny and A. Saxena. AFM characterization of the evolution of surface deformation during fatigue in polycrystalline copper. *Acta Materialia*, 49(18):3755–3765, October 2001.
- [125] M. Risbet, X. Feaugas, C. Guillemer-Neel, and M. Clavel. Use of atomic force microscopy to quantify slip irreversibility in a nickel-base superalloy. *Scripta Materialia*, 49(6):533–538, September 2003.

- [126] Yanjun Wang, Zitao Zeng, and Christian Robertson. Prediction of inter-granular crack initiation susceptibility in post irradiated grade 300 steels. *Modelling and Simulation in Materials Science and Engineering*, 31(5):055008, July 2023.
- [127] C. Robertson, Y. Li, and B. Marini. Dose-dependent strain localization and embrittlement in ferritic materials: A predictive approach based on sub-grain plasticity modelling. *Journal of Nuclear Materials*, 559:153417, February 2022.
- [128] K. Gururaj, C. Robertson, and M. Fivel. Post-irradiation plastic deformation in bcc Fe grains investigated by means of 3D dislocation dynamics simulations. *Journal of Nuclear Materials*, 459:194–204, April 2015.
- [129] D. Hull and D. J. Bacon. Chapter 2 - Observation of Dislocations. In D. Hull and D. J. Bacon, editors, *Introduction to Dislocations (Fifth Edition)*, pages 21–41. Butterworth-Heinemann, Oxford, January 2011.
- [130] K. Obtrlik, C. F. Robertson, and B. Marini. Dislocation structures in 16MND5 pressure vessel steel strained in uniaxial tension. *Journal of Nuclear Materials*, 342(1):35–41, June 2005.
- [131] Ludovic Vincent, Jean-Christophe Le Roux, and Said Taheri. On the high cycle fatigue behavior of a type 304L stainless steel at room temperature. *International Journal of Fatigue*, 38:84–91, May 2012.
- [132] R. A. Smith and K. J. Miller. Fatigue cracks at notches. *International Journal of Mechanical Sciences*, 19(1):11–22, January 1977.
- [133] J. G. Antonopoulos, L. M. Brown, and A. T. Winter. Vacancy dipoles in fatigued copper. *The Philosophical Magazine: A Journal of Theoretical Experimental and Applied Physics*, 34(4):549–563, October 1976. Publisher: Taylor & Francis _eprint: <https://doi.org/10.1080/14786437608223793>.